Magnetization Measurements in Ultrahigh Magnetic Fields

Dissertation
zur Erlangung des akademischen Grades
doctor rerum naturalium
(Dr. rer. nat.)
im Fach Physik
eingereicht an der

Mathematisch-Naturwissenschaftlichen Fakultät I
der Humboldt-Universität zu Berlin
von

Herrn Dipl.-Phys. Alexander Kirste
geboren am 12. August 1973 in Berlin

Präsident der Humboldt-Universität zu Berlin
Prof. Dr. J. Mlynek

Dekan der Mathematisch-Naturwissenschaftlichen Fakultät I
Prof. Dr. M. Linscheid

Gutachter:	1. Prof. Dr. M. von Ortenberg
	2. Prof. Dr. R. Manzke
	3. Prof. Dr. R. Grössinger

eingereicht am:	23. Oktober 2003
Tag der mündlichen Prüfung:	21. Mai 2004

Contents

Introduction

Despite the long history of observation and usage of magnetic phenomena, magnetism remains a field of considerable interest. During the last decades, a plenty of discoveries have emerged in this field thanks to new materials and powerful experimental techniques such as neutron diffraction, nuclear magnetic resonance, the Mössbauer effect or space-resolved methods such as magnetic force microscopy.

Remarkable as well is the improvement and development of applications based on magnetic phenomena, which have become possible by the enormous technological progress in the end of the twentieth century. While the compass remained the only important application until the modern era, permanent magnets used in electrical generators, motors and actuators fostered the technological revolution in the end of the nineteenth century. Nowadays, artificial materials are widely used in magnetic recording. Thin magnetic films or layered systems have replaced particle-like materials, and magnetic sensors take advantage of the giant magnetoresistance effect. A very good example containing all these components are modern hard disk drives, which have reached tremendous storage densities. Promising new technologies are expected in the future from the developing magnetoelectronics or spin-electronics, which combines traditional electronic elements with new effects based on interactions involving the spin of the charge carriers. One of the new applications emerging from the magnetoelectronics will be the non-volatile magnetic random access memory (MRAM). It will be available in a few years and is expected to have a huge potential. Doubtless much effort in basic research and further technological progress are necessary in order to push ahead these developments.

Magnetic fields have always been a powerful tool in solid-state physics. Even relatively small fields allow, for instance, to probe symmetries or to lift degeneracies. With regard to experimental techniques in the field of magnetism, conventional magnetometric measurements are an old workhorse examining macroscopic properties of the materials. However, strong magnetic fields beyond (50. . . 60) T have been rarely applied, and fields exceeding one megagauss (100 Tesla) have become available only by specialized techniques so that the range of very high magnetic fields is a rather unknown area in physics.

Magnetization measurements in high magnetic fields are useful to obtain detailed information about exchange interactions, magnetic anisotropy, spin structure and phase boundaries/transitions of the materials investigated as well as the Fermi surface geometry and superconducting critical parameters. Depending on the relation between the Zeeman energy and the intrinsic interaction energies, very intense magnetic fields can be necessary in some cases to observe the relevant phenomena.

Although ultrahigh magnetic fields can be generated only for a small duration due to the inevitable destruction of the field generating coils by the strong electromagnetic forces, they can be used for scientific experiments. The semidestructive *single-turn coil technique*, which is besides the fully destructive flux compression one of the few methods capable of reliably generating fields in excess of 100 T, is employed in this work. Semidestructive means that the equipment inside the coil consisting of cryostat, sample and sample holder survives the violent explosion of the coil and is generally not damaged. As a result, the single-turn coil technique allows efficient and inexpensive scientific experiments.

The measurement system is completed by an inductive magnetometer made up of a system of pick-up coils and special digitizers, both adapted to the single-turn coil generator with its difficult experimental conditions for electrical measurements. Nonetheless, reproducible experiments at low temperatures in fields up to nearly 200 T have become possible, in which the susceptibility of bulk samples can be measured.

From the point of view of materials or systems to be studied, compounds containing *rare-earth elements* are especially attractive. It is probably this family of elements, which has fostered both scientific results as well as technological progress. On the one hand the rare-earth ions have interesting and different magnetic properties depending on the number of electrons in the inner $4f$ shell. On the other hand they behave chemically very similar since their outermost electron shells have the same configuration. Thus it is not astonishing that plenty of results have been connected with the properties of these elements themselves as well as with the diversity of compounds that can be obtained by appropriate substitutions of atoms in the crystal lattice.

Compounds belonging to two different classes of materials have been investigated in this work: rare-earth zircons RXO_4 (R – rare-earth metal, X = V, As, P) and intermetallic compounds $R\mathrm{Mn_2Ge_2}$ (R – rare-earth metal or Y). While the rare-earth zircons are electrical insulators and form an ideal matrix to study the properties of the (non-interacting) R ions and their environment, the intermetallic compounds can be thought as natural layered systems with strong exchange interactions between the layers containing alternately R, Mn and Ge ions.

Although both systems are physically completely different, both show interesting magnetic properties at low temperatures. The rare-earth zircons $\mathrm{TmPO_4}$ and $\mathrm{PrVO_4}$ are so-called singlet or van Vleck paramagnets in which an energy level crossing of the lowest-lying energy levels causes magnetic anomalies. In contrast, various field-induced magnetic phase transitions are observed in the intermetallic compounds $R\mathrm{Mn_2Ge_2}$.

This thesis consists of two parts. Chapters 1-3 comprise technical aspects related to the experimental setup: the development of a magnetization measurement system for ultrahigh magnetic fields, a description of the total setup and its characterization, while chapters 4 and 5 deal with the experimental investigation of RXO_4 and $R\mathrm{Mn_2Ge_2}$ compounds, respectively.

Chapter 1

Magnetization Measurements in Ultrahigh Magnetic Fields

1.1 Introduction

From the experimental point of view, three (independent) main components are necessary to perform a magnetization measurement: the generator providing the magnetic field, a cryostat to cool down (or heat) the sample and a system measuring the response of the sample. All parts must be designed properly to work together, but in particular under the extreme conditions of pulsed ultrahigh magnetic fields, the dominating component confining the boundary conditions for the other components is certainly the field generator.

These aspects and related consequences will be discussed in this chapter, starting with the generation of ultrahigh magnetic fields in section 1.2. The method used to measure the response of the sample is based on inductive probes, which are similar to a gradiometer. For this reason, particular emphasis will be laid on field distribution and homogeneity.

The experimental boundary conditions in ultrahigh magnetic fields with microsecond duration result in several requirements to the measurement system. Possible designs and circuits for those systems are developed and discussed with respect to performance and applicability in section 1.3.

1.2 Generation of Ultrahigh Magnetic Fields

1.2.1 Techniques for High Magnetic Field Generation

In the design of high-field magnets, two essential problems are encountered: the electrical resistivity which calls for high power and causes enormous dissipation, and the magnetic forces which call for materials with exceptional mechanical strength.

In principle, the first problem could be solved by using superconductors. Unfortunately the superconducting state is destroyed by strong magnetic fields so that their practical use for high-field magnets is very limited, at least with presently known materials. However, type II superconductors, which remain still superconducting in high magnetic fields are used in superconducting DC magnets operating at liquid helium temperatures. The highest fields obtained by these magnets are slightly above 23 T so far [KMAW01].

Another means to cope with the problem of heating is to use pulsed magnets. The electrical conductor of the magnet is heated adiabatically during the pulse and the pulse duration is thus determined by the permissible amount of heat dissipated in the coil. This limit is given by the maximum temperature that can be allowed for particular parts or regions inside the coil. Due to magnetoresistance and skin effect, which increase strongly with magnetic field and become important above 50 T, a radial temperature distribution will result with the highest temperature in the coil center [Her99]. A local overheating may occur especially at the surfaces of the conductors.

The *maximum field* that can be generated without destruction of the coil is determined by the mechanical strength of the coil, which must contain the Maxwell stress. This stress increases proportional to the square of the magnetic field and is approximately 4 GPa at 100 T, which is beyond the yield strength of the strongest materials now available such as maraging steel, electrically non-conducting fiber composites, or well-conducting macro- and micro-composite wires. Thus the yield strength determines the maximum peak field of non-destructive magnets.

Though methods were developed to push on this limit towards even higher fields. However, this can be done only by accepting *destructive* or *semi-destructive* effects during field generation.

Considering these effects, intense magnetic fields can be classified into *very high* fields ranging from (20. . . 100) T (where heating effects and magnetic pressure begin to be important) and *ultrahigh* fields above 100 T or in the multi-megagauss range.

Non-Destructive Pulsed Fields

In principle, any electromagnet is a pulsed magnet because it is switched on and off, but more specific for this class of magnets is a pulse duration of order 1 s. Based on practical limitations of real pulsed magnets, a typical pulse duration is (10. . . 100) ms or even up to 1 s. In a narrow sense, "pulsed" denotes transient fields whose penetration (or skin) depth is smaller than the transverse dimensions of the current-carrying conductor [Kno70]. This definition refers to physical effects in the coil related to the pulsed nature of field and current.

Sometimes distinction is made between *long-pulse* and *short-pulse* fields. If referring to non-destructive magnets only, pulses with a duration of order 10 ms and 1 s, respectively, are meant. As opposed to that, the pair "long" and "short" can also distinguish between pulses from non-destructive and destructive magnets, respectively, where "short" denotes a pulse duration of order microseconds or fractions thereof. Although there is no established convention for quoting the pulse duration, in case of a capacitor discharge it is customary to identify the half period with it, i.e. the span of zero field − peak field − zero field.

An estimate for the *upper limit* B_S of the peak field based on mechanical strength can be derived by assuming an optimized coil with free-standing windings, i.e. with the materials strained to the tolerable maximum everywhere in the coil and excluding the transmission of radial and axial stress. According to [Her98] this limit is given by

$$B_\mathrm{S} = \sqrt{2\mu_0}\sqrt{\sigma_\mathrm{max}}\sqrt{\ln\alpha}, \tag{1.1}$$

where σ_max is the ultimate tensile strength of the materials (conductor and insulation) and α is the ratio of outer and inner diameter of the coil.

The scaling law for the *pulse duration* can be based on the concept of the action integral $J(T_0, T)$ describing the average temperature increase from T_0 to T if adiabatic heating of the current-carrying conductor can be assumed during the pulse [Her98, Her99]. The action integral is given by

$$J(T_0, T) = \int_{T_0}^{T} \frac{D c_p}{\rho}\, dT' = \int_{t_0}^{t} j^2\, dt', \tag{1.2}$$

where the conductor carrying the current density j is described by its electrical resistivity ρ, specific heat c_p and mass density D, all of which are temperature dependent, in general. This relation (1.2) can be transformed into a set of equations, which provide the dependence of pulse duration Δt and magnetic energy at peak field, W_p, on a given peak field B_p, pulse shape and coil geometry [Her98]:

$$\Delta t = \xi\, J(T_0, T)\, G_J \frac{a^2}{B_\mathrm{p}^2}, \tag{1.3}$$

$$W_\mathrm{p} = \frac{1}{2} L I_\mathrm{p}^2 = G_W a^3 B_\mathrm{p}^2, \tag{1.4}$$

$$\Delta t = \xi\, J(T_0, T)\, G_J G_W^{-2/3}\, W_\mathrm{p}^{2/3} B_\mathrm{p}^{-10/3}. \tag{1.5}$$

Here J is a weighted average of the action integral for the materials used in the windings, a is the radius of the bore, and G_J, G_W and ξ are factors depending on the geometry and on the pulse shape, respectively.

An immediate conclusion follows from (1.1) and (1.3): For a given amount of energy supplied by an energy source, higher fields are obtained with smaller bore and shorter pulse duration. This is because the coil volume is limited by the given energy and thus α can only be increased by reducing the bore.

For a given, practically usable field volume (or bore), the limiting factor for the peak field is the limited yield strength of the materials in the coil which have to withstand the enormous magnetic pressure $B_0^2/2\mu_0$ as a consequence of the energy density gradient. Actually, this mechanical stress becomes the main criterion in coil design for fields exceeding 40 T. As a consequence, either extremely strong wires are used as conductor or external reinforcement is applied layer by layer.

The highest fields achieved so far with these non-destructive, wire-wound magnets are 80 T in a 10 mm bore and a pulse duration of 7 ms [Kin01]. These record fields, however, can only be obtained at the expense of a very short lifetime of the magnet, i.e. typically a few shots at the highest fields. User magnets designed for 70 T in a 10 mm bore and 10 ms pulse duration should become available soon [Her01].

Since many years, several projects have been pursued to develop non-destructive 80 T and 100 T user magnets [Her01], but they have been only partly successful up to now. One of the most recent achievements in this respect is the coil-in/coil-ex magnet system of the European ARMS project, which has produced 76 T in a 15 mm bore [JFO+04].

Destructive Megagauss Fields

The generation of ultrahigh fields in excess of 100 T with a practically usable field volume and duration for solid-state physics is possible, but the destruction of the ”coils” cannot be avoided. The corresponding magnetic pressure $B_0^2/2\mu_0$ becomes so large that the yield strength of all known materials is exceeded and a destruction is thus inevitable.

The key to achieve and use nonetheless those ultrahigh energy densities is to concentrate a given amount of energy in a small volume so *quickly* that it cannot escape significantly in the time needed to reach the peak field. A pulse duration of the order of microseconds or fractions thereof is a direct consequence. Also shock waves generated by the fast-rising pressure pulse become important. Experiments in these fields must be finished before the (complete) destruction becomes effective. Two different techniques based on this principle are the *flux compression* and the *single-turn coil* technique.

The *flux compression* relies on the fast compression of the magnetic flux in a conducting cylinder, converting a part of the kinetic energy into magnetic field energy. The peak field depends directly on the implosion speed at the end of the process, which can be of the order of several km/s [Her99]. The compression can be driven either by high explosives or by magnetic forces.

By means of the explosive-driven flux compression, nowadays only applied at the VNIIEF in Sarov (Russia), fields up to (900. . . 1300) T can be routinely obtained [BDK+01]. A record field achieved recently [BBD+] was 2800 T. The electromagnetically driven flux compression is applied at the ISSP in Kashiwa (Japan). Fields above 600 T have been generated by this method [MMU+01].

Although the flux compression is capable of generating the highest fields, the most inconvenient disadvantage is that this method is fully destructive, i.e. the generator and materials therein are destroyed completely. The equipment inside the generator will be destroyed when it is hit by the arriving shock wave, i.e. at maximum field or just after the turnaround.

1.2.2 The Single-Turn Coil Technique

The *single-turn coil technique* relies on a fast capacitor discharge into a small single-turn coil. The rise time of this discharge must be fast enough that the peak field can be reached before the coil starts to expand appreciably. This can only be done if the corresponding circuit consisting of energy source (capacitor bank) and coil has a very small time constant.

The minimization of the time constant determines all other design parameters of the discharge circuit. A very low total inductance is needed, so that capacitor bank, lead conductors, switches and the coil must be optimized in that respect. Only a coil with a single turn can meet this requirement of very low inductance; peak currents will thus be in the megaampere range. Moreover, only a small capacitance can be allowed for the capacitor bank, but at the same time the amount of energy stored must not be less than a given value, which is needed to generate the field in a given volume and to compensate for dissipative losses. Therefore high charging voltages are necessary to adapt to these two requirements. A rough model for this system can be based on a simple LCR oscillating circuit assuming time-independent parameters.

The *coil dynamics*, comprising not only the mere expansion of the coil, but also processes in the coil (e.g. shock waves, phase changes, current density adjustment), is of utmost importance for the performance of this method. As indicated previously, the generation of ultrastrong magnetic fields relies on inertial confinement of the electrical conductor by which the field is set up. Its mechanical properties are less important, but good conductivity and large mass density are favourable so that copper is the material of choice. With regard to physical properties, gold is still better, but it would make experiments very expensive.

The wall thickness must be chosen to be optimal with respect to coil expansion and destructive effects directed to the coil center, which become bigger for heavier or massive coils. If coils are too thin, they may either be blown away too fast or explode prematurely due to the Joule heating. If they are too thick, the field/current ratio becomes smaller as the current spreads over the coil walls, while the expansion of the inner surface is hardly affected. The reason is the compression of the metal by the shock wave.

In an optimized coil, the inner surface will begin to move substantially only when the peak field is reached. As a crude criterion for using the coil at its full potential, the wall thickness ought to be of the order of the distance over which the magnetically induced shock wave travels back and forth during the rise time [Her99].

As revealed by high-speed photography, the coils are enveloped in a rapidly expanding fireball already at peak field; the effect increases very strongly with the peak field [NHG+85]. The very bright spots are most likely related to an electrical discharge (or arcing) in the surrounding of the coil. It is surprising that this is not at all reflected in the field curve, which is generally smooth beyond the first zero crossing. At those times, when the current carrying copper (being solid or liquid) is partly or completely vaporized, the electrical current continues to flow in a plasma.

As opposed to the flux compression, the single-turn coil technique can be used in a *semi*-destructive way leaving the material inside the coil (samples and cryostat) unharmed, since the coil fragments are accelerated radially from the coil center away. Compared to flux compression, another advantage, which is ideally suited for experiments is that at least up-sweep and down-sweep of the relatively smooth field pulse can be used, whereas in flux compression experiments it is only the branch with increasing field.

Nowadays, single-turn coil systems producing megagauss fields used for scientific materials research experiments are operated at the ISSP in Kashiwa (Japan) [MMU+01] and at the Humboldt-University at Berlin [OPS+01]. The maximum peak fields are beyond 300 T within 3 mm or 5 mm bore but diminish with increasing coil diameter.

1.2.3 Field Distribution in a Single-Turn Coil

With some limitations, a real single-turn coil can be regarded as a hollow cylinder (inner radius a, outer radius b) with a small feed gap, the geometrical wall thickness $t = b - a$ being either *thin* ($t \ll a$), *thick* ($t \sim a, b$) or in between.

The current distribution $j(r, z, t)$ inside the STC is generally a very complex function depending on many initial and boundary conditions, but it can be approximated in first order as rotational symmetric with respect to the cylinder axis. It is therefore illustrating to look at the properties of those systems.

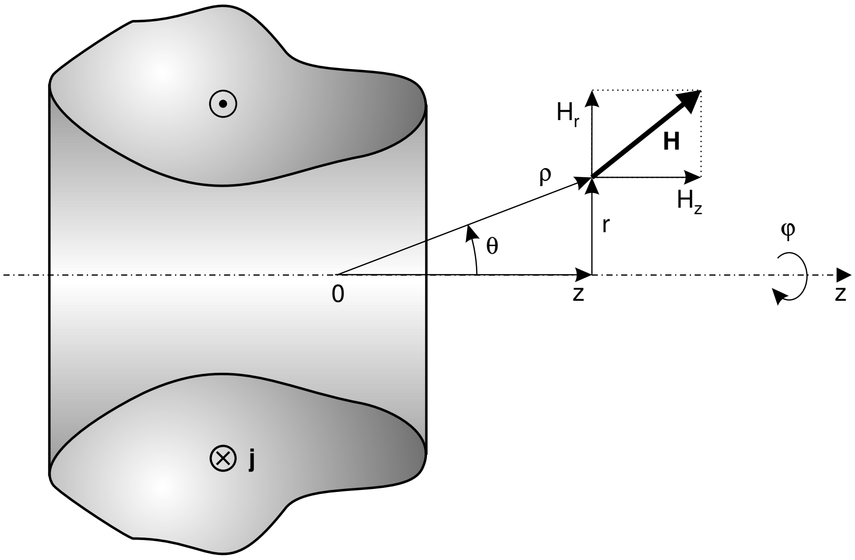

Figure 1.1: Poloidal magnetic field $\mathbf{H}(z,r)$ generated by an axisymmetric current distribution $\mathbf{j} = j\mathbf{e}_\varphi$ with its components in cylindrical coordinates (z, r, φ).

Magnetic Field Configuration of Axisymmetric Systems

In axisymmetric systems there is rotational symmetry about the z-axis and the currents are purely azimuthal, $\mathbf{j} = j_\varphi \mathbf{e}_\varphi$. The related magnetic field is consequently poloidal and has no component along $\mathbf{e}_\varphi$, see figure 1.1. In empty space, where $\mathbf{j} = 0$, the magnetic field problem reduces to a potential problem for the magnetic scalar potential ϕ described by the Laplace equation $\Delta\phi = 0$. Using cylindrical coordinates (z, r), the Laplace equation is given by

$$\frac{1}{r}\frac{\partial}{\partial r}\left[r\frac{\partial\phi}{\partial r}\right] + \frac{\partial\phi^2}{\partial z^2} = 0. \tag{1.6}$$

The field, expressed as the gradient of the scalar potential, $\mathbf{H}(z,r) = -\boldsymbol{\nabla}\phi$, has the components

$$\mathbf{H} = (H_z, H_r) = \left(-\frac{\partial\phi}{\partial z}, -\frac{\partial\phi}{\partial r}\right). \tag{1.7}$$

From these general equations one can derive particular relations between the components of $\mathbf{H}$ by an expansion near the axis [Smy50, Kno00],

$$\phi(z,r) = \sum_{n=0}^{\infty} \frac{(-1)^n}{n!n!}\phi_0^{(2n)}(z)\left(\frac{r}{2}\right)^{2n}, \tag{1.8}$$

where $\phi_0^{(n)}(z) = \frac{\partial^n}{\partial z^n}\phi_0(z)$ and $\phi_0(z) = \phi(z,0)$.

The field components of the series expansion follow from (1.7),

$$H_z(z,r) = \sum_{n=0}^{\infty} \frac{(-1)^n}{n!n!} H_0^{(2n)}(z)\left(\frac{r}{2}\right)^{2n} \quad \text{and} \quad H_r(z,r) = \sum_{n=0}^{\infty} \frac{(-1)^{n+1}}{n!(n+1)!} H_0^{(2n+1)}(z)\left(\frac{r}{2}\right)^{2n+1} \tag{1.9}$$

with $H_0^{(n)}(z) = \frac{\partial^n}{\partial z^n}H_0(z)$ and $H_0(z) = H_z(z,0)$.

As a direct and general consequence of the rotational nature of $\mathbf{H}$, these solutions (1.9) provide full magnetic field $\mathbf{H}(z,r)$ around the symmetry axis in a volume containing no currents by only knowing the component $H_0(z) = H_z(z,0)$ (and its derivatives) at the symmetry axis.

For points near the symmetry axis (small r) we get from (1.9) in first-order approximation from H_r, for $n = 0$,

$$H_r(z,r) \approx -\frac{r}{2}\frac{\partial}{\partial z}H_z(z,0) \tag{1.10}$$

and from H_z differentiated with respect to r, for $n = 1$,

$$-2\left[\frac{\partial}{\partial r}H_z(z_0,r)\right]_{r=\varepsilon} \approx \varepsilon H_0^{(2)}(z_0) \approx \left[\frac{\partial}{\partial z}H_z(z,0)\right]_{z=z_0+\varepsilon} - \left[\frac{\partial}{\partial z}H_z(z,0)\right]_{z=z_0} \tag{1.11}$$

for small ε. Around a point $(z_0, 0)$ on the axis where $\boldsymbol{\nabla} H_z$ vanishes, the latter approximation can be further simplified to

$$-2\left[\frac{\partial}{\partial r}H_z(z_0,r)\right]_{r=\varepsilon} \approx \left[\frac{\partial}{\partial z}H_z(z,0)\right]_{z=z_0+\varepsilon} \quad \left(\approx \varepsilon H_0^{(2)}(z_0)\right). \tag{1.12}$$

That is, when looking at the gradient of the axial field component H_z around such a point, the component (or increment) along the axis is twice as large in absolute value as the one perpendicular to it. Qualitatively, this relation (for absolute values) holds true for the first non-vanishing derivative $H_0^{(2n)}(z_0)$ with a yet larger difference between axial and radial direction, as can be inferred from (1.9).

Thus it can be concluded that the homogeneity of the axial field component is always better in radial than in axial direction. If there is even additional mirror symmetry with respect to a plane through $z = 0$, $H_0(z)$ is an even function and the following expansions hold true:

$$H_z(z,r) = H_0(0) + H_0^{(2)}(0)\left(\frac{z^2}{2} - \frac{r^2}{4}\right) - H_0^{(4)}(0)\left(\frac{z^2r^2}{8}\right) + O(z^4r^4) \tag{1.13}$$

$$H_r(z,r) = -zr\left\{\frac{1}{2}H_0^{(2)}(0) + \frac{1}{4}H_0^{(4)}(0)\left(\frac{z^2}{3} - \frac{r^2}{4}\right) - H_0^{(6)}(0)\frac{z^2r^2}{96} + O(z^4r^4)\right\} \tag{1.14}$$

The better homogeneity of both field components in radial direction becomes clearly visible.

While no time dependence was considered in the above deduction, currents and fields in real problems are time dependent. In the near field limit, which can certainly be applied to problems inside the coil, the resulting potential is identical to that of the magnetostatic problem except for the time dependence. Hence a time dependence can simply be included by using time dependent expansion coefficients $H_0^{(n)}(z,t)$. Apart from the time dependence, all relations regarding the structure of the field or field homogeneity remain unchanged.

Effects in Real Single-Turn Coils

In real single turn-coil systems several effects contribute to change current distribution or distort field symmetry. We can distinguish between effects caused by the connecting flanges to supply the current to the coil and effects inherent in the single-turn coil under steady or pulsed operation.

- Due to the lead-in conductors and the feed gap there is no longer perfect rotational symmetry but there is still full twofold mirror symmetry.

- Due to the fast-pulsed operation of the single turn-coil, which is inevitable for high field generation, effects related to field diffusion (skin effect ...) have to be considered. Depending on current density, magnetic field and material of the coil, properties (e.g. electrical resistance) and conditions in the coil may change dramatically during the pulse as a result of energy dissipation, coil expansion and magnetoresistance.

Although all effects can be understood qualitatively, the comprehensive problem of the *coil dynamics* including all effects at the same time becomes so complex[1] that it would need tremendous efforts to derive a complete solution. Another obstacle is that not all material properties are known under these extreme conditions.

---

[1] A complete solution of the complex nonlinear problem of the coil dynamics (current distribution, coil expansion) including the shock characteristics requires the solution of the set of partial differential equations of magnetohydrodynamics in two dimensions [NHG+85].

However, numerical solutions were obtained for special cases considering only some of these effects (stationary coil with full rotational symmetry, inhomogeneous Joule heating, temperature dependent resistance) in [NHG⁺85] and [PPM⁺99].

Three main effects shall be considered here, all of which play a role also for DC currents.

1. The *edge effect* is the increase of the current density at the edges of the conductor. For DC currents, this effect can be modelled within potential theory. For pulsed currents, nonlinear magnetic diffusion[2] has to be included and the edge effect becomes even stronger. Generally, the pronunciation of this effect depends on the ratio of frequency and resistance, ω/ϱ. For the configuration of a thin single-turn solenoid with infinite conductivity the current distribution was numerically calculated by Bardotti et al. [BBG64]. The result is reproduced in figure 1.2, showing the divergence of the current density at the corners.

   The current concentration at the edges increases with decreasing aspect ratio, i.e. axial width over diameter in the case of a coil or collector width over collector gap in the case of a parallel-plate transmission line.

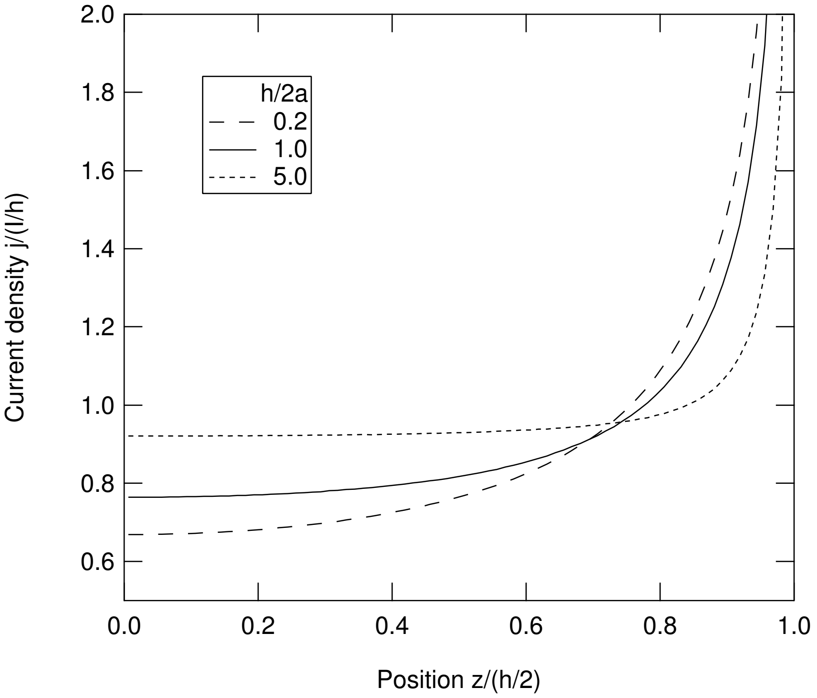

Figure 1.2: *Edge effect.* Current density $j(z)$ as function of the axial position $z/(h/2)$ in thin single-turn solenoids having various ratios of width h to radius a. The smaller the aspect ratio $h/2a$ is, the more pronounced is the edge effect, i.e. the increase of the current density at the edges.

2. The *adaption effect* or *mismatching effect* is due to the junction of collector and solenoid with different pronunciation of the edge effect, which is larger for the coil. Thus current continuity requires axial currents to flow in the vicinity of the junction. In the picture of current line-density, the net effect is a bending of the field lines towards the coil corners as can be seen in figure 1.3.

3. The *collector effect* assumes the coil to be fed by a tapering collector, converging towards the coil. Therefore an additional amount of current is concentrated at the coil ends. In the current line-density picture this will lead to a bending of the field-lines away from the coil corners, see figure 1.4.

---

[2] This problem can be put down to solving a linear electrical network including mutual inductances between the constituent current tubes [PPM⁺99].

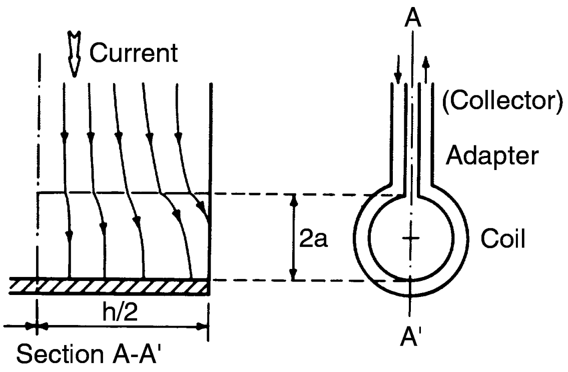

Figure 1.3: *Adaption effect.* The field lines of the current line-density are bent towards the coil corners at the passage from the adapter (collector) to the coil.

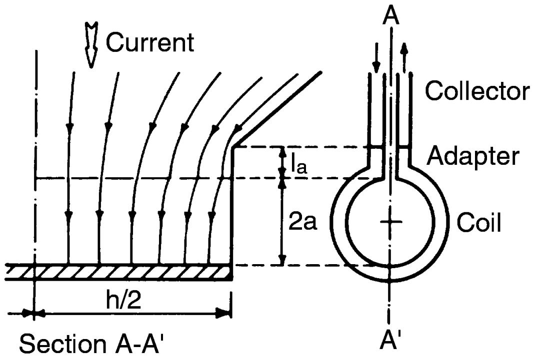

Figure 1.4: *Collector effect.* The field lines of the current line-density are bent away from the coil corners at the passage from the adapter to the coil.

While the edge effect may improve the field homogeneity in short coils, adaption effect and collector effect deteriorate the homogeneity and produce additional azimuthal field components. Despite the distorted symmetry, the influence on any measurement system in such a field, e.g. compensated pick-up coils, can be kept as low as possible if this system is matched to the field symmetry.

The understanding and combination of these mechanisms allows one to reduce the magnitude of these often disturbing effects (e.g. by shaping coil, adapter and collector). It should be pointed out, however, that an optimization would have to take into account the dramatic effects of current density adjustment during high field pulses, which are caused by field and current diffusion in the conductor as well as coil deformation.

To get a better understanding of these time dependent effects and the transient behaviour in the coil, some of the aspects should be reflected in the following.

Irrespective of a coil expansion there is an adjustment (or change) of the current distribution during the pulse as is shown by (numerical) calculations in [NHG$^+$85] and [PPM$^+$99]. The initial current distribution is almost exclusively confined to the inner surface and the edges of the coil with a pronunciation of the inner corners. As time goes on, the current diffuses into the coil and is quenched subsequently by resistive heating, i.e. the domain of maximum current density is driven from the coil surface towards the conductor bulk.

Besides these most prominent features, another effect pointed out in [PPM$^+$99] is that the magnetic field $\mathbf{B}(\mathbf{r},t)$ is in both, amplitude and time dependence a function of the position $\mathbf{r}$. In other words, a separation of $\mathbf{B}(\mathbf{r},t)$ into spatial and time dependent factors, $\mathbf{B}(\mathbf{r}) \cdot f(t)$, is not possible. It is predicted, for example, that the point of time correlated with maximum field

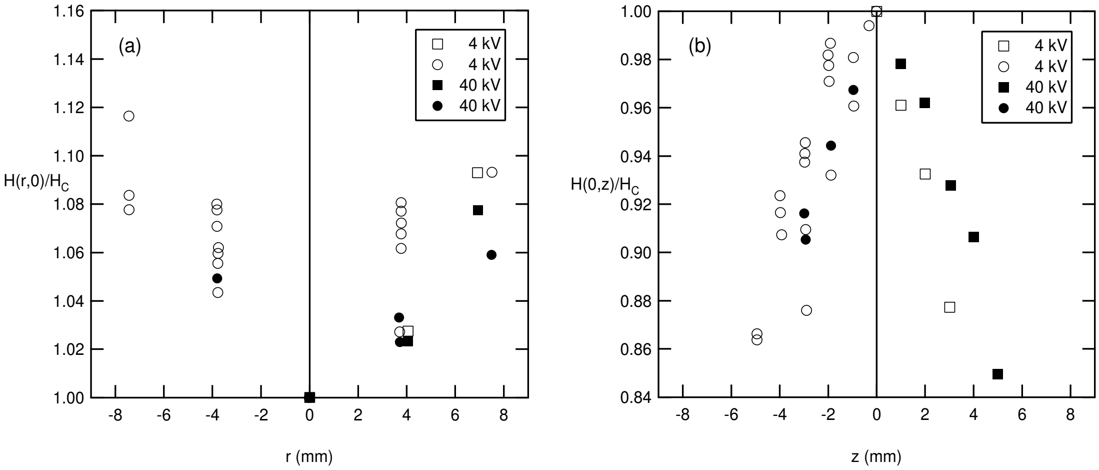

Figure 1.5: Field inhomogeneity of an 18 × 18 × 3 mm^3 single-turn coil in radial (a) and axial (b) direction. The data are taken from [TAN$^+$88] (squares) and [ATN$^+$89] (circles).

depends on the position z on the coil axis. The corresponding time difference increases with the peak field as shown by the simulation for moderate values. This has serious consequences for all measurements, which probe the field over a non-negligible volume, as is the case for magnetization measurements.

Experimental Results

Since the field homogeneity is so important for magnetization experiments, it was investigated experimentally in [TAN$^+$88] and [ATN$^+$89]. This was done by measuring the induced voltages of the field pick-up coils at four different positions in an 18 × 18 × 3 mm^3 single-turn coil along both directions, radial and axial. The results for two different charging voltages or peak fields, respectively, are reproduced in figure 1.5.

As expected, the field distribution inside the coil is such that the coil center forms a saddle point. It is also obvious that the field homogeneity along the radial direction is much better than in axial direction, according to [TAN$^+$88] by a factor of four. Qualitatively, this is exactly what was predicted in the preceding subsections for an axisymmetric system.

Another finding, which was pointed out in the same publication, is that the homogeneity in radial direction was almost independent of the current in the coil, whereas in axial direction a strong dependence on the coil current was reported. Taking into account the data of all measurements, this result seems to be not that obvious.

Recent results related to the adjustment of the current distribution are presented in [PPM$^+$99]. Experimental evidence of the *phase shifts* in the field distribution, which are caused by the characteristic time and position dependent current displacement in the coil, was obtained by evaluating the time dependence of the field measured at two different positions in one and the same field pulse.

The experiments were performed in a 12 × 12 × 3 mm^3 single-turn coil at moderate peak fields for two probes located along the coil axis – one in the coil center, the other one at the upper or lower coil edge. The limitation to low peak fields, which kept the influence of the coil expansion as low as possible, enabled the authors to attribute any effects to a redistribution of the current in the conductor material.

The time difference of the field maxima at these two positions was found to increase with the charging voltage (or peak field) and exceeded 20 ns at 10 kV and 50 ns at 15 kV.

1.3 Design Aspects of a Magnetization Measurement System

1.3.1 Magnetometer for Use in Pulsed Ultrahigh Magnetic Fields

Since magnetism is a relatively wide-ranging subject, there is a vast range of techniques, which can be used to investigate magnetic parameters that are of interest. Methods for measuring magnetic moments or magnetic susceptibility can be based on

- detecting the magnetic flux change caused by the sample by measuring the voltage induced in pick-up coils,
- measuring the dipole field of a magnetized specimen or the corresponding flux (changes) by means of SQUIDs or other methods,
- measuring the forces exerted on a magnetized sample in an inhomogeneous (or gradient) magnetic field,
- measuring the torque exerted by a magnetized sample in a homogeneous magnetic field,

or even other effects related to magnetism.

While these methods are fairly straightforward to implement in stationary fields, difficulties arise in strong pulsed fields, and only very few of them are suitable for use in ultrahigh magnetic fields of microsecond duration. This is because severe restrictions are posed by the experimental boundary conditions, the most critical of which is certainly the short duration of the pulse. Although the force method could be adapted to (long-) pulsed fields by Kapitza in 1931 [Kap31], the method is inappropriate for the use in fast transient fields.

Another possibility, which is suitable for transient fields, but limited to a small class of specimens is a magnetooptical measurement based on the Faraday effect [Ede72], [MPP$^+$98]. The Faraday effect manifests in the rotation of the polarization plane of linearly polarized radiation passing through the sample to be investigated. The quantity to be measured is the transmission (i.e. intensity) of the radiation transmitted through polarizer, sample and analyzer from which the rotation angle of the polarization plane can be derived. Assuming the propagation direction of the radiation to be parallel to the magnetic flux density $\mathbf{B}$, the rotation angle is proportional to $B = \mu_0(H + M)$.

Taking the above facts into consideration, the most convenient and appropriate method for use in transient fields consists in using inductive magnetometers. This method is based on a very common principle, measuring the voltage in a pick-up coil, which is induced by a fixed sample in a varying field.

The inductive probes, which can have arbitrary shape, in principle, measure the time derivative of the enclosed flux $\Phi = \int_F \mathbf{B}\, d\mathbf{F}$, where the magnetic flux density $\mathbf{B}$ in matter is given by $\mathbf{B} = \mu_0(\mathbf{H} + \mathbf{M})$. Assuming a location-independent time dependence, the following equation

$$U_{\mathrm{ind}}(t) = -\frac{d\Phi}{dt} = \tilde{\alpha}\frac{dB(t)}{dt} = \tilde{\beta}\left(\frac{dM(t)}{dt}\right) + \tilde{\gamma}\left(\frac{dH(t)}{dt}\right) \tag{1.15}$$

holds true for the induced voltage $U_{\mathrm{ind}}(t)$. The coefficients $\tilde{\beta}$ and $\tilde{\gamma}$ describe the coupling of the flux of sample ($\leftrightarrow \mathbf{M}(\mathbf{r})$) and field ($\leftrightarrow \mathbf{H}(\mathbf{r})$), respectively, to the probe.

Knowing the coefficients $\tilde{\beta}$, $\tilde{\gamma}$ and dH/dt, the magnetization M can be determined from the induced voltage U_{ind}. Since one is only interested in the magnetization signal, which is often small compared to that from the field, it is advantageous to have coils with $\tilde{\gamma} \ll \tilde{\beta}$, or preferably $\tilde{\gamma} = 0$. This is realized by *compensated* coils, where the flux of the exciting (background) field is just cancelled out, i.e. $\tilde{\gamma} \cong 0$.

In some designs the compensated coils consist of two identical coils located close to each other with the windings having an opposite sense of rotation (see figure 1.7, type A,B). Although the flux of a homogeneous background field is cancelled out, existing field gradients may still lead to a non-compensated net flux. Thus this type of coil acts as a gradiometer probing the gradient of the background field along a particular direction. Of course, a more detailed analysis of these coils can be extended with respect to higher order derivatives of the field.

Only the application of these compensated coils permits to obtain sufficiently well resolved magnetization data, since resolution and dynamic range of the recording devices are limited and the subsequent subtraction of the component related to the exciting field introduces always an error.

Assuming $\tilde{\gamma} = 0$ for well-compensated pick-up coils, the magnetization is then given by the expression

$$M(t) = \frac{1}{\tilde{\beta}} \int_{t_0}^{t} U_{\mathrm{ind}}(t')\, dt' + M_0, \tag{1.16}$$

where M_0 is the initial magnetization at t_0. Provided that the experimental conditions of subsequent experiments are fully comparable, the results for M can be improved by subtracting signals obtained with and without sample.

Appendix A derives a useful reciprocity theorem, which simplifies the calculation of $\tilde{\beta}$, the coupling coefficient to the sample. The following subsection 1.3.2 develops the theory necessary to calculate $\tilde{\gamma}$, the coupling coefficient to the field.

1.3.2 Basics of Compensated Pick-up Coils

While the previous subsection referred to the flux induced from a magnetized sample, the following one will deal with the flux induced in a compensated pick-up coil which is placed in a given magnetic field $\mathbf{B}$.

Any *compensated* pick-up coil can be thought of consisting of two partial coils, which are opposite to each other so that the total enclosed flux Φ in a (homogeneous) magnetic field is just cancelled out. Ideally, the two partial areas are exactly equal and their normal vectors are exactly opposite to each other. This would be a perfectly compensated coil with vanishing flux in a homogeneous magnetic field of arbitrary orientation.

Often, however, compensated coils lack these ideal properties. The wire has a finite diameter causing a non-negligible pitch of the windings; the spatial extent of the coil may become effective. Moreover, magnetic fields are inhomogeneous to a certain extent.

Nevertheless, a simple model can explain basic characteristics of such a coil in a homogeneous magnetic field. It is assumed that the two partial coils, which form the compensated coil, have areas A_i and normal vectors $\mathbf{n}_i$, $i = 1, 2$, respectively. In general these quantities are *effective* values, where A_i is the area corresponding to extreme (maximum) enclosed flux of the partial coil i in homogeneous magnetic field and $\mathbf{n}_i$ the related normal vector; 2γ being the angle between $\mathbf{n}_1$ and $-\mathbf{n}_2$.

The total flux of the compensated coil in a field $B\mathbf{e}_z$ is then given by

$$\Phi(\alpha) = BA_1 \cos(\alpha + \gamma) - BA_2 \cos(\alpha - \gamma), \tag{1.17}$$

where α is a tilt angle around one axis perpendicular to z, see figure 1.6. The flux can become zero at a tilt angle $\alpha_0 = \arctan[(1-a)/(1+a) \cdot \cot(\gamma)]$, where $a = A_2/A_1$; it is always zero if $\gamma = 0$ and $a = 1$; there is no solution if $\gamma = 0$ and $a \neq 1$. Hence it is possible to reach perfect compensation at a definite tilt angle α_0, though the axes of the partial coils are not necessarily parallel to the field direction. On the other hand, this means also that an almost ideal compensation (with respect to one direction) can get worse if the coil is tilted.

Besides a small or vanishing flux, another important criterion for good compensation is the small value of $d\Phi/d\alpha$. Assuming a good compensation, i.e. $a \approx 1$ $(A \approx A_1 \approx A_2)$ and $\gamma \ll 1$ as well as small tilt angles $\alpha \ll 1$, the relation

$$\frac{d\Phi}{d\alpha} \approx -2\gamma BA \tag{1.18}$$

can be derived from (1.17) showing that the misalignment angle 2γ between the two partial coils is a crucial design parameter.

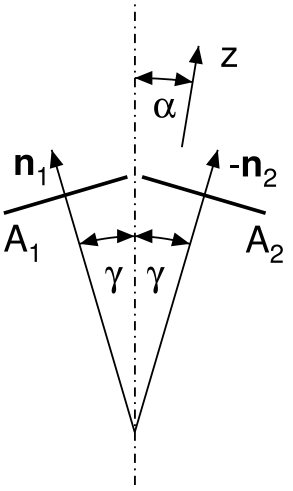

Figure 1.6: Schematic of a compensated pick-up coil consisting of two coils with effective areas A_1 and A_2. The effective normal vectors $\mathbf{n}_1$ and $\mathbf{n}_2$ are nearly opposite to each other and include an angle of 2γ.

To simplify the above treatment, it was assumed that the tilt axis (angle α) and the axis of the misalignment angle γ are parallel. In practice two independent tilt axes (and angles α, β) have to be considered.

A more detailed analysis of pick-up coils requires to calculate the actual contour integral of the vector potential $\mathbf{A}$ along the contour c of the coil,

$$\Phi = \int_F \mathbf{B}\, d\mathbf{F} = \int_F \boldsymbol{\nabla}\times\mathbf{A}\, d\mathbf{F} = \oint_{c=\partial F} \mathbf{A}\, d\mathbf{r} \tag{1.19}$$

for a given magnetic field $\mathbf{B} = \mu\mathbf{H}$. For an axisymmetric current distribution around $\mathbf{e}_z$ the vector potential $\mathbf{A} = A_\varphi \mathbf{e}_\varphi$ in a space not containing any current can be expressed analogously to (1.9) by

$$A_\varphi(z,r) = \mu \sum_{n=0}^{\infty} \frac{(-1)^n}{n!(n+1)!} H_0^{(2n)}(z) \left(\frac{r}{2}\right)^{2n+1} . \tag{1.20}$$

The result of calculations using (1.19) and (1.20) for all coil types shown in figure 1.7 confirms what could have been anticipated. Even in a homogeneous field a perfect angle independent compensation cannot be reached. The reason is the finite and non-negligible pitch of the turns, forming a helix on which all coils are based. This influence cannot be cancelled out in the two partial coils. As function of the two tilt angles around x- and y-axis, the lines of constant flux in a homogeneous magnetic field are parallel and for small tilt angles also equidistant.

The degree of compensation of a coil at a fixed tilt angle can be estimated by the full area compensation ratio, i.e. the ratio

$$r = \frac{\Delta A_{\text{tot}}}{A_{\text{tot}}} = \frac{\Delta A_{\text{tot}}}{NA}, \tag{1.21}$$

where ΔA_{tot} is the non-compensated area, $A_{\text{tot}} = NA$ the total (compensated) area and N the number of turns. Well-compensated coils with $r \sim 1\%$ or lower can be produced only if deviations from the planned (often highly symmetric) coil design are very small. This shall be demonstrated by an example.

A circular disc with diameter d has the area $A = (\pi/4)\, d^2$. A small deviation Δd of the diameter introduces a relative change of the area of $\Delta A/A = 2\Delta d/d$. For a typical value of $d = 1.4\,\text{mm}$ and a deviation $\Delta d = 0.01\,\text{mm}$, the relative change in area is about 0.014. An understanding of this direct proportionality, the orders of magnitude involved and consequences for the compensation are not only relevant during production of the coils but also when an uneven shrinking of the two partial coils may occur.

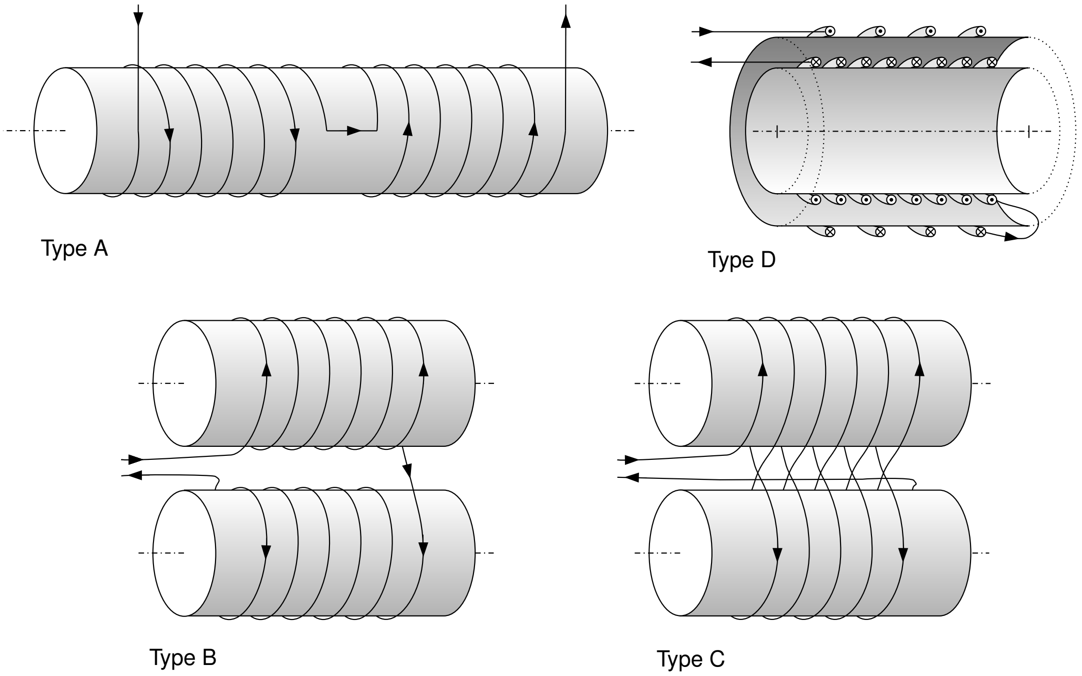

Figure 1.7: Various types of compensated pick-up coils: Axial type (A), Radial type (B), Radial alternative type (C), Coaxial type (D).

1.3.3 Realization of Compensated Pick-Up Coils

Inductive probes used to measure magnetization of samples in a varying magnetic field must consist at least of a field pick-up coil and a compensated pick-up coil. Both are arranged close together so that the field is measured near the sample but the influence of the sample on the field pick-up coil still remains small. Several designs of pick-up coils, which were used in non-destructive pulsed fields, can be found in [MMD80], [MRS85], [GES$^+$95], [EGD$^+$01] and [LVHH95].

Various types of compensated pick-up coils are depicted in figure 1.7. Basically it can be distinguished between axial, radial and coaxial types, where the compensation of the latter two can be implemented either in the usual form (i.e. with coil and compensation coil) or by winding the turns alternatively in opposite directions.

Table 1.1: Important properties of various types of compensated pick-up coils. The exact meaning of the columns is given in the text.

Type	Gradient	High Voltage	Manufacturing	Compensation	Symmetr. Comp.
(A) Axial	z	critical	very easy	very good	yes
(B) Radial	r	critical	easy	very good	yes
(C) Radial, alt.	r	ok	easy	very good	yes
(D) Coaxial	(z,r)	critical	complicated	good – poor	no
(E) Coaxial, alt.	(z,r)	ok	very complicated	good – poor	no

Besides the key point of a good compensation ratio, other, more technical and practical properties play a role in manufacturing and application of these coils, which are summarized in table 1.1.

The arrangement of the two partial coils with respect to the field direction z determines the component of the gradient, which is picked up by the compensated coils. This behaviour is pronounced for the axial type (z-component) and the radial type (r-component) but less distinct for the coaxial type. This consideration is important when the field inhomogeneity becomes percepti-

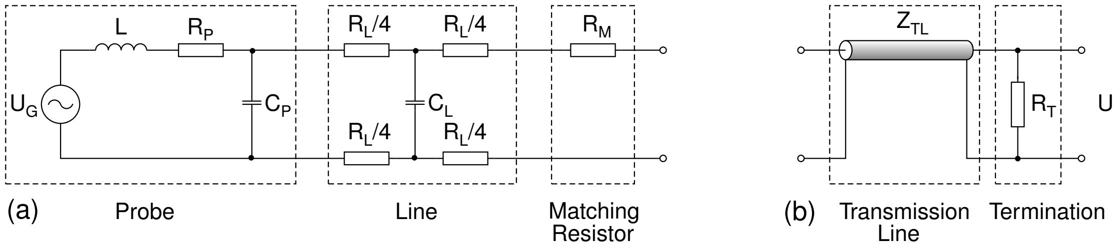

Figure 1.8: (a) Circuit equivalent to the inductive probe including line and matching resistor R_M; (b) Transmission line with impedance Z_TL and termination resistor R_T.

ble.

An important technical criterion is to avoid high voltages, which may cause electrical breakdowns due to insufficient insulation, leading to a destruction of the pick-up coil. Coils that are compensated by alternatively wound turns in opposite direction, such as type C in figure 1.7, greatly diminish this risk. This kind of winding is possible for radial and coaxial types.

A crucial practical consideration is the manufacturing of these coils, which should be possible with a justifiable effort and the necessary preciseness. While axial and radial types are relatively easy to produce, this is much more difficult for the coaxial types. This finds also an expression in the quality of the compensation ratios, which are obtained on average for a typical coil of the respective type. In general, extremely well compensated coils can be obtained if the two partial coils are identical or symmetrical.

Further parameters are inductance, capacitance, symmetry of wiring and the maximum number of turns per length.

Typical full area compensation ratios of these coils with $N = 5\dots30$ turns are in the order of 1% but can range from 10^{-1} to 10^{-4} depending on coil type and quality of manufacturing.

1.3.4 Electrical Circuit of Inductive Probe Systems

In particular in short-pulse experiments, where the relevant physical quantities are measured as function of time it is important to understand and optimize the response of the measurement system to external excitations. For a typical pulse duration of a few microseconds high frequency components up to 100 MHz may arise and must be recorded with smallest possible deviations from the input signal. Especially at these high frequencies parasitic capacitances and inductivities take effect and may influence the response considerably.

Experimental and theoretical investigations of the response of inductive probe systems used in transient magnetic fields can be found for instance in [SA60], [FZ69] and [Kno70].

The partial system measuring the magnetization signal consists generally of the compensated pick-up coil with a short piece of lead wire (a thoroughly twisted pair of thin wire) as well as a (coaxial) cable to transmit the signal to a recording device. Since very high frequency components are present, matched cable termination is absolutely necessary. In addition, there is a deliberately inserted (matching) resistor between the twisted lead-in wire and the cable, seeming not necessary at first sight. Its function becomes clear later on.

An appropriate circuit of such a system is given in figure 1.8, stray capacitances to the environment are neglected, however. The actual probe, i.e. the compensated pick-up coil is described by the self-inductance L, its internal resistance R_P and the distributed capacitance C_P. Its is followed by an electrically short line ($l < \lambda/4$), approximated by its capacitance C_L and resistance R_L. The transmission line is terminated with R_T, usually equal to the cable impedance Z_TL. This cable is not directly connected to the wires from the probe, but there is a matching resistor R_M inserted.

Measurements of Segre and Allen [SA60] show that the steady state response of small magnetic probes can be described by the circuit of figure 1.9 for frequencies at least as high as 30 MHz. This circuit can be considered as low pass consisting of inductance L, capacitance C and resistance R, where the inductance is supplemented with a series resistance r. The voltage U_G produced in the

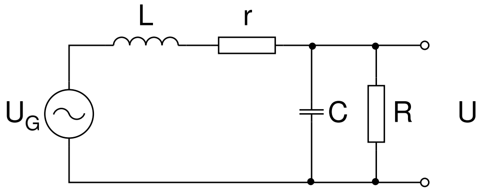

Figure 1.9: Circuit of the inductive probe system obtained from the circuit of figure 1.8 with inductance L and lumped elements r, C and R.

branch of the inductance is equal to that produced in an ideal pick-up coil.

For an analysis of the probe circuit of figure 1.8 it is useful to take advantage of some simplifications and approximations. First it is assumed that the transmission line is terminated with its impedance, i.e. $R_\mathrm{T} = Z_\mathrm{TL}$, so that the cable with termination can be replaced by the resistance R_T only. Second, the network of resistances and capacitances of probe and line is simplified. This can be done easily if either C_P or $R_\mathrm{L}/4$ can be neglected compared to C_L or R_P, respectively. Otherwise more complicated and frequency-dependent transformations must be used to simplify this part. For the typical compensated coils used in this work, both C_P and $R_\mathrm{L}/4$ can be neglected.

Assuming that only C_P can be neglected, the circuit of figure 1.8 is equivalent to that of figure 1.9 with lumped elements $r = R_\mathrm{P} + R_\mathrm{L}/2$, $C = C_\mathrm{L}$ and $R = R_\mathrm{M} + R_\mathrm{T} + R_\mathrm{L}/2$. Or if the two resistances $R_\mathrm{L}/4$ between C_P and C_L are neglected, we obtain $r = R_\mathrm{P}$, $C = C_\mathrm{P} + C_\mathrm{L}$ and $R = R_\mathrm{M} + R_\mathrm{T} + R_\mathrm{L}/2$.

The matching resistance R_M (as part of R) is used to optimize the response of the system. Since most of the parameters of the probe system are fixed (R_T) or can, due to boundary conditions, only be changed within narrow boundaries (e.g. L, R_P or C_L, R_L), this resistance is the only parameter that can be adjusted independently and easily. This optimization problem is subject of appendix B.

1.3.5 Field Measurement

The precise and reliable measurement of the magnetic field is an important prerequisite for all applications. The most common method is to measure the voltage induced in a calibrated pick-up coil [MH85]. Such a pick-up coil is simply made of one or more turns of thin wire to form a definite area in the order of a few mm^2. It has typically a very low inductance, though its response in the probe system is exactly described by the considerations of appendix B.

The induced voltage is proportional to the time derivative of the enclosed flux. It may amount to a few kilovolts even for small coils and can contain very high frequency components up to 10^2 MHz.

In order to measure the signal of the field pick-up coil several possibilities exist with regard to signal transmission (long or short cable, with or without matched termination) and in which form the signal should be digitized (directly or integrated).

When devising such a system one should keep in mind that due to the high field sweep rates the induced voltage in typical pick-up coils of a few mm^2 can reach values beyond 1 kV. Thus termination with the cable impedance, which is in the order of $10^2\,\Omega$ (e.g. $50\,\Omega$ for RG58 coaxial cable) may cause enormous currents. This is especially critical due to the high current load of the thin wires used and the high forces acting on the coil. Pick-up coils with much smaller area, which would reduce voltage and current, are not advisable, however, because the coil area cannot be reduced without increasing the uncertainty of the measurement due to the finite diameter of the wire used.

If the cable is electrically short, i.e. if it is physically shorter than a quarter wavelength of the transmitted signals, matched termination may be omitted and all these problems can be avoided.

The second consideration concerns the actual measurement of the signal with a transient recorder – either directly using a voltage divider or after passing an integrator. In particular the impact of high-frequency components will be different.

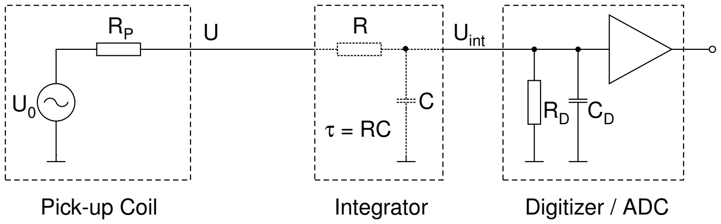

Figure 1.10: Equivalent circuit of the field measurement system applying an *RC* integrator. The circuit representing the pick-up coil is simplified and limited to the internal resistance R_P.

An ideal voltage divider does not change the distribution of the power spectral density, so the output is attenuated by a frequency-independent factor. A suitable voltage divider has to be compensated with respect to its internal inductances and capacitances as well as to the input impedance of the digitizer[3] for two reasons. Besides a simple distortion of high-frequency components, enormous voltage peaks may arise in the output if large slopes are present in the time derivative of the input signal. They can interfere with the digitizer and cause an overload.

On the other hand, the use of an integrator avoids some of these problems. The transfer function of an ideal integrator has a slope of -6dB/octave (or -20 dB/decade) and a constant phase of -90°. Higher frequencies are thus damped in the output. Strong, disturbing high-frequency signals are often produced in pulsed-field experiments capable of generating megagauss fields. They may easily exceed the signal from the fundamental frequency and thus they limit the resolution of the field measurement. Hence the resolution can be improved by using an integrator because these high-frequency signals are suppressed or damped in the output.

Problems may originate from a non-ideal behaviour of internal parts in the high-frequency limit, so that the circuit operates in this range no longer as an integrator.

Errors related to an *RC* integrator, which are caused by its finite time constant $\tau = RC$ as well as input resistance R_D and capacitance C_D of the digitizer measuring the integrated voltage can be removed by partial numerical integration [GCFT68], [MH85],

$$\int^t U(t')\,dt' = R(C + C_D)\,U_\mathrm{int}(t) + (1 + R/R_D)\int^t U_\mathrm{int}(t')\,dt', \tag{1.22}$$

where U is the input (or probe) voltage and U_int the *RC* integrated voltage at the input of the recording instrument.

The use of an *RC* integrator without matched cable termination according to figure 1.10 unites many advantages. Due to its internal structure with relatively large values of R and C, errors related to a combined (and often varying) resistance of cable and probe $R_\mathrm{P} \ll R$ (typically $R_\mathrm{P}/R \sim 10^{-4}$) as well as finite input capacitance $C_D \ll C$ (typically $C_D/C \sim 10^{-4}$) can be neglected. Also the probe current remains relatively small because it is typically $R \sim 10^4\,\Omega$.

As a final remark, the choice between integrated or direct measurement of the induced voltage changes also the influence of errors, which enter in different parts of the measurement system (e.g. baseline shift of the digitizer), but any of those effects depend much on the actual conditions.

1.3.6 Shielding of the Measurement System

When devising a complete measurement system, two strategies may be pursued to achieve a good signal-to-noise ratio or to enable sensitive measurements at all. The first one is to construct the field generator in such a way that any possible or unwanted interference to the measurement system made up of probes and recording devices is avoided by shielding the generator, the second one consists in shielding the measurement system in such a way that it becomes insusceptible to any unwanted external interference.

---

[3] For high frequencies the input capacitance becomes relevant and cannot be neglected.

While the first method has been implemented for instance for a single-turn coil system [MSP$^+$98, PPM$^+$98] or other pulse power systems by placing these systems completely in a large Faraday cage, it is only useful for equipment not located inside the Faraday cage.

If there are any electrical probes inside the field coil, the problem of suppressing unwanted interference requires different approaches.

In general, four main mechanisms of interference to the measurement system can be distinguished [Sch91]:

- galvanic coupling (wiring),
- capacitive coupling (E-field),
- magnetic coupling (H-field),
- radiation coupling (E/H-field).

By means of operating the measurement system freely floating, galvanic coupling to any other system can be safely avoided; galvanic coupling within the measurement system may still occur.

The strength of the latter three mechanisms depends much on actual conditions. Owing to the operating conditions of the single-turn coil system with high voltages and trigger pulses with short rise times it is likely that capacitive and radiation coupling may occur, but due to high currents magnetic coupling will play a major role. In order to reduce external disturbance to the measurement system, it is desirable to diminish the strength of all of these couplings.

At the same time the magnetic coupling is essential inside the field coil – it provides the magnetic field to the sample and the probe and should therefore not be reduced. This is the problem that has to be solved for electromagnetic shielding in megagauss fields: providing an adequate reduction of capacitive and radiation coupling in the vicinity of the coil or even in its inner volume without diminishing the magnetic coupling. Thus enclosing the measurement system in a conducting screen having a wall thickness comparable or larger than the skin depth is no appropriate solution to this problem.

Though, possible electro(static) shields inside those regions with both high B and high dB/dt may be constructed by means of:

- thin-walled cylinders,
- slit cylinders,
- wire metals / weir conductors.

Design rules and limitations of these types are discussed in the following.

Thin-Walled Cylinder

Analytical results shall be derived for the case of an infinitely long, thin-walled cylinder in a parallel, steady sinusoidal magnetic field. An external boundary field

$$H_\mathrm{e} = H_0 \cos \omega t \tag{1.23}$$

is assumed. In the thin-sheet approximation, i.e. if the wall thickness d of the cylinder is much smaller than the harmonic skin depth $\delta = \sqrt{2/\omega\sigma\mu_0}$, the inner field is given by

$$H_\mathrm{i} = H_0 \frac{1}{1+x^2} (\cos \omega t + x \sin \omega t), \tag{1.24}$$

where $x = \omega\tau = r_0 d/\delta^2$ is a dimensionless quantity and r_0 is the radius of the cylinder[Kno00].

The difference between inner and external field is small for $x \ll 1$ and determines also the resulting magnetic pressure Δp, which acts alternately expanding and compressing on the cylinder.

It can be derived either as the difference of the magnetic pressures or by means of the induced surface current. Using (1.23) and (1.24) we get for $x \ll 1$

$$\Delta p = p_\mathrm{e} - p_\mathrm{i} \approx -p_0 \cdot 2\cos\omega t \sin\omega t \quad , \quad p_0 = x \cdot \frac{1}{2}\mu_0 H_0^2, \tag{1.25}$$

where p_0, the amplitude of the magnetic pressure, is directly proportional to x.

Besides the angular frequency ω and the radius r_0 of the shield, which are determined by the field and the experimental setup, respectively, another boundary condition is imposed by the maximum permissible pressure on the hollow cylinder. This determines the allowable x for a given peak field H_0.

Thus the product σd is determined by these quantities, and accordingly, the sheet resistance of the screen must be chosen as

$$R_\square = \frac{1}{\sigma d} = \frac{\mu_0 \omega r_0}{2x}. \tag{1.26}$$

To give some numerical values, the following conditions will be used here and in the following examples: $\mu_0 H_0 = 100\,\mathrm{T}$, $\omega = 2\pi \cdot 100\,\mathrm{kHz}$, $r_0 = 2.5\,\mathrm{mm}$.

The magnetic pressure at 100 T is about 4 GPa, so that $x \leq 10^{-6}$, if a pressure of 10 kPa on the cylinder is allowable, see (1.25). The resulting sheet resistance (1.26) is therefore $R_\square \approx 1000\,\Omega$.

The actual screen effect to external electrical fields depends not only on $R_\square$ but also on the source of the disturbance. It can be expected, however, that this screen will not be very effective. Another difficulty will arise from the fact that typical metals such as copper or aluminum cannot be used as conducting screen since their conductivities would lead to an impractically small wall thickness ($d < 1\,\text{Å}$). On the other hand, for conducting non-metals it is not sure whether the ohmic law will apply in the given regime with high electrical field strengths.

The second potential problem besides the magnetic pressure is the magnetic heating, caused by eddy currents, which generate Joule's heat. The linear current density, constant through the conductor due to the thin-sheet approximation ($d \ll \delta$) is found to be [Kno00]

$$s = -H_0 \frac{x}{1+x^2}(x\cos\omega t - \sin\omega t). \tag{1.27}$$

The total dissipated energy in the cylindrical shell per unit length during one period is thus

$$W = 2\pi \left(\frac{1}{2}\mu_0 H_0^2 \cdot \pi r_0^2\right) \frac{x}{1+x^2}. \tag{1.28}$$

Using $x \leq 10^{-6}$, $d \sim 10\,\mu\mathrm{m}$ and typical values for the specific heat, it turns out, that the temperature increase in the order of (1..10) K will not be critical and is less restricting than the magnetic pressure.

Slit Cylinder

A thin-walled cylinder with a slit along the cylinder axis may seem to overcome the problem of azimuthal eddy currents, which attenuate the magnetic field in the interior of the cylinder. Provided that the wall thickness of the cylinder is small enough, heating will not impose the limiting factor.

Nevertheless, two severe problems still exist. The first one is the high voltage induced across the (narrow) slit. Assuming a field rise velocity of $\mu_0 \dot{H} = 6.3 \cdot 10^7\,\mathrm{T/s}$ as derived from (1.23), the induced voltage amounts to $U_\mathrm{ind} = \pi r_0^2 \cdot \mu_0 \dot{H} \approx 1.2\,\mathrm{kV}$. Since these voltages may easily reach higher values, it is difficult to protect the screen against electrical breakdown.

The second drawback is accounted for by the eddy currents still flowing in the screen. They affect the field homogeneity and symmetry so that the field distribution will depend on the position of the slit.

Wire Metal / Weir Conductor

The design of a weir conductor consists of many insulated, thin wires, which are arranged parallel to each other and parallel to the magnetic field. The cross-section of this construction can have arbitrary shape, but is typically a circle, so that a cylinder is formed by the wire metal. There is a high conductivity along the cylinder axis, but no conductivity perpendicular to this axis, except inside the cross-section of the single wires.

The idea behind this design is to use a "material" with a highly anisotropic conductivity tensor, having conductivity only along one direction. A parallel magnetic field can freely diffuse through this material because azimuthal eddy currents screening the interior of the cylinder are suppressed. The shielding of (quasistatic) electrical fields, however, is not affected by that.

Again, the practical realization by means of insulated wires requires them to be thin enough in order to keep magnetic heating small. It can be stated generally that a conducting slab or sheet, which is placed in a varying, parallel magnetic field, should be split up into as many isolated thinner slabs as possible if the dissipated Joule heat has to be kept as small as possible.

As an example, magnetic heating shall be illustrated for a thin rod in a parallel, steady boundary field $H = H_0 \sin \omega t$. The radius a of the rod shall be much smaller than the flux skin depth, or accordingly $a \ll \delta/2$ in the steady case; the conductivity is assumed to be constant.

The increase of the internal energy density (heat) $Q(r,t)$ at the radius r and time t is given by [Kno70]

$$Q(r,t) = \frac{1}{2}\mu_0 H_0^2 \left(\frac{r}{\delta}\right)^2 \frac{1}{4}(2\omega t + \sin 2\omega t). \tag{1.29}$$

The temperature increase is therefore proportional to $(r/\delta)^2$, provided that $a \ll \delta/2$. Using the conditions as before, the harmonic skin depth is $\delta = 0.2\,\mathrm{mm}$ for copper at room temperature. Thus the surface temperature of a copper wire of $50\,\mu\mathrm{m}$ diameter will increase after a half period ($t = \pi/\omega$) by 28 K, which is still tolerable.[4]

As a result of these considerations, the best and most reliable design of a screen for the application in megagauss fields (i.e. regions with both high B and high dB/dt) takes advantage of a wire metal.

With regard to the electromagnetic shield of the whole measurement system, methods like the *bypass technique* [Sch91] are advantageous to prevent disturbing currents from flowing on the cable sheath. However, sufficient shielding can only be obtained by enclosing all parts of the system, including the pick-up coil. This becomes possible by means of a wire metal.

---

[4] The heating of a thin slab is analogous, but the surface temperature will be four times larger for a comparable thickness of $2a$.

Chapter 2

Experimental Setup

2.1 The Single-Turn Coil Megagauss Generator

2.1.1 General Description

A schematic of the single-turn coil generator is given in figure 2.1. Its dimensions are roughly 5.5 m × 2.5 m × 1.5 m. The whole system including all high-voltage components is located inside a large Faraday cage. All signal lines for remote control are based on optical fibers or pneumatic systems. The only electrical connection penetrating the cage is the strongly filtered power-supply line.

Capacitor Bank and Strip Transmission Line

The energy is stored in a capacitor bank made up of 20 capacitors, which are arranged in ten modules. Each module consists of two capacitors, one switch with trigger circuit and a couple of charging resistors, see also figure 2.2. The total energy of the bank is 225 kJ at a maximum voltage of 60 kV.

The capacitors, produced by Maxwell Laboratories, Inc., have a capacitance of 6 mF (± 10%) each and are rated for a maximum voltage of 60 kV and a peak current of 250 kA [Max]. The internal inductance of a capacitor is approximately 40 nH.

The ten modules are arranged on both sides along a parallel-plate transmission line, the so-called strip transmission line. The insulation between the two plates is made up of several layers of polyethylenterephtalate and polyimide so that it can safely withstand the maximum static high voltage of the bank as well as additional dynamical voltage step-ups. On the other hand, the plate

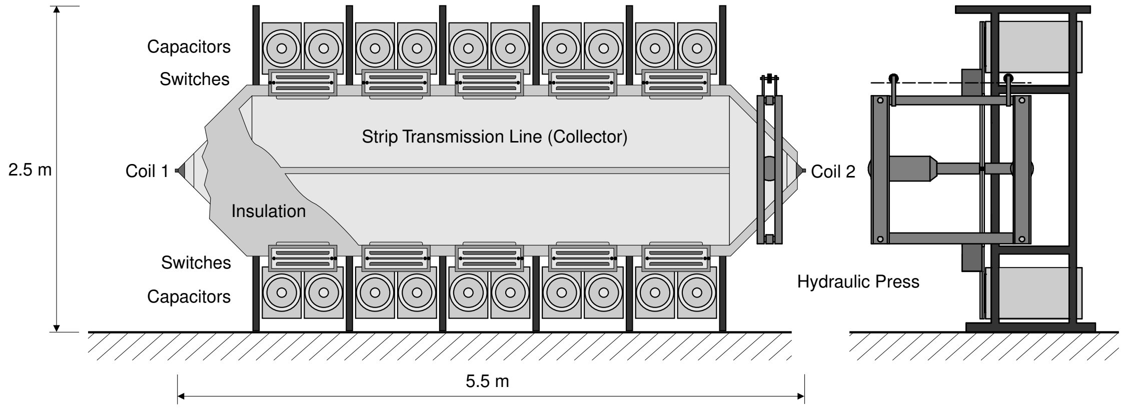

Figure 2.1: Schematic front and side view of the generator. Capacitors and switches are arranged in ten modules on both sides along the horizontal collector. The two coil terminals on both ends can be used alternately.

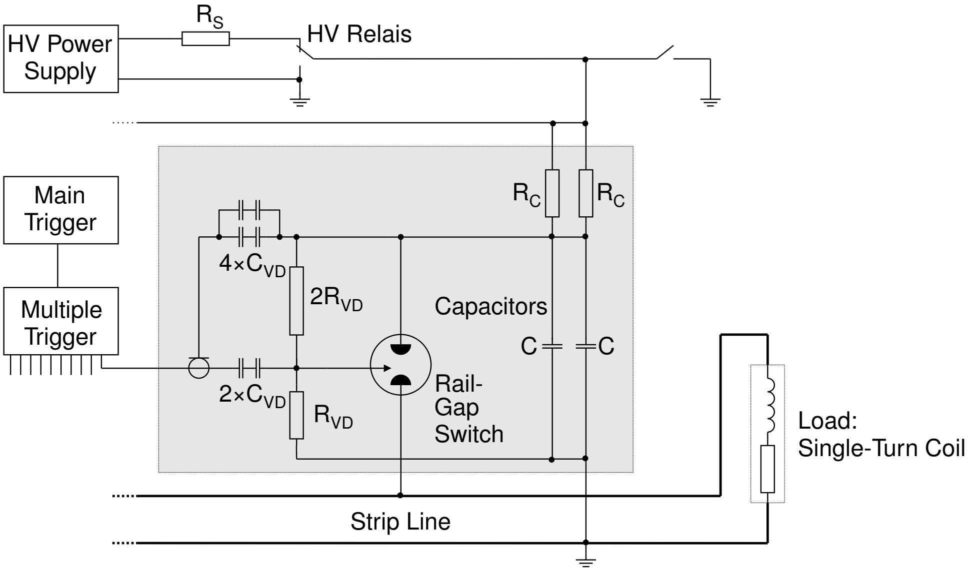

Figure 2.2: Scheme of trigger and high-voltage circuit. Only one module (marked as gray box) out of a total of ten is shown. The values are $R_S = 10\,\mathrm{k\Omega}$, $R_C = 100\,\mathrm{k\Omega}$, $C = 6.5\,\mu\mathrm{F}$, $R_{\mathrm{VD}} = 50\,\mathrm{M\Omega}$ and $C_{\mathrm{VD}} = 1\,\mathrm{nF}$.

separation was kept as small as possible to obtain a small separation-to-width ratio of 1:400 and thus the smallest inductivity possible. This ratio corresponds to a value of about 2.5 nH/m [Sto00].

Special care has been taken in order to prevent surface sliding discharges, spray discharges or even disruptive discharges [Bar99, Sto00].

A Maxwell CCDS-460 power supply with 4 kW output power can charge the capacitor bank to its maximum voltage of 60 kV in less than one minute. Charging as well as discharging of the modules is done via couples of parallel 100 kΩ resistors R_c, which will also dissipate the energy in case of an emergency shutdown, see figure 2.2.

High-Voltage/High-Current Switches and Trigger Circuit

The discharge of the capacitor bank into the single-turn coil requires switches with low inductance, fast rise time and the capability of high current transfer. All these demands are met by the so-called rail-gap switches, i.e. gas-plasma switches with long, parallel electrodes (the rails). The type used is the Model 40200 rail-gap switch from Maxwell Laboratories, Inc., USA. It operates at a maximum voltage of 120 kV and allows peak currents of 750 kA. The switch inductance is 20 nH, the time-delay jitter is less than 2 ns [Max89].

During operation the interior is filled with a pressurized dielectric gas, a mixture of either Ar and O_2 or Ar and SF_6 for operation in the range 10 to 30 kV or 25 to 120 kV, respectively. Once the electrode spacing is adjusted to a given operating range, in our case 30 to 60 kV, the switches can be used at various operating voltages within the given range by using different gas pressures.

The switching process is triggered when a high-voltage pulse is applied to the knife-edged trigger electrode, which is positioned between the two main electrodes.

In order to initiate the simultaneous firing of all modules, a 50 kV trigger generator (Maxwell Model 40168) supplies a pulse to a multiple trigger generator (Maxwell Model 40151-B). The latter provides a trigger voltage ≥ 60 kV at the ten installed output trigger cables. Both trigger generators, which are based on spark-gap switches, have output rise times of < 10 ns and a jitter < 1 ns [Max86]. The trigger equivalent circuit is shown in figure 2.2.

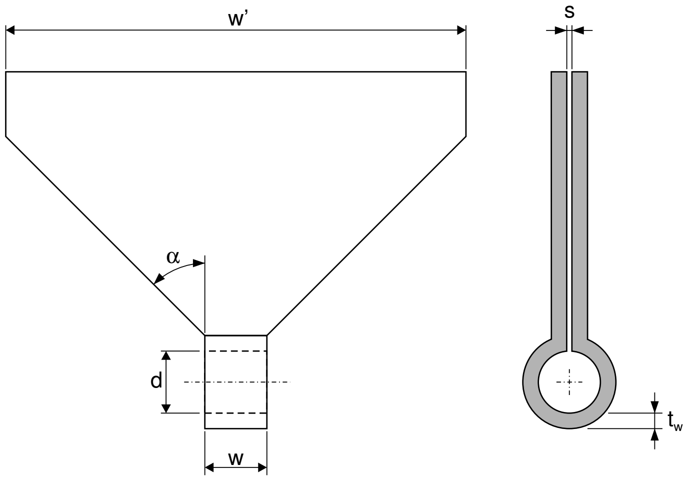

Figure 2.3: Top view and cross-section of a typical single-turn coil.

Front End

The main purpose of the front end is to allow a quick and reliable mounting and dismounting of the single-turn coil and besides this to give a protection against the blast of the exploding coil.

For this purpose the tapering ends of the strip-transmission line have coil terminals carried out as fitting parts into which the feed flanges of the single-turn coil can be inserted. Stable mechanical and electrical contact is provided by soft copper strips attached to pressure rails on each side of the coil bridging the fitting parts and the coil. The high forces ($\sim$ 100 kN) needed to clamp the coil between these contact parts are applied by means of a hydraulic press. This contact is capable of sustaining high peak currents in the megaampere range and withstanding the high forces during the field pulse.

Single-Turn Coil Design

The design of the field generating single-turn coil follows the original one proposed by Forster and Martin [FM67]. The coils are made from an hour-glass shaped sheet of copper, 2.5 or 3.0 mm thick, by bending the bridge which connects the two tapered connecting flanges, see figure 2.3. This allows a complete renunciation of any joints and a cost effective mass production becomes possible.

For high field coils, the (initial) aspect ratio w/d between axial width w and inner diameter d is chosen to reach both, a high current density and a low inductance at the same time. The current density increases with decreasing axial width, whereas the inductance diminishes with increasing axial width. To be more exact, the inductance L_{STC} of the single-turn coil itself, which is to be distinguished from the inductance L_{flange} of the feed flanges (counting to the external circuit inductance) is approximately proportional to $d^2/(2w + d)$, see [FM67]. Typical values are in the order of some nanohenry.

Since both aims cannot be achieved at the same time, a compromise has to be made so that the aspect ratio is generally in the order of 1, depending also on bank inductance and space required in the coil. A minimum acceptable value will be fixed by demands on the field homogeneity.

All the coils we used in our experiments have an aspect ratio of $w/d = 1{:}1$.

2.1.2 Generator Performance

Field and Current Pulse

In the simplest model the discharge of the energy stored in the capacitor bank into the single-turn coil can be described by means of a simple LCR series circuit with appropriate initial conditions.

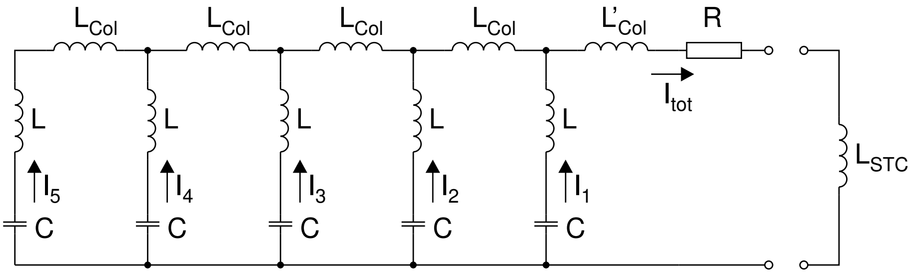

Figure 2.4: Equivalent high-voltage/discharge circuit of the generator. The strip-line is represented by the horizontal inductances L_{Col}, whereas the ten modules are described by five segments with inductance L and capacitance C. All dissipative losses are included in R; L_{STC} is the inductance of the single-turn coil.

This gives damped oscillations of current and magnetic field in the coil, assuming the field to be proportional to the current. Using this model, field curves with low peak field obtained in the limit of non-destructive operation can be well approximated, but values for L,C,R based on a best fit differ from lumped values derived from single parts. One reason for that is the realization of the capacitor bank along an extended strip-line (collector) (see figure 2.1) with finite inductance and capacitance per length, which requires a modified and more complex model.

In this way, an improved model of the Berlin generator is given in [PPM$^+$99]. The basic equivalent model of the capacitor bank consists of five segments, each of which containing portions of total bank capacitance and inductance and which are mutually coupled via the finite collector inductance L_{Col}. All dissipative losses in the entire circuit are included as a lump sum in R. Another inductivity L_{STC} is representing the single-turn coil. The according circuit is shown in figure 2.4.

In the limit of vanishing collector inductance L_{Col} this model is, of course, completely equivalent to the one aforementioned. For finite collector inductance, however, effects on the coil current can be expected since the structure resembles an electrical delay line. A simulation shows that in particular the partial current I_1 of the module which is most close to the single turn-coil is affected and exhibits significant deviations from the other partial currents I_2 to I_5, see also figure 2.5.

Nevertheless, neither the total current through the coil, nor its derivatives show noticeable deviations from a smooth behaviour. Although the values of L_{Col} are in the order of the other inductances, the difference in the time dependence compared to a simple LCR series circuit with *adjusted* parameters is relatively small. It should be emphasized, however, that there is no direct relationship between the parameters of the two models.

Another, more dramatic effect is caused by the finite collector capacitance. In comparison to the basic model of figure 2.4, a lumped capacitance C_{Col} has to be supplemented in each module as indicated in figure 2.6a.

Typically, the collector capacitance C_{Col} is in the order of a few nanofarad, whereas the bank capacitances C are several microfarad. This leads to the situation that the larger capacitances C drive not only the main coil current as calculated in figure 2.5 with the main component around 80 kHz but also superimposed high-frequency oscillations in the range around 10 MHz. The result is a step-like behaviour of the coil current as shown in figure 2.6b. Indeed, these high-frequency oscillations are observed in the field traces and its derivatives, as can be seen in figure 2.7. The dominating high-frequency component is always at 16 MHz.

With regard to magnetization measurements these oscillations are rather disadvantageous as is the case for every disturbance diminishing the smooth time variation of the magnetic field. However, there is no chance to overcome this drawback without decreasing the maximum peak field.

Amplitude and damping of these oscillations depend on resistive dissipation in the capacitor bank and especially in the single-turn coil, which is heated up during the pulse. Hence, the damping is stronger for higher charging voltages and smaller coils, as can be seen in figure 2.7.

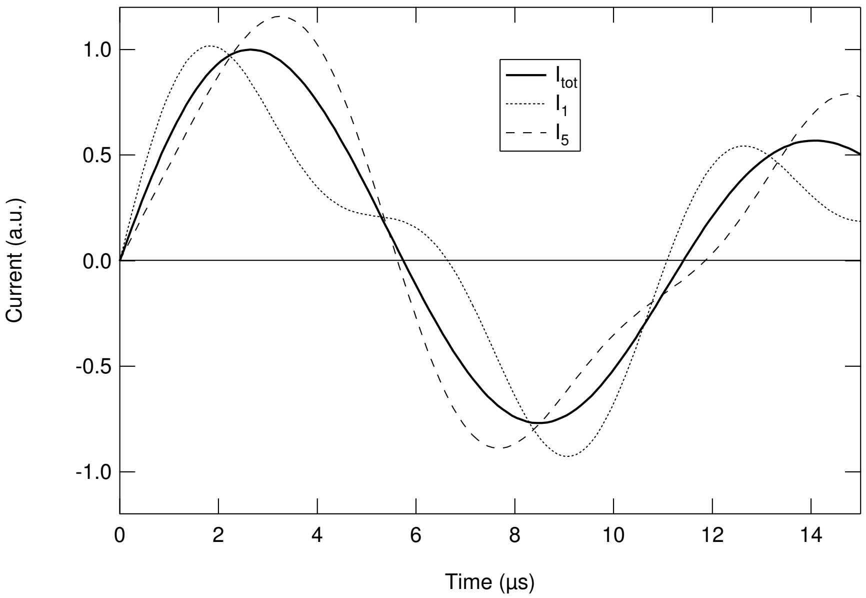

Figure 2.5: Partial currents I_1, I_5 and total current I_{tot} in the generator according to figure 2.4. The current I_{tot} is normalized to its maximum, I_1 and I_5 according to the average of all partial currents.

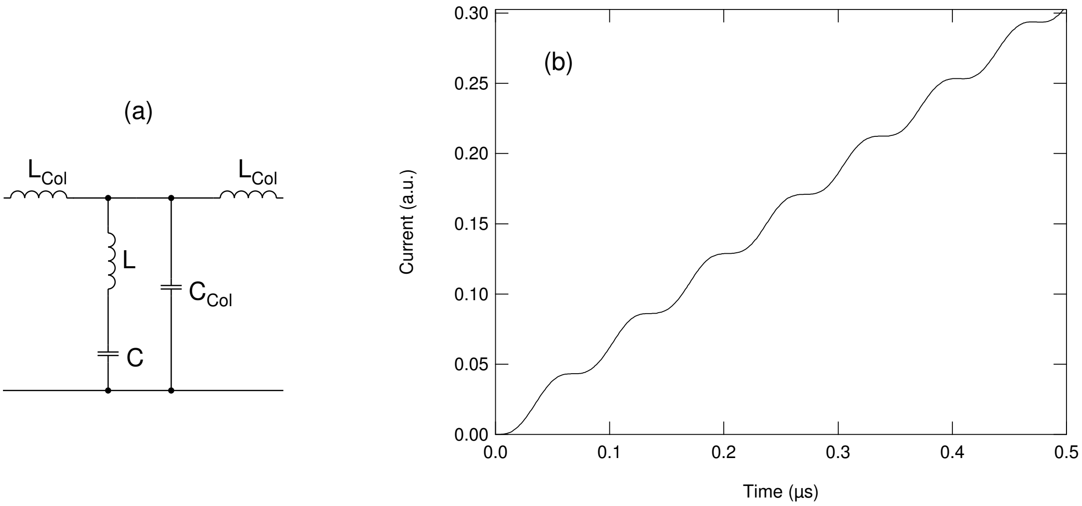

Figure 2.6: (a) Refined equivalent circuit of a module (cf. figure 2.4) including now the finite collector capacitance C_{Col}. (b) Simulation of high-frequency oscillations in the coil current. The current is normalized to its maximum.

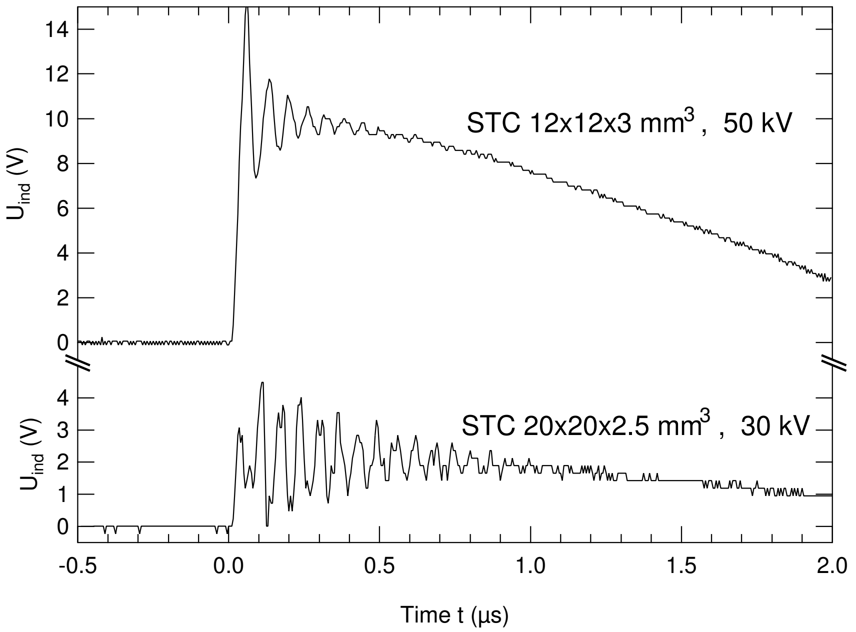

Figure 2.7: High-frequency oscillations in the field as observed by the induced voltage of a compensated pick-up coil for different single-turn coils and charging voltages.

An electrical network model analogous to figures 2.4 and 2.6a supplemented with appropriate resistances is, however, not capable of producing quantitatively correct results of both, field pulse and high-frequency oscillations at the same time. The difficulty arises from different effective resistances due to different skin depths of the corresponding frequency components. The frequencies differ at least by a factor of 100, the resistivities by a factor of 10. In practice, an even faster decay of the high-frequency oscillations can be expected based on interference effects of the partial currents driven by the ten modules, which are likely to have slightly different resonance frequencies [Mül02].

Maximum Field vs. Energy and Coil Size

Figure 2.8 shows the dependence of the peak field on energy, i.e. charging voltage, and coil size. The relation between peak field and charging voltage is nearly linear for the configuration space examined, i.e. coil diameters not too small and charging voltages not too high. Smaller coils allow higher peak fields on the expense of lower field homogeneity.

Although there is a certain scattering of the points in figure 2.8, field pulses of subsequent experiments are quite reproducible with respect to peak field, trigger oscillations and other characteristics. The scattering reflects slightly different charging voltages, varying conditions of current contacts and different pick-up coils.

Coil Dynamics and Related Phenomena

The coil dynamics (i.e. the expansion and deformation of the coil, current displacement, *phase shifts* and other effects) as discussed in section 1.2.3 plays a crucial role not only for performance limitations but also for the field homogeneity. In particular for high energies (i.e. high charging voltages) and at times comparable or larger than the pulse duration certain phenomena occur which are beyond considerations in [NHG$^+$85] or [PPM$^+$99].

Figure 2.9 shows some irregularities occurring near the second zero crossing of the field. The time derivative of the field has a distinct peak, and the signal of the empty compensated coil, reflecting also the spatial field derivative, shows even larger oscillations. This means that enormous

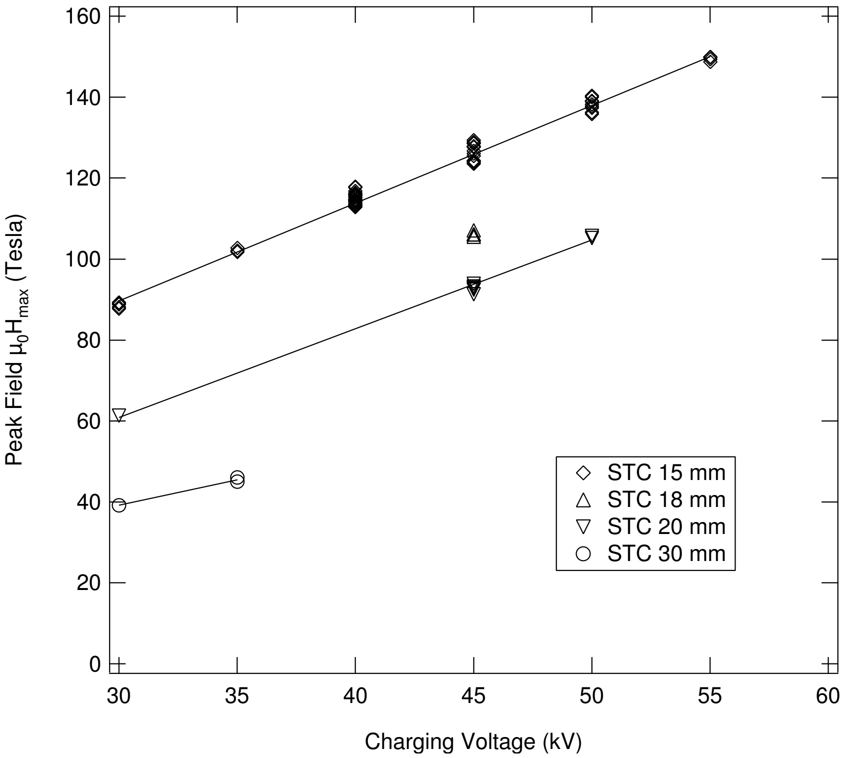

Figure 2.8: Energy dependence of peak fields generated by single-turn coils of various sizes specified by inner diameter and width. Every point belongs to an independent experiment; the lines are only a guide to the eye.

Table 2.1: Dependence of the irregularities occurring in the field pulse $H(t)$ and its time derivative dH/dt on coil sizes and charging voltages U_{HV}. The numbers given in the table mark the first appearance of these irregularities as counted by the number of the corresponding zero crossing of $H(t)$.
Figures in parentheses: rare or weak occurrence; "< 1": irregularities appear already at the end of the main field pulse, clearly before the first zero crossing of $H(t)$; hyphenated figures: irregularities occurring in between; dots: no data available.

U_{HV}	30 kV	35 kV	40 kV	45 kV	50 kV	55 kV	60 kV
STC $10 \times 10 \times 3$ mm^3	·	·	1	·	1	·	·
STC $12 \times 12 \times 3$ mm^3	·	(< 1)	·	1	1	1	·
STC $15 \times 15 \times 2.5/3$ mm^3	2	2	(< 1) / 2	1	1	1	·
STC $18 \times 18 \times 2.5$ mm^3	·	·	·	$< 1 - 2$	1	·	·
STC $20 \times 20 \times 3$ mm^3	(> 4)	·	2	2	2	2	$< 1 - 2$
STC $22 \times 22 \times 2.5$ mm^3	(> 4)	·	2-3 / 3	2	1-2	·	·

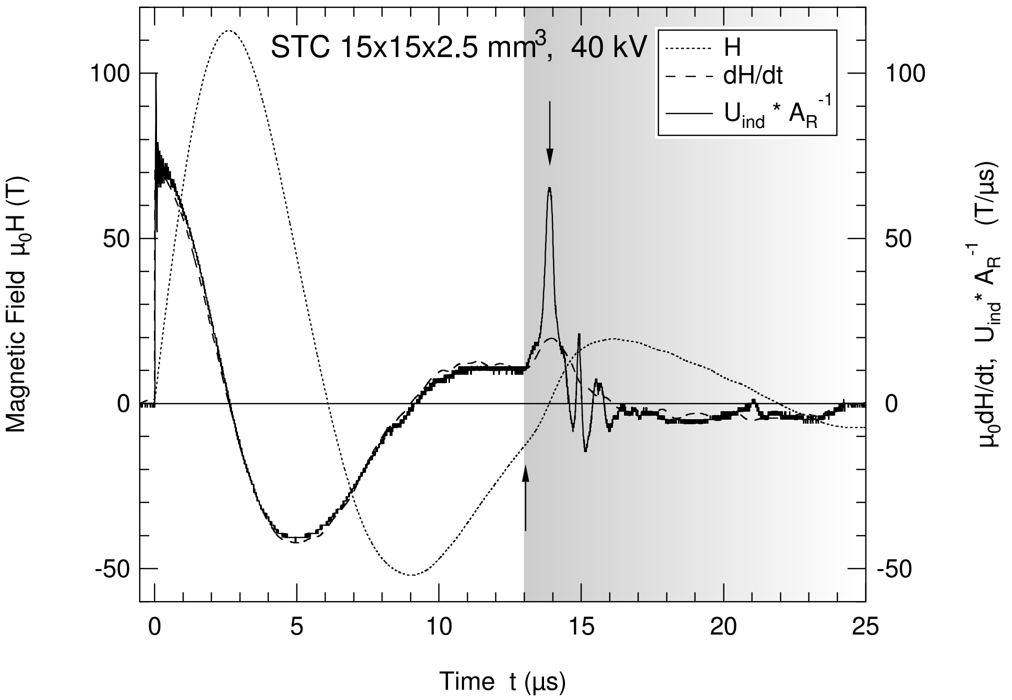

Figure 2.9: Field pulse $H(t)$, time derivative dH/dt and signal of the compensated coil $U_{\mathrm{ind}}A_{\mathrm{R}}^{-1}$ (scaled by A_{R} to match dH/dt) obtained in a 15x15x2.5 mm^3 single-turn coil with 40 kV charging voltage. Some irregularities (marked by arrows) occur near the second zero crossing of H as indicated by a peak in the field derivative and much larger oscillations in the signal of the compensated coil. The data in the shaded area are thus no longer useful for the experiment.

disturbances of the field homogeneity take place at these times. The data in the shaded area are thus no longer useful for the experiment.

An examination for various coil sizes and charging voltages reveals that these phenomena coincide almost always with a zero crossing of the field. For high energies (i.e. high charging voltages) and small coils these phenomena may take place already around the first zero crossing, i.e. just at the end of the main field pulse. Table 2.1 summarizes the onset of these high-energy phenomena for various configurations.

As a consequence, these effects pose a severe limitation for magnetization measurements in the *highest fields*, which require high energies and small single-turn coils. In this case, the data at the end of the down-sweep must be considered as useless or invalid since they reflect mainly the field inhomogeneity rather than the response of a sample. The maximum field up to which the down-sweep is not impaired is about 115 T, obtained by a $15 \times 15 \times 3$ mm^3 single-turn coil at 40 kV charging voltage.

Question arises about the origin of this phenomenon. Obviously it requires a certain minimum energy density of Joule heat of the coil conductor and secondly relatively low fields seem to be another precondition. Thus after a certain (short) time the amount of energy deposited in the coil conductor will be sufficient to change the state of the material, i.e. to liquefy or vaporize at least a part of the material. Moreover, the expansion of the coil or conductor material will be already appreciable at the occurrence of this effect.

A possible explanation, which should also account for the disturbance of the field homogeneity, is based on plasma or arc initiations due to the high voltage present at low fields. This could also be connected with the magnetic compression force on the current carrying conductor, which is effective during large fields with large coil currents flowing, while its absence near the field zero may allow a fast expansion of the hot plasma.

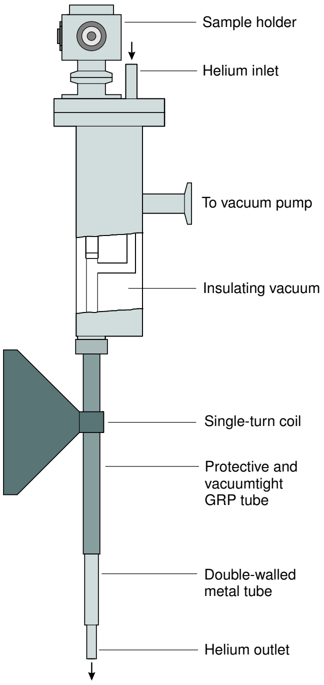

Figure 2.10: Schematic side view of a Helium flow cryostat designed for use in the single-turn coil.

2.2 The Cryostats

Two different kinds of cryostats have been developed for the use with the single-turn coil technique: a helium flow cryostat and a helium bath cryostat. To be applicable for this purpose, the tail and all parts in the vicinity of the single-turn coil must be electrically insulating in order to avoid eddy currents. That is, instead of metals other materials such as glass fiber reinforced plastics (GRP) and epoxy resin are used, which have to be helium-tight in addition. Easily replaceable protective tubes are an integrated part of both types of cryostats.

Figure 2.10 schematically illustrates constructive details of the helium flow cryostat. Three tail sizes with outer diameters between 14 mm and 10 mm are available. The respective usable inner diameters are 7.5 mm and 5 mm. A temperature of nearly 4.2 K can be reached in this cryostat. It is controlled by the pressure put on the helium vessel and measured by a calibrated thermocouple. The thermocouple (Chromel-CuFe (0.15%)[1]) is used at a reference temperature of 77 K in liquid nitrogen (LN_2).

Bath cryostats can be used due to the vertical bore orientation of the single-turn coil. Up to two litres of liquid helium (LHe) can be stored in the present system allowing an operating time of up to four hours. Besides the thermal insulation provided by an insulating vacuum there is a continuous radiation shield of liquid nitrogen. The tail consists of two inner tubes made of epoxy resin with an insulating vacuum in between and a replaceable outer tube made of GRP. The latter is used as a part of the radiation shield and as protective tube at the same time. Outer diameter and usable inner diameter of the tail are 14 mm and 7 mm, respectively. Temperatures down to 2 K can be reached by reducing the vapour pressure above the LHe level. Calibrated Allen-Bradley resistors are used to measure the temperature and the level of the LHe.

Matching these specifications with the performance of the single-turn coil generator, the following combinations of temperature and field are possible:

- $T \geq 4.2\,\mathrm{K}$, $B \leq 180\,\mathrm{T}$ in 12x12x3 mm^3 STCs,
- $T \geq 2.0\,\mathrm{K}$, $B \leq 150\,\mathrm{T}$ in 15x15x3 mm^3 STCs.

---

[1] Manufactured by Lake Shore, USA.

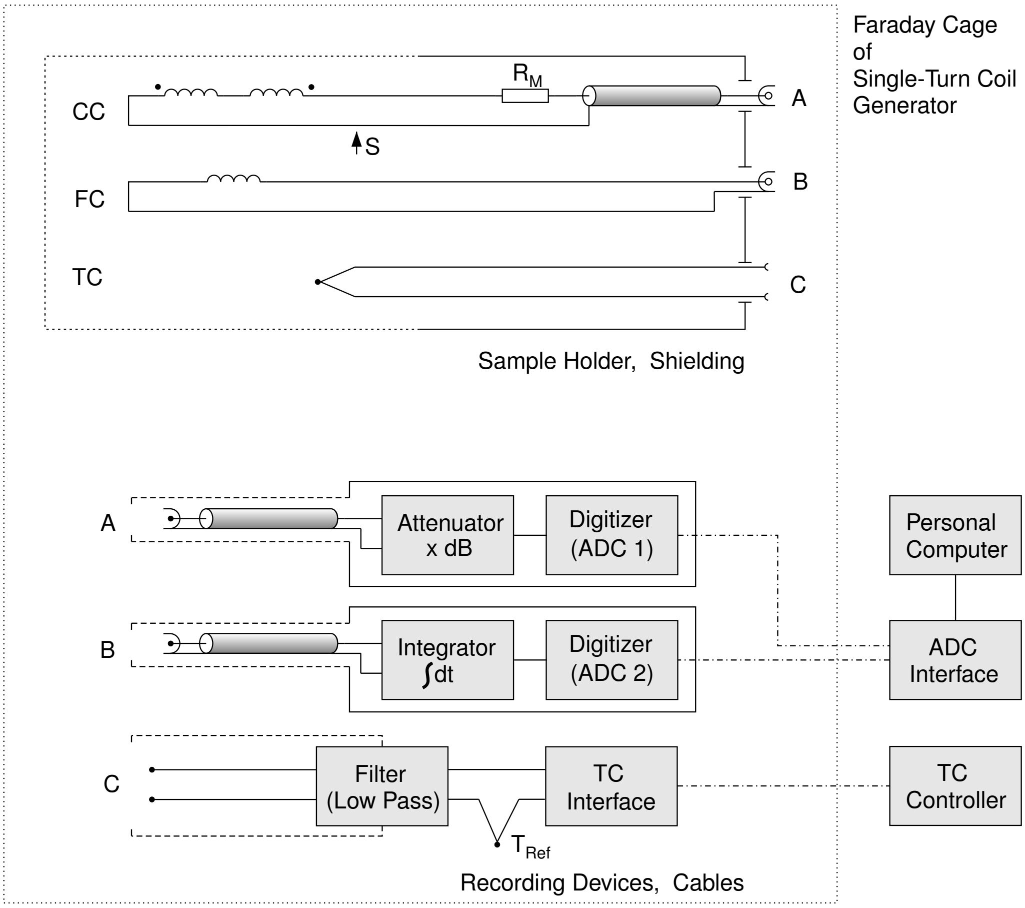

Figure 2.11: Block diagram of the measurement system. The electromagnetic shielding of the system allows the maximum bandwidth possible for the two channels of compensated pick-up coil (CC) and field pick-up coil (FC), whereas the thermocouple (TC) requires only quasi-DC sampling. Optical signal transmission via glass fibers is used to control the recording devices and to read out the data.

2.3 Measurement System and Data Acquisition

Figure 2.11 shows a block diagram of the measurement system. In order to suppress trigger noise and other unwanted interference to the measurement system, the whole system consisting of pick-up coils, cables and recording devices is enclosed in an electromagnetic screen, which is necessarily implemented as a wire metal in the vicinity of the single-turn coil, see section 2.3. Of course it must allow the maximum bandwidth possible for the two channels of compensated pick-up coil and field pick-up coil, whereas this is not necessary for the temperature measurement. In order to avoid any (unfiltered) electrical connections through the electromagnetic screen and the Faraday cage of the field generator, optical signal transmission via glass fibers is used to control the recording devices and read out the data.

Details of all main components are given in the following subsections.

2.3.1 Field Measurement

The pulsed magnetic field is monitored by means of a calibrated pick-up coil. This is made up of up to four turns of 60 μm copper wire with double grade polyimide insulation.

The induced voltage is fed directly into a passive *RC* integrator and measured by an analog-to-digital converter (ADC) according to figure 1.10, thus taking advantage of the benefits described in section 1.3.5. Since the cable from the pick-up coil to the integrator is only about 1.5 m in length,

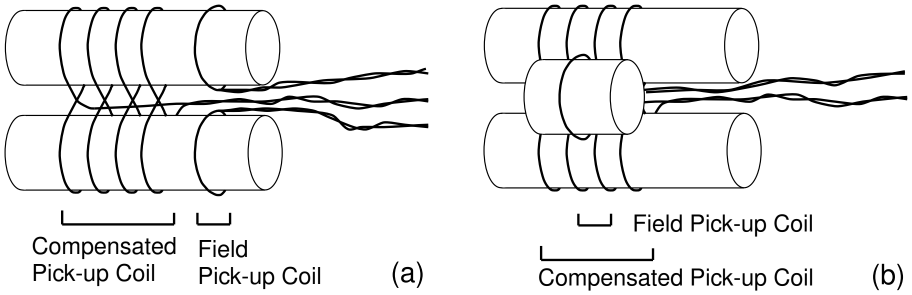

Figure 2.12: Possible arrangements of field pick-up coils and compensated pick-up coils.

impedance matched termination was omitted. The digitized data are stored and transmitted optically via glass fiber to a computer.

Calibration is performed individually for all field pick-up coils by comparing their areas with that of a similar-sized reference coil with well-known area. The calibration procedure is based on measuring alternately the voltages induced in the reference coil and the coil under test. This procedure is performed in a homogeneous, alternating magnetic field at frequencies around 100 kHz, which is comparable to the fundamental frequency of the magnetic field pulse. The area of the calibrated reference coil was $A_{\mathrm{ref}} = 4.342\,\mathrm{mm}^2$.

The thoroughly designed RC integrator (time constant $\tau = 1.00\,\mathrm{ms}$) is compensated for the serial inductance of the integrating capacitor and adapted for use with the analog-to-digital converters (see section 2.3.4 and [MSP$^+$98]), so that the necessary corrections differ slightly from those in (1.22). The field $B(t)$ and the measured integrated voltage U_{int} are related by

$$A \cdot B(t) = \int^t U(t')\,dt' = \tau\, U_{\mathrm{int}}(t) + \int^t U_{\mathrm{int}}(t')\,dt', \tag{2.1}$$

where A is the coil area and U is the induced probe voltage. The correction term is generally not larger than 0.5% of the peak field. The non-negligible temperature dependence $A(T)$ of the coil area is also taken into consideration. This correction is of order -2% when cooling from room temperature to liquid helium temperature.

2.3.2 Pick-up Coils – Design and Calibration

All pick-up coils unite the field pick-up coil and the compensated pick-up coil cast in a single piece of epoxy resin. Possible arrangements are shown in figure 2.12, where type (b) is the preferred one.

For the compensation coils we used exclusively the radial alternatively wound type, which is depicted as type C in figure 1.7. This type consists of two partial coils in parallel configuration, each having 15 to 30 turns. They are produced by alternatively winding 60 μm copper wire in opposite direction around two parallel cylinders having an identical diameter of 1.40 mm. By winding either one or two turns before switching to the other side, the windings have either a spacing corresponding to single wire diameter or lie close without a gap, respectively.

A Braunbek coil [Bra34] with a nominal radius of $r_0 = 15\,\mathrm{mm}$ is used to check the compensation. Its field homogeneity around the coil center is better than 10^{-4} within a radius of $0.34 r_0 \approx 5\,\mathrm{mm}$ and within an axial displacement of $\pm 0.31 r_0 \approx \pm 5\,\mathrm{mm}$. This coil type is preferable to long coils or Helmholtz coils with a comparable homogeneous field volume since its stray field is decreasing faster. The angle dependence of the compensation can be measured by tilting and rotating of the Braunbek coil, thus adjusting the magnetic field direction with respect to the pick-up coil.

Such a characterization is important since the quality of compensation is affected by the misalignment angle 2γ of the two partial coils as defined in section 1.3.2. The effect of $\gamma \neq 0$ is directly reflected in the angle dependence of the full area compensation ratio $r(\alpha, \varphi)$. For fixed azimuthal angle φ, the slope of $r(\alpha)$ is just the component of the misalignment angle 2γ parallel to the tilt angle α, see (1.18).

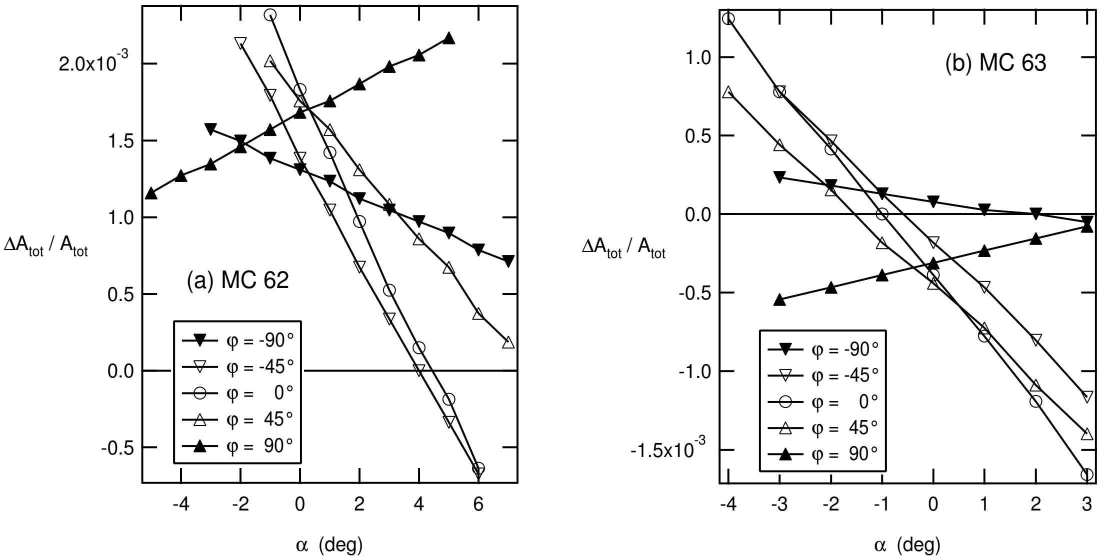

Figure 2.13: Dependence of the full area compensation ratio of two typical compensated coils on the tilt angle α. It was measured for several tilt axes with the azimuthal angle φ around the field axis.

Results for typical compensated coils obtained with a lock-in amplifier in AC fields at a frequency of 100 kHz are shown in figure 2.13. The full area compensation ratios $r(\alpha, \varphi)$ are $r(0,0) = (1.5 \pm 0.3) \cdot 10^{-3}$ for coil MC62 and $r(0,0) = (0.3 \pm 0.1) \cdot 10^{-3}$ for coil MC63, respectively. The misalignment angle can be read as maximum derivative of all curves, it is approximately $2\gamma \approx 1.4°$ (MC62) and $2\gamma \approx 1.3°$ (MC63), respectively, at $\varphi \approx 0°$.

The limitation for reaching extremely good compensation ratios in practice becomes evident from these results. Although it is possible to produce coils with a compensation ratio of 10^{-4} or even better for one fixed alignment of coil and field orientation, values obtained in the single-turn coil are often worse due to the lower field homogeneity and the uncertainty in the alignment.

2.3.3 The Sample Holder

Figure 2.14 shows a schematic of the sample holder together with a 15 mm single-turn coil and the removable shield as a part of the sample holder. Except the wires all materials in the vicinity of the field coil are non-metals.

Hence the pick-up coil is attached to a short plastics tube, this one to a hard paper tube and this one to a stainless steel tube ending in the socket terminal. On one hand this construction keeps thermal conductivity within reasonable limits, on the other hand in case of damage at the lower part of the sample holder it minimizes secondary damage to the upper part.

The wiring, i.e. thermocouple, twisted pair and coaxial cable is contained inside the concentric tubes, the largest of which has an outer diameter smaller than 5 mm. The matching resistor connecting the twisted lead wire from the compensated coil and the coaxial cable is placed in roughly 10 cm distance from the coil.

The electromagnetic shield, implemented as composite tube, relies on the properties of a weir conductor according to section 1.3.6. It is made up of a plastics tube as support and the actual wire metal, which consists of many insulated, parallel wires fixed on thin adhesive tape. To provide contact to the sample holder, the wires are bared on one end. The wire used is again polyimide insulated copper wire with 60 μm diameter. The spacing between the wires can be extended up to a few wire diameters without observing any reduction of the shielding effect.

The shield can be mounted and demounted from the end of the sample holder, thus permitting an easy access to the pick-up coil. It is long enough to protrude sufficiently over pick-up coil and single-turn coil. Inner and outer diameter are about 5 mm and 6 mm, respectively. Electrical

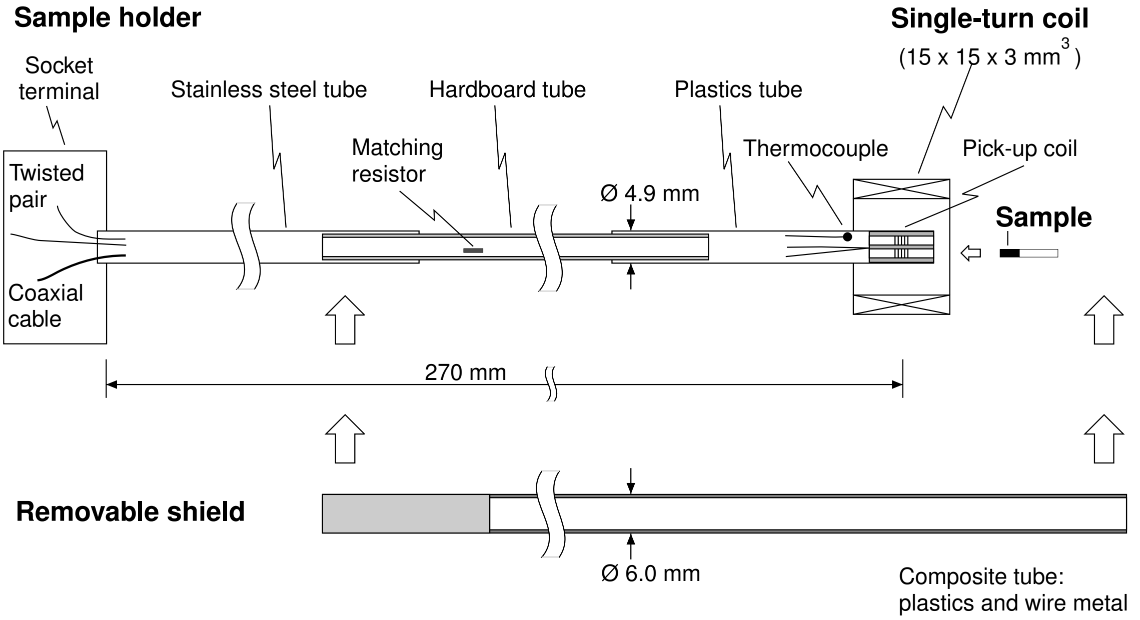

Figure 2.14: Sectional drawing of sample holder and removable shield designed for magnetization experiments in ultrahigh magnetic fields. With a length of about 27 cm, this sample holder is adapted to the helium flow cryostat shown in figure 2.10. The removable electrical shield allows to insert the sample (often attached to a small handle) into the pick-up coil from the outer end. The wiring inside the tube made of coaxial cables and twisted pair is only partially shown.

contact is provided by clamping the screen onto the stainless steel tube.

Although the sample holders for flow and bath cryostat differ slightly in design and length, they are based on the same construction principle.

The compensation of the whole system is checked again in the alternating, homogeneous field produced by the tiltable and rotatable Braunbek coil.

2.3.4 Recording Devices

For safety reasons and noise reduction all control and measurement systems feature complete galvanic isolation from the field generator. According to this philosophy the measurement devices inside the Faraday cage have battery-based power supplies and fiber optic signal transmission.

Both signals from field pick-up coil and compensated pick-up coil are measured by analog-to-digital converters (ADCs) specially developed for the use inside the Faraday cage, i.e. in an environment with strong electromagnetic interference. This device combines a digitizer, intermediate storage, an electro-optical converter and the battery-based power supply in a single, well-shielded case.

The 8-bit digitizer has a sampling rate of 200 Ms/s and stores 8192 data points in its internal memory before they are read out. Input resistance and capacitance are about 10 kΩ and 10 pF, respectively. The input voltage range is (0. . . 2) V with an adjustable offset voltage. Further details can be found in [MSP$^+$98].

Since conventional voltmeters can be destroyed by the strong electromagnetic fields inside the Faraday cage, another specially developed device is used to monitor the thermocouple voltage [MSP$^+$98]. This system comprises an input filter (with clamping and amplification), an electro-optical converter and a battery-based power supply in a single, well-shielded case.

Chapter 3

Performance Tests of the Measurement System

Although many aspects and components of the experimental setup have been analyzed separately in the previous chapter, the functioning of the system as a whole was not specified.

In order to test the total performance of the whole system, reference measurements under genuine experimental conditions had to be carried out. This is also the only practicable way to test the electromagnetic shielding as well as the degree of compensation realized under dynamic conditions, while frequency and transient response can be determined by different methods.

As an introduction, section 3.1 gives an example of genuine experimental data and describes how to evaluate these data. It is followed by section 3.2 dealing with the field calibration and section 3.3 examining the frequency and transient response of the measurement system. Section 3.4 treats the electromagnetic interference and its suppression by means of electromagnetic shielding. Important consequences for the evaluation of data resulting from the quality of compensation are discussed in section 3.5. Results concerning the sensitivity in relatively low fields are given in section 3.6.

3.1 Raw Data and Evaluation Procedure

Figure 3.1 shows raw data obtained in a real experiment with $\mathrm{HoMn_2Ge_2}$ powder at 7 K. The data representing the magnetic field $B(t)$ and the pick-up voltage $U_{\mathrm{ind}}(t)$ induced in the compensated coil are functions of the time t. This fact and the conversion to $U_{\mathrm{ind}}(B)$ will produce specific errors, which must be considered in the evaluation of the data. Sections 3.2 and 3.3 deal with these problems.

The differential susceptibility dM/dH is calculated according to (1.15) and

$$\frac{dM}{dH} = \frac{dM}{dt} \cdot \left(\frac{dH}{dt}\right)^{-1} . \tag{3.1}$$

Ideally, the proportionality $U_{\mathrm{ind}}(t) \propto dM/dt$ holds for perfect compensated coils, and an additional contribution $U'_{\mathrm{ind}}(t) \propto dM/dt$ will arise from non-perfect compensation. In both cases, the induced voltage vanishes at field maxima or minima, i.e. when $dH/dt = 0$. This is in contrast to experimental data, for which a finite voltage (or a phase shift) is observed. The consequence, a divergence of dM/dH at field maxima or minima, is analyzed in section 3.5.

Two further details concerning the evaluation and interpretation of data become clear from figure 3.1. The first characteristic, which must not be attributed to a response of the sample, are the trigger oscillations starting at $t = 0$ or $H = 0$. The origin of these high-frequency oscillations was discussed in section 2.1.2. Secondly, at those times with large field sweep rates, mainly at $t = 0$ or at the end of the down-sweep, the pick-up voltage becomes often very large resulting in a cutoff due to the limited range of the digitizers.

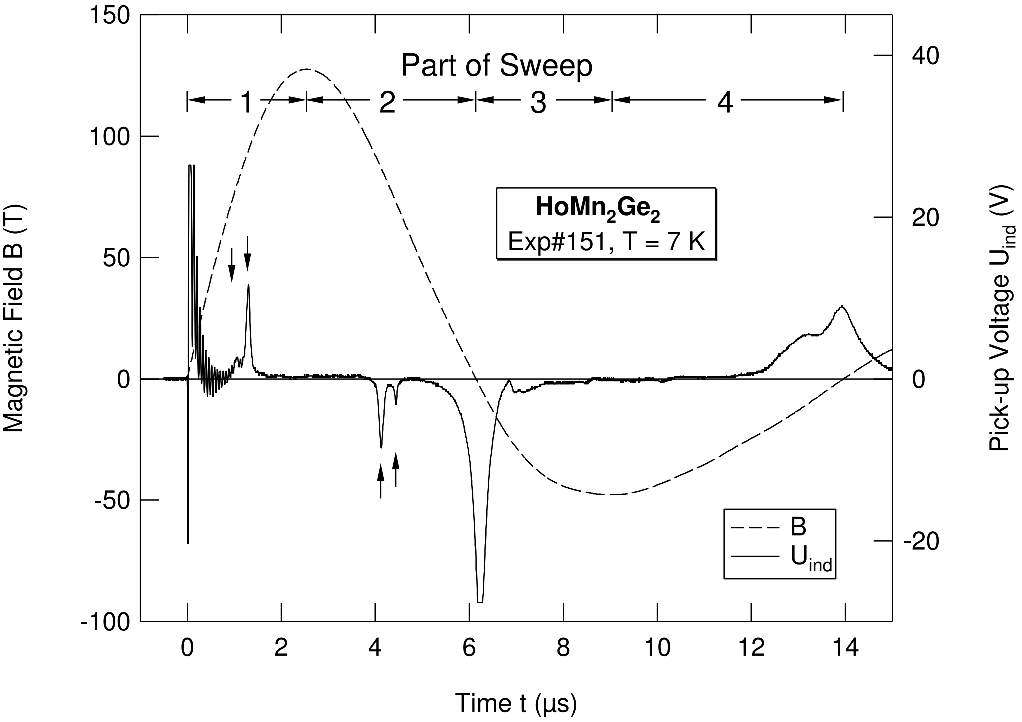

Figure 3.1: Raw data of magnetic field $B(t)$ and pick-up voltage $U_{\mathrm{ind}}(t)$ as a function of time t as measured for HoMn$_2$Ge$_2$ powder at $T = 7\,\mathrm{K}$. The resulting differential susceptibility $dM(H)/dH$ is shown in figure 5.9.

Evaluating the data shown in figure 3.1 leads to a differential susceptibility presented in figure 5.9. The two peaks in up- and down-sweep correspond to sharp maxima in dM/dH.

3.2 Field Calibration

In any pulsed-field experiment it is necessary to correlate the field data $B(t)$ with other data $F(t)$ measured as function of time t in order to obtain the relevant data $F(B)$ as function of the field. Any incorrect correlation of the two data sets results in an error of the field calibration. While in optical cyclotron resonance experiments it is often possible to yield this correlation by matching the data of up-sweep and down-sweep, this is no longer possible for magnetization experiments, since hysteresis effects cannot be ruled out.

To avoid this time-shift procedure, we have carried out a detailed experimental analysis of the response of our system by means of a simple and direct method. Using compensated coils of type (a) in figure 2.12, a tiny excitation coil was inserted into the pick-up coil instead of a sample and produced sharp voltage peaks in both signal channels at the same time. Although the level of the induced signals was rather small, the high repetition rate made a reliable synchronization possible. Finally, the uncertainty in the synchronization is not larger than one time step, i.e. $\Delta t = 5\,\mathrm{ns}$.

A second contribution to the uncertainty of $B(t)$ is the possible variation of the baseline $\Delta B_0(t)$ of the digitizer during the magnetic pulse. Mainly these uncertainties have to be considered when comparing corresponding structures in up- and down-sweep, whereas errors of the pick-up coil area A and the integrator time constant τ enter in addition for absolute values of $B(t)$.

Summarizing these contributions yields

$$\Delta B(t) = \Delta B_0(t) + \frac{dB(t)}{dt}\Delta t \; + \; B(t)\left(\frac{\Delta A}{A} + \frac{\Delta\tau}{\tau}\right) \; + \; \Delta B_{\mathrm{Rest}}(t). \qquad (3.2)$$

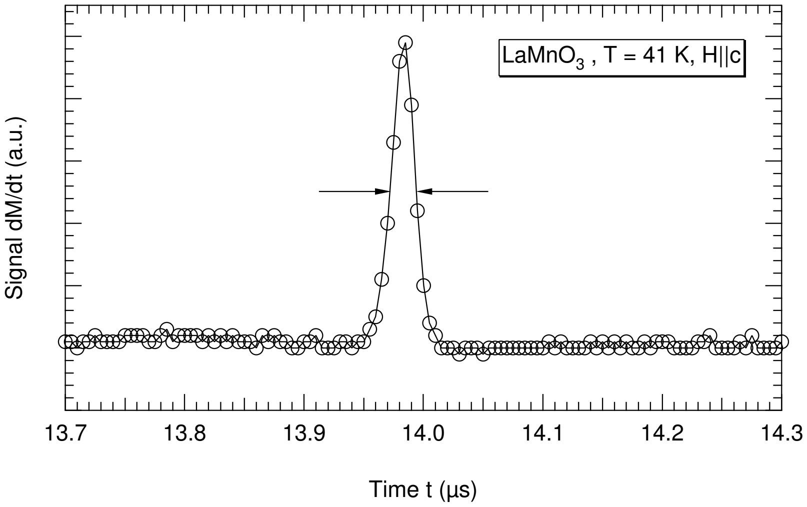

Figure 3.2: Transient response to a magnetization change as measured in an experiment. A narrow peak caused by the weak ferromagnetism of LaMnO3 is observed during the (second) zero crossing of the field. The FWHM is 5 data points or 25 ns.

For a typical experiment up to 100 T we have a maximum uncertainty ΔB of less than 2 T. In particular for the field values of any two corresponding events in up- and down-sweep, the field readings have thus a maximum uncertainty of 2 × 2 T.

3.3 Frequency and Transient Response

Frequency and transient response of the compensated coil are checked basically by means of a tiny excitation coil placed in the compensated coil instead of a sample. Two methods can be applied to rate the response:

1. The transient response of the system is checked by excitation with a step function and monitored on an oscilloscope. Comparison of input and output signal permits to deduce on the transient response. This method is also used for a fine-tuning of the matching resistance R_{M} (see section 1.3.4).

   Figure 3.2 shows the signal obtained from a LaMnO$_3$ sample in a real experiment. A sharp peak appears during the (second) zero crossing of the magnetic field due to the weak ferromagnetism of LaMnO$_3$. The full width at half maximum (FWHM) of this peak is only 5 data points or 25 ns.

2. The frequency response is tested by excitation with an alternating sinusoidal current with frequencies up to 100 MHz. Figure 3.3 shows the result for a compensated coil with relatively large inductivity (29 turns without spacing, 1.4 mm diameter) including the wiring. The cutoff frequency f_c is above 30 MHz and marks the lower limit among the coils used. Typical configurations using compensated coils with fewer turns and smaller inductance have higher cutoff frequencies f_c up to 60 MHz.

   There is a deviation between measured and calculated behaviour at the highest frequencies $f > f_c$ in figure 3.3. Possible reasons are deficiencies of the theoretical model put forward in section 1.3.4 or the influence of the measurement method at these high frequencies.

In summary, rise and fall time are of order ~ 10 ns, and the cutoff frequency is ~ 60 MHz.

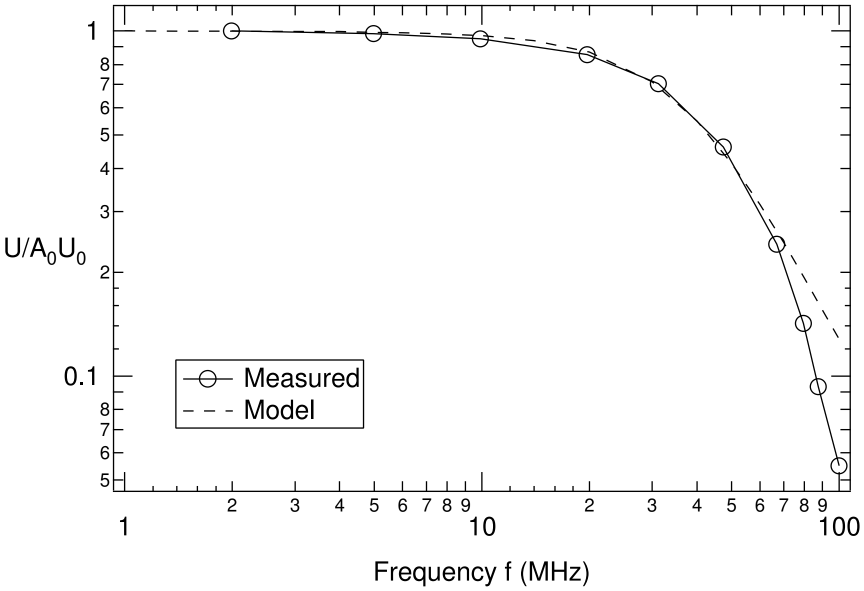

Figure 3.3: Frequency response of a compensated coil (29 turns without spacing, 1.4 mm diameter) including wiring (solid line) and calculation according to equation (B.6) (broken line).

3.4 Electromagnetic Shielding of the Measurement System

In order to estimate the efficiency of the screening, it is necessary to determine the voltage caused by an external source of interference with and without electromagnetic screen. However, this cannot be done by simply comparing the voltage produced by the empty compensated coil in two subsequent experiments, since the non-negligible voltage, which is induced in the residual area of the compensated coil is superimposed to the disturbance and may alter the result.

Hence, the efficiency of the screening was tested by means of a slightly modified measurement system, avoiding inductive contributions from the compensated coil. It was prepared by short-circuiting the compensated pick-up coil at point S in figure 2.11.

Figure 3.4 shows the result of such a measurement with short-circuited compensated pick-up coil and full screening applied to the measurement system. With typical attenuation there is only extremely little trigger noise. Apart from this and the bit noise, the signal is obviously free from any disturbances and deviations from zero voltage.

For comparison, figure 3.5 shows the result of a reference experiment without full screening. The voltage of the empty compensated coil contains dramatically larger trigger noise as well as other high-frequency noise appearing as spikes and damped oscillations. Since such interference is not all present if full shielding is applied, the following conclusions can be drawn.

The magnetic field pulse produced by the single-turn coil is quite smooth with two exceptions. These are the damped high-frequency trigger oscillations with well-defined frequency and the irregularities occurring at larger times as result of high energies and high fields as described in section 2.1.2. At the same time this means that the electromagnetic interference observed with improper shielding is caused by capacitive or radiation coupling.

3.5 Quality of Compensation

The quality of compensation is easily checked by means of reference experiments, i.e. measurements with empty pick-up coils but otherwise unchanged conditions. Figures 3.6 and 2.9 reproduce the results of those measurements.

Evaluating the data of figure 2.9, the residual uncompensated area A_R is approximately 0.135 mm^2 corresponding to a compensation ratio of $r \approx 4 \cdot 10^{-3}$ for this pick-up coil. It should be noted

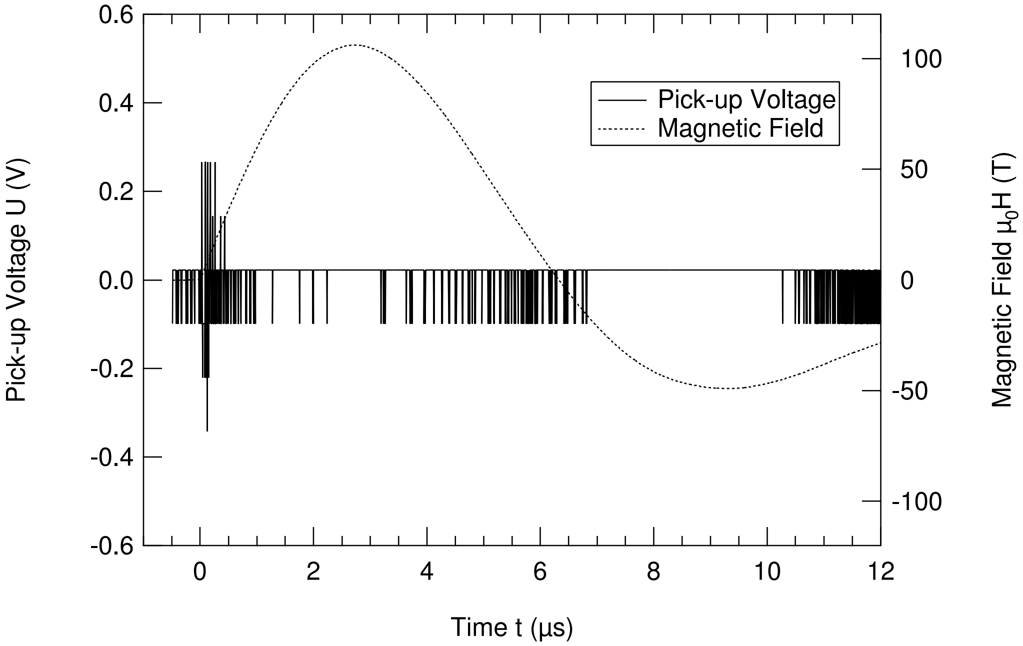

Figure 3.4: Signal from the short-circuited compensated pick-up coil obtained with full screening of the measurement system. Apart from the small trigger noise and the bit noise, no other disturbances are visible.

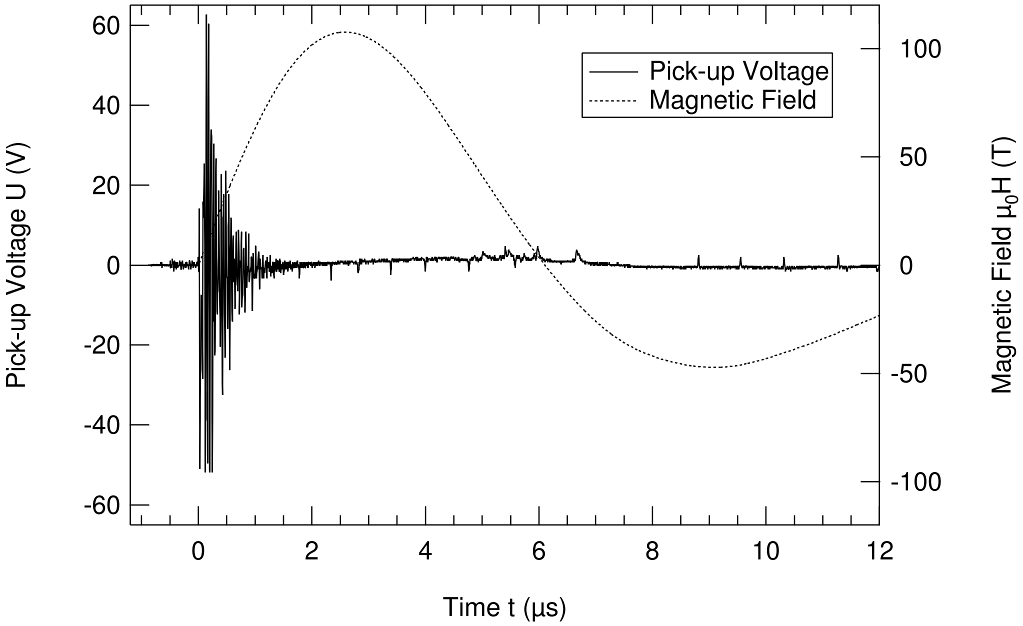

Figure 3.5: Reference experiment without full shielding of the measurement system. Large trigger noise and small spikes are present in the pick-up voltage of the empty compensated coil.

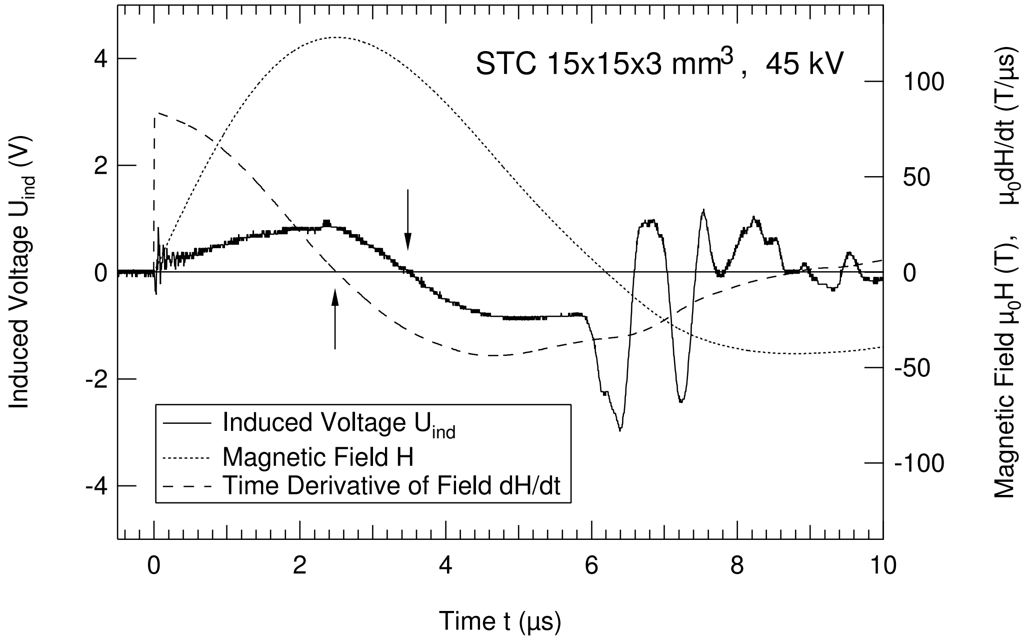

Figure 3.6: Reference experiment with an empty compensated coil. The time dependence of the small voltage U_{ind} induced in the compensated coil and that of the time derivative of the field dH/dt do not coincide; the difference in the zero crossings, marked by arrows, is remarkable.

that the compensation ratio r remains constant throughout the main pulse, i.e. the voltage U_{ind} induced in the compensated coil is proportional to the time derivative dH/dt of the magnetic field. Only if this condition is fulfilled it is possible to consider the effect of non-ideal compensation easily.

The situation changes, however, when measuring with better compensated coils and at increased sensitivity. As can be seen from figure 3.6, the induced voltage from the compensated coil and time derivative of the field are not at all proportional but have a distinct time dependence.

One reason for this deviation is probably the dependence of the compensation on the alignment of field and compensated coil as discussed in section 1.3.2, i.e. a change in the spatial arrangement of compensated coil and field profile during the field pulse. In addition to that, an explicitly different time dependence of the field for different positions must be taken in account. Such a complicated dependence $\mathbf{H}(\mathbf{r}, t)$ of the field produced by the single-turn coil was discussed in section 1.2.3.

Evaluating the data in figure 3.6, the initial compensation ratio of about $r_0 \approx 1.2 \cdot 10^{-4}$ ($A_{\text{R}} \approx 0.003\,\text{mm}^2$) is increasing to approximately $r \approx 8 \cdot 10^{-4}$ ($A_{\text{R}} \approx 0.02\,\text{mm}^2$).

Consequences for the Evaluation of Data

As a consequence, the induced voltage cannot be described by the simple equation (1.15), and an elimination of the spurious background signal caused by the non-ideal compensation becomes very difficult. Hence the integration of the measured voltage according to (1.16) does not necessarily give the true value of the magnetization.

Nevertheless, the time derivative of the magnetization dM/dt, in the ideal case proportional to the voltage measured, can be determined without making too large errors. The differential susceptibility dM/dH is generally well approximated for lower fields, where dH/dt is large, but may deviate remarkably from the true value near the peak field H_{max}, where dH/dt approaches zero. Errors appear to be significant if there is a strong divergence of the calculated values $(dM^+/dH)|_{H\to H_{\text{max}}}$ and $(dM^-/dH)|_{H\to H_{\text{max}}}$ for increasing and decreasing field, respectively. A good example demonstrating this fact are the experimental curves shown in figure 5.9, which were obtained on HoMn_2Ge_2. The lowest curve exhibits nearly ideal behaviour up to the peak field, while the quality of the two

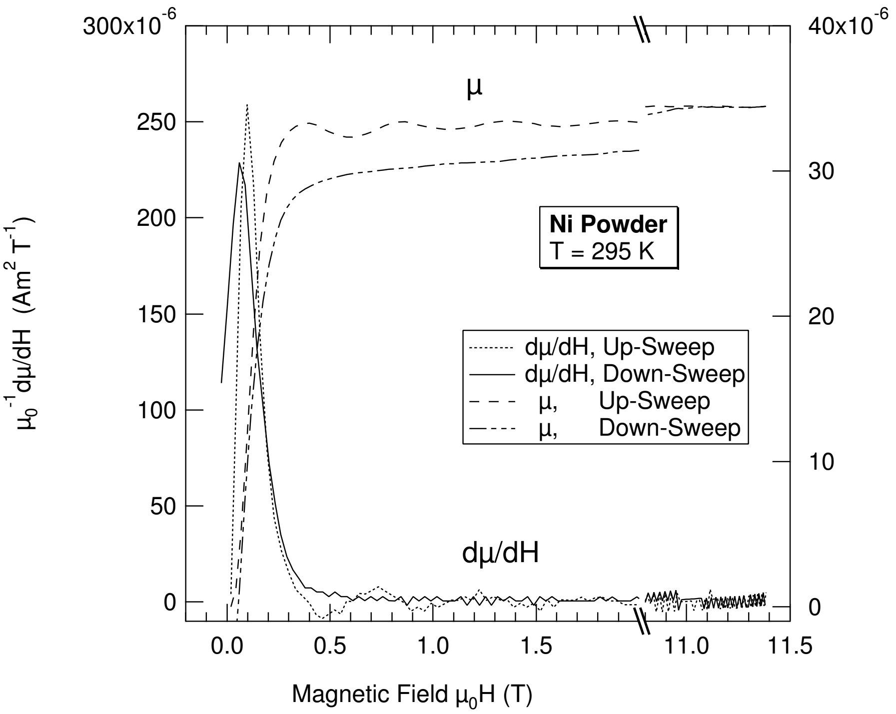

Figure 3.7: Field derivative $d\mu/dH$ as measured and magnetic moment μ obtained by numerical integration for a sample containing less than 1 mg of Ni powder dispersed in an electrical insulating matrix.

upper curves is worse due to the considerable influence of the background signal. However, despite the divergence near the peak field, susceptibility peaks and "structures" of dM/dH in lower fields can be identified in all curves.

In conclusion the differential susceptibility dM/dH determined from the measurement is often a good representation of the true value, whereas the calculation of the magnetization $M(H)$ involves much larger uncertainties and is therefore avoided. Generally, the results of sensitive measurements can be improved by subtracting the background signal obtained in subsequent reference experiments under the same conditions.

3.6 Sensitivity in Low Fields

In order to check the sensitivity of the measurement system for special application in low fields, tests with Ni powder were performed at room temperature and relatively low fields. Test samples were prepared by dispersing fine Ni powder in an electrically insulating matrix (Stycast 1266) in order to avoid eddy currents.

Field pulses not higher than 12 T allowed non-destructive and thus frequent operation. Another advantage is that the field homogeneity remains constant over many oscillations in contrast to semi-destructive operation, which is inevitable at producing (much) higher peak fields. The background signal due to non-ideal compensation is proportional to the field derivative and can be easily subtracted from the voltage measured.

Figure 3.7 shows both the field derivative of the magnetic moment $d\mu/dH$ and the magnetic moment μ obtained by numerical integration for a sample containing less than 1 mg of Ni. The background signal, corresponding to a residual, uncompensated area of 0.067 mm^2, was subtracted from $d\mu/dH$ before integration. Using a calibrated measurement system, the magnetic moment of the sample was determined as $3.2 \cdot 10^{-5}$ Am^2 (0.032 emu) at 1 T [Noj03].

It can be concluded from this result that magnetic moments of order $(10^{-6} \ldots 10^{-5})$ Am^2 can be detected under good conditions in the single-turn coil system.

Chapter 4

Magnetization of the Rare-Earth Zircons $PrVO_4$ and $TmPO_4$

The chapter starts with a short introduction to rare-earth zircons in general and $PrVO_4$ and $TmPO_4$ in particular. This is followed by a section introducing the theory necessary to calculate energy levels, magnetization and magnetocaloric effect in these compounds.

The main part consists of two separate sections for $PrVO_4$ and $TmPO_4$, which comprise experimental results, calculations and discussions. While section 4.4 on $PrVO_4$ gives a complete and detailed description of the important subjects, the subsequent section 4.5 on $TmPO_4$ will be more concise with emphasis on pointing out essential differences.

4.1 Introduction

4.1.1 Rare-Earth Zircons RXO_4

The rare-earth (RE) zircons RXO_4 (R – rare-earth ion, X = V, As, P) are electrical insulators, which do not show magnetic ordering even at very low temperatures since the magnetic exchange and dipolar interactions are weak. As a result, the highest magnetic ordering temperature does not exceed 3.5 K [MRK95]. As opposed to the RE compounds, RE metals have ordering temperatures between 8 K (Nd) and 293 K (Gd) [JM91].

The RE zircons crystallize at room temperature in the tetragonal zircon structure with space group $D_{4h}^{19} = I4_1/amd$ in which each X ion is surrounded by an oxygen tetrahedron and each RE ion by eight nearest-neighbour oxygen atoms [Wyc65]. Figure 4.1 shows the unit cell of the zircon structure, which contains four formula units. The lattice constants are $a = 7.3657\,\text{Å}$, $c = 6.4707\,\text{Å}$ for $PrVO_4$ and $a = 6.8411\,\text{Å}$, $c = 5.9878\,\text{Å}$ for $TmPO_4$, respectively [KKS98].

The R^{3+} and X^{5+} ions occupy sites of tetragonal symmetry, where all RE sites are magnetically equivalent with the site point group $\overline{4}2m$ (D_{2d}), i.e. there are no inequivalent sites for RE ions.

Owing to the transparency of the RE zircons, optical spectroscopy has been widely applied so that a plenty of reliable information about the wave functions and energy levels depending on the crystal field is available.

Especially those two features, making the observation and interpretation of many effects much easier and unambiguous, render these compounds particularly appropriate for experimental and theoretical investigations.

This applies exactly to the study of energy level crossing effects. The tetragonal local symmetry at the RE sites gives rise to a rich weakly degenerate spectrum of the RE ion. Applying (strong) magnetic fields can lead to various level crossings, which can be studied by different methods such as fluorescence and optical absorption spectra, electron paramagnetic resonance (EPR), specific heat at low temperatures and paramagnetic susceptibility.

While low temperature spectroscopy and EPR experiments provide generally information about a single electronic level of the ground multiplet, specific heat and magnetic susceptibility measure-

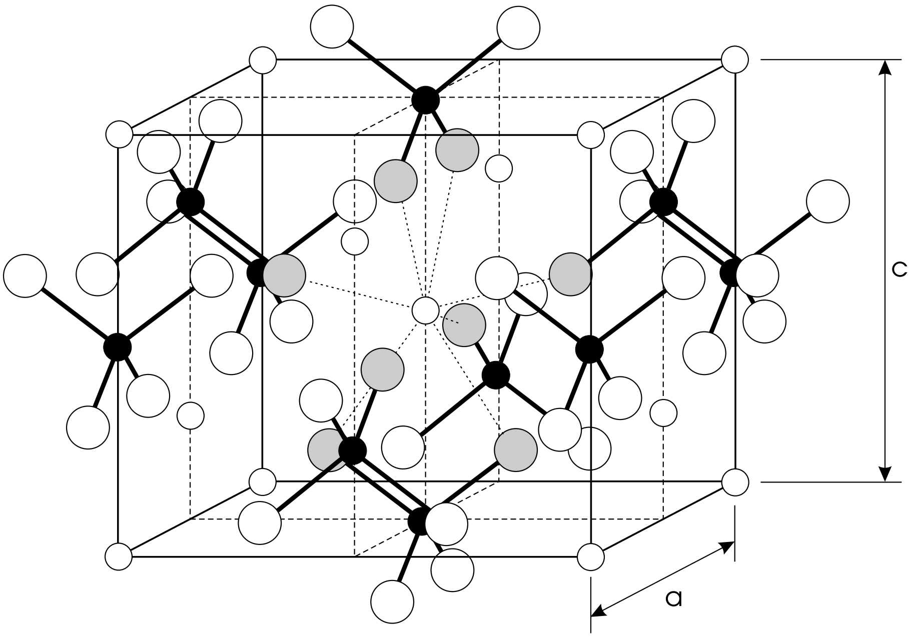

Figure 4.1: Perspective drawing of the tetragonal unit cell of the zircon structure RXO_4 containing $Z = 4$ formula units. Small open circles represent the rare-earth ions R, small closed circles represent the X atoms, and the large open circles represent the oxygen atoms.

ments depend on the population density of various levels of the ground multiplet and provide in turn a useful check of proposed electronic structures of ions in paramagnetic substances. Low temperature magnetization measurements are the method of choice in order to detect magnetic anomalies caused by energy level crossings, in particular if these occur at high magnetic fields.

Calculations in [KKP+97] have shown that crossing or approaching of energy levels in a magnetic field take place for all RE vanadates and phosphates. Depending on the orientation of the magnetic field, one or two crossovers occur in high, very high or ultrahigh magnetic fields. For instance crossovers should occur below 40 T in $DyPO_4$, $TmPO_4$, $TbVO_4$, below 100 T in $PrVO_4$, $ErPO_4$ and up to 300 T. . . 500 T in $NdVO_4$ and $TmVO_4$.

It is known that the crossing of the ground level of a magnetic ion by one of the excited levels is accompanied at low temperatures by an abrupt increase of the magnetization M and a pronounced maximum of the (differential) susceptibility dM/dB. Investigations of these anomalies provide valuable information about the crystal field of the RE zircons. Generally, the character of these magnetic anomalies depends on the character of the energy level interaction and it is different for different RE ions.

The CF mixing of the eigenfunctions is almost the same for RE vanadates and arsenates, but changes drastically for RE phosphates. This is due to the fact that the second-order CF parameter, B_2^0, (see section 4.2.1) changes in sign in RE phosphates, the other CF parameters being almost unchanged [BPKK91].

Another effect of the tetragonal local symmetry at the RE sites is a non-zero quadrupole moment, even without an external magnetic field. The absence of inequivalent sites for RE ions results in pronounced magnetoelastic effects, spontaneous as well as field induced [KKS98]. In the RE zircons they are not overshadowed by ordering effects since magnetic interactions are weak. Hence these compounds are also advantageous for studying magnetoelastic effects throughout the series of RE ions.

RE zircons are also known to be the archetype Jahn-Teller (JT) compounds, some of which exhibit a spontaneous tetragonal-orthorhombic transition [GG75]. They have motivated a great number of studies of the Jahn-Teller coupling.

4.1.2 The Singlet Paramagnets $PrVO_4$ and $TmPO_4$

The RE zircons $PrVO_4$ and $TmPO_4$ belong to the so-called singlet or van Vleck paramagnets, which are generally characterized by a temperature independent (at low temperatures) and anisotropic paramagnetic susceptibility. The reason is the energy gap ΔE between the non-magnetic ground state (singlet) and the excited states of the partially filled $4f$-shell of the RE ions; the gap ΔE is caused by the crystal field (CF).

An additional external magnetic field induces a magnetic moment to the ground state through the excited states. Moreover, the electron-nuclear coupling leads to a considerable enhancement of the external magnetic field at the nucleus making these compounds so-called enhanced nuclear magnets.

Magnetic anomalies due to an energy level crossing of the ground singlet by an excited level occur for $TmPO_4$ around 30 T and for $PrVO_4$ around 50 T, respectively, for the magnetic field parallel to the crystalline c-axis. While the level crossing in $TmPO_4$ could still be probed in the stationary magnetic fields available, those are too low for $PrVO_4$.

Pulsed magnetic fields, however, allow the convenient investigation of the crossover in both materials. It turns out that the magnetocaloric effect plays an important role in these pulsed-field experiments and cannot be neglected. This is confirmed by the fact that the susceptibilities for isothermal and adiabatic magnetization processes are markedly distinct in the vicinity of the level crossing at the critical field H_c. In the adiabatic process there is a monotonous temperature decrease for increasing field up to H_c and a subsequent increase after the crossover. The consequence is a more pronounced (i.e. narrower and larger) peak of the magnetic susceptibility at the crossover compared to the isothermal process.

4.2 Theoretical Description

4.2.1 The Hamiltonian

To calculate the relevant energy levels of the RE ions in the crystalline environment we use the Hamiltonian

$$\mathcal{H} = \mathcal{H}_{\mathrm{CF}} + \mathcal{H}_{\mathrm{Z}} + \mathcal{H}_{\mathrm{N}} \tag{4.1}$$

for a single ion that includes the CF Hamiltonian $\mathcal{H}_{\mathrm{CF}}$, the Zeeman term $\mathcal{H}_{\mathrm{Z}}$ and the hyperfine term $\mathcal{H}_{\mathrm{N}}$.

Of course, the Hamiltonian (4.1) is not complete under all conditions and, depending on the actual physical problem, further interactions must be considered if necessary. For example, the description of intermultiplet mixing requires the free ion Hamiltonian $\mathcal{H}_{\mathrm{FI}}$, which represents the usual contributions to the electronic energy including kinetic energy, nuclear Coulomb potential, electron-electron repulsion and spin-orbit coupling. Also magnetoelastic interactions $\mathcal{H}_{\mathrm{ME}}$ or pair quadrupole interactions $\mathcal{H}_{\mathrm{Q}}$ may become important.

Since we are interested in the thermodynamical properties below room temperature, we neglect intermultiplet mixing. The ground multiplet forms then an adequate space of functions for calculating the magnetic properties, and we can write the CF Hamiltonian in terms of the equivalent operators O_n^m:

$$\mathcal{H}_{\mathrm{CF}} = \sum_{n,m} \theta_n \, B_n^m \, O_n^m \quad \text{with} \quad n = 2, 4, 6, \quad m = 0, 4, \quad m \leq n, \tag{4.2}$$

where the CF parameters [Hut64]

$$B_n^m = A_n^m \, \langle r^n \rangle \tag{4.3}$$

are usually fitted to experimental data. The θ_n $(n = 2, 4, 6)$ are the Stevens multiplying factors $\theta_2 = \alpha_J$, $\theta_4 = \beta_J$, $\theta_6 = \gamma_J$. The matrix elements of the equivalent operators O_n^m as well as the Stevens multiplying factors are given in [Hut64].

For tetragonal symmetry (point group D_{2d}) there are five CF parameters in the CF Hamiltonian,

$$\mathcal{H}_{\mathrm{CF}} = \alpha_J \, B_2^0 \, O_2^0 + \beta_J (B_4^0 \, O_4^0 + B_4^4 \, O_4^4) + \gamma_J (B_6^0 \, O_6^0 + B_6^4 \, O_6^4), \tag{4.4}$$

where the z-axis of the coordinate system is oriented parallel to the c-axis of the tetragonal unit cell.

The states for the RE ions are characterized by $|LSJM_J\rangle$ or short $|JM_J\rangle$. Within the manifold considered, i.e. the ground multiplet, the total angular momentum J is constant.

The Zeeman coupling between the $4f$ magnetic dipole moment of the electronic state and the internal magnetic field $\mathbf{B} = \mu_0\mathbf{H}$ (external applied field corrected for demagnetization effects) is described by

$$\mathcal{H}_\mathrm{Z} = -g_J\mu_B\mathbf{B}\cdot\mathbf{J}, \tag{4.5}$$

where g_J is the Landé g-factor, and μ_B is the Bohr magneton. $\mathbf{J}$ is the operator of the total angular momentum, $\mathbf{J} = \mathbf{L} + \mathbf{S}$.

The matrix elements of $\mathcal{H}_\mathrm{Z}$ are determined as usual by

$$\langle JM'_J \,|\, J_z \,|\, JM_J\rangle = M_J\,\delta_{M'_J,M_J} \tag{4.6}$$

$$\langle JM'_J \,|\, J_\pm \,|\, JM_J\rangle = \sqrt{J(J+1) - M_J(M_J \pm 1)}\,\delta_{M'_J,M_J\pm 1} \tag{4.7}$$

where $J_\pm = J_x \pm iJ_y$ are the ladder operators.

The hyperfine coupling is generally described by

$$\mathcal{H}_\mathrm{N} = -\mathbf{I}\cdot\mathbf{A}_J\cdot\mathbf{J} - \gamma_I\hbar\,\mathbf{B}\cdot\mathbf{I}, \tag{4.8}$$

where $\mathbf{I}$ is the operator of the nuclear spin, the tensor $\mathbf{A}_J$ is a coupling constant, and γ_I is the nuclear gyromagnetic ratio. The first term represents the magnetic hyperfine interaction between the nuclear magnetic dipole moment and an "effective" electronic magnetic dipole moment, which depends strongly on the electronic state of the ion. The second term represents the interaction of the (free) nuclear magnetic dipole moment with the external magnetic field.

We may also introduce another form,

$$\mathcal{H}_\mathrm{N} = -\mathbf{I}\cdot(\underline{\gamma} - \gamma_I)\hbar\cdot\mathbf{B} - \gamma_I\hbar\,\mathbf{B}\cdot\mathbf{I}, \tag{4.9}$$

where $\underline{\gamma}$ is the magnetogyric hyperfine tensor, and $(\underline{\gamma}-\gamma_I)$ describes the enhancement of the nuclear magnetism. This implies that $\underline{\gamma}$ is temperature dependent and may also become field dependent at high magnetic fields resulting from changing energy levels and occupation.

Bleaney et al. chose this form in order to describe nuclear magnetic resonance in $\mathrm{PrVO_4}$ [BHR+78] and $\mathrm{TmPO_4}$ [BPW83]. From fitting experimental data to the Hamiltonian

$$\mathcal{H}_\mathrm{N} = -\hbar\left[\gamma_{\|}B_zI_z + \gamma_\perp(B_xI_x + B_yI_y)\right] + P\left[I_z^2 - \frac{1}{3}I(I+1)\right] \tag{4.10}$$

they obtain temperature dependent parameters $\gamma_{\|}$, $\gamma_\perp$ and P. The last term in (4.10) with P, the nuclear electric quadrupole interaction tensor [Ble88], was considered only for $\mathrm{PrVO_4}$, not for $\mathrm{TmPO_4}$.

The standard relation [BPW83]

$$(\underline{\gamma} - \gamma_I)\hbar\cdot\mathbf{B} = A_J\frac{\langle\boldsymbol{\mu}\rangle}{\mu_B\,g_J} \tag{4.11}$$

opens up another way to determine $\underline{\gamma}$, if the thermally averaged electronic magnetic moment $\langle\boldsymbol{\mu}\rangle$ is known. Both quantities, $(\underline{\gamma}-\gamma_I)$ and $\langle\boldsymbol{\mu}\rangle$, have exactly the same temperature dependence, whereas A_J (scalar) is constant.

4.2.2 Magnetization and Magnetic Susceptibility

The important physical quantity measured in the experiment is the magnetic susceptibility. As a response function it describes how the magnetization $\mathbf{M}$ of a system depends on an external magnetic field $\mathbf{H}$. In the most general case, as generalized susceptibility $\underline{\chi}(\mathbf{q},\omega)$, the tensor involves the dependence on wavevector $\mathbf{q}$ and frequency ω.

Assuming a static magnetic field ($\omega = 0$) yields the static susceptibility $\underline{\chi}(\mathbf{q})$. If both, field and magnetization, are homogeneous ($\mathbf{q} = 0$), then the magnetic susceptibility $\underline{\chi}$ is defined as

$$\chi_{\alpha\beta}(T, \mathbf{H}) = \left(\frac{\partial M_\alpha}{\partial H_\beta}\right)_T \tag{4.12}$$

and depends generally on temperature T and field $\mathbf{H}$.

Magnetization and static-susceptibility tensor may be derived as first and second derivatives of the free energy, respectively. Starting from the partition function of the canonical ensemble

$$Z = \mathrm{Tr}\left\{\mathrm{e}^{-\beta\mathcal{H}}\right\}, \tag{4.13}$$

where $\beta = (k_B T)^{-1}$, the expectation value of an operator A is calculated by means of the density operator $\hat{\rho} = Z^{-1}\mathrm{e}^{-\beta\mathcal{H}}$ as

$$\langle A \rangle = \mathrm{Tr}\{A\hat{\rho}\} = \frac{1}{Z}\mathrm{Tr}\left\{A\,\mathrm{e}^{-\beta\mathcal{H}}\right\}. \tag{4.14}$$

The free energy F is

$$F = U - TS = -k_B T \ln Z = -\frac{1}{\beta}\ln Z, \tag{4.15}$$

with U as internal energy and S as entropy. The derivative of the free energy with respect to a variable x is

$$\frac{\partial F}{\partial x} = -\frac{1}{\beta Z}\frac{\partial Z}{\partial x} = \frac{1}{Z}\mathrm{Tr}\left\{\frac{\partial \mathcal{H}}{\partial x}\mathrm{e}^{-\beta\mathcal{H}}\right\} = \left\langle \frac{\partial \mathcal{H}}{\partial x}\right\rangle. \tag{4.16}$$

Since the operator $\boldsymbol{\mu}$ of the magnetic moment is

$$\boldsymbol{\mu} = -\boldsymbol{\nabla}_{\mathbf{B}}\mathcal{H}, \tag{4.17}$$

its expectation value can be expressed either using (4.14) as

$$\langle \boldsymbol{\mu} \rangle = \frac{1}{\beta Z}\boldsymbol{\nabla}_{\mathbf{B}} Z = \frac{1}{\beta}\boldsymbol{\nabla}_{\mathbf{B}} \ln Z, \tag{4.18}$$

or using (4.16) as

$$\langle \boldsymbol{\mu} \rangle = -\boldsymbol{\nabla}_{\mathbf{B}} F. \tag{4.19}$$

The magnetization $\mathbf{M}$ is the average magnetic moment per volume, so that

$$\mathbf{M} = n\,\langle \boldsymbol{\mu} \rangle \tag{4.20}$$

holds for localized moments, assuming identical ions with a density of $n = N/V$.

Using (4.19), the susceptibility can be defined as second derivative of the free energy:

$$\chi_{\alpha\beta}(T, \mathbf{H}) = n\left(\frac{\partial \langle \boldsymbol{\mu} \rangle_\alpha}{\partial H_\beta}\right)_T = -\frac{n}{\mu_0}\left(\frac{\partial^2 F}{\partial H_\alpha \partial H_\beta}\right)_T. \tag{4.21}$$

4.2.3 The Magnetocaloric Effect

The magnetocaloric effect denotes the temperature change of a magnetic sample during the process of its adiabatic magnetization in an external magnetic field. Under adiabatic condition we have

$$\delta Q = 0 = C_H dT + \mu_0 T\left(\frac{\partial M}{\partial T}\right)_H dH, \tag{4.22}$$

where $C_H = (\partial Q/\partial T)_H$ is the heat capacity at constant field. Rearranging this expression we arrive at

$$dT = -\mu_0\frac{T}{C_H}\left(\frac{\partial M}{\partial T}\right)_H dH, \tag{4.23}$$

describing the temperature change dT for an infinitesimal small field change $\mu_0 dH$. The sign of the "differential" magnetocaloric effect dT/dH is governed by the sign of the derivative $(\partial M/\partial T)_H$. For a step-like isothermal magnetization curve (where the step is smeared out for increasing temperature) this derivative is positive as the crossover field is approached so that a cooling takes place. The cooling is then followed by a subsequent heating as the field increases further above the crossover field.

The total heat capacity C_H consists of the lattice contribution C_{lat} and the electronic part C_{el} (which includes the nuclear part as well):

$$C_H = C_{\text{lat}} + C_{\text{el}}. \tag{4.24}$$

According to the Debye model the lattice heat capacity is

$$C_{\text{lat}}(T) = \frac{12\pi^4}{5} k_B \nu \left(\frac{T}{T_{\text{D}}}\right)^3 \tag{4.25}$$

with the Debye temperature T_{D} and ν atoms per elementary cell. For the zircon lattice we assume $T_{\text{D}} = 275\,\text{K}$ [KKKSS87] and $\nu = 6$.

The electronic and nuclear contributions to the heat capacity are calculated the usual way according to $C = dU/dT$, where

$$U = \langle \mathcal{H} \rangle = -\frac{1}{Z}\frac{\partial Z}{\partial \beta} = -\frac{\partial}{\partial \beta} \ln Z. \tag{4.26}$$

Thus we obtain

$$C = \frac{1}{k_B T^2}\left[\left\langle \mathcal{H}^2 \right\rangle - \langle \mathcal{H} \rangle^2\right], \tag{4.27}$$

which relates the heat capacity to the difference of two expectation values for a given energy spectrum.

4.3 Sample Preparation

The measurements were performed on single-crystal samples, grown by the well-known method of spontaneous crystallization from solution, with molten PbO-PbF$_2$-V$_2$O$_5$-H$_3$BO$_3$ as solvent for the vanadates and with molten PbO-PbF$_2$-PbP$_2$O$_7$-H$_3$BO$_3$ as solvent for the phosphates [KKK$^+$01]. Crystals in form of long needles of rectangular cross section with a typical size of $1 \times 1 \times 5\,\text{mm}^3$ grow by slow cooling of the lead-based melt. The long dimension is parallel to the fourfold symmetry axis (c-axis, [001] direction), and the natural faces are (100) and (010). The crystals were transparent and slightly coloured.

4.4 PrVO$_4$

First results of the differential magnetic susceptibility of PrVO$_4$ were published in [KKP$^+$00]. Those measurements at 4.2 K applied pulsed magnetic fields up to 400 T produced by the destructive flux-compression technique with the field being along the tetragonal axis of the crystal. The total rise time of the field was about 15 μs.

The authors found a pronounced peak of dM/dH at the field $B_c^{(\uparrow)} \approx 45\,\text{T}$. The width of the peak is about 6 T (FWHM) and thus smaller than in case of isothermal magnetization. On the other hand it is also much larger than in the adiabatic case. Reasons for this disagreement were discussed, but remained still unclear. Questionable was also the exact value of B_c since the field calibration of the flux compression is not very precise at relatively low fields.

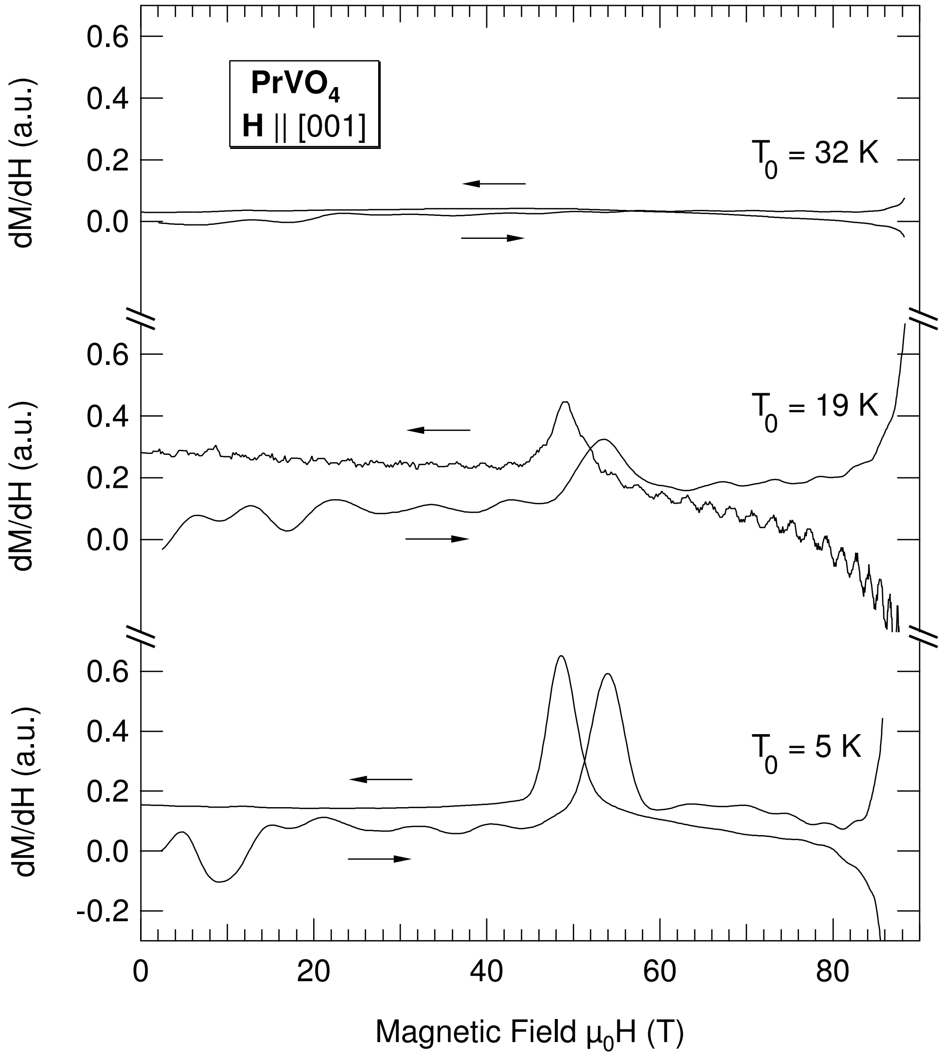

Figure 4.2: Experimental differential susceptibility dM/dH of PrVO$_4$ for a magnetic field along the tetragonal axis and three different (initial) temperatures $T_0 = 5\,\mathrm{K}$, $19\,\mathrm{K}$, $32\,\mathrm{K}$.

4.4.1 Experimental Results

In order to verify the crossover field and to study the sweep rate dependence, hysteresis phenomena and the temperature dependence, new experiments were carried out using the single turn-coil technique. The field pulse applied here is characterized by a duration of $2.7\,\mu\mathrm{s}$ for the up- and $3.3\,\mu\mathrm{s}$ for the down-sweep, respectively.

Figure 4.2 shows the experimental results for the differential susceptibility dM/dH for a magnetic field along the tetragonal axis for three different (initial) temperatures $T_0 = 5\,\mathrm{K}$, $19\,\mathrm{K}$, $32\,\mathrm{K}$. Distinct peaks of dM/dH occur for $T_0 = 5\,\mathrm{K}$ and $19\,\mathrm{K}$ at $B_c^{\uparrow} = 54.1\,\mathrm{T}$ for the up-sweep and $B_c^{\downarrow} = 48.5\,\mathrm{T}$ for the down-sweep. They are due to the crossing of the lowest energy levels of the Pr^{3+} ion. The sweep rates are as high as $40\,\mathrm{T}/\mu\mathrm{s}$ at $B_c^{\uparrow}$ and $33\,\mathrm{T}/\mu\mathrm{s}$ at $B_c^{\downarrow}$, respectively.

Increasing the initial temperature to $T_0 = 32\,\mathrm{K}$ results in a differential susceptibility without pronounced peak, i.e. the magnetization curve has no sharp jump at B_c.

Another feature observed for $T_0 = 5\,\mathrm{K}$ as well as $T_0 = 19\,\mathrm{K}$ is a pronounced hysteresis of the peak position between up-sweep and down-sweep of about $\Delta B_c \approx 5\,\mathrm{T}$. This value is definitely beyond the maximum error of $2\,\mathrm{T}$ at about $50\,\mathrm{T}$, which is due to the field calibration.

Table 4.1: Crystal field parameters B_n^m for Pr^{3+} ions in PrVO$_4$.

Substance	B_2^0	B_4^0	B_6^0	B_4^4	B_6^4	Unit	T/K	Reference
PrVO$_4$	-77	71	-68	970	-200	cm^{-1}	7	[AAB94]
PrVO$_4$	**-50.07**	**181.32**	**-93.08**	**1018.7**	**10.42**	cm^{-1}	-	[Sid02]

Regardless of the hysteresis phenomenon the average of $B_c^{\uparrow}$ and $B_c^{\downarrow}$ may be adopted for calculations and discussion, where hysteresis does not play a role. In the following we will thus use $B_c = (B_c^{\uparrow} + B_c^{\downarrow})/2 = 51.3\,\mathrm{T}$ for 5 K and 19 K. This value is about 10% larger than that of [KKP$^+$00].

4.4.2 The Hamiltonian

The Hamiltonian used to describe Zeeman effect and magnetic characteristics is given in (4.1) including (4.2) ($\mathcal{H}_{\mathrm{CF}}$), (4.5) ($\mathcal{H}_{\mathrm{Z}}$) and (4.8) ($\mathcal{H}_{\mathrm{N}}$). A complete solution of the problem requires the CFPs, g_J, and the magnetogyric hyperfine tensor to be known.

Investigations by means of fluorescence, Raman and far infrared spectroscopy yielded the positions of the excited low-lying energy levels of PrVO$_4$ [BHR$^+$78] at low temperatures up to 20 K. The first excited singlet is about $35\,\mathrm{cm}^{-1}$, the first excited doublet $84\,\mathrm{cm}^{-1}$ above the ground singlet, respectively. The positions of the remaining levels of the $^3H_4$ multiplet were estimated in [BHR$^+$78] by an extrapolation procedure based on the properties of a CF Hamiltonian of tetragonal symmetry and the experimental data on nuclear magnetic resonance obtained at low temperatures (2 K. . . 20 K) and magnetic fields below 1 T. The resulting energy values and wavefunctions of the Pr^{3+} ion made it possible to account for the nuclear magnetic resonance data as well as low-temperature magnetic susceptibility data, but CF parameters were not given in [BHR$^+$78].

Crystal field parameters were deduced in [AAB94] from the spectroscopic information of [BHR$^+$78] and magnetization measurements in the temperature range 4 K. . . 40 K and fields up to 5 T oriented along and perpendicularly to the tetragonal axis. It should be noted that these CFPs give wave functions for all levels and positions of the upper levels of the multiplet being substantially different from those proposed in [BHR$^+$78]. Another critical discrepancy is the resulting crossover field of 86.5 T, which is much higher than our experimental finding of $B_c \approx 51.3\,\mathrm{T}$.

In order to find a suitable set of CFPs, the following data were incorporated: the crossover field $B_c \approx 51.3\,\mathrm{T}$, the spectroscopic information of [BHR$^+$78], the temperature dependent initial magnetic susceptibility $\chi = (\chi_{\|} + 2\chi_{\perp})/3$ of a polycrystal from [GAC87] and magnetization data from [BHR$^+$78] and [AAB94], both shown in figure 4.3. While J-mixing and intermediate coupling is taken into account in [KKK$^+$01] in the spectroscopic calculations, it is not considered in this work. The corresponding CFPs used in this work [Sid02] are given in table 4.1.

The resulting CFPs allow to account for the experimental crossover field and the initial magnetic susceptibility within experimental accuracy, see figure 4.3. They are also within the variation of the parameters throughout the rare-earth series (see e.g. [BGH$^+$88]) except B_4^0, which might be considered slightly too large. Calculations show, however, that this parameter is rigidly connected with the gap between the ground and the first excited singlet. All attempts to find a different parameter set with a smaller B_4^0, i.e. redistributing the effect of this quantity to other parameters, failed.

Another interesting feature is the fact that the shift of the ground singlet, i.e. the state $|4; 2^S\rangle = (|4; +2\rangle + |4; -2\rangle)/\sqrt{2}$, with increasing magnetic field depends strongly on the position of the similar singlet at the upper end of the spectrum. This means that the crossover field provides information on the splitting of the whole multiplet.

The energy levels of the ground multiplet of the Pr^{3+} ion obtained with the CFPs [Sid02] of table 4.1 are given in table 4.2.

The hyperfine interaction is based on (4.9) or (4.10) with parameters derived from (4.11). Although hyperfine parameters are given in [BHR$^+$78], these are only valid in low fields compared to the crossover field B_c as a result of the approximation used in [BHR$^+$78]. Deducing the hyperfine

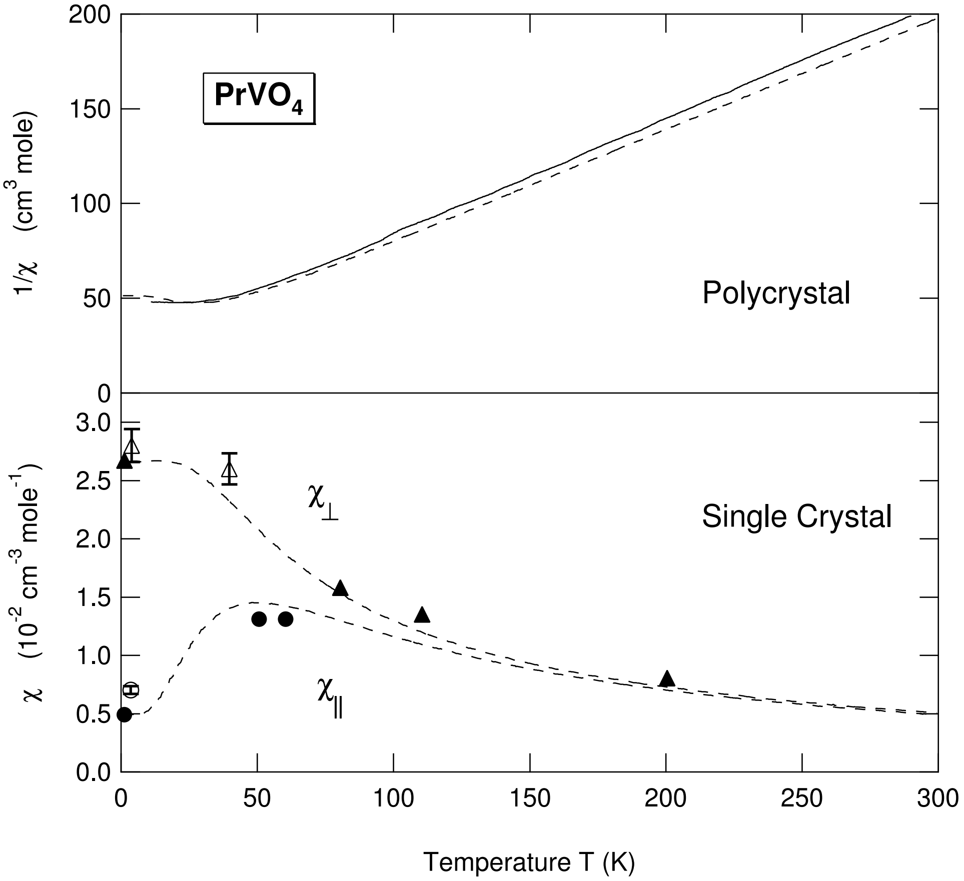

Figure 4.3: Temperature dependence of the reciprocal susceptibility $1/\chi$ for a polycrystal of PrVO$_4$ (upper part) and of the susceptibility χ of a PrVO$_4$ single crystal (lower part). Experimental data are represented by the solid line [GAC87], open symbols [AAB94] and closed symbols [BHR$^+$78], respectively. The dashed lines are calculations according to [KKK$^+$01].

Table 4.2: Energy levels of Pr^{3+} in PrVO$_4$. S and D denote singlets and doublets, respectively.

Level	S	S	D	S	S	S	D
Energy (cm^{-1})	0	35	84	103	260	273	544

parameters from (4.11) is favourable because they are valid within the entire field range, regardless of the level crossing.

Two important facts related to the use of (4.11) should be mentioned here. The parameter set ($\gamma_{\|,i}$ and $\gamma_{\perp,i}$) for each level i is calculated using the corresponding individual contribution of the level to $\langle \boldsymbol{\mu} \rangle$ in (4.18). These parameter sets (or susceptibilities) can be considered independently for (at least) the ground singlet and the first excited singlet. This is possible because these two levels are not connected by magnetic dipole matrix elements [BHR$^+$78].

The isotope ^{141}Pr has a nuclear spin of $I = 5/2$, $\gamma_I/2\pi = 12.6\,\mathrm{MHz/T}$ and $A_J/h = 1093\,\mathrm{MHz}$ [BHR$^+$78]. Thus we use $A_J/h\,g_J = 1357\,\mathrm{MHz}$.

4.4.3 Zeeman Effect and Magnetization Curves

Figure 4.4 shows the Zeeman effect for a magnetic field oriented along the tetragonal axis of PrVO$_4$ without regard of the hyperfine coupling. The overall splitting of the ground multiplet is of order $500\,\mathrm{cm}^{-1}$, but only the four lowest-lying levels are reproduced in the figure.

Taking also hyperfine coupling into account splits each level into $2I + 1 = 6$ hyperfine levels. This is shown in the inset of figure 4.4.

A crossing of the two lowest levels takes place at $B_c \approx 51.3\,\mathrm{T}$. The symmetry of these levels[1] is such that this crossing occurs without a gap if $\mathbf{H} \parallel [001]$ exactly. A small deviation of the field orientation from [001] results in the interaction of the ground and the first excited levels and a gap near B_c develops, see figure 4.5. At a misalignment angle of $\Theta = 5^\circ$ the gap comprises $\sim 0.25\,\mathrm{cm}^{-1}$ and B_c increases slightly by 0.4 T.

Applying the magnetic field along the [110] direction leads to a crossover at about 260 T.

The magnetization curves were calculated according to (4.18). This is easily done in the isothermal case, where the temperature is held constant. The adiabatic case is more complicated because the magnetocaloric effect has to be taken into account and the temperature varies with the field.

Figure 4.6 depicts the magnetization curves for the main crystallographic directions for both cases, isothermal and adiabatic, at an (initial) temperature of $T_0 = 5\,\mathrm{K}$. Magnetization jumps are associated with the crossing of the lowest-lying energy levels. The jump of $\sim 2.5\mu_B/\mathrm{f.u.}$ for $\mathbf{H} \parallel [001]$ is much larger than that for $\mathbf{H} \parallel [110]$ with $\sim 0.7\mu_B/\mathrm{f.u.}$.

From comparing isothermal and adiabatic magnetization curves for the same initial temperature, it can be clearly seen that the adiabatic curves are much steeper than the isothermal ones if the field is along [001] or [110]. This indicates that a cooling takes place when the crossover field is approached. If the field is along the [100] direction, adiabatic and isothermal magnetization curves coincide, which is an inherent feature of the Van Vleck character of magnetization along the easy direction.

4.4.4 Magnetocaloric Effect and Adiabatic Magnetization

The magnetization curve measured, whether it is isothermal or adiabatic in the limiting cases, depends on how the experiment is carried out. In particular in our case, where short-pulse fields have been applied, it is necessary to calculate adiabatic curves in order to interpret experimental data.

Isothermal conditions can be generally assumed if the experiment is done in quasistatic fields as long as no special definitions are referred to. In contrast the character of the thermal regime

---

[1] The wave function of the ground singlet is $|4; 2^S\rangle$, while the first excited singlet is given by $|4; 4^S, 0\rangle$, i.e. a mixture of $|4; 4^S\rangle$ and $|4; 0\rangle$ states.

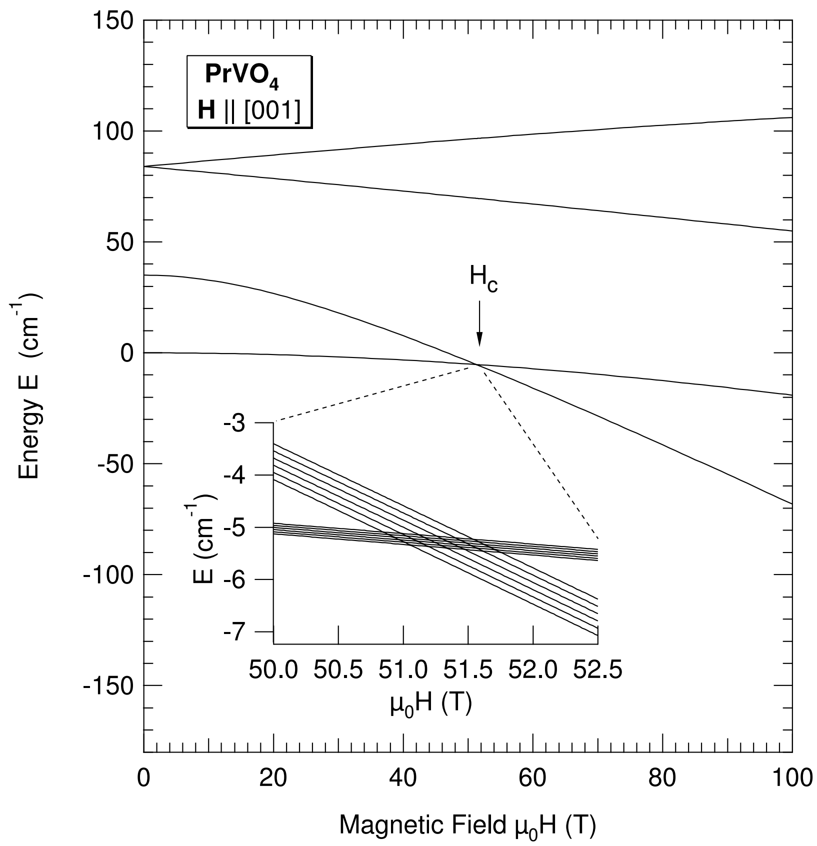

Figure 4.4: Zeeman effect for the four lowest-lying electronic levels of the ground multiplet of $PrVO_4$ for $\mathbf{H} \parallel [001]$. The inset shows the Zeeman effect with regard to hyperfine coupling for the two lowest-lying levels.

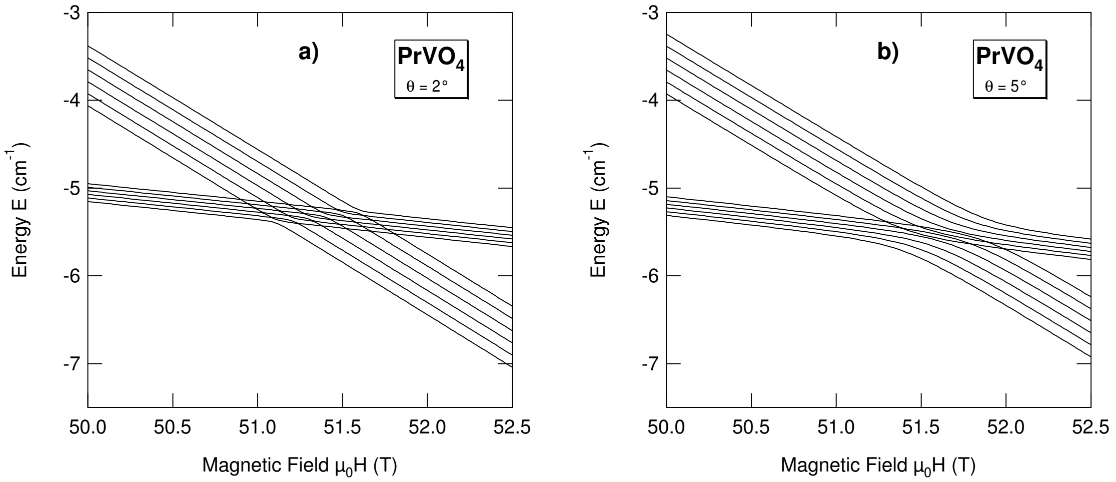

Figure 4.5: Dependence of the Zeeman effect on the misalignment angle θ between magnetic field $\mathbf{H}$ and the tetragonal axis [001]. The diagrams show the two lowest-lying levels with regard to hyperfine coupling for $\theta = 2°$ (a) and $\theta = 5°$ (b), respectively.

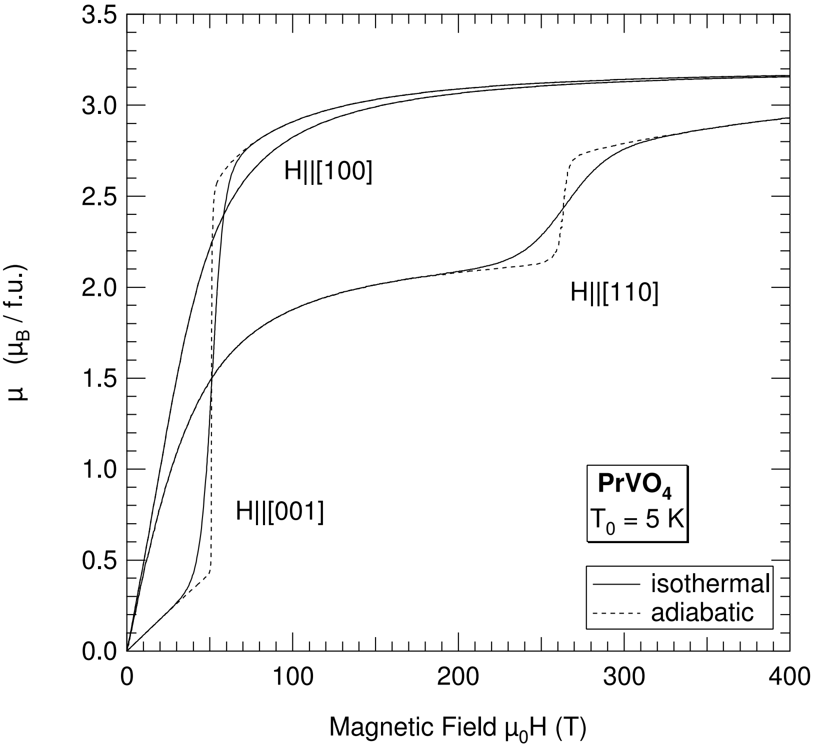

Figure 4.6: Calculated magnetization curves for PrVO$_4$ for an initial temperature $T_0 = 5\,\mathrm{K}$ and $\mathbf{H} \parallel [001]$. The magnetization process is either isothermal (solid lines) or adiabatic (dashed line).

in pulsed magnetic fields depends on the field sweep rate, thermal parameters of the samples and conditions of the heat exchange between sample and cooling bath. Normally it is polytrophic, i.e. intermediate between isothermal and adiabatic regime.

According to estimates of [LSK$^+$97] the magnetization process is close to being adiabatic for field sweep rates of at least 10^3 T/s, if a sample with dimensions of several millimetres is in good contact with the cooling bath (liquid nitrogen or liquid helium). Decreasing the field sweep rate to (1...10) T/s makes the magnetization process practically isothermal.

The field sweep rates in our experiments are of order 10^7 T/s and exceed the upper estimates of [LSK$^+$97] by four orders of magnitude. Hence we will consider the magnetization process of the crystalline sample as adiabatic.

The calculation of the magnetocaloric effect makes use of (4.23), giving the temperature change ΔT for a small step from H to $H + \Delta H$ with the step size ΔH chosen sufficiently small. Each field step requires thus the complete deduction of the spectrum and wavefunctions of the Pr^{3+} ion by numerical diagonalization of (4.1). To complete a step, M, $(\partial M/\partial T)_H$, C_H and finally ΔT are derived. The appropriate choice of ΔH is easily checked by comparing "up-sweep" and "down-sweep" of a calculation, which have to be identical within this model.

The total heat capacity C_H (4.24), consists of the lattice part (4.25) and the electronic part derived from the spectrum using (4.27) and a Boltzmann distribution for the average.

Figure 4.7 depicts temperature T and electronic heat capacity C_{el} under adiabatic conditions as function of the magnetic field for various initial temperatures T_0. The lattice heat capacity C_{lat} is much smaller compared with C_{el} and not shown. The character of the adiabatic magnetization is governed by the initial temperature T_0, which is also reflected in the temperature curves. We can distinguish three cases:

1. $T_0 < T_{01} \approx (9\ldots10)\,\mathrm{K}$: There is a strong cooling down to some decimals of Kelvin and the magnetocaloric effect is asymmetric with reference to H_c. Above H_c the temperature

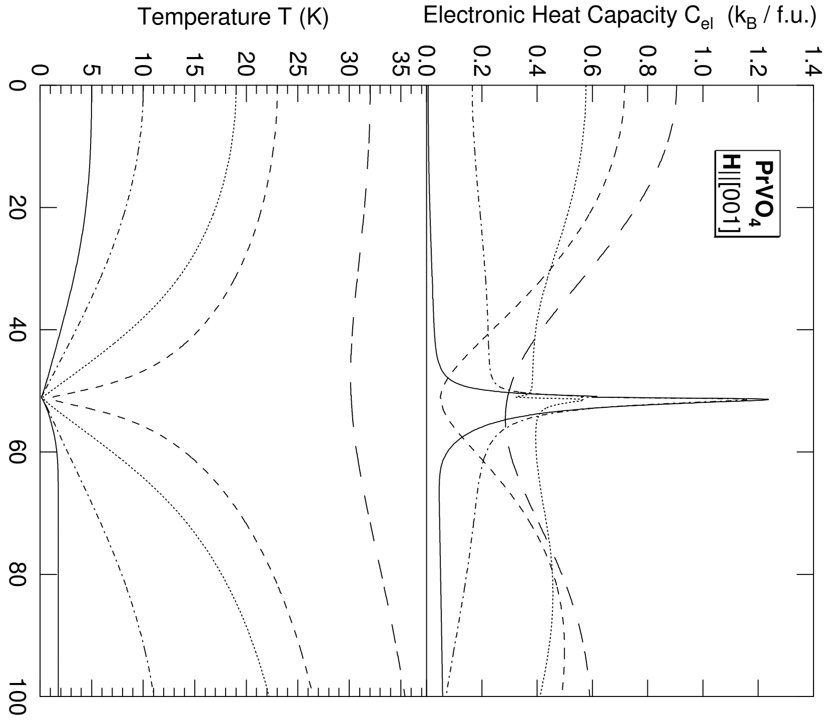

Figure 4.7: Field dependence of the electronic heat capacity (upper part) and magnetocaloric effect (lower part) in PrVO$_4$ under adiabatic magnetization for various initial temperatures and $\mathbf{H} \parallel [001]$.

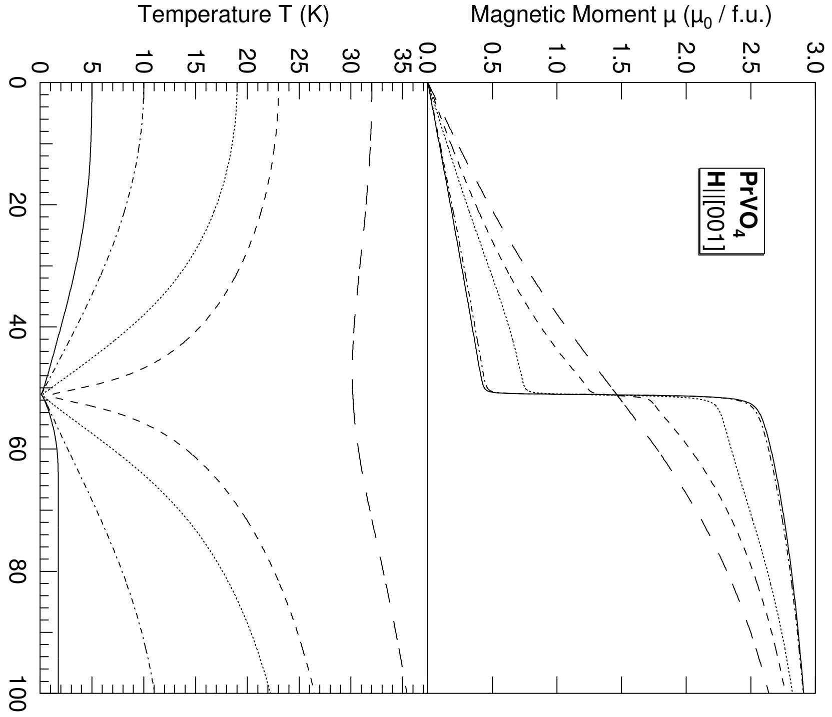

Figure 4.8: Adiabatic magnetization curves (upper part) and magnetocaloric effect (lower part) in PrVO$_4$ for various initial temperatures T_0 between 5 K to 32 K and $\mathbf{H} \parallel [001]$.

reaches a maximum value lower than T_0 and remains almost constant. This is connected with a different rate of change of the magnetic part of the entropy prior and after the crossover: A substantial decrease of $(\partial M/\partial T)_H$ occurs for $H > H_c$ because the electrons already occupy the lowest energy level, and a further lowering of this level with increasing field cannot change the entropy.

2. $T_{01} < T_0 < T_{02}$: There is still a strong cooling down to some decimals of Kelvin but the magnetocaloric effect is mainly symmetric with reference to H_c.

3. $T_0 > T_{02} \approx (23 \ldots 23.5)\,\mathrm{K}$: The pronounced magnetocaloric effect disappears. Only slight temperature changes occur.

The minimum temperatures reached at the crossover are $T_{\min} = 0.11\,\mathrm{K}$ for $T_0 = 5\,\mathrm{K}$ and $T_{\min} = 0.27\,\mathrm{K}$ for $T_0 = 19\,\mathrm{K}$. It is evident that the hyperfine interaction plays an important role in the immediate vicinity of the level crossing, where the temperature becomes comparable to the splitting of the nuclear multiplet, see figures 4.4 and 4.5. Thus it is clear that the minimum temperatures $T_{\min}$ depend sensitively on the hyperfine coupling. The different hyperfine splitting of the lowest-lying levels is the main reason for the asymmetric character of $C_{\mathrm{el}}(H)$ in the vicinity of H_c.

Figure 4.8 shows temperature and adiabatic magnetization curves as function of the magnetic field for various initial temperatures T_0. The different character of the adiabatic magnetization depending on the initial temperature is easily seen:

1. $T_0 < T_{01}$: There is a sharp jump in the magnetization at H_c and all curves are similar regardless of T_0, i.e. the jump value $\Delta\mu$ is nearly the same.

2. $T_{01} < T_0 < T_{02}$: There is still a sharp jump in the magnetization at H_c but the jump value $\Delta\mu$ decreases noticeably with increasing T_0. It should be pointed out that the width of the magnetization jump remains to be small even if the jump value $\Delta\mu$ decreases. This is a unique feature, which is opposed to the isothermal case.

3. $T_0 > T_{02}$: The distinct jump in magnetization, i.e. the nearly vertical part near H_c disappears completely.

Both characteristic temperatures T_{01} and T_{02} are closely related to the electronic structure of the RE ion, which is formed by the crystal field and hyperfine interactions.

The calculated magnetocaloric effect is caused by the electronic subsystem of the compound. Whether the temperature of the sample is diminished to the calculated values depends on the spin-lattice relaxation times. A comparison of experimental and calculated widths of the dM/dH peak at H_c could provide information on this issue.

4.4.5 Magnetic Susceptibility

Figure 4.9 reproduces experimental $(dM/dH)_{\mathrm{exp}}$ and calculated differential susceptibilities $d\mu/dH$ for the initial temperatures 5 K and 19 K, where $(dM/dH)_{\mathrm{exp}}$ was shifted along the H-axis to coincide with the calculated peaks at $H = H_c$. The peaks of the isothermal susceptibility are drawn for comparison. Their width is much larger than the experimental ones of 3.7 T (FWHM) for both temperatures. This is an undoubted indication for the cooling of the sample, especially for $T_0 = 19$ K with a larger effect.

On the other hand, the peaks calculated for (fully) adiabatic magnetization are too narrow compared with the experimental ones. The disagreement is larger for the lower temperature, and it is even bigger if the hyperfine splitting of the electronic levels is not taken into account. Such a disagreement was also observed in [KKP$^+$00] at another field sweep rate. Possible reasons for this discrepancy are discussed in the following.

Any misorientation of the magnetic field from the [001] direction leads to a broadening of the peak. However, this effect is too small in PrVO$_4$ as can be seen from figure 4.9. The peak width increases only insignificantly even at a misorientation angle of $\Theta = 5^\circ$.

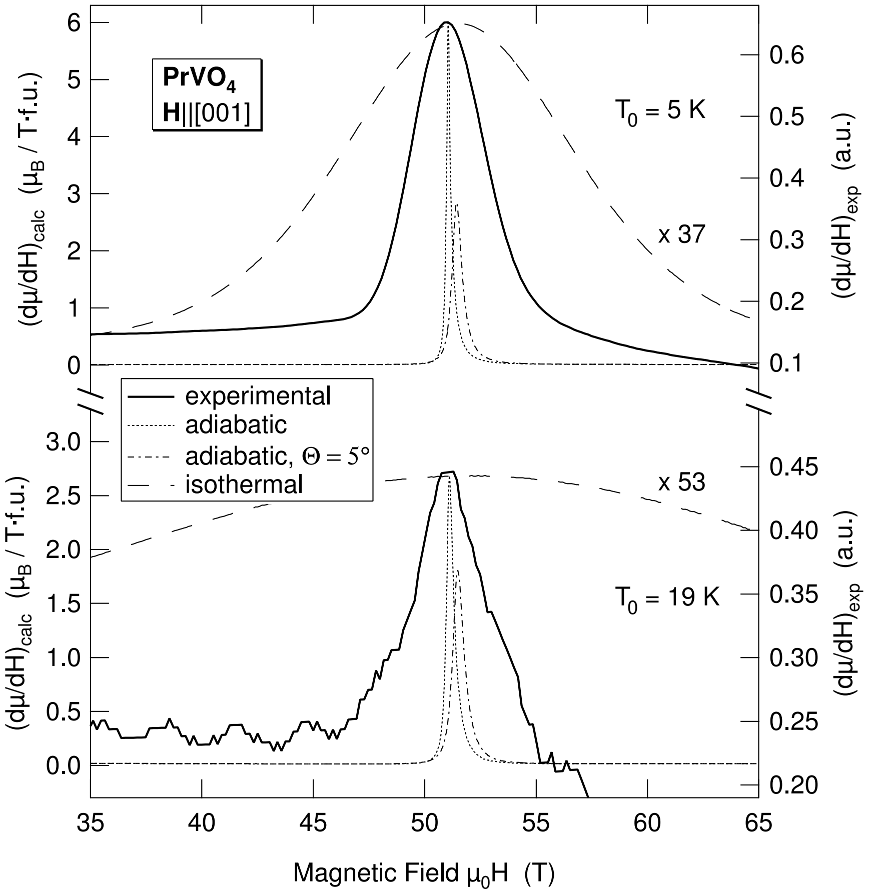

Figure 4.9: Comparison of experimental differential susceptibility dM/dH (thick solid lines) with theoretical calculations for PrVO$_4$, $\mathbf{H} \parallel [001]$. In order to coincide with the calculated peaks at $H = H_c$, the experimental curves were shifted along the H-axis. The dashed lines represent isothermal magnetization, while the dotted and the dash-dotted lines are associated with an adiabatic magnetization process. An additional misalignment angle of $\Theta = 5°$ was taken into account for the dash-dotted line.

Another reason that cannot be excluded could be – in analogy to HoVO$_4$, another Van Vleck paramagnet – a complicated structure of the peak, which gives rise to a broadening of the peak if it is not resolved.

Such a fine structure of the peak at the crossover in HoVO$_4$ was observed in both static [MRK95] and pulsed fields [KP94]. It involved two peaks resulting in a minimum width of 1.5 T in the isothermal regime at 0.1 K [MRK95]. The authors of [MRK95, KP94] supposed either the effect of mechanical stresses in the clamped sample or the presence of inequivalent sites for the RE ion. The possibility of spin ordering in a magnetic field as reason for the complicated peak structure was discussed in [Ama93].

It may also be supposed that the discrepancy between observed and calculated adiabatic peaks is associated with a substantial increase of the spin-lattice relaxation times near the crossover, causing also the hysteresis between up- and down-sweep. According to the estimates of [AMT96] for RE Van Vleck dielectric paramagnets listed in the review, these times are of order $(0.1 \ldots 1)$ ns. Though in the low-temperature range (< 1 K) there is a rather wide spread of the spin-lattice relaxation times in such compounds, and according to some estimates in [AK72, AMT96] they may run from $(0.1 \ldots 1)$ ms.

I should be pointed out again that the deviation between experimental and calculated peaks is smaller for $T_0 = 19$ K than for $T_0 = 5$ K. This difference may be due to the larger magnetocaloric effect, i.e. stronger cooling for smaller initial temperatures. Provided a rapid increase of the spin-lattice relaxation time occurs with decreasing temperature, it is possible to regard the magnetization process for $T_0 = 19$ K to be closer to the adiabatic case than for $T_0 = 5$ K. It is anticipated that the agreement between experimental and calculated susceptibilities will be better for higher temperatures ($19\,\mathrm{K} < T_0 < T_{02}$), since the minimum temperature will be higher and an essential increase of the spin-lattice relaxation time will not occur.

The hysteresis phenomena between up- and down-sweep may also be related to spin-lattice relaxation times comparable to the characteristic time needed for the magnetization change, which is of order 0.1 μs.

4.5 TmPO$_4$

TmPO$_4$ is expected to be a suitable material for studies of enhanced nuclear spin systems. The enhancement factors (1+K) of the hyperfine enhanced effective field were determined by NMR measurements and are 78 for the field along the a-axis [SHO80] and 3.2 for the field along the c-axis corresponding to $\gamma_\perp/2\pi = 276$ MHz/T and $\gamma_\parallel/2\pi = 11.34$ MHz/T at helium temperatures, respectively [BPW83].

Although the enhancement factor is considerable, it was expected that the ordering temperature of nuclear magnetic moments may be very low, possibly in the μK range since the nuclear moment of the Tm nucleus $\mu = 0.2308\mu_N$ is quite small and the lattice constants are relatively large in this compound. Bleaney [BPW83] predicted that the ordering temperature for the ^{169}Tm nuclear spins in TmPO$_4$ should be about 6 μK. Thus TmPO$_4$ offers the possibility of reaching μK temperatures by adiabatic demagnetization from initial fields of less than 1 T. Indeed the minimum temperature reached in adiabatic demagnetization experiments [SIO81] was about 0.4 mK.

It was predicted in previous works (e.g. [KKP$^+$97]) that in TmPO$_4$ a crossing of the lowest energy levels occurs for a magnetic field of $\sim$ 30 T directed along the tetragonal axis, which should be accompanied by pronounced anomalies in magnetic and magnetoelastic properties of the compound at low temperatures.

4.5.1 Experimental Results

First experiments, which had been performed in *long-pulse fields* and measured the differential susceptibility with the field oriented along the tetragonal axis [001] were only partly successful. The peak of dM/dH appeared at about 30 T, but it was much wider than expected [Kaz01]. Possible reasons for that could be a sweep rate of order 300 T/s, which is not enough for adiabatic magnetization or a misorientation of the crystal, which will be discussed in sections 4.5.3 and 4.5.5.

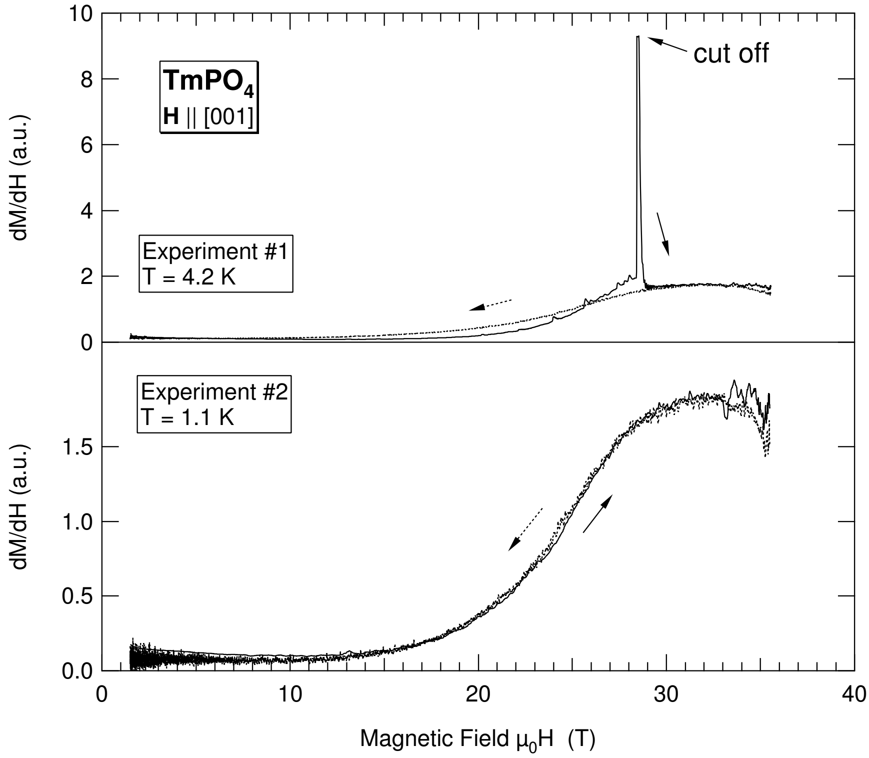

Figure 4.10: Differential susceptibility of $TmPO_4$ measured in a long-pulse field $\mathbf{H} \parallel [001]$. The sample broke during the up-sweep of the first experiment.

The measurements were repeated under the same conditions in fields up to 35 T, but special care was taken to avoid the misorientation effect. The crystal, well-oriented along the [001] direction, was tightly enclosed in a small cylinder made of epoxy resin. The results [Kir01, KKH$^+$04] are shown in figure 4.10.

The first experiment with this sample was performed at 4.2 K, and a very sharp peak at $B_c^\uparrow = 28.5\,\mathrm{T}$ was observed in the up-sweep, whereas no sign of it can be seen in the down-sweep. Another difference is apparent in the data below $B_c^\uparrow$: The slope in the down-sweep is smaller than in the up-sweep. The result of the second experiment at 1.1 K is nearly identical to that of the down-sweep of the first experiment, showing a wide peak centered at about 32 T. Its width (FWHM) is approximately 15 T.

An inspection of the sample after these experiments turned out that it was broken into pieces, which were still in the pick-up coil. This naturally explains the measured results. Obviously the well-oriented crystal broke near the crossover field B_c. The sharp peak is then the response of the sample before or during the destruction of the crystal, after which a good alignment with respect to the field can no longer be assumed.

The destruction of the sample could be caused by strong internal forces due to a structural phase transition [MK97] or strong (external) forces resulting from a torque on the crystal. Such a torque results from the magnetic moment perpendicular to the field direction, which occurs around B_c if there is a small misalignment of the field with respect to the [001] direction.

Problems of that kind did not arise in measurements performed with the *single-turn coil technique*. Figure 4.11 reproduces the differential susceptibility dM/dH for the initial temperature $T_0 = 2.2\,\mathrm{K}$ and $\mathbf{H} \parallel [001]$, where the peak fields varied between 39 T and 112 T. The dependence of dM/dH on initial temperatures T_0 ranging from 2 K to 18 K is given in figure 4.12. Since the magnetic anomaly occurs around 30 T, it is recorded four times in one experiment. When evaluating the data it should be considered that data from up- and down-sweep are generally more significant than those obtained at larger times and reversed field direction.

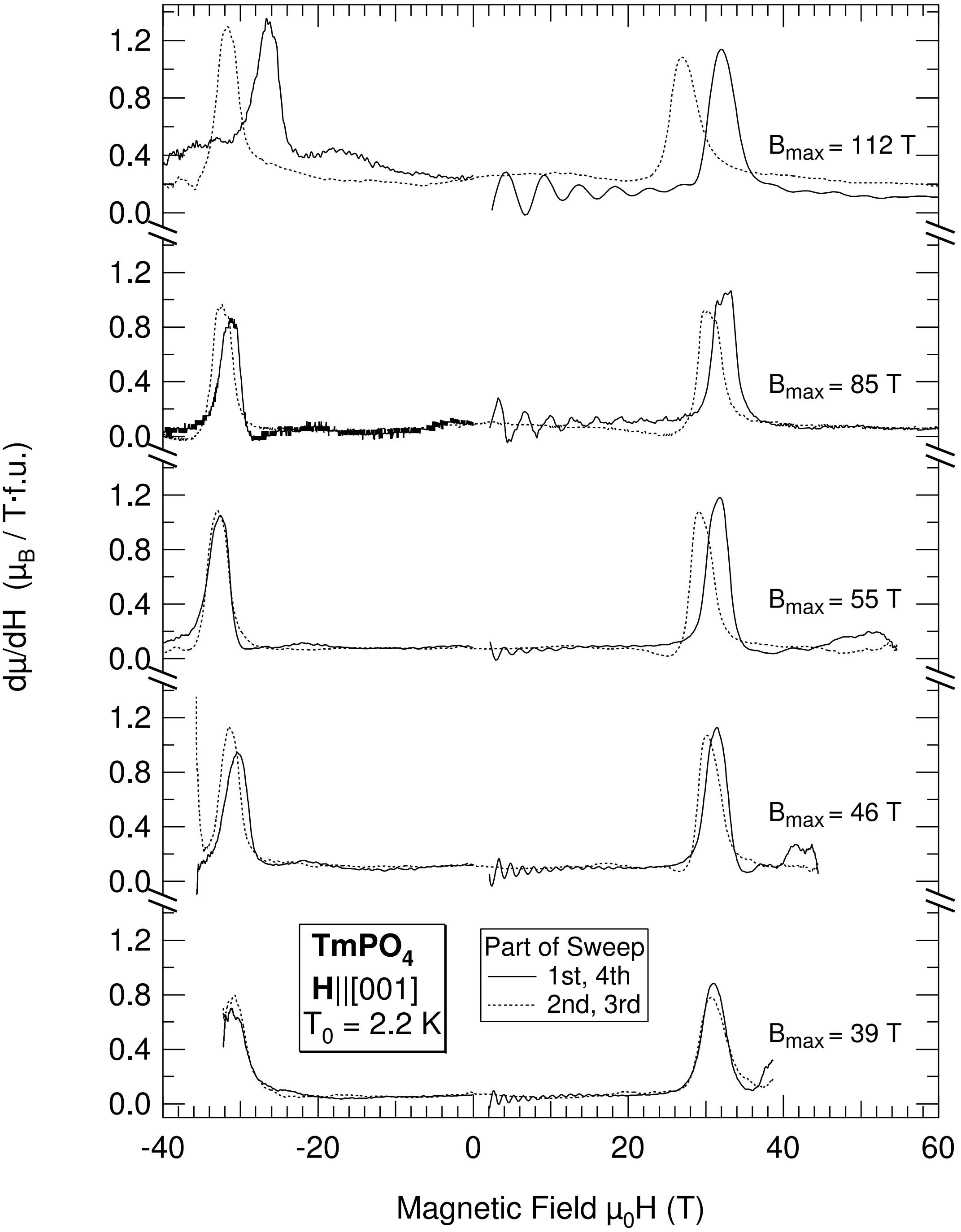

Figure 4.11: Experimental differential susceptibility $d\mu/dH$ of TmPO$_4$ for a magnetic field parallel to the tetragonal axis and various peak fields $B_{\max}$ increasing from 39 T to 112 T.

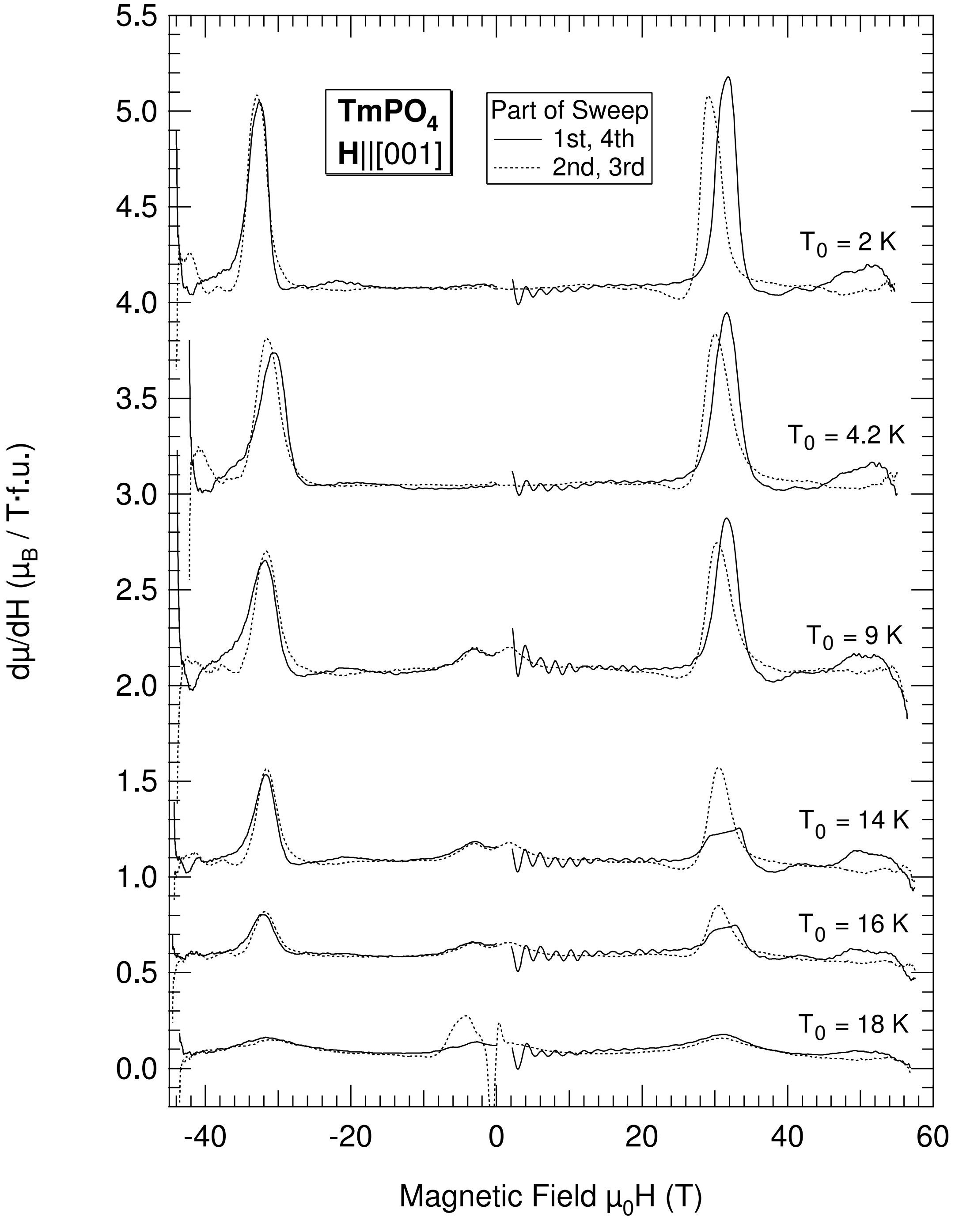

Figure 4.12: Experimental differential susceptibility $d\mu/dH$ of $TmPO_4$ for a magnetic field parallel to the tetragonal axis and various initial temperatures T_0 increasing from 2 K to 18 K. The curves have offsets of 0, 0.5, 1, 2, 3 and 4, respectively. Please note that the two peaks of the up-sweep for 14 K and 16 K are cut off as a result of a measurement overrange.

Table 4.3: Experimental data for TmPO$_4$, **H** $\parallel$ [001]: Maxima of dM/dH obtained at the initial temperature T_0 occur at $B_c^{\uparrow}$ and $B_c^{\downarrow}$ in up- and down-sweep, respectively; $B_c = (B_c^{\uparrow} + B_c^{\downarrow})/2$ and $\Delta B_c = B_c^{\uparrow} - B_c^{\downarrow}$. ΔB is the width of the peak, $B_{\max}$ is the maximum field of the pulse.

T_0 / K	$B_{\max}$ / T	$B_c^{\uparrow}$ / T	$B_c^{\downarrow}$ / T	B_c / T	ΔB_c / T	ΔB / T
2.2	39	31.0	30.8	30.9	0.2	3.4
	46	31.3	30.1	30.7	1.2	3.1
	55	31.8	29.2	30.5	2.6	3.2
	85	32.2	30.4	31.3	1.8	3.4
	112	32.2	27.0	29.6	5.2	4.0
2.2	55	31.8	29.2	30.5	2.6	3.2
4.2		31.5	30.0	30.8	1.5	3.7
9		31.7	30.3	31.0	1.4	3.5
14		(31.3)	30.5	30.9	(0.8)	3.6
16		(31.4)	30.6	31.0	(0.8)	3.4
18		31.3	30.7	31.0	0.6	~ 6.9
Results of another crystal with larger misorientation effect						
5	57	31.3	29.6	30.5	1.7	13
	116	33.2	27.2	30.2	6	11

Table 4.4: Crystal field parameters B_n^m for Tm^{3+} ions in TmPO$_4$.

Substance	B_2^0	B_4^0	B_6^0	B_4^4	B_6^4	Unit	T/K	Reference
TmPO$_4$	227	40	-63	1003	75	K	-	[LSA$^+$93]
TmPO$_4$	**258**	**47**	**-67**	**989**	**60**	K	-	[MRK96]

The experimental findings can be summarized as follows.

- *Influence of the initial temperature* T_0. Sharp maxima occur for all temperatures except the highest one, 18 K, for which the peak is less pronounced. The peak height decreases with increasing T_0, but the peak width ΔB remains small.

- *Influence of the maximum field* $B_{\max}$ *(or the field sweep rate* $dH/dt \propto B_{\max}$*).* The hysteresis of the peak positions $\Delta B_c = B_c^{\uparrow} - B_c^{\downarrow}$ is increasing with $B_{\max}$. However, the peak width ΔB seems to be independent of $B_{\max}$.

- *Shape of the* dM/dH *peak.* The shape of the peaks is clearly asymmetric for initial temperatures up to 14 K, probably also for $T_0 = 16$ K. This refers to both, up- and down-sweep, while the shape is apparently reversed for up- and down-sweep.

Detailed values of B_c and other quantities are given in table 4.3. The average crossover field is $B_c = 30.9$ T and the experimental accuracy in this field range is 1.5 T.

4.5.2 The Hamiltonian

As in the case of PrVO$_4$, the Hamiltonian (4.1) is used, but in contrast to PrVO$_4$, accurate crystal field parameters are available and listed in table 4.4.

The CFPs of [MRK96], deduced on the basis of neutron spectroscopy data and CFPs from [LSA$^+$93] describe perfectly the level scheme of the low-lying levels [LSA$^+$93] and the temperature

Table 4.5: Energy levels of Tm^{3+} in $TmPO_4$. S and D denote singlets and doublets, respectively.

Level	S	D	S	D	S	S	S	D	S	S
Energy (cm^{-1})	0	28.9	77.9	135	184	244	278	281	384	387

variations of the initial susceptibilities [MRK96]. Moreover, they reproduce the crossover field B_c very well so that they will be used in this work.

The ground multiplet $^3H_6$ of the Tm^{3+} ion has a singlet, a doublet and another singlet as lowest-lying levels, where the latter are about $29\,\mathrm{cm}^{-1}$ and $78\,\mathrm{cm}^{-1}$ above the ground singlet, respectively.

The energy levels of the ground multiplet of the Tm^{3+} ion obtained with the CFPs of [MRK96], are given in table 4.5.

Hyperfine parameters are given in [BPW83]. They were derived from NMR data using an approximation, which is not appropriate for strong fields, where a level crossing takes place. Thus we use again (4.11) as described in section 4.4.2. The isotope ^{169}Tm has the nuclear spin $I = 1/2$, $\gamma_I/2\pi = -3.52\,\mathrm{MHz/T}$ and $A_J/h = -393.5\,\mathrm{MHz}$ [BPW83]. Thus we use $A_J/h\,g_J = -338.1\,\mathrm{MHz}$.

4.5.3 Zeeman Effect and Magnetization Curves

Figure 4.13 shows the Zeeman effect of the four lowest-lying energy levels, where the field is oriented along the tetragonal axis. The hyperfine interaction splits each level into $2I + 1 = 2$ hyperfine levels as is depicted in the inset of figure 4.13.

A crossing of the two lowest levels occurs at $B_c = 31.2\,\mathrm{T}$ for $\mathbf{H} \parallel [001]$. This agrees very well with the experimental result of $(30.9 \pm 1.5)\,\mathrm{T}$. The model predicts another level crossing in the vicinity of 500 T at the same field orientation. Though, level crossings for different field directions do not occur.

The level crossing at $\approx 31\,\mathrm{T}$ takes place without a gap if the field is exactly aligned along the [001] direction. Small deviations from this alignment result in the interaction of the ground and the first excited levels so that a gap near B_c develops. Thus any misorientation results in a deformation of the magnetization curve and the susceptibility peak smears out, i.e. it is broadened. The experimental difficulty is to keep the misalignment as small as possible.

As opposed to $PrVO_4$, for which the misorientation effect is negligible, it is substantial in $TmPO_4$ as can be seen from figure 4.14. This follows from the electronic structure of the Tm^{3+} ion in this compound [KOD+03]. That level, which is strongly mixed with the ground level by a perpendicular field component $H_{\perp c}$ is the first excited level that approaches and crosses the ground level of $TmPO_4$. A similar level in $PrVO_4$ is the second excited level, which is not involved in the crossover.

At the same time this effect must be taken into account in any comparison of experimental data with theoretical calculations because a deviation from the exact case $\mathbf{H} \parallel [001]$ will occur in any experimental setup.

Figure 4.15 depicts the magnetization curves for the main crystallographic directions. The magnetization jump is associated with the crossing of the lowest-lying energy levels. The jump of $\sim 2.7\mu_B/\mathrm{f.u.}$ at $\approx 31\,\mathrm{T}$ is much larger than that near 500 T with $\sim 1.2\mu_B/\mathrm{f.u.}$.

Adiabatic magnetization curves also shown in this figure differ from the isothermal curves only for $\mathbf{H} \parallel [001]$, i.e. for the field direction with crossovers. The magnetization jump is much steeper in the adiabatic case as the temperature of the crystal decreases when the crossover is approached.

4.5.4 Magnetocaloric Effect and Adiabatic Magnetization

Due to the experimental conditions it is also for $TmPO_4$ absolutely necessary to take the magnetocaloric effect into account. For the calculation and interpretation, the magnetization process will be assumed as being reversible adiabatic. This is certainly justifiable for the experiment performed

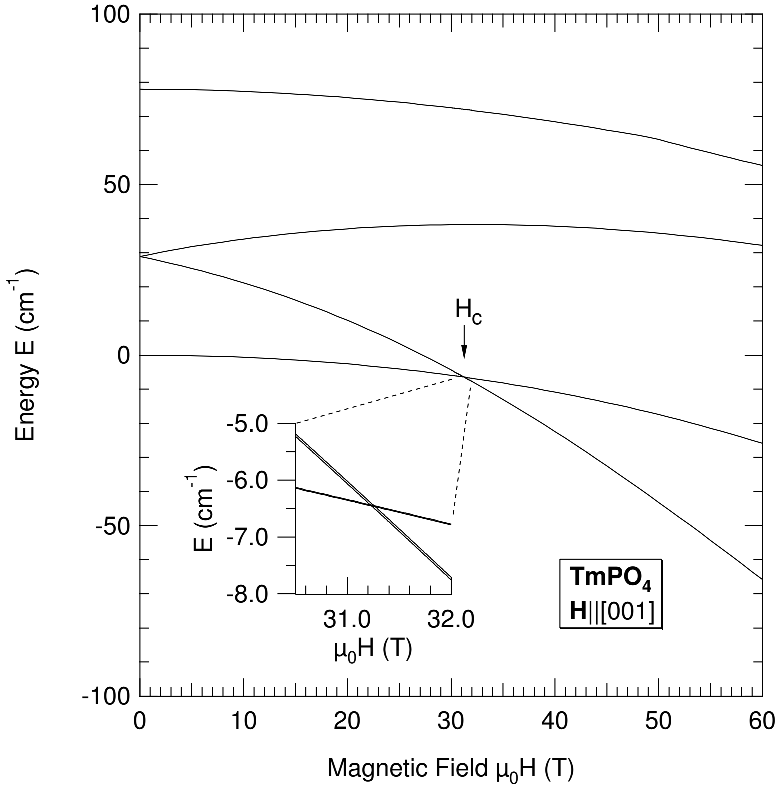

Figure 4.13: Zeeman effect for the four lowest-lying electronic levels of the ground multiplet of TmPO$_4$ for $\mathbf{H} \parallel [001]$. The inset shows the Zeeman effect with regard to hyperfine coupling for the two lowest-lying levels.

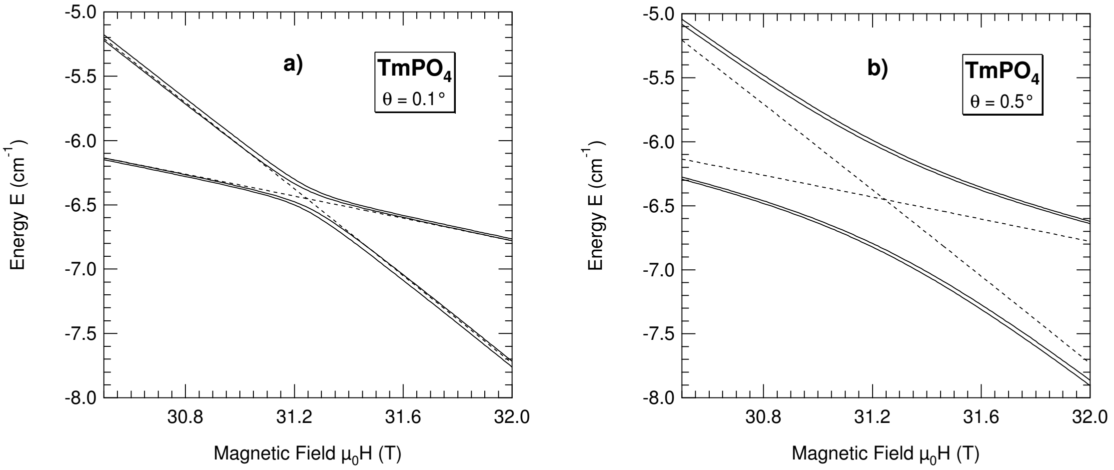

Figure 4.14: Dependence of the Zeeman effect on the misalignment angle θ between magnetic field $\mathbf{H}$ and the tetragonal axis [001]. The diagrams show the two lowest-lying levels with regard to hyperfine coupling for $\theta = 0.1°$ (a) and $\theta = 0.5°$ (b), respectively.

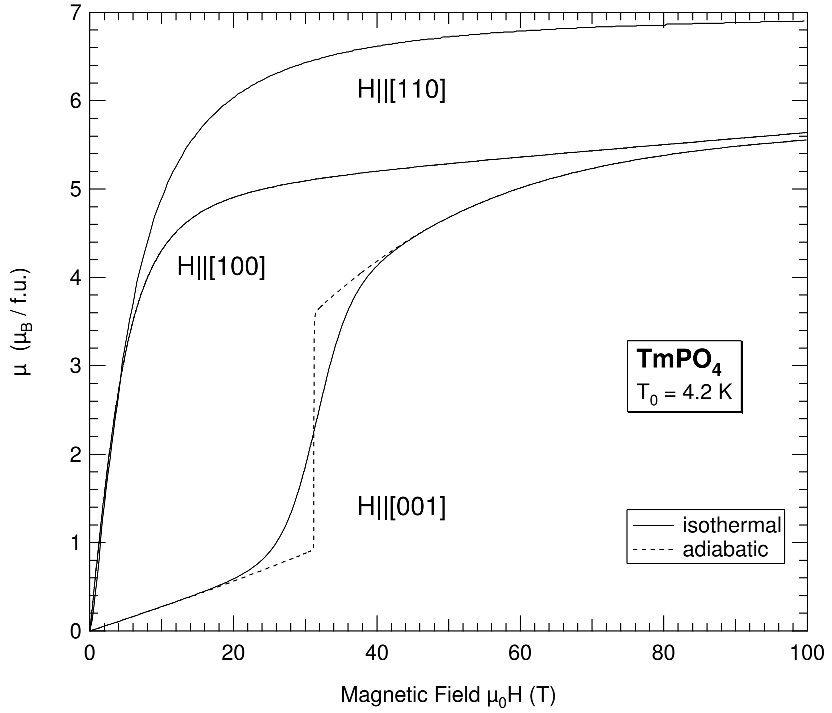

Figure 4.15: Calculated magnetization curves for TmPO$_4$ for an initial temperature $T_0 = 4.2\,\mathrm{K}$ and $\mathbf{H} \parallel [001]$. The magnetization process is either isothermal (solid lines) or adiabatic (dashed line).

at $T_0 = 2.2\,\mathrm{K}$ with $B_{\max} = 39\,\mathrm{T}$, for which up- and down-sweep are almost identical, showing only little hysteresis. Hysteresis phenomena manifest for larger field sweep velocities, but shape and width of the peaks in dM/dH associated with the crossover are very similar. Thus calculations are performed the same way as for PrVO$_4$ in section 4.4.4, assuming an adiabatic magnetization process. Only the field-step size ΔH in (4.23) has to be chosen smaller, since the hyperfine splitting is smaller than in PrVO$_4$.

In the vicinity of the crossover the temperature can approach a few mK, which is comparable to the splitting of the nuclear multiplet. It is the hyperfine Hamiltonian $\mathcal{H}_{\mathrm{N}}$ in (4.1), which is then of great importance. If one restricts to the terms $\mathcal{H}_{\mathrm{CF}} + \mathcal{H}_{\mathrm{Z}}$ only, the calculation of the adiabatic magnetization process in a field exactly along the tetragonal axis results in an "overcooling" at the crossover for initial temperatures $T_0 < 18\,\mathrm{K}$ [KOD$^+$03]. This means, disregarding $\mathcal{H}_{\mathrm{N}}$ in the case $\mathbf{H} \parallel [001]$ and $T_0 < 18\,\mathrm{K}$ leads to incorrect results. Also the nuclear specific heat gives an important contribution to C_{el}.

Figure 4.16 shows the electronic heat capacity C_{el} and the temperature T for various initial temperatures T_0 for $\mathbf{H} \parallel [001]$. The lattice part C_{lat} is much smaller and not drawn.

Although it is not very well seen in figure 4.16, the narrow peak of C_{el} at H_c for $T_0 < 9\,\mathrm{K}$ consists of two distinct peaks, separated by a local minimum. These anomalies in $C_{\mathrm{el}}(H)$ are similar to the Schottky-type anomalies in $C(T)$. Any asymmetry in the immediate vicinity of the crossover is due to the different hyperfine splitting of the levels, which act as ground level prior to and after the crossover, see figures 4.13 to 4.14. Of course, this effect is relevant only at low temperatures.

The two characteristic temperatures, analogous to those of PrVO$_4$ introduced in section 4.4.4, are $T_{01} \sim 9\,\mathrm{K}$ and $T_{02} \approx (17\ldots18)\,\mathrm{K}$ for TmPO$_4$. T_{02} is clearly defined by the different characteristics of $T(H)$ for different T_0. T_{01} is not so well determined from $T(H)$ alone, but considering $C_{\mathrm{el}}(H)$ and $M(H)$ too makes it unambiguous.

Assuming the magnetization is fully adiabatic, the sample should cool down from $T_0 = 4.2\,\mathrm{K}$ to $T_{\min} = 2.9\,\mathrm{mK}$ as the crossover is approached, and heat up again. The minimum temperature

T_{min} increases if the field is not perfectly aligned along the [001] direction. It increases to 53 mK for a misalignment angle $\Theta = 0.1°$ and to 0.31 K for $\Theta = 1°$ and $T_0 = 4.2$ K. The magnetization jump is affected at the same time – it is smeared out.

Figure 4.17 shows temperature and adiabatic magnetization curves as function of the magnetic field for various initial temperatures T_0. The dependence of $M(H)$ on the initial temperature T_0 is exactly as for PrVO$_4$:

1. $T_0 < T_{01}$: There is a sharp jump in the magnetization at H_c and all curves are similar regardless of T_0, i.e. the jump value $\Delta\mu$ is nearly the same.

2. $T_{01} < T_0 < T_{02}$: There is still a sharp jump in the magnetization at H_c but the jump value $\Delta\mu$ decreases noticeably with increasing T_0. The width of the magnetization jump remains to be small.

3. $T_0 > T_{02}$: The distinct jump in magnetization, i.e. the nearly vertical part near H_c disappears completely.

Whether the temperature of the sample is diminished to the calculated values depends on the spin-lattice relaxation times. Although a comparison of experimental and calculated widths of the dM/dH peak at H_c could in principle provide information about this point, it is hardly possible since the contribution from the misorientation effect (i.e. the misalignment angle Θ) is unknown.

4.5.5 Magnetic Susceptibility

Comparisons of experimental differential susceptibilities dM/dH with theoretical calculations are presented in figures 4.18 and 4.19 for various cases and conditions.

The experimental peak widths $\Delta B = (3 \ldots 4)$ T of dM/dH are for all temperatures larger than the calculated ones derived under adiabatic conditions and in a field $\mathbf{H}$ aligned exactly along the tetragonal axis. Question arises about possible reasons. As was already pointed out in the last section, with the information available it cannot be distinguished between inherent effects of the compound (e.g. effects related to spin-lattice relaxation times, ...) and the misorientation effect.

Another reason, the possible broadening caused by the measurement system can be ruled out. The minimum duration of the system's response to extremely short excitation pulses ($\Delta\tau \ll \tau_{\mathrm{p}}$) is $(0.5 \ldots 1)\tau_{\mathrm{p}}$, [2] where τ_{p} is the characteristic time constant of the system as defined in appendix B. The duration of the system's response to longer excitation pulses is not (much) prolonged. However, there is a delay of $\sim 0.5\tau_{\mathrm{p}}$. The minimum width is therefore $\Delta B = (0.5 \ldots 1)\, \tau_{\mathrm{p}}\, (dB/dt) = 0.4$ T assuming a sweep rate of 20 T/μs at the crossover and $\tau_{\mathrm{p}} = 20$ ns for the measurement system used. This reasoning is confirmed by the data obtained at reversed field direction, where the sweep rate is significantly lower, but the peak width is unchanged.

The influence of $\mathcal{H}_{\mathrm{N}}$ on the susceptibility peak was investigated in [KOD$^+$03]. Different choices of the hyperfine parameters and of the form of $\mathcal{H}_{\mathrm{N}}$ lead to considerable changes of the peak width and height. This holds in particular for fields exactly parallel to the tetragonal axis, whereas any misorientation from the [001] direction diminishes this effect. The hyperfine coupling becomes rather unimportant for misorientation angles $\Theta > 1°$.

Figure 4.18 investigates the influence of the misorientation effect for $T_0 = 2$ K. Experimental and calculated adiabatic susceptibilities are comparable for $\Theta \approx 1.5°$ with regard to the peak width, though the shape is different. The same is true at higher temperatures, see figure 4.19.

It can be concluded that the misalignment angle should not exceed 1.5°, but it must not be necessarily so large, it can be smaller. Broadening is also possible due to a rapid increase of the spin-lattice relaxation time or due to a complicated structure of the peak, when it is not resolved. As discussed already in section 4.4.5 such a structure was observed in HoVO$_4$ [MRK95, KP94]. Examining the peaks of the measurement with $B_{\mathrm{max}} = 85$ T in figure 4.11 reveals some small structures at the top of the peaks, which could be an indication for this phenomenon. Closely related to this question is the asymmetric shape of peak. Although the misorientation effect affects the shape, it cannot completely explain all deviations.

---

[2] The shape of the pulse is no longer maintained in this case.

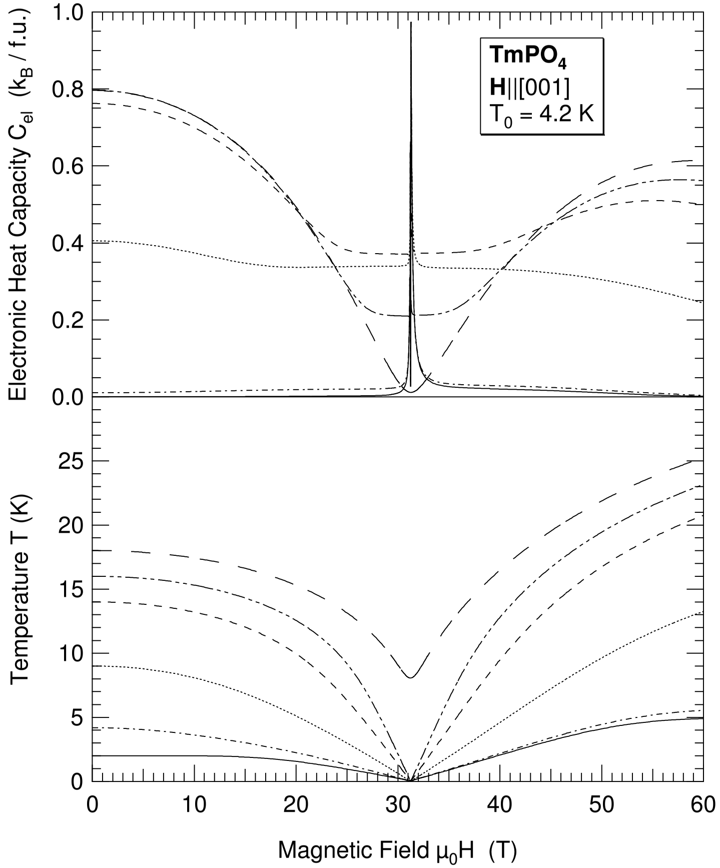

Figure 4.16: Field dependence of the electronic heat capacity (upper part) and magnetocaloric effect (lower part) in $TmPO_4$ under adiabatic magnetization for various initial temperatures and $\mathbf{H} \parallel [001]$.

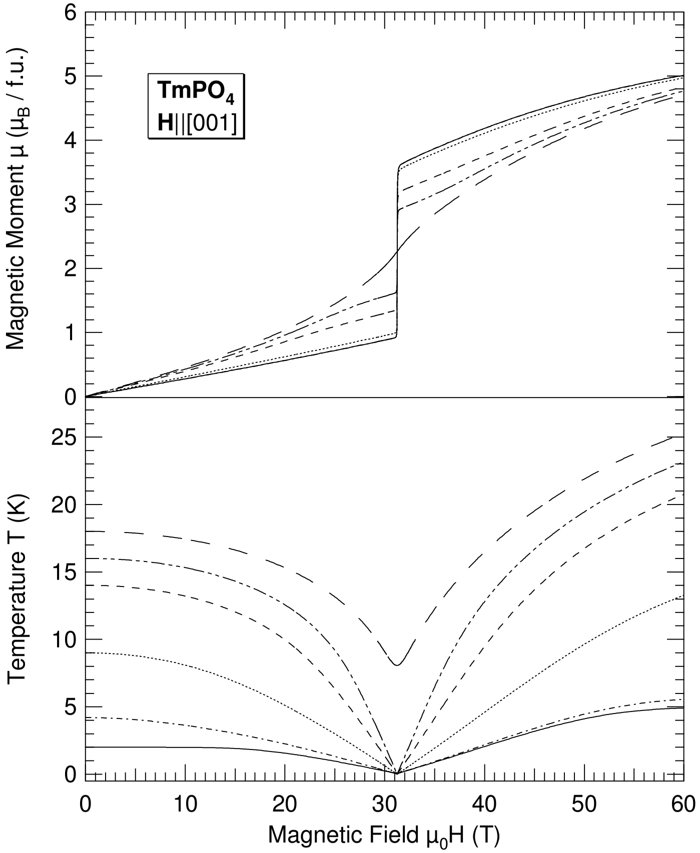

Figure 4.17: Adiabatic magnetization curves (upper part) and magnetocaloric effect (lower part) in $TmPO_4$ for various initial temperatures T_0 between 2 K to 18 K and $\mathbf{H} \parallel [001]$.

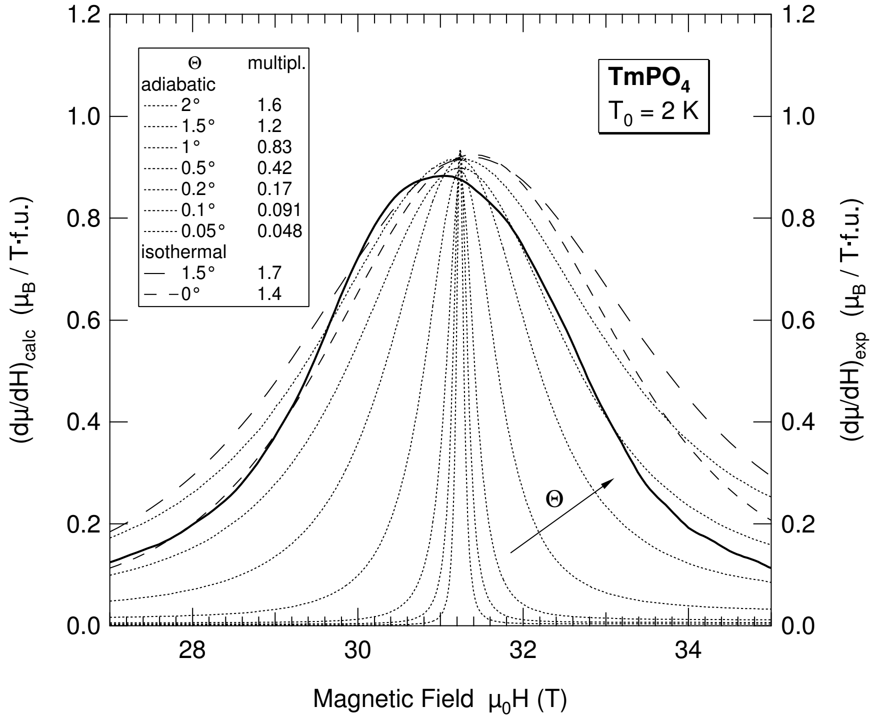

Figure 4.18: Comparison of experimental differential susceptibility dM/dH (thick solid line) with theoretical curves for $TmPO_4$ in a magnetic field **H** slightly tilted with regard to the [001] direction. The dotted lines represent adiabatic magnetization for various misalignment angles Θ, while the dashed lines are for isothermal magnetization. Please note the different scales given by the multiplication factor in the legend.

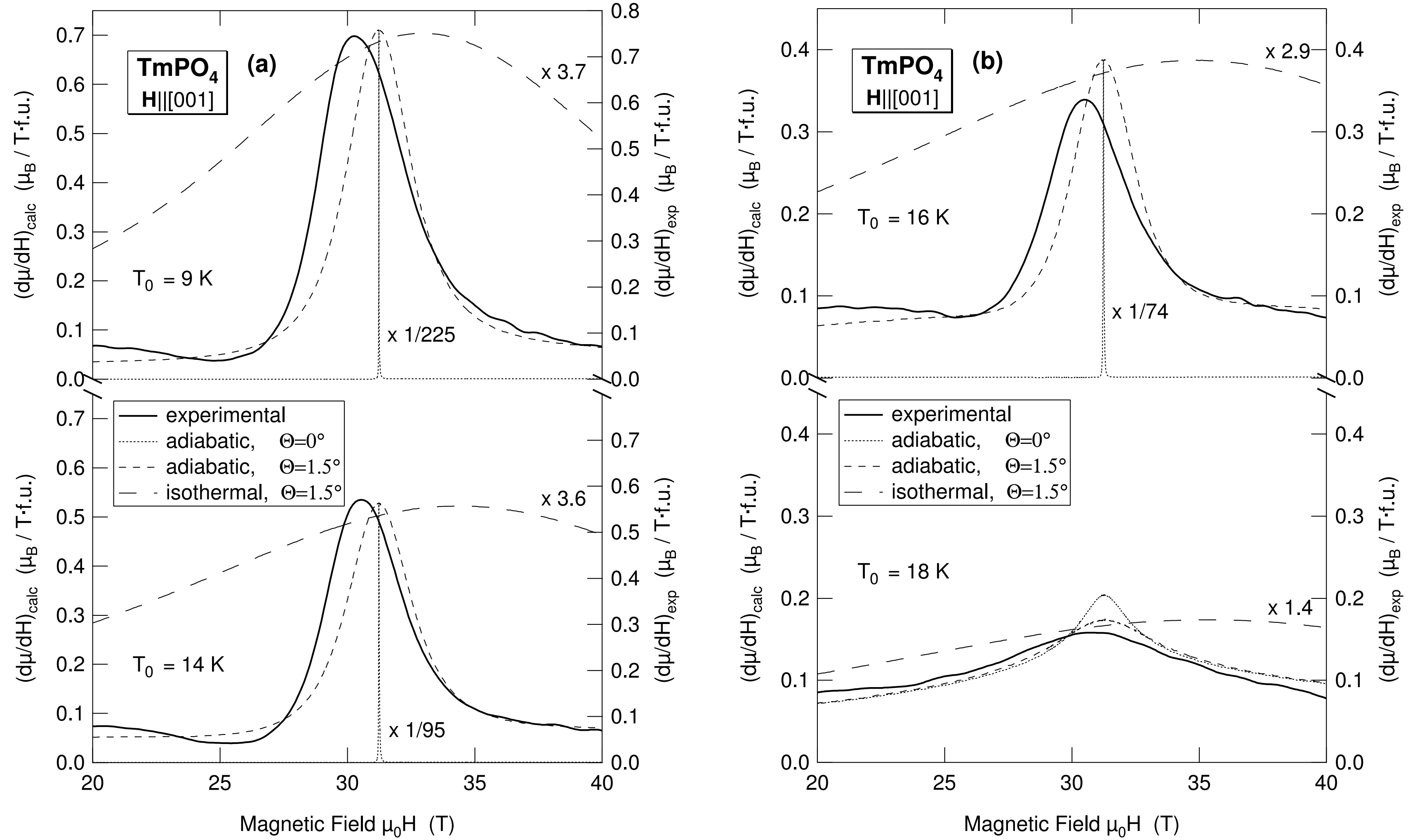

Figure 4.19: Comparison of experimental differential susceptibility dM/dH (thick solid lines) with theoretical calculations for $TmPO_4$. The magnetic field $\mathbf{H}$ is tilted by a small angle Θ with regard to the [001] direction. Equal scaling is maintained within (a) and (b). Scaling factors, if applied, are given at the respective curves.

In order to investigate those phenomena (shape of the peak, broadening, hysteresis) more precisely and under different conditions, measurements at very low temperatures down to 40 mK in long-pulse fields were planned and started, but failed due to the destruction of the sample (section 4.5.1).

Exchange and dipole interactions are extremely small in $TmPO_4$ so that magnetic ordering in a magnetic field near the crossover is not likely to occur. Hence it is not expected to contribute to the broadening of the peak.

In particular with regard to the hysteresis phenomena, information about the spin-lattice relaxation time in high magnetic fields would be helpful. The dependence of this quantity on temperature (20 mK. . . 2 K) and magnetic field (< 1 T) was measured in [SHO80, SIO81]. As far as we know, no information is available at high magnetic fields.

Chapter 5

Magnetization of Intermetallic Compounds $\boldsymbol{R}\mathrm{Mn_2Ge_2}$

5.1 Introduction

In the past years magnetic properties of $R\mathrm{Mn_2Ge_2}$ and $R\mathrm{Mn_2Si_2}$ compounds have been studied extensively by means of magnetometric and neutron diffraction methods, resulting in a better understanding of those systems and in the discovery of interesting phenomena like reentrant ferromagnetism. However, the behaviour of these intermetallics in strong magnetic fields has been studied less intensively. This is not astonishing because fields as high as 100 T are necessary in order to observe interesting new phenomena.

It was found that even in the highest fields employed so far in these experiments, about (30. . . 40) T, the measured magnetization was considerably lower than the theoretical saturation magnetization for a parallel orientation of the R and Mn subsystems. This led to the assumption that additional field-induced magnetic phase transitions could be observed in stronger fields.

Thus experiments were devised and performed, in which the magnetic properties of $R\mathrm{Mn_2Ge_2}$ compounds were examined in ultrastrong magnetic fields. The results of these measurements are presented in this chapter.

This chapter starts with some basic concepts, followed by a section on the magnetization behaviour of simple ferrimagnets. A small section is devoted to experimental techniques related to intermetallics in high pulsed fields. The central part dealing with the $R\mathrm{Mn_2Ge_2}$ intermetallics are sections 5.5-5.7, which present two particular models, the experimental results and the discussion.

5.2 Basic Concepts

5.2.1 $4f$ Magnetism and $3d$ Magnetism

Although both rare-earth (R) and transition (T) metals may be magnetic, their properties are completely different originating from the different spatial extent of the wavefunctions of the open electron shell. The R elements have an open $4f$ shell, which is closely bound inside the outer closed shells of the ion, i.e. beneath filled $5s$ and $5p$ shells. In most chemical compounds the rare earths appear as tripositive ions so that the number of electrons increases from $4f^1$ in Ce (*light* R) to $4f^{14}$ in Lu (*heavy* R), see table C.1.

This means that the spin-orbit coupling in $4f$ ions is much larger than the crystal field effect acting on the electrons. Compared to the $3d$ series, the spin-orbit coupling in the $4f$ series is much larger since the R elements are more heavy, but it is not too large so that the Russel-Saunders coupling scheme can be used. Both the orbital moment L and the spin moment S are good quantum numbers; the total angular moment $J = L + S$ is a constant of motion and can be calculated using Hund's rules.

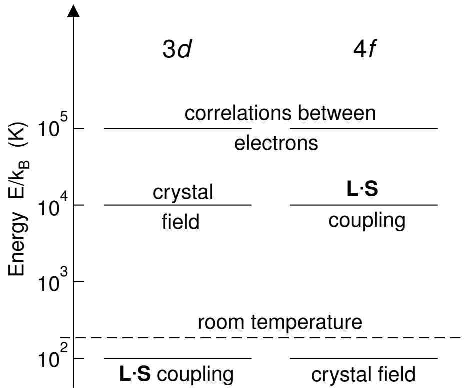

Figure 5.1: Crystal field and spin-orbit interaction in $3d$ and $4f$ ions (after [BGV88]).

The magnetic moment μ is related to J by the Landé factor g_J,

$$g_J = 1 + \frac{J(J+1) + S(S+1) - L(L+1)}{2J(J+1)}. \tag{5.1}$$

The magnitude of the magnetic moment is equal to $\mu_{\text{eff}} = g_J \mu_B \sqrt{J(J+1)}$. Experimentally it is directly determined by measuring the susceptibility of a compound in its paramagnetic region, requiring thus the limit of vanishing applied magnetic field. In a magnetically ordered state, the magnetic moment per ion saturates and equals the moment along the quantization axis. It is given by $\mu_{\text{sat}} = g_J \mu_B J$. In all kinds of compounds the experimentally found values for the R moment agree quite well with the calculated ionic moment.

The transition metals have an open $3d$ shell, which makes the crystal field effect much stronger than the spin-orbit coupling. Consequently the relative importance of both interactions is inverted in R and T elements as is shown in figure 5.1. If the crystal field perturbation is strong enough (and the symmetry low enough), the orbital degeneracy is completely lifted and the orbital ground state is a singlet. This results in a 'quenching' of the angular momentum L of the ion, i.e. the expectation values of all components of L vanish and we observe "spin-only" magnetic properties. The total angular moment in $3d$ metals is then (in good approximation) $J = S$.

Although this approach yields qualitatively and even quantitatively acceptable results, its physical picture is incorrect. The problem is to choose for the d electrons between a localized "atomic orbitals" description, as usually taken for the more localized $4f$ shells of R metals, and an extended "molecular orbital" approach as for the others (sp shells). In a crystal, the atomic $3d$ levels mix with those ones of neighbouring ions and form energy bands of delocalized states.

The magnetic moment of the itinerant $3d$ electrons is caused by the difference of spin-up and spin-down electrons. Since accurate calculations of the $3d$ moments in a particular material require advanced and complicated theory, but are still not very reliable, an experimentally found pseudo-spin is attributed to each $3d$ ion and can be used in calculations involving the $3d$-$4f$ exchange interaction.

In both $4f$ and $3d$ systems there are interactions which couple the respective electrons of different ions. These may take different forms, but the most important ones are of the exchange type, giving rise to cooperative magnetic properties.

5.2.2 Exchange Interaction and Magnetic Ordering

Below a certain critical temperature T_C and in the absence of an external magnetic field the individual magnetic ions of most intermetallic compounds are magnetically ordered. The reason for this ordering is the exchange interaction. Mainly indirect exchange and itinerant exchange occur in metallic systems; direct exchange and superexchange are important mechanisms in non-metallic systems.

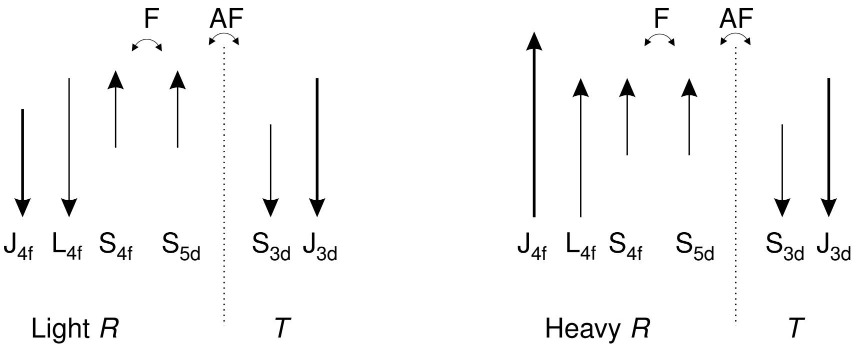

Figure 5.2: Coupling scheme between $3d$ (T) moments and $4f$ (light R, heavy R) moments according to Campbell [Cam72].

The exchange interaction between different $3d$ ions is by far the strongest interaction, followed by the coupling between $4f$ and $3d$ ions of intermediate strength. While the former interaction is important for the ordering temperature, the latter transfers the magnetocrystalline anisotropy of the $4f$ ions to the $3d$ moments and the magnetic ordering of the $3d$ moments to the $4f$ ions. The exchange interaction between different $4f$ ions is relatively small and often neglected.

For R-T intermetallics, it is important to understand the nature of the coupling between R and T moments. The $3d$-$4f$ exchange interaction is indirect since the electron-density distributions do not overlap, and it is found that the coupling between $4f$ and $3d$ spins is always antiferromagnetic. Thus the moments of the $3d$ ions align parallel to the moment of light R ions (La–Eu) and antiparallel to the moment of heavy R ions (Gd–Lu). This coupling scheme is schematically shown in figure 5.2. According to Campbell [Cam72] it is explained by the fact that the spin of the $5d$ conduction electrons is always parallel to that of the $4f$ electrons, and the exchange interaction between the $4f$ electrons and the symmetry-compatible $3d$ electrons is invariably antiferromagnetic with respect to the d electrons involved.

At zero temperature the magnetization in the ordered region is equal to the free-ion value. At finite temperatures there is a competition between the thermal energy, which tends to randomize the magnetic moments, and applied and exchange fields, which tend to align the moments. Within the concept of localized moments and mean-field theory, an average molecular field B_m present on each atom acts in addition to the external applied field B_0. The molecular field depends only on the number of nearest neighbours, the moment of the neighbours and the interaction constants.

The ordering temperature T_C (the Curie temperature) is defined as temperature above which the magnetization vanishes in zero field. In a simple model [Bus88] considering only the dominating $T-T$ and $R-T$ interactions n_{TT} and n_{RT}, respectively, the ordering temperature depends only on these two constants and the Curie constants of the T and R ions.

In the paramagnetic regime, i.e. above T_C, the macroscopic magnetization is zero in vanishing field and an external applied field tends to align the thermally disordered moments slightly. The susceptibility within the mean-field model is given by

$$\chi = \frac{C_T}{T - T_\mathrm{C}}, \tag{5.2}$$

which is the Curie-Weiss law. C_T is the Curie constant of the transition-metal ion.

In the case of antiferromagnetic compounds, the susceptibility has a maximum at the ordering temperature T_N, the Néel temperature.

5.2.3 Magnetocrystalline Anisotropy

Magnetic anisotropy is mainly due to the single-ion anisotropy caused by the crystal field in $4f$ ions. For $3d$ ions the orbital angular momentum $\mathbf{L}$ is generally quenched, and to first-order approximation, there is no coupling between the crystal and the magnetic moment of the ion so that there is no single-ion anisotropy. However, in many cases **L** is not completely quenched and the residual angular moment induces single-ion anisotropy.

The perturbing Hamiltonian of the crystal field $\mathcal{H}_{\mathrm{CF}}$ can be expanded in spherical harmonics $Y_n{}^m(\theta_i, \phi_i)$ [Hut64]:

$$\mathcal{H}_{\mathrm{CF}} = \sum_i \sum_{n=2}^{6} r_i^n \sum_{m=-n}^{n} A_n^m \, Y_n{}^m(\theta_i, \phi_i), \tag{5.3}$$

where the sum over i is restricted to electrons in unfilled shells. A_n^m are the expansion coefficients and n is the crystal-field order. Stevens' "Operator Equivalents" method [Ste52] allows to rewrite this sum by means of operators O_n^m having similar transformation properties:

$$\mathcal{H}_{\mathrm{CF}} = \sum_{n=2}^{6} \sum_{m=-n}^{n} A_n^m \, \Theta_n^m \, \langle r^n \rangle \, O_n^m = \sum_{n=2}^{6} \sum_{m=-n}^{n} \Theta_n \, B_n^m \, O_n^m. \tag{5.4}$$

Here Θ_n are multiplicative factors and B_n^m are the crystal field parameters. The O_n^m depend only on the total angular moment J of the ion, and if the crystal has uniaxial symmetry, the crystallographic c-direction can be chosen as quantization direction of J_z.

Assuming that the electron distribution is not disturbed by the crystal field, the anisotropy energy $E_{\mathrm{A}} = \langle \Psi \,|\, \mathcal{H}_{\mathrm{CF}} \,|\, \Psi \rangle$ is given by

$$E_{\mathrm{A}} = K_1 \sin^2\theta + (K_2 + K_2^{'} \cos 4\phi) \sin^4\theta + (K_3 + K_3^{'} \cos 6\phi) \sin^6\theta, \tag{5.5}$$

where θ and ϕ are polar and azimuthal angles of the magnetization of the sublattice measured with respect to the c-axis and a-axis, respectively. The temperature dependent anisotropy constants $K_l^{(')}$, $l = 1, 2, 3$, which are of second, fourth and sixth order in the crystal-field term, can be calculated from (5.4). For example, K_1 is given by [LD75]

$$K_1 = -\frac{3}{2} B_2^0 \left\langle O_2^0 \right\rangle + 5 B_4^0 \left\langle O_4^0 \right\rangle + \frac{21}{2} B_6^0 \left\langle O_6^0 \right\rangle. \tag{5.6}$$

Calculations of the anisotropy at $T > 0$ require thermal averages of the Stevens' operator equivalents. Since these and the magnetization are both related to $\langle \mathbf{J} \rangle$, the reduced magnetization $m(T) = M(T)/M(0)$ may be used to express the temperature dependence of the anisotropy. Based on simple classical arguments [Aku36, CC66] the coefficients obey the so-called power-law

$$K_l(T) = K_l(0) \, m(T)^{2l^2 + l}. \tag{5.7}$$

Thus at high temperatures the anisotropy energy is frequently approximated by

$$E_{\mathrm{A}} = K_1 \sin^2\theta. \tag{5.8}$$

It should be pointed out that the power law and approximations based on it are valid for localized spins, i.e. applicable only to the $4f$ anisotropy, but even for these ions deviations from this law may occur.

The anisotropy constants K_l are mostly used as fit parameters determined from experimental data. Such a phenomenological model (5.5) is even used to describe the smaller anisotropy of the transition-metal sublattice. The $3d$ magnetic moment and anisotropy are roughly independent of the temperature T, provided T is much lower than the ordering temperature.

On the basis of (5.8), two different cases of anisotropy exist. If $K_1 > 0$, the minimum energy is reached for $\theta = 0$, i.e. the magnetization is along the crystallographic c-axis. This is called *easy-axis anisotropy*. The second case, *easy-plane anisotropy*, occurs if $K_1 < 0$ and the easy direction of magnetization is within the (a, b)-plane.

5.3 Magnetization Behaviour of Ferrimagnets

Depending on the R ion the R-T coupling is ferromagnetic for light R and antiferromagnetic for heavy R, respectively. While in the first case both magnetic sublattices are aligned parallel in any magnetic field, the situation is different in the second case: Ferrimagnetism results from the antiparallel alignment in low fields, but strong fields may convert the orientation into a finally parallel alignment. An applied magnetic field $\mathbf{B}$ tends to align the magnetization vector of both sublattices along the field direction $\mathbf{B}/B$ through the Zeeman energy $-\mathbf{M}\cdot\mathbf{B}$. The competition between applied field and exchange interaction determines the alignment of the sublattices: from antiparallel in zero field to parallel in strong fields.

The free energy of a ferrimagnetic compound consisting of two magnetic sublattices with magnetic moments $\mathbf{M}_R$ and $\mathbf{M}_T$ can be described within mean-field theory by [ZLB+93]

$$E = E_{\mathrm{A}}^{R}(\theta_R,\phi_R) + E_{\mathrm{A}}^{T}(\theta_T,\phi_T) + n_{RT}\mathbf{M}_R\cdot\mathbf{M}_T - (\mathbf{M}_R+\mathbf{M}_T)\cdot\mathbf{B}. \tag{5.9}$$

The first two terms represent the magnetocrystalline anisotropies of the R and T sublattices with θ_i and ϕ_i as polar and azimuthal angles of the respective moment $i = R, T$. The third term represents the R-T exchange interaction being proportional to the intersublattice molecular-field coefficient $n_{RT}(>0)$ and the moment vectors $\mathbf{M}_R$ and $\mathbf{M}_T$. The last term is the Zeeman energy in an external field $\mathbf{B}$. It is surprising that this two-sublattice model based on the free energy (5.9), even with the simplest possible assumption regarding the angular dependence of the anisotropy energies, can account for a variety of magnetization processes [ZZXC92].

Usually, at low temperatures, the magnetocrystalline anisotropy of the R sublattice strongly dominates that of the T sublattice justifying that the latter can be neglected. In this case, the magnetization of the R sublattice can be considered as fixed in the easy direction. Furthermore, at temperatures well below the ordering temperatures, both sublattices are spontaneously magnetized to saturation. The magnetization process then merely corresponds to a change of the direction of the T-sublattice moment with respect to that of the R moment from antiparallel to parallel configuration while the anisotropy energy E_{A}^{R} remains unchanged. Therefore (5.9) can be simplified to

$$E = E_{\mathrm{A}}^{R} + n_{RT}M_RM_T\cos\alpha - M\cdot B \quad , \quad M = \sqrt{M_R^2 + M_T^2 + 2M_RM_T\cos\alpha}, \tag{5.10}$$

where M is the resulting magnetization, which is always parallel to the field, and $\alpha = \sphericalangle(\mathbf{M}_R,\mathbf{M}_T)$ is the angle between the two sublattice moment vectors. Thus it is implicitly assumed that a two-sublattice system (crystal) is used, which is *free to orient itself* in the external applied field $\mathbf{B}$. The orientation of the crystal is given by the direction of the R moment.

The equilibrium state of this system is found by minimizing (5.10) with regard to α and the field as parameter. Figure 5.3 shows the resulting magnetization curve $M(B)$ and the angle $\alpha(B)$.

At low fields, the moment configuration is strictly antiparallel and $M = |M_R - M_T|$, $\alpha = \pi$. Beyond a critical field $B_{\mathrm{cr},1} = n_{RT}|M_R - M_T|$ the sublattice moments start to bend towards each other until the critical field $B_{\mathrm{cr},2} = n_{RT}(M_R + M_T)$ is reached. The magnetization is described by $M = B/n_{RT}$ for $B_{\mathrm{cr},1} < B < B_{\mathrm{cr},2}$ so that n_{RT} can be derived from the high-field slope $\partial M/\partial B = 1/n_{RT}$. At $B_{\mathrm{cr},2}$ the sublattice moments are forced to a parallel alignment, $\alpha = 0$, and the magnetization reaches its largest value, $M = M_R + M_T$.

The three phases occurring in this model, characterized by the magnetic configuration, are the ferrimagnetic (Fi) and the ferromagnetic (F) phases with collinear moment vectors as well as the non-collinear (NC) phase.

If the magnetocrystalline anisotropy of the T sublattice is not neglected, the minimization of the free energy can no longer be solved analytically, but numerical methods are used. Extensive research on the calculation of magnetization processes in ferrimagnets has been done by Zhao [ZLB+93, ZCBB93] and Zhang [ZZCB97].

In the minimization problem of the free energy (5.9) with anisotropy energies (5.5) four angles (θ_R, θ_T, ϕ_R, ϕ_T) occur as free parameters, which have to be varied over their allowed space in order to find the (absolute) minimum.

For simplicity and due to limitations of computer speed, special cases are considered so that the number of free parameters is reduced. If the in-plane anisotropies are neglected and negative values

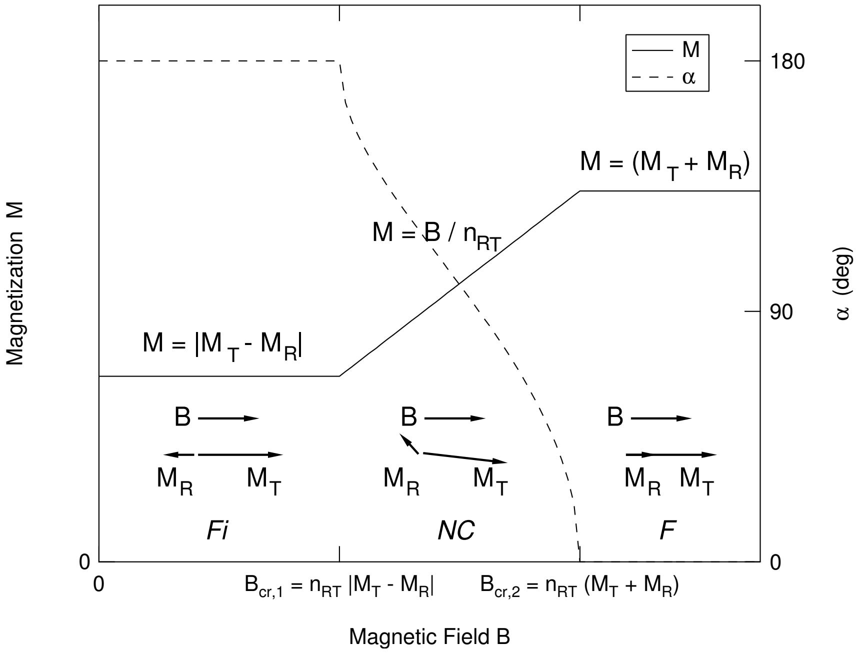

Figure 5.3: Field dependence of the resultant magnetization M of a free ferrimagnetic two-sublattice R-T system with zero T-sublattice anisotropy and large R-sublattice anisotropy. The angle α is the angle between $\mathbf{M}_R$ and $\mathbf{M}_T$.

of θ_R and θ_T are introduced, the angles ϕ_R and ϕ_T can be discarded as was shown in [ZLB$^+$93]. Zhao has also treated two different cases, in which the number of free parameters is reduced to two.

Zhang et al. [ZZCB97] have investigated the bending processes in a ferrimagnet for anisotropy energies (5.5) of different order. If only second-order anisotropies are considered for both sublattices, the problem can still be treated analytically. First-order transitions, i.e. first-order moment reorientations (FOMR), occur when there are two minima for the anisotropy energy corresponding to the ferrimagnetic (Fi) and ferromagnetic (F) states. Depending on the relative strengths of exchange interaction and anisotropy energies, different magnetization curves involving FOMR will occur, whereas FOMR will not be found if the exchange interaction is too strong. With the inclusion of higher-order anisotropies, new types of transitions become possible and the magnetization process becomes very complicated. For example, two FOMR transitions may occur in one magnetization curve.

Global and Local Energy Minimization

For the magnetization process $\mathbf{M}(\mathbf{B})$ of a system it is not only important, which configuration yields the absolute minimum of free energy for a given field value B, but also whether this minimum can be occupied. The magnetic anisotropy may cause energy barriers between the actual moment directions of the sublattices and those corresponding to the global minimum, which prevent the rotation of the sublattice moments into the directions of the global minimum. In a model based on local energy minimization, the magnetization is calculated under the assumption that existing energy barriers between local minima cannot be overcome.

Compared to the usual model based on global energy minimization, local energy minimization leads to completely different results [Gro98]. A very important effect is the creation of hysteresis, so that the magnetization in increasing field may differ from that in decreasing field. This will happen whenever a first-order magnetization process appears. As a consequence the transition fields of first-order magnetic phase transitions shift to higher fields for increasing magnetic field.

The relation of magnetic anisotropy to the exchange interaction determines whether the hysteresis is large or not.

The magnetization curves based on local and global energy minimization are identical from zero field until a first-order metamagnetic phase transition takes place. After the phase transition, the magnetization of the global-minimum curve is in between the values of the local-minimum curves for increasing and decreasing field.

5.4 Experimental Techniques

With regard to sample and magnetization process, different boundary conditions may be applied. One of the most important boundary conditions refers to the mounting or suspension of the sample in the sample holder. This means that the sample can be either fixed or may freely rotate depending on direction and magnitude of the applied magnetic field.

The second case of a free sample is one precondition in order to make use of (5.10), which was derived from the more general expression (5.9). Compared to fixed single crystals, the description of the magnetization process of free samples in terms of the two-sublattice model is much simpler. However, a disadvantage may come into play if this method is applied in short-pulse fields. Due to the moment of inertia of the sample, dynamics becomes involved additionally in the magnetization process whenever the sample will rotate. This will complicate the evaluation of experimental data and experiments conducted either in slowly varying or short-pulse fields may yield different results.

Another important matter is the structure of the sample. Distinction has to be made between single crystals and samples consisting of fine particles or even powder. On the one hand single crystals are not always available and measurements of all possible configurations are laborious. On the other hand it is not possible to circumvent these measurements by using polycrystalline samples because the analysis of those results is extremely difficult.

In some cases it is also possible to produce special oriented samples from powder consisting of single-crystalline and single-domain particles. This method can be used if the magnetic anisotropy of the material at the processing temperature is large enough, so that the particles, immersed in fluid epoxy resin, can orient in an applied magnetic field, while the epoxy cures and fixes the particles. This was done, for example, in [SWSG98] with the $\mathrm{Gd}_{1-x}\mathrm{La}_x\mathrm{Mn}_2\mathrm{Ge}_2$ system in a field of 1.5 T at room temperature. A nearly perfect orientation was obtained for $x \geq 0.05$, while it was not complete for smaller x.

Both single crystals and powder samples can be investigated as fixed or free samples. A *free-powder* sample consists of single-crystalline, single-domain particles, which may freely rotate in an applied magnetic field. Ideally, the magnetization measured on such samples should coincide with that obtained from spherical single crystals, which can freely rotate in their sample holder.

Measurements on loose powders have been shown to give direct information on the R-T exchange coupling constant [VRF90] and even anisotropy constants could be derived [ZLB$^+$93]. Advantageous on loose powders is not only their easy preparation, but also their description in terms of the two-sublattice model. Though, the relation between transitions observed in free and fixed sample measurements is not well explored.

Powders – whether loose or fixed – are always required if well-conducting materials shall be examined in short-pulse fields. This avoids or at least reduces eddy currents, which will be induced otherwise due to the strong field sweep rates dB/dt.

Depending on the compound to be examined and the peak fields available, it is not always possible to observe the rotation of the moments starting at $B_{\mathrm{cr},1} = n_{RT}|M_R - M_T|$, since the R-T interaction is often very strong. In order to exceed $B_{\mathrm{cr},1}$ nonetheless, it is then necessary to dilute the transition-metal sublattice or the rare-earth sublattice in such a way that the resultant magnetization $|M_R - M_T|$ becomes sufficiently small [VRF90]. This is possible if the substitutions of the matrix do not destabilize the original structure too easily. On the other hand, it is uncertain whether such a substitution affects the magnetic properties by still other mechanisms.

The latter is the case with $R_{1-x}R'_x\mathrm{Mn}_2\mathrm{Ge}_2$ intermetallics. It is well known that the magnetic properties of the Mn subsystem in these compounds depend extremely sensitive on the lattice parameters.

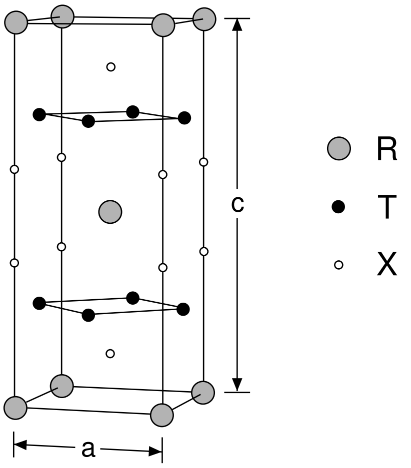

Figure 5.4: Crystal structure of the intermetallic compounds RT_2X_2 (R – rare-earth metal, T – transition metal, X = Si, Ge. The structure is of the $ThCr_2Si_2$ type, which is body-centered tetragonal.

5.5 The Intermetallic Compounds $R\mathrm{Mn_2Ge_2}$

Among many "families" of intermetallic compounds, the intermetallic ternary compounds RT_2X_2 consisting of rare earth R, transition metal T and X = Si or Ge turned out to be particularly interesting. These compounds exhibit various properties such as superconductivity, Kondo effect, giant magnetoresistance and a variety of partly unusual magnetic phenomena [SL89].

They crystallize in the body-centered tetragonal structure of the well-known $ThCr_2Si_2$ type with space group $I4/mmm$ [SL89, BS65], see figure 5.4, which is the case for $R\mathrm{Mn_2Ge_2}$ compounds, or in the primitive tetragonal $CaBe_2Ge_2$-type structure. The ratio of c/a of about 2.5 in all cases is quite large so that a large anisotropy of physical properties may be expected. The structure can be thought of consisting of atomic layers with a sequence of -T-X-R-X-T- along the c-axis. This layer structure is also reflected in their magnetic properties. With regard to the Mn atoms, the interlayer distance $d^c_{\mathrm{Mn-Mn}}$ along the c-axis is nearly twice as large as the intralayer distance $d^a_{\mathrm{Mn-Mn}}$ within the c-plane. In $R\mathrm{Mn_2Ge_2}$, the distances are $d^c_{\mathrm{Mn-Mn}} \sim (5.5\ldots5.6)$ Å and $d^a_{\mathrm{Mn-Mn}} \sim (2.8\ldots2.9)$ Å.

Among the RT_2X_2 compounds, both R and T atoms have magnetic moments only in the case T = Mn, i.e. except for Mn compounds, no magnetic moment is localized on the T atom.

The Mn-Mn interlayer exchange interaction is highly sensitive to the lattice spacing [Szy92]. Depending on the Mn-Mn interatomic distance $d^a_{\mathrm{Mn-Mn}}$ within the (001) Mn layer (intralayer), the magnetic alignment along the c-axis of adjacent Mn layers is either parallel for $d^a_{\mathrm{Mn-Mn}} > 2.87$ Å (i.e. $a > 4.06$ Å) or antiparallel otherwise [SS82].

Especially neutron diffraction studies have been used to improve the understanding of the magnetic structures. As to the Mn magnetic moments, compounds with light R show an intralayer antiferromagnetic coupling of the in-plane components [VWRM94, VWRM95b, VWRM95a, VMR96b], while compounds with heavy R have no intralayer (in-plane) spin component [VWRM95a, VMT$^+$92]. In $R\mathrm{Mn_2Ge_2}$ compounds, the in-plane antiferromagnetism can be commensurate or incommensurate with the lattice periodicity. Details of the magnetic ordering are given in [VMR96a, VMR96b]. Table 5.1 summarizes the interlayer and intralayer magnetic coupling of the Mn sublattice in $R\mathrm{Mn_2Ge_2}$ compounds depending on the atomic spacing [DAE$^+$02].

Concerning the strength of the coupling within and in between the two magnetic subsystems in $\mathrm{RMn_2Ge_2}$, the intralayer Mn-Mn ferromagnetic exchange interaction is found to be the strongest interaction [SL89]. Both the interlayer Mn-Mn exchange interaction and the R-Mn exchange interaction are weaker by approximately one order of magnitude. The R-R exchange is still weaker by one order of magnitude [KLO$^+$01].

Both the exchange interaction between Mn layers and between Mn and R layers is antiferromagnetic in compounds with heavy R or Y. The competition of these two antiferromagnetic

Table 5.1: Intra- and interlayer magnetic coupling of the Mn sublattice in RMn$_2$Ge$_2$ compounds in dependence on the atomic spacing. For the intralayer coupling in-plane and out-of-plane components are distinguished. Abbreviations: AF. . . antiferromagnetic, F. . . ferromagnetic, 0. . . no component existing. Details are given in the text.

Mn-Mn inter-atomic distance	lattice constant	R	intralayer		interlayer
			in-plane	out-of-plane	
$2.87\,\text{Å} < d^a_{\text{Mn-Mn}}$	$4.06\,\text{Å} < a$	light R	AF	F	F
$2.84\,\text{Å} < d^a_{\text{Mn-Mn}} < 2.87\,\text{Å}$	$4.02\,\text{Å} < a < 4.06\,\text{Å}$		AF	F	AF
$d^a_{\text{Mn-Mn}} < 2.84\,\text{Å}$	$a < 4.02\,\text{Å}$	heavy R	0	F	AF

interactions initiates a number of spontaneous and field-induced phase transitions at temperatures below T_C.

Generally, this hierarchy of various exchange interactions determines the magnetic properties of RMn$_2$Ge$_2$ compounds, and makes magnetic transitions especially at low temperatures complicated.

When R is non-magnetic, i.e. R = La, Lu or Y, the ordering in the ground state at low temperatures is either ferromagnetic as for LaMn$_2$Ge$_2$ below $T_C \approx 327$ K, or antiferromagnetic as for YMn$_2$Ge$_2$ below $T_C \sim 427$ K. Magnetic measurements on Y$_{1-x}$La$_x$Mn$_2$Ge$_2$ revealed that a thermally induced AF to F transition occurs when the temperature is increased [FIO$^+$86]. This behaviour is ascribed to a change of the intralayer Mn-Mn distance, having an influence on the interlayer coupling constant.

When R is a magnetic ion, the energy of the R-Mn exchange interaction plays an important role. For any light R except Sm, the compounds have a ferromagnetic structure below T_C [NRBW75].

In the case of heavy R, the compounds have two magnetic ordering temperatures. The Mn subsystem in these compounds becomes antiferromagnetically ordered below the Néel temperature of $T_N \sim (350\ldots450)$ K, while the R subsystem remains paramagnetic (i.e. magnetically disordered), since the effective field of two adjacent Mn layers acting on the R subsystem is just cancelled out [Szy92].

Below the second ordering temperature T_0, the R subsystem is ferromagnetically aligned [SL89]. For certain compounds (R = Gd, Tb, Dy) this transition is of first order, and at the same time the Mn subsystem is also transformed into the ferromagnetic state due to the antiferromagnetic R-Mn exchange interaction. As a result, the whole structure is ferrimagnetic. The second ordering temperatures are $T_0 = 96$ K and 95 K for GdMn$_2$Ge$_2$ and TbMn$_2$Ge$_2$, respectively, and 36 K for DyMn$_2$Ge$_2$.

In contrast to the above compounds, those with R = Ho, Er, Tm have an R-Mn exchange interaction, which is weaker so that the Mn subsystem remains in the antiferromagnetic state down to the lowest temperatures [SL89, LSBS90]. In these compounds, the long-range magnetic ordering within the R subsystem takes place below 10 K.

Detailed magnetic investigations were carried out on some RMn$_2$Ge$_2$ single crystals [SFF$^+$83, Shi84]. It was found that the [001] direction (the tetragonal axis) is the easy magnetization axis for R = Gd, Tb, Dy, Ho, while it is the [110] direction for R = Er. Since the saturation magnetic moments at 4.2 K are much smaller than the theoretical value for a free R^{3+} ion, it is concluded that the ordering is ferrimagnetic or non-collinear.

5.6 Theoretical Description

In the recent series of experimental and theoretical investigations of magnetic properties of the RMn$_2$Ge$_2$ intermetallics, Gd$_{1-x}$Y$_x$Mn$_2$Ge$_2$ and Gd$_{1-x}$La$_x$Mn$_2$Ge$_2$ were the first compounds to be studied in high magnetic fields [SGG$^+$99, GLS$^+$00b, GLS$^+$00a]. A modified Yafet-Kittel model allowed to provide a good description of the experimentally observed phase transitions. However, in the course of these investigations, it turned out that the model failed in some cases to match experimental and theoretical data quantitatively. This understanding was confirmed as results obtained in ultrahigh magnetic fields became available.

An analysis of experimental results on $\mathrm{DyMn_2Ge_2}$ has shown that this simple model is not capable of describing the magnetic properties of this compound even qualitatively. In order to overcome this problem, the Yafet-Kittel Model was extended by considering further interactions between next-to-nearest magnetic layers. Both models are introduced in the following.

5.6.1 Yafet-Kittel Model

This model was used in earlier publications to describe the behaviour of the intermetallic compounds $\mathrm{Gd}_{1-x}\mathrm{Y}_x\mathrm{Mn_2Ge_2}$ and $\mathrm{Gd}_{1-x}\mathrm{La}_x\mathrm{Mn_2Ge_2}$ [SGG$^+$99, GLS$^+$00b, GLS$^+$00a]. The Yafet-Kittel model [YK52] for a ferrimagnet with antiferromagnetic exchange interaction in one of the sublattices was modified by adding magnetic anisotropy. It was further assumed that one sublattice is unstable and is split into two equivalent sub-sublattices. In the case of the intermetallic compounds $R\mathrm{Mn_2Ge_2}$, the R sublattice is stable while the Mn sublattice is unstable.

In the framework of the Yafet-Kittel model, the magnetic energy is given by

$$\begin{aligned} E &= -\lambda_{\mathrm{Gd-Mn}}\mathbf{M}_{\mathrm{Gd}}\cdot(\mathbf{M}_{\mathrm{Mn}_1}+\mathbf{M}_{\mathrm{Mn}_2})-\lambda'_{\mathrm{Mn-Mn}}M^2_{\mathrm{Mn}}-\lambda_{\mathrm{Mn-Mn}}\mathbf{M}_{\mathrm{Mn}_1}\cdot\mathbf{M}_{\mathrm{Mn}_2} \\ &\quad -\frac{1}{2}\lambda_{\mathrm{Gd-Gd}}M^2_{\mathrm{Gd}}-\frac{K}{2M^2_{\mathrm{Mn}}}(M^2_{\mathrm{Mn}_1,\mathrm{c}}+M^2_{\mathrm{Mn}_2,\mathrm{c}})-\mathbf{B}\cdot(\mathbf{M}_{\mathrm{Gd}}+\mathbf{M}_{\mathrm{Mn}_1}+\mathbf{M}_{\mathrm{Mn}_2})\,, \end{aligned} \tag{5.11}$$

where the first term describes the exchange interaction between the Gd and the Mn subsystems ($\lambda_{\mathrm{Gd-Mn}} < 0$). The second term describes the intralayer Mn-Mn interaction ($\lambda'_{\mathrm{Mn-Mn}} > 0$), the third one is the interlayer Mn-Mn exchange ($\lambda_{\mathrm{Mn-Mn}} \gtrless 0$ depending on $d^a_{\mathrm{Mn-Mn}}$). The fourth term corresponds to the exchange interaction in the Gd subsystem, the fifth term is associated with the magnetic anisotropy of the Mn subsystem, where $M_{\mathrm{Mn}_1,\mathrm{c}}$ and $M_{\mathrm{Mn}_2,\mathrm{c}}$ are the magnetization components along the c-axis, and K is the uniaxial anisotropy constant. The last term is the Zeeman energy.

In addition to the phases that can occur in a ferrimagnet with intrasublattice ferromagnetic interactions, i.e. the collinear ferrimagnetic (Fi) and ferromagnetic (F) phases as well as the non-collinear (NC) phase, new magnetic phases can emerge in the modified model. The one is the AF phase, in which the unstable sublattice is in the antiferromagnetic state. The other one is the trigonal (T) phase, in which the magnetic moments of the unstable sub-sublattices are neither parallel to each other nor to moment of the stable sublattice. These configurations are schematically given in figures 5.11 and 5.12.

In summary, this model takes into consideration intralayer exchange interactions in R and Mn layers as well as interlayer interactions between corresponding *nearest* layers of magnetic atoms (R-Mn and Mn-Mn) in the molecular field approximation.

5.6.2 Extended Molecular Field Model

The theoretical approach used to describe the magnetic phases of $\mathrm{DyMn_2Ge_2}$ [GEK$^+$01] and $\mathrm{HoMn_2Ge_2}$ [GEK$^+$02] is based on a molecular field model. It takes into account not only exchange interactions between nearest layers of magnetic atoms, but also those between next-to-nearest magnetic layers. This appears to be quite natural since the exchange interaction in the $R\mathrm{Mn_2Ge_2}$ compounds (apart from the indirect exchange through Ge) is mediated by the conduction electrons and is thus a long-range interaction. Considering also crystal field effects depending on the R^{3+} ions, non-equivalent positions of magnetic moments may occur in both, the R and the Mn magnetic subsystems of the crystal.

The occurrence of non-equivalent positions and exchange interactions between different layers of magnetic ions are explicitly taken into account in the model.

The effective Hamiltonian of an R^{3+} ion in the ith position, which is subjected to a tetragonal crystal field and an external magnetic field $\mathbf{B}$ is

$$\mathcal{H}^{(R,i)} = \alpha_J\, B_2^0\, O_2^0 + \beta_J(B_4^0\, O_4^0 + B_4^4\, O_4^4) + \gamma_J(B_6^0\, O_6^0 + B_6^4\, O_6^4) - g_J\mu_B\, \mathbf{J}^{(i)}\cdot(\mathbf{B}+\mathbf{B}_{\mathrm{m}}^{(R,i)}) \tag{5.12}$$

in the molecular field approximation. Here $\alpha_J, \beta_J, \gamma_J$ are multiplicative factors, O_n^m are equivalent operators and B_n^m crystal field parameters, see also section 5.2.3. In the Zeeman term, $\mathbf{J}^{(i)}$ is the angular momentum operator of the R ion, g_J is the Landé factor, and $\mathbf{B}_{\mathrm{m}}^{(R,i)}$ is the molecular field strength with the components

$$B_{\mathrm{m}\,j}^{(R,i)} = \sum_l \lambda_{11}^{(l)} m_j^{(R,l)} + \sum_k \lambda_{12}^{(k)} m_j^{(\mathrm{Mn},k)} \qquad , \qquad j = x, y, z. \tag{5.13}$$

The components of the lth R moment and the kth Mn moment are given by

$$m_j^{(R,l)} = \mu_B g_J \left\langle J_j^{(l)} \right\rangle \quad , \quad m_j^{(\mathrm{Mn},k)} = \mu_B g_J \left\langle S_j^{(k)} \right\rangle \qquad , \qquad j = x, y, z, \tag{5.14}$$

where $\mathbf{S}_{\mathbf{j}}^{(\mathbf{k})}$ is the spin momentum operator of Mn, and g is the g-factor. The parameters $\lambda_{11}^{(l)}$ and $\lambda_{12}^{(k)}$ describe the R-R and R-Mn exchange interactions between atoms corresponding to different layers l and k, respectively. Since these parameters enter additively in all expressions, they are subsequently condensed in the total parameters λ_{11} and λ_{12}.

In the effective Hamiltonian for the itinerant electrons of the Mn d subsystem

$$\mathcal{H}^{(\mathrm{Mn},k)} = -g\mu_B\, \mathbf{S}^{(k)} \cdot \mathbf{B}^{(\mathrm{Mn},k)} \tag{5.15}$$

only exchange interactions for the kth Mn atom are considered. The effective field $\mathbf{B}^{(\mathrm{Mn},k)}$ acting on the kth Mn atom is composed of the external field $\mathbf{B}$ oriented at an angle θ with respect to the c-axis of the crystal and the molecular field $\mathbf{B}_{\mathrm{m}}^{(\mathrm{Mn},k)}$:

$$B^{(\mathrm{Mn},k)} = B\cos(\theta - \theta_k) + B_{\mathrm{m}}^{(\mathrm{Mn},k)}, \tag{5.16}$$

where

$$B_{\mathrm{m}}^{(\mathrm{Mn},k)} = \sum_{n=k,k\pm1,\dots} \lambda_{22}^{(n)} m^{(\mathrm{Mn},k)} \cos(\theta_n - \theta_k) + \lambda_{12} \sum_i \left(m_z^{(R,i)} \cos\theta_k + m_x^{(R,i)} \sin\theta_k \right). \tag{5.17}$$

Here θ_k is the polar angle of the kth Mn magnetic moment and $\lambda_{22}^{(n)}$ describes the exchange interaction between Mn atoms of the layers k and n. As the anisotropy of the Mn subsystem is small compared to the exchange interaction, it is considered by an additive term in the thermodynamic potential.

For the convenience of notation, exchange constants I together with additional factors are condensed in the exchange parameters λ according to

$$\lambda_{11} = \frac{(g_J - 1)^2}{g_J \mu_B} I_{11} \quad , \quad \lambda_{12} = \frac{g_J - 1}{g_J \mu_B} I_{12} \quad , \quad \lambda_{22}^{(n)} = \frac{1}{g\mu_B} I_{22}^{(n)}. \tag{5.18}$$

The thermodynamic potential Φ per formula unit in the molecular field approximation is determined by

$$\begin{aligned}\Phi = \frac{1}{N}\Bigg\{ & -k_B T \sum_{i=1}^{N} \ln Z_i + \frac{1}{2} \sum_{i=1}^{N} \mathbf{m}^{(R,i)} \cdot \mathbf{B}_{\mathrm{m}}^{(R,i)} \\ & -k_B T \sum_{k=1}^{2N} \ln Z'_k + \frac{1}{2} \sum_{k=1}^{2N} \mathbf{m}^{(\mathrm{Mn},k)} \cdot \mathbf{B}_{\mathrm{m}}^{(\mathrm{Mn},k)} + \sum_{k=1}^{2N} K \sin^2\theta_k \Bigg\},\end{aligned} \tag{5.19}$$

where N is the number of non-equivalent formula units. The partition function Z_i of the ith R moment is evaluated by means of numerically calculated eigenvalues of $\mathcal{H}^{(R,i)}$ as defined in (5.12), which involves the solution of the corresponding self-consistent problems. Since $S = 1$ for the Mn spins, the partition function of the kth Mn moment is given by $Z'_k = \exp(-x_k) + 1 + \exp(+x_k)$, where $x_k = g\mu_B B^{(\mathrm{Mn},k)}/k_B T$. Further, K is an anisotropy constant of the Mn subsystem. The second and fourth terms in (5.19) are correcting terms in the molecular field theory.

Providing the necessary parameters of the system, the magnetic phase diagram can be calculated on the basis of the thermodynamic potential (5.19). This is done by finding the minimum of the thermodynamic potential for the various magnetic structures. First-order phase transitions are determined from the condition of equal potentials of the respective phases.

Table 5.2: Critical fields of induced magnetic phase transitions occurring in the highest fields in $R\mathrm{Mn_2Ge_2}$ powder at a temperature of 5 K. . . 10 K. Each field contains the values found in increasing ($H_c^{\uparrow}$) and decreasing ($H_c^{\downarrow}$) field, the resulting mean value H_c and the half width of the hysteresis $\Delta H_c/2 = (H_c^{\uparrow} - H_c^{\downarrow})/2$. All values are given in Tesla.

R		Gd		Tb		Dy		Ho		Er		Y	
$H_c^{\uparrow}$	$H_c^{\downarrow}$	104	113	121	115	113	107	95	87	93	87	48. . . 54	≤ 59
H_c	$\pm\Delta H_c/2$	109	± 5	118	± 3	110	± 3	91	± 4	90	± 3	55. . . 56	$\sim \pm 3$
$H_c^{\uparrow}$	$H_c^{\downarrow}$				105			79	73			35	41
H_c	$\pm\Delta H_c/2$							76	± 3			38	± 3
$H_c^{\uparrow}$	$H_c^{\downarrow}$			54	49								
H_c	$\pm\Delta H_c/2$			51	± 2								

5.7 Experimental Results

5.7.1 Sample Preparation

Polycrystalline samples of the intermetallic compounds were prepared by melting the initial elements (with a purity of 99.9%) in an induction furnace under quasi-levitation conditions in an argon atmosphere. In order to improve the homogeneity, the samples were remelted three times and then annealed at 750°C for 170 hours in a dynamic vacuum.

The single-phase nature of the samples prepared in such a way was subsequently checked by means of x-ray diffraction analysis.

5.7.2 Magnetization in High and Ultrahigh Magnetic Fields

Magnetization measurements at low temperatures in high and ultrahigh magnetic fields produced by the single-turn coil technique were performed for the intermetallic compounds $R\mathrm{Mn_2Ge_2}$ with R = Gd, Tb, Dy, Ho, Er and Y, i.e. with heavy R and the non-magnetic Y.

All experiments were conducted with powdered samples having a particle size of about $10\,\mu$m. The powder was filled into a small tube and finally sealed, but not fixed so that the basic condition for a free powder is fulfilled. However, it is not certain whether the samples will behave as a free powder. The pulse duration is of order $6\,\mu$s and thus very short. Also a possible friction between the particles cannot be ruled out, which may affect the rotation of the powder particles. Low temperatures of 5 K. . . 10 K were chosen for all measurements.

The results of these experiments are reproduced in the figures 5.5 to 5.10; each figure combines the differential susceptibility dM/dH of one compound for different or similar peak fields $B_{\max}$, but otherwise unchanged conditions. Peaks or plateaus associated with jumps or a distinct increase in the magnetization, respectively, are marked by arrows for both increasing and decreasing field.

It is found that the magnetization of all investigated materials undergoes diffuse metamagnetic transitions in strong fields. The values of the critical fields are different for increasing and decreasing fields, which is characteristic for first-order transitions.

Table 5.2 summarizes the critical fields of the phase transitions in $R\mathrm{Mn_2Ge_2}$ powder occurring in ultrahigh fields. It contains the mean values of the critical fields $H_c = (H_c^{\uparrow} + H_c^{\downarrow})/2$ in increasing and decreasing fields as well as the half width of the hysteresis $\Delta H_c/2 = (H_c^{\uparrow} - H_c^{\downarrow})/2$.

The variation of the peak field $B_{\max}$ allows either to utilize the maximum field possible (around 150 T in this series) or to focus with increased sensitivity on the behaviour at "lower" fields, if the peak fields are reduced. This can be seen, for instance, in figure 5.6 from comparing the upper curve ($B_{\max} \approx 55\,\mathrm{T}$) with the two lower curves ($B_{\max} > 100\,\mathrm{T}$).

It is also evident that the peak field $B_{\max}$ or the field sweep rate dH/dt have an influence on the induced phase transitions. This refers to both, the mean field H_c of a phase transition and

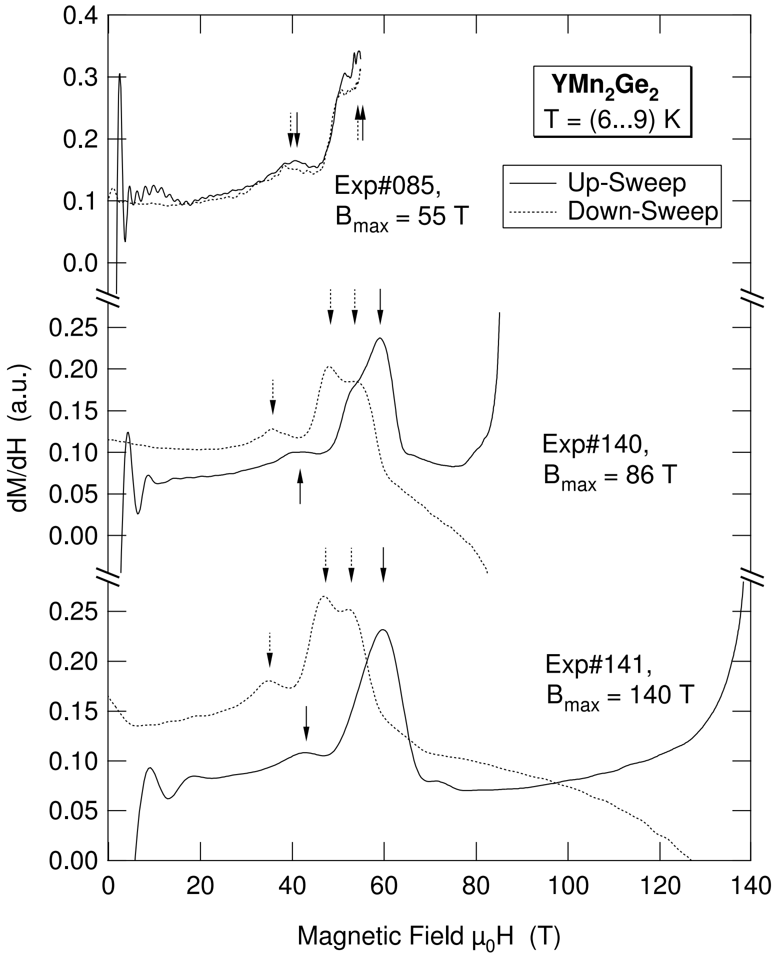

Figure 5.5: Differential susceptibility of YMn_2Ge_2 powder at low temperatures.

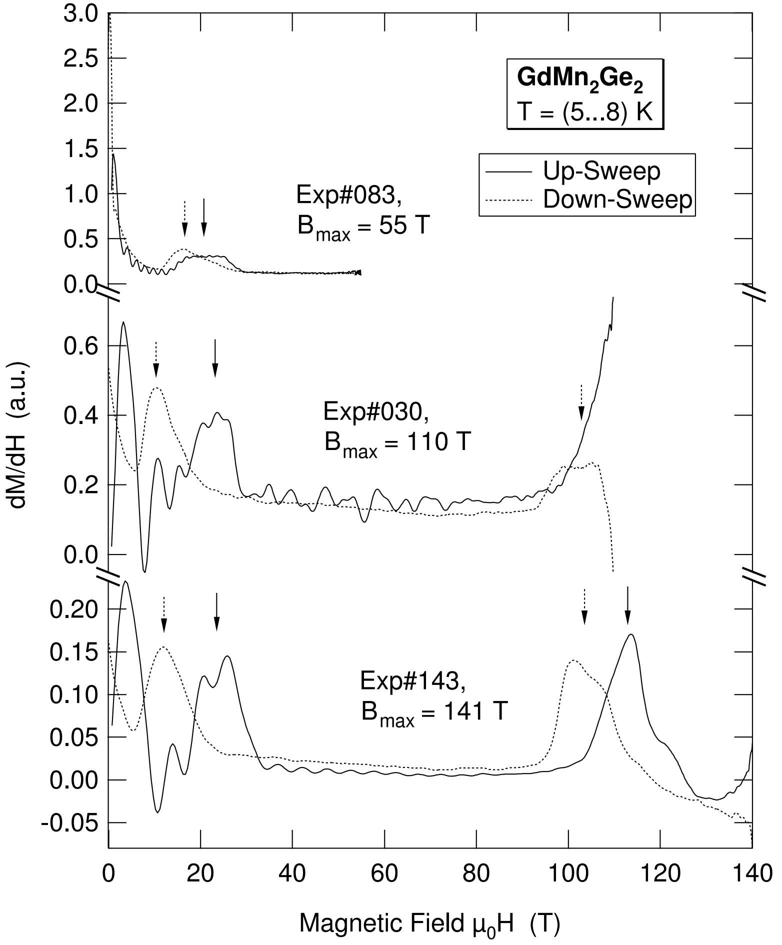

Figure 5.6: Differential susceptibility of $GdMn_2Ge_2$ powder at low temperatures.

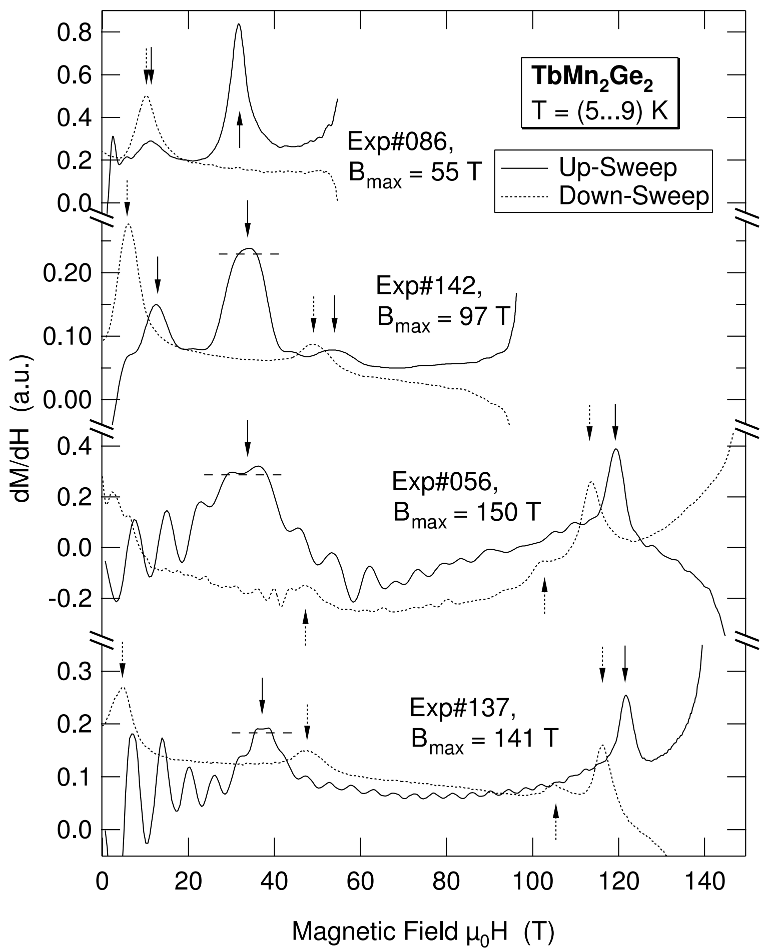

Figure 5.7: Differential susceptibility of TbMn$_2$Ge$_2$ powder at low temperatures.

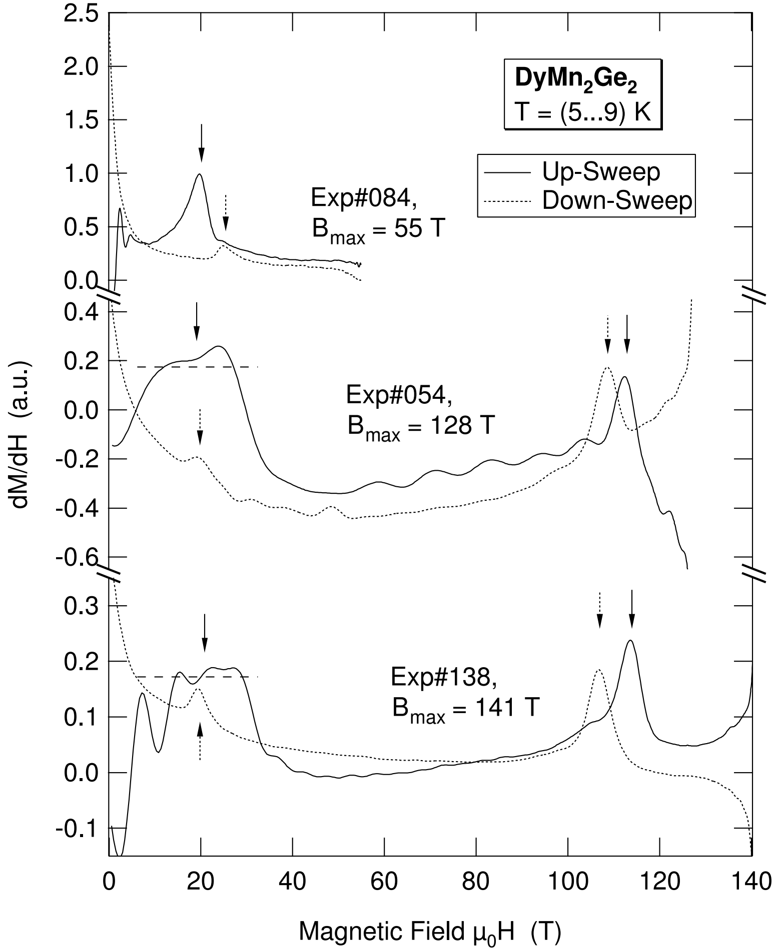

Figure 5.8: Differential susceptibility of DyMn$_2$Ge$_2$ powder at low temperatures.

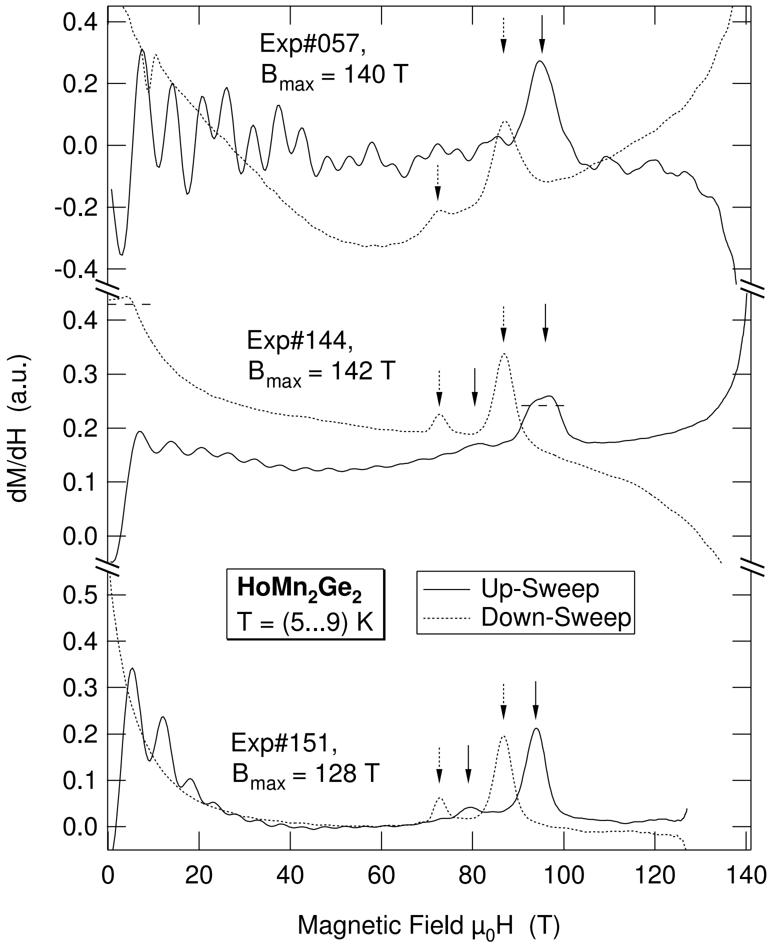

Figure 5.9: Differential susceptibility of $HoMn_2Ge_2$ powder at low temperatures.

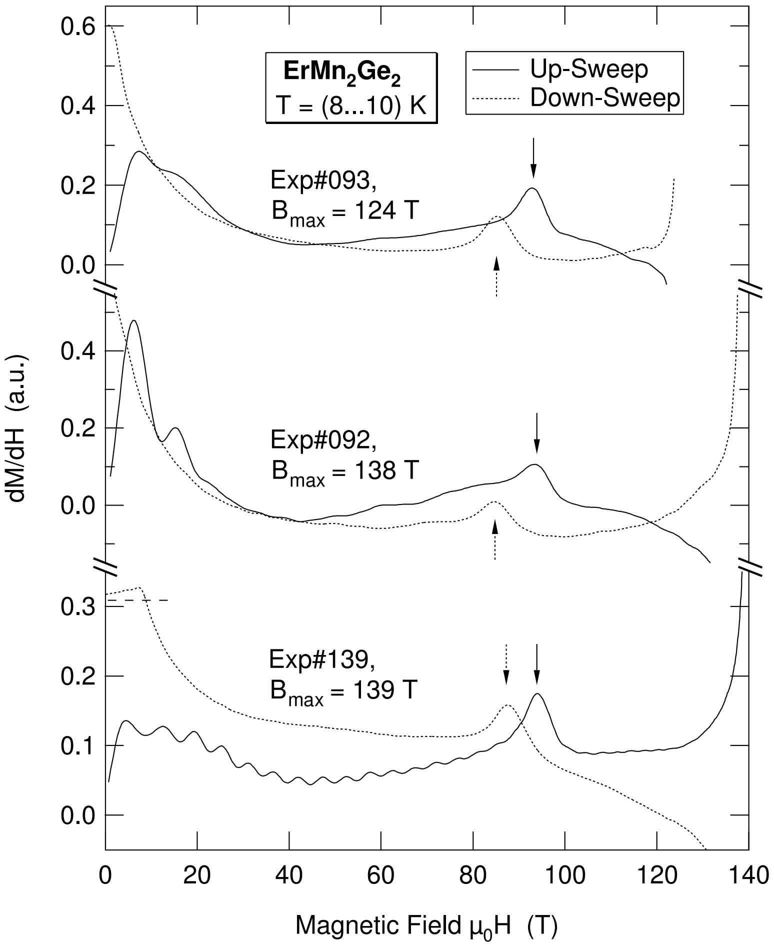

Figure 5.10: Differential susceptibility of $ErMn_2Ge_2$ powder at low temperatures.

the hysteresis between up- and down-sweep ΔH_c. Such a behaviour, which is apparently affected by relaxation effects associated with the pulsed nature of the magnetization has been observed for most of the compounds. Recently, such effects were also reported to occur in $DyMn_2Ge_2$ at low temperatures [LLVB02].

The quality of the experimental data can be estimated from a comparison of independent experiments. This is well illustrated by the example of $HoMn_2Ge_2$ in figure 5.9, showing three measurements with comparable peak field, $B_{\max} \sim (130 \ldots 140)$ T. The upper curve was measured without electromagnetic shielding and the up-sweep contains strong (trigger) noise despite careful smoothing. This is suppressed in the middle curve by applying the special shielding so that the small peaks at 79 T and 73 T can be identified in both up- and down-sweep. However, both experiments lack of a good compensation, which results in a deviation of up- and down-sweep apart from the phase transitions. The best measurement with regard to all aspects is reproduced in the lower curve. Having an extremely small background signal and only small (trigger) noise, any ambiguities are avoided in the interpretation of the data.

Specific aspects of the particular compounds are discussed in the following sections.

5.7.3 YMn_2Ge_2

In contrast to all other $R$$Mn_2Ge_2$ compounds investigated, the R = Y ion is non-magnetic. Thus, from the magnetic point of view, it contains only the Mn subsystem. As a function of the temperature, there is only one transition from the paramagnetic state above T_N to the antiferromagnetic state below T_N with antiferromagnetic interlayer coupling and ferromagnetic intralayer alignment. The magnetic structure is then of the AFil type with an easy axis anisotropy [VMR96b], i.e. the Mn moments are aligned along the c-axis . The Néel temperature T_N was determined as 427 K in [Gua99] or 395 K in [SL89].

At low temperatures, the antiferromagnetic Mn subsystem undergoes at least one induced phase transition in high magnetic fields. In [KLO+01], the largest dM/dH peak occurring in strong fields is associated with a spin-flop transition to the non-collinear phase (AF phase $\longrightarrow$ T phase) or a metamagnetic transition to the ferromagnetic state. However, closer inspection of this wide peak at ~ 55 T suggests that it may consist of two individual peaks, which holds in particular for the down-sweep (figure 5.5). Question arises about the origin of the peak at 38 T, which was not identified before, because it is relatively small. It corresponds to a small magnetization change only, much lower than that at ~ 55 T.

The assumption that the phase transitions in the other $R$$Mn_2Ge_2$ compounds with magnetic R observed in strong fields are associated only with a change in the magnetic structure of the Mn subsystem is confirmed by the fact that YMn_2Ge_2 exhibits such field-induced phase transitions.

It is interesting to note that the small dM/dH peak, which precedes the larger one(s) occurring in strong fields, appears not only in YMn_2Ge_2, but also in the compounds with R = Tb, Ho and possibly Dy.

5.7.4 $GdMn_2Ge_2$

For R = Gd, Tb and Dy there exists an antiferromagnetic state below T_N, analogous to that of YMn_2Ge_2. However, the energy difference between the antiferromagnetic state and the ferrimagnetic state is relatively small and the increasing strength of the R-Mn exchange interaction at low temperatures stabilizes a ferrimagnetic structure [WYS96]. This results in a first-order transition from the AF to the Fi state in these compounds with decreasing temperature. $GdMn_2Ge_2$ has an intralayer Mn-Mn distance $d^a_{\mathrm{Mn-Mn}}$, which is just below the critical value separating AF and F coupling between neighbouring Mn layers.

The easy control of $d^a_{\mathrm{Mn-Mn}}$ around this value by partial substitution of Gd is one of the reasons making these compounds so interesting. The difference of the metallic radii of Gd and Y is small. Thus the lattice parameter a in $Gd_{1-x}Y_xMn_2Ge_2$ does not change significantly with x and can be neglected in first approximation. In contrast, a increases substantially with increasing La content in $Gd_{1-x}La_xMn_2Ge_2$ and causes the Mn-Mn interlayer exchange interaction to change from antiferromagnetic to ferromagnetic at a certain composition. Another aspect of $GdMn_2Ge_2$

is that Gd is in an S-state ($\langle \mathbf{S} \rangle = 7/2$, $\langle \mathbf{L} \rangle = 0$). Thus the $4f$-electrons of Gd do not contribute much to the magnetocrystalline anisotropy.

Magnetic properties of the pure material were examined using magnetic fields up to 5 T in [IHS86], 6 T in [SFF+83] and 15 T in [KOY89]. It was found that $GdMn_2Ge_2$ orders antiferromagnetically (AF) below $T_N = 365$ K, and a transition to the ferrimagnetic (Fi) phase occurs at $T_C = 95$ K. Above T_C, the Gd subsystem becomes paramagnetic, but the Mn subsystem remains antiferromagnetically coupled.

The system $Gd_{1-x}La_xMn_2Ge_2$ was investigated in [SWSG98] using pulsed fields up to 40 T, and metamagnetic phase transitions have been observed. The magnetization of oriented powder samples of pure $GdMn_2Ge_2$ exhibits two step transitions for $\mathbf{H} \parallel [001]$ at 4.2 K, whereas no stair-like behaviour has been detected in the perpendicular direction. The transitions for $\mathbf{H} \parallel [001]$ occur at $B_{t1} \approx 21$ T and at $B_{t2} \approx 30$ T, the latter corresponding to a much smaller change in magnetization. The first transition at B_{t1} agrees exactly with our results shown in figure 5.6. However, it is remarkable that the corresponding transition in decreasing field occurs at significantly smaller fields (≈ 16 T) and is even smaller (≈ 10 T) if the peak field of the pulse exceeded 100 T.

Furthermore, it is emphasized in [SWSG98] that the absolute value of magnetization after the transition (approximately $6\,\mu_B$ / f.u. at 40 T, 4.2 K) is clearly smaller than $M = (1-x)M_{\mathrm{Gd}}$ in both directions parallel and perpendicular to the easy axis. Based on this fact and on the magnitude of the magnetization jump the authors of [SWSG98] suggest that the induced magnetic structure in the Mn sublattice is different from a simple antiferromagnetic one and may not be a simple collinear structure. However, the induced magnetic structure in the high-field region could not be unambiguously revealed.

At the same time, Guanghua et al., who investigated both $Gd_{1-x}Y_xMn_2Ge_2$ [SGG+99] and $Gd_{1-x}La_xMn_2Ge_2$ [GLS+00b, GLS+00a], predicted on the basis of the Yafet-Kittel model that in $GdMn_2Ge_2$ one or more first-order magnetic phase transitions will occur from the AF phase to the T phase in stronger fields (> 40 T).

Indeed, such metamagnetic phase transition is observed at about 109 T ($B_c^{\uparrow} = 104$ T, $B_c^{\downarrow} = 113$ T) at 5 K. Although the corresponding dM/dH peaks are not as wide as those of YMn_2Ge_2, their shape with a shoulder near the top (lowest curve in figure 5.6) is similar, which could indicate a rather complicated magnetization process or a multiple phase transition. No further metamagnetic transitions have been detected in higher fields up to 500 T [KLO+01]. Hence, the sublattices can be supposed to be in the trigonal or ferromagnetic state after this phase transition.

The calculations of Guanghua et al. within the framework of the Yafet-Kittel model [Gua99, GLS+00a] assume magnetic moments of $7\,\mu_B$ for M_{Gd}, the theoretical value for a free Gd^{3+} ion, and $1.8\,\mu_B$ for M_{Mn}, respectively, as well as the exchange parameters $\lambda_{\mathrm{Gd-Mn}} = -7.7\,\mathrm{T}/\mu_B{\cdot}$f.u., $\lambda_{\mathrm{Mn-Mn}} = -10.9\,\mathrm{T}/\mu_B{\cdot}$f.u., $\lambda_{\mathrm{Gd-Gd}} = -2.2\,\mathrm{T}/\mu_B{\cdot}$f.u., and an anisotropy constant of $K = 15.8\,\mathrm{T}/\mu_B{\cdot}$f.u.

Figure 5.11 shows the resulting calculated magnetization for $\mathbf{H} \parallel c$ at 5 K. First-order phase transition occur at 38 T (T → AF) and 70 T (AF → T), second-order phase transitions at 24 T (Fi → T) and 84 T (T → F).

It is obvious from comparison with experimental data that the calculated value of the critical field for the magnetic transition from AF to T phase (70 T) is considerably lower than the experimental value of 109 T. Besides results on other compounds, this fact confirms the approximate nature of the Yafet-Kittel model. One disadvantage of this model is certainly that only the exchange interaction between adjacent planes is taken into consideration, which is the nearest neighbour approximation. Apparently this is not sufficient for an adequate description of long-range interactions such as the exchange interaction through conduction electrons.

Nevertheless, this model should yield a qualitative picture of the magnetic phase transitions occurring in $GdMn_2Ge_2$. The H-T phase diagrams for $\mathbf{H} \parallel c$ and $\mathbf{H} \perp c$ calculated with the Yafet-Kittel model are reproduced in figure 5.12.

A final remark refers to recent results concerning the exact alignment of the Mn magnetic moments [FF01], [VMR96b]. According to these studies the Mn moments within the layers are coupled non-collinear ferromagnetically below $T_N = 365$ K. That means, there is both the ferromagnetically coupled out-of-plane component and an additional antiferromagnetic in-plane component.

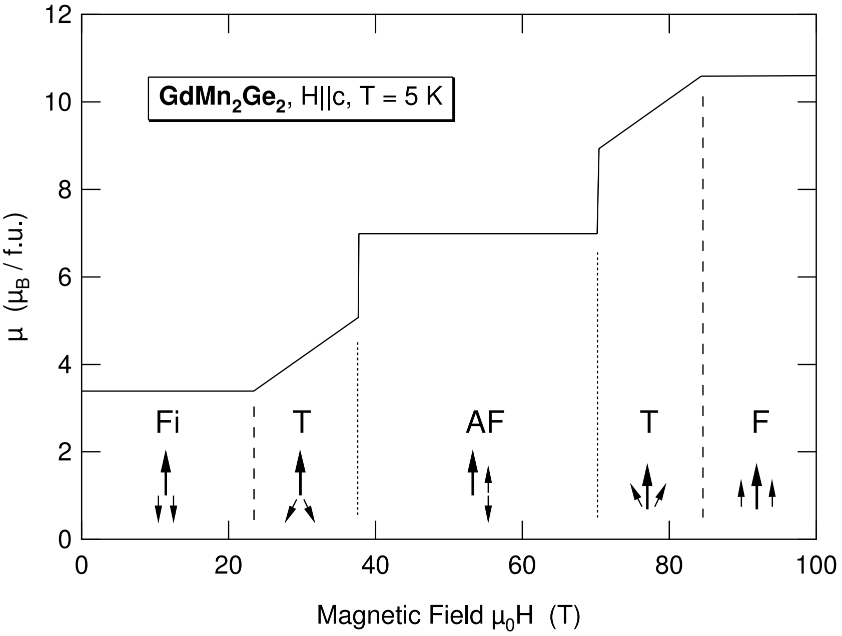

Figure 5.11: Calculated magnetization of GdMn2Ge2 for **H** ∥ c at $T = 5\,\mathrm{K}$ after [Gua99].

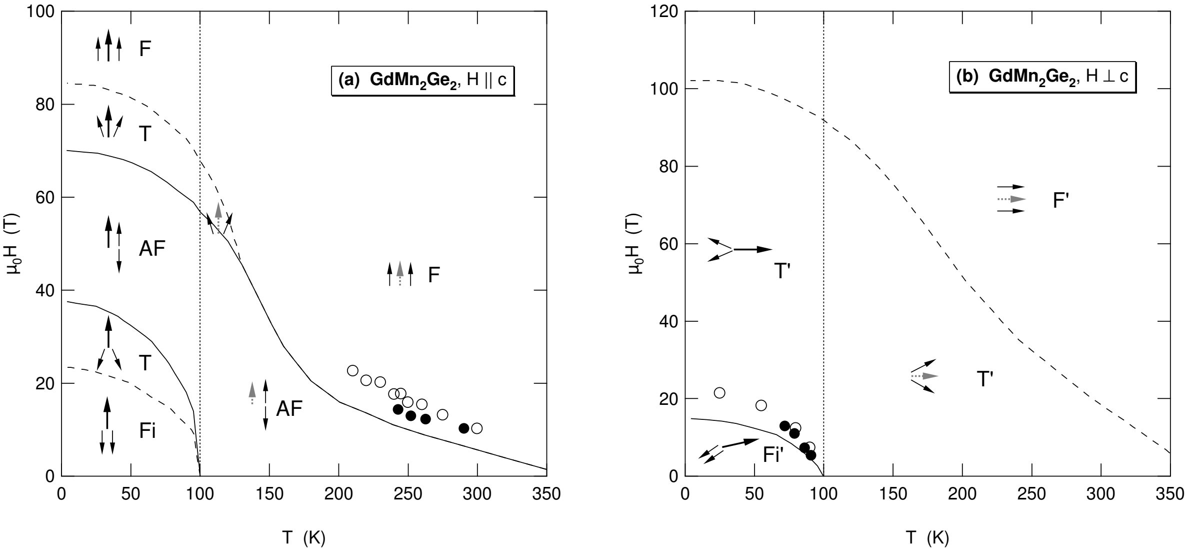

Figure 5.12: Calculated phase diagram of GdMn2Ge2 for **H** ∥ c and for **H** ⊥ c after [Gua99]. The full and broken lines mark the critical fields of the first and second-order phase transitions, respectively. Experimental results are from [KOY89] (full circles) and [Gua99] (open circles). Solid arrows represent the magnetic moments of Gd and Mn in ordered states, whereas gray arrows indicate paramagnetic Gd moments above the Curie temperature, which is indicated by the vertical, dotted line.

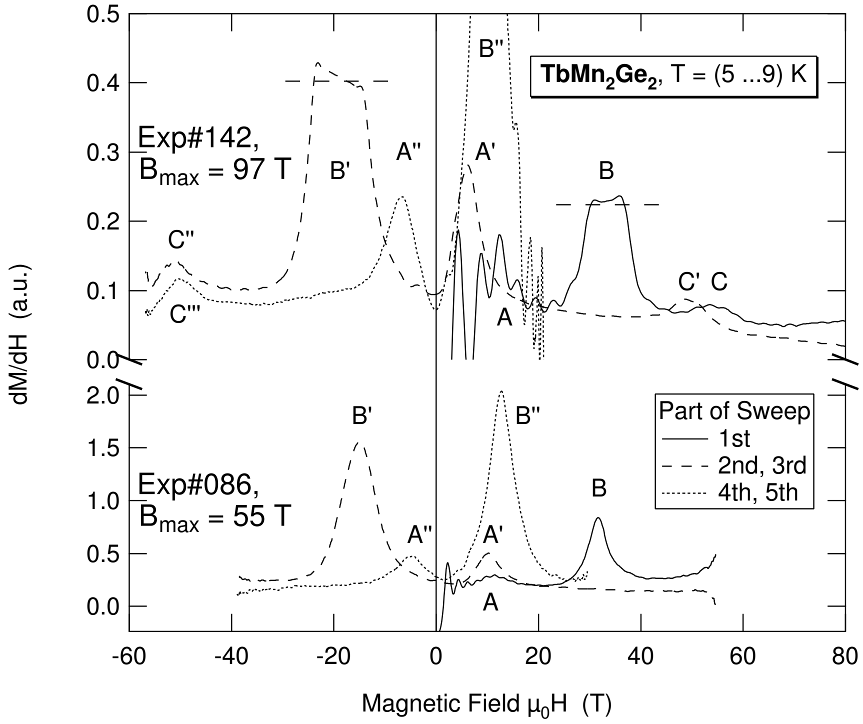

Figure 5.13: Field sweep dependence of the differential susceptibility of $TbMn_2Ge_2$ powder at $T = (5 \ldots 9)$ K. The diagram covers five successive sweeps of the entire field pulse. Corresponding peaks are labelled by the same letter, while one or more primes (') indicate repeated occurrence. Dashed horizontal lines mark the peaks as cut off.

The ferromagnetic component is stacked along the c-axis in the sequence $+ - +-$, forming the well-known AF coupling of adjacent Mn layers. According to [VMR96b] this behaviour is owing to the cell parameters of $GdMn_2Ge_2$ and might also appear at low temperatures.

5.7.5 $TbMn_2Ge_2$

Compared to the other intermetallics, $TbMn_2Ge_2$ exhibits a more complicated magnetic behaviour as is reproduced in figure 5.7. The Mn moments order antiferromagnetically along the tetragonal axis below $T_N = 413$ K. Below 105 K a collinear ferromagnetic order of the Tb moments parallel to the tetragonal axis is observed [VMR96a]. At the same time, the Mn subsystem switches from antiferromagnetic to ferromagnetic alignment [DAE+02]. Thus $TbMn_2Ge_2$ is ferrimagnetic at low temperatures.

Proceeding from these facts, the properties of $TbMn_2Ge_2$ should be similar to those of $GdMn_2Ge_2$. However, the magnetocrystalline anisotropy is found to be much larger in $TbMn_2Ge_2$: $\sim 10^8$ erg/cm^3 compared to $\sim 10^6$ erg/cm^3 in $GdMn_2Ge_2$ [SFF+83]. This may explain major differences between these two compounds.

The first-order phase transition to the high-field phase occurs at a very high field of 118 T. Another first-order phase transition having a relatively small change in magnetization is found at about 50 T. The corresponding dM/dH peak shown in figure 5.13 is labelled as "C".

Further peaks in dM/dH, pronounced and partly large in magnitude are detected in fields up to 33 T. In figure 5.13 these peaks are labelled as A, B, A', B', ... and table 5.3 summarizes their field values. According to their occurrence and peak height, an arrangement into the two groups "A" and "B" seems to be reasonable. Those belonging to "A" have a small magnitude and occur in small fields during down-sweeps only (except A itself). In contrast, those belonging to "B" have a large magnitude and occur in larger fields during up-sweeps only. It should be pointed out that

Table 5.3: dM/dH peaks below 40 T observed in $TbMn_2Ge_2$ powder at $T = (5 \ldots 9)$ K during five successive sweeps of the entire field pulse. The field values are given in order of occurrence during the entire field pulse. Bold numbers correspond to peaks with a relatively large magnitude.

Experiment	Peak fields	Field values (Tesla)						
	(max. / min.)	A	B	A'	B'	A"	B"	...
1	+55 T / -40 T	11	**32**	10	**-15**	-5	**13**	...
2	+97 T / -57 T	12	**33**	6	**-20**	-7	**10**	...

this classification holds even considering the fact that the critical field values vary appreciably. In particular the variation of the peak B is dramatic: field values of 32 T – 15 T – 13 T – ... or 33 T – 20 T – 10 T – ..., respectively, were found in successive up-sweeps.

In consequence, the *M*-*H* loop exhibits a distinct hysteresis, but depends on the peak field or field sweep rate. However, the mechanism causing this behaviour is not quite clear, and it cannot be decided from the data available, whether the peaks are due to one or two first-order phase transitions. Both relaxation effects as well as increasing temperature during the field sweep could have an influence on the observed magnetization curve. Sweep rate dependent effects have been reported also in [LLVB02], where $DyMn_2Ge_2$ powder samples have been investigated in long-pulse fields. Nonetheless, the hysteresis effects are likely to be caused by the very high magnetic anisotropy of $TbMn_2Ge_2$.

5.7.6 $DyMn_2Ge_2$

The magnetic behaviour of $DyMn_2Ge_2$ is still more intricated than that of $GdMn_2Ge_2$. Magnetic and neutron-diffraction studies on single crystals [Shi84] proved that the Mn moments order antiferromagnetically below $T_N = 431$ K. However, according to the results of [Shi84] and [VMT+92, KOO+95], where neutron diffraction was applied on powders, $DyMn_2Ge_2$ experiences two first-order magnetic phase transitions at low temperatures. One is at $T_2 = (37.5 \ldots 40)$ K, the other one at $T_1 = (33 \ldots 35)$ K. Similar to $GdMn_2Ge_2$, the magnetic moments order collinear ferrimagnetically (Fi) below T_1 and collinear antiferromagnetically (AF) for $T_2 < T < T_N$, where the Dy moments are disordered.

The structure in the temperature range $T_1 \ldots T_2$ has not been conclusively established, and the results given in [KOYY91], [VMT+92] and [KOO+95] are contradictory. According to [VMT+92] three phases coexist in this temperature range: Fi, AF and IM, an intermediate phase in which the moments in the Mn layers alternate in the sequence $- + - - + -$ along the *c*-axis. The magnetic unit cell is then given by $a' = a$, $c' = 3c$. According to [KOO+95] the AF phase does not exist below T_2, but a single incommensurate phase with a tentative wave vector of $\mathbf{k} \approx (0, 0, 0.65)$.

Extensive magnetization measurements on single crystals at low temperatures were performed in steady fields up to 5 T [WTHS00] and up to 15 T [KOYY91]. High pulsed fields up to 50 T were utilized in [LLVB02], however, with samples prepared as free powder. In that respect, it becomes clear from the experimental comparison in [LLVB02] that different conditions (free-powdered sample or single crystal, steady field or pulsed field) may lead to different results. While the magnetization of a free powder at 7 K did not show any anomalies up to 12 T in steady fields when measuring with a vibrating magnetometer, the same curve measured in pulsed fields indicates a field-induced transition at about 10 T in the up-sweep.

A theoretical description of the magnetic phase transitions based on the extended molecular field model (see section 5.6) was used in [GEK+01] in order to construct the *H*-*T* phase diagram of $DyMn_2Ge_2$. Exchange parameters and crystal field parameters were derived as well from the experimental data.

In the following, the phase transitions induced by magnetic fields parallel to the tetragonal axis shall be analyzed in more detail [GEK+01], starting with the low temperature regime, $T \sim 4.2$ K.

The initial phase is the Fi phase, in which all Mn moments are antiparallel to the moments $\mathbf{M}_{\mathrm{Dy}}$ of Dy. First-order phase transitions occur in the vicinity of 7 T [KOYY91], near 30 T [GEK+01, LLVB02], and near 110 T. The latter, obtained on a powder sample, is attributed to crystallites for which the field is oriented along the tetragonal axis because no other first-order phase transitions are possible at these high fields for other field orientations.

The phase following the Fi phase at higher fields is called intermediate (IM) phase. Based on the magnetization value of that phase [KOYY91] and the studies of [VMT+92], it is assumed that this phase is characterized by a reorientation of every third layer of the Mn subsystem along the field direction. That means, this structure consists of antiferromagnetic and ferromagnetic Mn blocks, in which the Dy ions are disordered or ordered due to the Dy-Mn exchange, respectively, in zero field. The IM phase is then made up of a sequence of two blocks of the AF phase followed by one block of the Fi phase.

As the transition at about 7 T is from Fi to IM phase, the AF phase with an antiferromagnetic ordering of the Mn subsystem and the F phase, in which the magnetic moments of both subsystems are parallel to the field, are identified as high-field phases. The corresponding critical fields of the first-order phase transitions at helium temperatures are found to be $B_{\mathrm{Fi}\to\mathrm{IM}} = 7\,\mathrm{T}$, $B_{\mathrm{IM}\to\mathrm{AF}} = 32\,\mathrm{T}$ and $B_{\mathrm{AF}\to\mathrm{F}} = 110\,\mathrm{T}$. In the low temperature expansion of (5.19), these fields are given by

$$\begin{aligned} B_{\mathrm{Fi}\to\mathrm{IM}} &= -\lambda_{12}M + \left(\lambda_{22}^{(1)} + \lambda_{22}^{(2)}\right)m \\ B_{\mathrm{IM}\to\mathrm{AF}} &= -\lambda_{12}M + \left(\lambda_{22}^{(1)} - \lambda_{22}^{(2)}\right)m \\ B_{\mathrm{AF}\to\mathrm{F}} &= -\lambda_{12}M - \left(\lambda_{22}^{(1)} + \lambda_{22}^{(2)}\right)m. \end{aligned} \tag{5.20}$$

Knowing the magnetic moments $M = m^{(\mathrm{Dy})}$ and $m = m^{(\mathrm{Mn},1)} = m^{(\mathrm{Mn},2)} = \ldots$, which are the saturation moments of Dy and Mn, respectively, allows to calculate the exchange parameters λ_{12} (Dy-Mn), $\lambda_{22}^{(1)}$ (Mn-Mn interaction in adjacent layers) and $\lambda_{22}^{(2)}$ (Mn-Mn interaction in alternate layers).

At 4.2 K, the electronic ground state of the Dy^{3+} ions is formed by the lower level of the ground Kramers doublet split by exchange and external fields, and according to [VMT+92] it is nearly a pure $|15/2\rangle$ state. Thus we may take $M = 10\mu_B$ for Dy and assume $m = 2.2\mu_B$ for Mn [KOYY91]. Using the above values, the three exchange parameters in (5.20) can be determined as $\lambda_{12} = -5.85\,\mathrm{T}/\mu_B$, $\lambda_{22}^{(1)} = -20\,\mathrm{T}/\mu_B$ and $\lambda_{22}^{(2)} = -3.5\,\mathrm{T}/\mu_B$. The total magnetization curve at low temperatures for a field along the tetragonal axis is shown in figure 5.14.

The intralayer Mn-Mn exchange interaction $\lambda_{22}^{(0)}$, determined from T_{N}, $\lambda_{22}^{(1)}$ and $\lambda_{22}^{(2)}$ is $\lambda_{22}^{(0)} = 2\cdot 10^3\,\mathrm{T}/\mu_B$ [GEK+01]. In some cases it is necessary to consider the temperature dependence of the Mn-Mn exchange interaction associated with the thermal expansion of crystal lattice. Phenomenologically, $\lambda_{22}^{(1)}$ depends in a linear form on the lattice constant a [BBB99]. However, this temperature dependence can be neglected for temperatures below 70 K as calculations show.

In order to construct the *H*-*T* phase diagram, the temperature dependence of the critical fields is calculated by means of the thermodynamic potential (5.19). Although crystal field parameters for the Dy^{3+} ion were determined in [VMT+92], some of them were changed in [GEK+01] in order to describe the magnetization for $\mathbf{H} \perp c$ correctly. On the contrary, crystal field effects are rather unimportant for $\mathbf{H} \parallel c$. The exact value of the exchange parameter λ_{11} (Dy-Dy) could not be derived from the available experimental data, but only an upper bound based on the absence of the Fi phase above T_2 . The value used for the calculation, $\lambda_{11} = 0.49\,\mathrm{T}/\mu_B$, corresponds to a Curie temperature of $T_{\mathrm{C}} = 25\,\mathrm{K}$ for the Dy subsystem.

Figure 5.15 depicts the calculated *H*-*T* phase diagram including experimental data. All phase transitions are of first order. The calculated critical field $B_{\mathrm{Fi}\to\mathrm{IM}}$ is in good agreement with experimental data obtained on a single crystal [KOYY91], whereas the calculated field $B_{\mathrm{IM}\to\mathrm{AF}}$ decreases more slowly with increasing temperature compared to experimental data of a free powder [LLVB02]. Concerning the phase transition $B_{\mathrm{Fi}\to\mathrm{IM}}(T)$, only one experimental point has been determined so far.

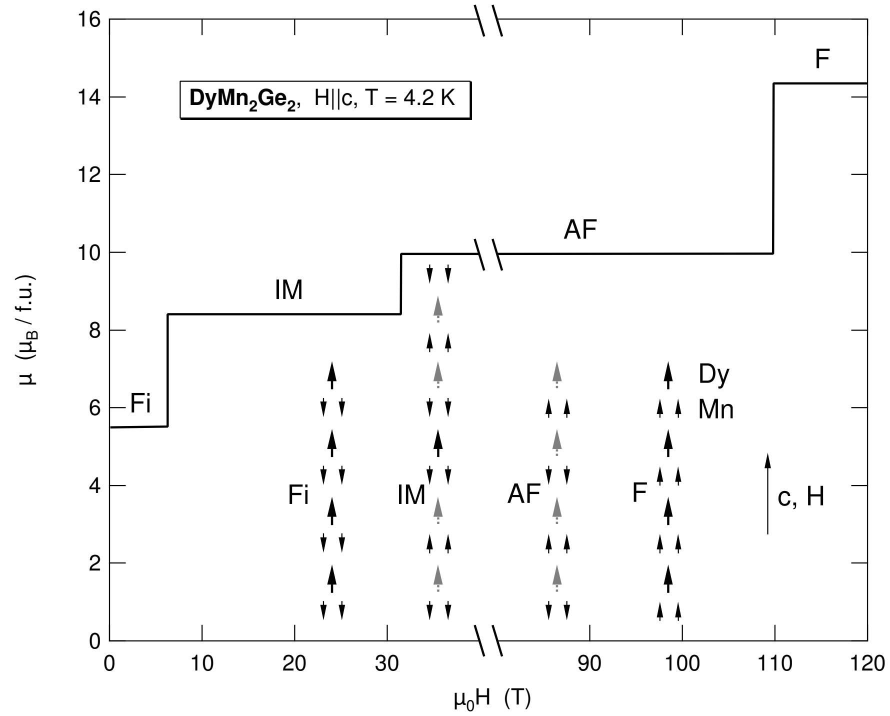

Figure 5.14: Calculated magnetization of $DyMn_2Ge_2$ for $\mathbf{H} \parallel c$ at $T = 4.2\,K$ after [GEK+01]. Solid arrows represent the magnetic moments of Dy and Mn in ordered states, whereas gray arrows indicate paramagnetic Dy moments.

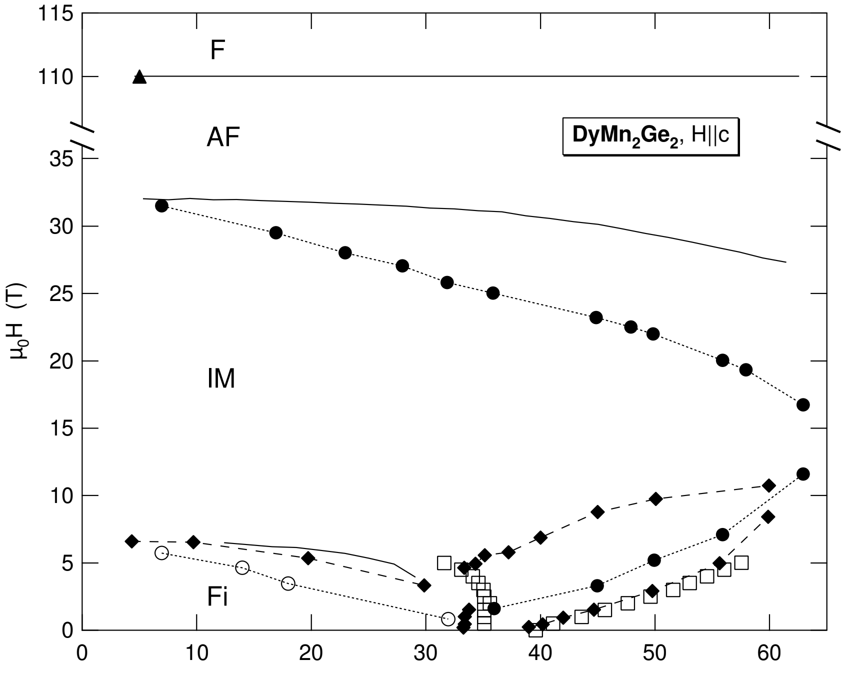

Figure 5.15: Phase diagram of $DyMn_2Ge_2$ for $\mathbf{H} \parallel c$. The full lines correspond to calculations in [GEK+01], symbols belong to experimental data (squares – [WTHS00], single crystals; diamonds – [KOYY91], single crystals; circles – [LLVB02], free powder; triangle –this work, powder).

5.7.7 $\mathbf{HoMn_2Ge_2}$

The Mn subsystem in $\mathrm{HoMn_2Ge_2}$ becomes antiferromagnetically ordered below $T_\mathrm{N} = 460\,\mathrm{K}$ [SL89], where the Mn moments are collinear with respect to the tetragonal axis. It was found that this ordering persists down to 1.3 K [VMR96a]. Unlike other $R\mathrm{Mn_2Ge_2}$ compounds (R = Gd, Dy, Tb) the rare-earth subsystem in $\mathrm{HoMn_2Ge_2}$ remains disordered to very low temperatures due to the weak R-Mn exchange interaction. An ordering of the Ho moments, characterized by a superposition of two sinusoidally modulated structures with different wave vectors, is observed below $T_\mathrm{N}^\mathrm{Ho} = 2.5\,\mathrm{K}$ by means of neutron diffraction [VMR96a].

The large peak in the differential susceptibility at 91 T measured on a powder sample at 5 K is interpreted as first-order phase transition from AF to F phase for a field oriented along the tetragonal axis.

Compared to $\mathrm{DyMn_2Ge_2}$, fewer parameters are necessary to calculate the H-T phase diagram. For the Mn subsystem both the intralayer exchange interaction ($\lambda_{22}^{(0)}$) and the exchange interaction between adjacent layers ($\lambda_{22}^{(1)}$) are considered. The Ho-Ho exchange interaction (λ_{11}) is neglected because it is so small. The exchange interaction between the Ho and Mn subsystems is again summarized in λ_{12}.

This time, the dependence of the interlayer Mn-Mn exchange interaction on the lattice parameter a, leading to a temperature dependence of $\lambda_{22}^{(1)}$, is taken into account by the relationship

$$\lambda_{22}^{(1)} = \rho(a - a_c) \tag{5.21}$$

with $a_c = 4.045\,\mathrm{Å}$ for $R\mathrm{Mn_2Ge_2}$ [GEK$^+$02].

Crystal field parameters were determined and refined in [GEK$^+$02] on the basis of (high-field) magnetization data. As these data show, the crystal field affects the magnetic moment of the Ho ion substantially. At low temperatures, the magnetization saturates at $8.3\,\mu_B$/f.u., which is much lower than the theoretical value of $10\,\mu_B$ for a free Ho^{3+} ion.

The low temperature expansion of (5.19) gives

$$B_{\mathrm{AF}\to\mathrm{F}} = -\lambda_{12}M - \lambda_{22}^{(1)}m, \tag{5.22}$$

for a field parallel to the tetragonal axis, where M and m are the saturation moments of Dy and Mn, respectively. The critical field is $B_{\mathrm{AF}\to\mathrm{F}} = 91\,\mathrm{T}$, $M = 8.3\,\mu_B$ for the Ho moment and $m = 2.3\,\mu_B$ is assumed for the Mn moment in the AF phase [VMR96a]. This allows to determine the linear combination of the two exchange parameters, and using in addition results from $\mathrm{DyMn_2Ge_2}$, the individual parameters can be derived by two different methods. Both methods yield similar values, $\lambda_{12} = (-23 \pm 2)\,\mathrm{T}/\mu_B$ and $\lambda_{22}^{(1)} = (-4.5 \pm 0.5)\,\mathrm{T}/\mu_B$ [GEK$^+$02].

The temperature dependence of the critical field $B_{\mathrm{AF}\to\mathrm{F}}$ is calculated by means of (5.19), taking into account (5.21) and experimental data of $a(T)$. The intralayer Mn-Mn exchange interaction $\lambda_{22}^{(0)} = 2.1 \cdot 10^3\,\mathrm{T}/\mu_B$ was determined using $T_\mathrm{N} = 460\,\mathrm{K}$ and the value of $\lambda_{22}^{(1)}$. Figure 5.16 shows the resulting phase diagram.

The nature of a second first-order phase transition, corresponding to the smaller susceptibility peak at 76 T (see figure 5.9) remains unsolved so far. However, since similar peaks are found also in other compounds ($\mathrm{YMn_2Ge_2}$, $\mathrm{TbMn_2Ge_2}$) it can be concluded that this phase transition must be caused by the Mn subsystem. In $\mathrm{YMn_2Ge_2}$, only the Mn subsystem is magnetic, while in $\mathrm{HoMn_2Ge_2}$, the rare-earth subsystem is paramagnetic in the temperature region examined. Thus the second first-order phase transition with smaller change in magnetization is also due to the Mn subsystem.

5.7.8 $\mathbf{ErMn_2Ge_2}$

The properties of $\mathrm{ErMn_2Ge_2}$ are comparable to those of $\mathrm{HoMn_2Ge_2}$. The Mn sublattice orders antiferromagnetically below $T_\mathrm{N} = 475\,\mathrm{K}$, where the moments are aligned along the tetragonal axis [SL89]. The Er subsystem becomes ferromagnetic at a rather low Curie temperature, $T_\mathrm{C} = 5.5\,\mathrm{K}$ [VMR96a]. However, the Er moments are aligned perpendicularly to the tetragonal axis.

At 8 K, only one clear phase transition at 90 T is observed as shown in figure 5.10.

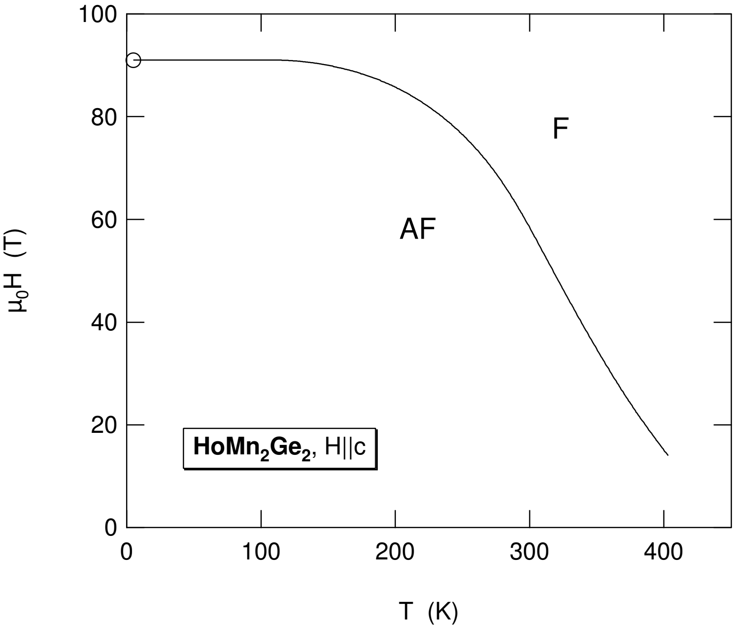

Figure 5.16: Calculated phase diagram of $HoMn_2Ge_2$ for $\mathbf{H} \parallel c$ after [GEK+02].

Summary and Future Prospects

In this thesis we have systematically investigated the magnetic properties of different materials in ultrahigh magnetic fields up to 150 T produced by the single-turn coil technique. In particular we have examined the van Vleck paramagnets $\mathrm{PrVO_4}$ and $\mathrm{TmPO_4}$ as well as the intermetallic compounds $R\mathrm{Mn_2Ge_2}$ (R = Gd, Tb, Dy, Ho, Er, Y) at low temperatures.

The decisive prerequisite for this study, which had to be developed first for application with the existing single-turn coil generator in Berlin, is an efficient and sensitive measurement system (magnetometer). Due to the disadvantageous boundary conditions imposed by the field generator, this required a completely new and different design compared to existing conventional magnetometers for quasi-DC or non-destructive pulsed magnets. In contrast to those magnets, the total field volume available in the single-turn coil is naturally very small, so that the lower field homogeneity becomes in particular important. As to the spatial dependence, the homogeneity is better in radial than in axial direction, but regarding the time dependence, there is the phenomenon of the "phase shifts", which means that a factorial separation of the total field dependence into time dependent and space dependent functions is not possible. The second difference compared to non-destructive pulsed magnets is an extremely short pulse duration with very high dB/dt, which makes proper matching of the pick-up coils and matched cable termination absolutely necessary.

As both boundary conditions require the manufacturing of very well compensated pick-up coils with high voltage insulation strength, we favour compensation coils of the radial type with alternative winding. Typical full area compensation ratios of $\sim 10^{-4}$ and the absence of any failure prove this concept appropriate.

Completely unprecedented is the application of a comprehensive electromagnetic shielding, which makes use of a wire metal. The concept was newly devised and successfully put into operation. Although strong electromagnetic interference is often seen as a disturbance that can hardly be avoided in electrical measurements involving probes near or inside the single-turn coil, this problem can be overcome by an appropriate electromagnetic shielding. Partly consisting of a wire metal it suppresses to a large extent unwanted electromagnetic interference effects to the measurement system but does not reduce the amplitude of the magnetic field pulse. As it turned out, the shielding is one of the key factors for sensitive magnetization measurements.

Besides the performance of the magnetometer, some inherent characteristics of the field pulse may affect the quality and sensitivity of measurements as well. Irrespective of the charging voltage high-frequency trigger oscillations are caused by the finite collector capacitance, while their damping depends implicitly on the charging voltage. At the highest charging voltages, irregularities of the field homogeneity occur at the end of the main pulse, probably due to plasma or arc initiations. Apart from these two effects, the field pulse is a relatively smooth function of time. Some of these characteristics had been predicted or observed before, but clear and detailed experimental evidence is presented for the first time in this work.

Although the total measurement system functions efficiently as intended there is one drawback, which is related to the uncompensated background signal superimposed to the response of the sample. Since the time dependence of the background signal can deviate significantly from the ideal behaviour proportional to the time derivative of the field, a proper elimination is not possible. This proves to be a real problem and is the actual reason for the fact that absolute values of magnetization cannot reliably be determined for the highest fields. Fortunately this problem diminishes with decreasing amplitude of the applied field, so that the experimental study of the rare-earth zircons $PrVO_4$ and $TmPO_4$ benefits from the relatively low peak fields necessary.

At low temperatures, both van Vleck paramagnets exhibit anomalies in their differential susceptibility caused by a crossover of the lowest-lying energy levels, which takes place at about 50 T for $PrVO_4$ and at about 30 T for $TmPO_4$. These anomalies occur in a field along the tetragonal axis ($H \parallel [001]$) and have been investigated for single crystals of both compounds at different temperatures and varying field sweep rates. While level crossings in other rare-earth zircons have been investigated before, we have performed the first experimental study of the level crossing phenomena in $PrVO_4$ and $TmPO_4$.

It has been shown that the magnetocaloric effect plays an important role in (short-) pulsed fields. A cooling of the sample takes place when the crossover is approached, followed by a subsequent heating as the magnetic field increases further. The consequence is a more pronounced peak of the magnetic susceptibility at the crossover compared to the isothermal case. The character of the magnetocaloric effect depends on the initial temperature and three different regimes can be distinguished as could be confirmed experimentally. According to calculations the minimum temperatures can be as low as some decimals of Kelvin for $PrVO_4$ and can even approach some mK for $TmPO_4$ for an initial temperature of 4.2 K. This has two important consequences.

The very low temperatures may affect the spin-lattice relaxation times and secondly, the hyperfine interaction plays an important role in the immediate vicinity of the level crossing in both enhanced nuclear magnets. This is related to the fact that the level crossing occurs in both compounds without a gap if the field is oriented exactly along the tetragonal axis. Any misorientation results in a gap that causes a deformation of the magnetization curve and the susceptibility peak smears out. While this effect is rather unimportant for $PrVO_4$, it is crucial for $TmPO_4$.

Hysteresis effects in the critical field of the susceptibility peaks between up- and down-sweep have been observed in both compounds. The reason for this effect is not quite clear yet, but an increased spin-lattice relaxation time in the vicinity of the crossover could contribute to this phenomenon as well as to the broadening of the susceptibility peak. Though, without supplementary measurements it is not possible to answer this question.

For $TmPO_4$, however, a variety of interesting measurements is possible since the level crossing can be reached even in DC fields, in which the magnetic field can be tuned or modulated around the critical field of 31 T. Isothermal conditions over a wide temperature range would be useful as well. From the theoretical point of view, the correct implementation of the hyperfine interaction (including parameters) for $TmPO_4$ has still to be solved. This is important because the width of the susceptibility peak for $H \parallel [001]$ depends largely on this contribution.

Powder samples of the intermetallic compounds $R\mathrm{Mn_2Ge_2}$ (R = heavy rare-earth metal, Y) have been examined at low temperatures in fields up to 150 T, and field-induced metamagnetic transitions have been observed in all compounds. Depending on the rare-earth ion and temperature, one or more metamagnetic phase transitions occur for each compound, most of which have been experimentally observed for the first time within this investigation.

The critical fields of those transitions, which take place in the highest fields, range from 90 T for $ErMn_2Ge_2$ to 118 T for $TbMn_2Ge_2$, whereas a value of 55 T was found for YMn_2Ge_2. As is characteristic for first-order phase transitions, the critical fields are different for increasing and decreasing field.

The observed phase transitions are associated with a change in the magnetic structure of the Mn subsystem only. This is confirmed by the fact that YMn_2Ge_2, containing the non-magnetic Y, exhibits also a field-induced phase transition. This compound has only the antiferromagnetic Mn subsystem.

Details of the individual compounds are discussed on the basis of the Yafet-Kittel model and an extended molecular field model. The phase transitions observed here help to identify the variety of possible configurations in the H-T phase diagram as well as to calculate exchange parameters within the models used. These results involve the critical fields of the susceptibility peaks related to the high-field transitions with a relatively large change in magnetization.

After increasing the sensitivity of the measurement system, however, additional peaks associated with a smaller change in magnetization have been detected in some of the $R\mathrm{Mn_2Ge_2}$ compounds. The nature of these new first-order phase transitions has not been established yet.

Disadvantageous in that respect is that absolute values of magnetization could not be determined.

A very interesting magnetization behaviour is certainly found in $TbMn_2Ge_2$. At least three first-order phase transitions are found at low temperatures, and in addition the M-H loop exhibits pronounced hysteresis effects.

So far we have examined the field-induced phase transitions only at one very low temperature. Additional measurements at higher temperatures would allow an experimental construction of the phase diagrams. However, this would not remove uncertainties about the actual configuration of the respective phases. For this purpose absolute values of magnetization are necessary, which can be determined by means of the present system only in exceptional cases. Another question concerns the influence of the (free) powder on the results, which is used instead of single crystals. Although this problem is a field of its own, doubts in interpretation of some susceptibility peaks could be ruled out by use of oriented fixed-powder samples. Due to the large anisotropy of the susceptibility of $R\mathrm{Mn_2Ge_2}$ compounds, such samples can be easily prepared.

This thesis intended to explore the possibilities and the potential of magnetization measurements in ultrahigh magnetic fields in general and with the single-turn coil in particular. We think that there is still room for improvements, making those measurements still more precise or expanding their applicability. With respect to the latter point we have already started experiments, which examine the spin dynamics of nano-scale magnets. These experiments make use of relatively low but quickly changing fields produced by the single-turn coil.

Zusammenfassung und Ausblick

In Rahmen dieser Arbeit wurden systematisch die magnetischen Eigenschaften verschiedener Materialien in ultrahohen Magnetfeldern untersucht. Insbesondere untersuchten wir die van Vleck-Paramagnete $PrVO_4$ und $TmPO_4$ sowie die intermetallischen Verbindungen $R\mathrm{Mn_2Ge_2}$ (R = Gd, Tb, Dy, Ho, Er, Y) bei tiefen Temperaturen. Die dafür notwendigen Magnetfelder bis zu 150 T wurden mittels der *single-turn coil*-Methode erzeugt.

Die entscheidende Grundlage für diese Untersuchungen, die zunächst für die Anwendung in dem in Berlin existierenden Magnetfeldgenerator (*single-turn coil generator*) entwickelt werden mußte, ist ein leistungsfähiges Meßsystem (Magnetometer). Aufgrund der ungünstigen, durch den Magnetfeldgenerator verursachten Randbedingungen erforderte dies ein vollständig neuartiges Design, das sich stark von üblichen Magnetometern unterscheidet, die für den Einsatz in quasi-DC oder nichtdestruktiv gepulsten Magneten konzipiert sind. Im Gegensatz zu diesen Magneten ist das gesamte nutzbare Feldvolumen in der *single-turn coil* sehr klein, sodaß der Feldhomogenität eine besondere Bedeutung zukommt. Bezüglich der räumlichen Abhängigkeit ist die Homogenität in radialer Richtung besser als axialer Richtung. Hinsichtlich der Zeitabhängigkeit tritt jedoch das Phänomen der ,,Phasenverschiebungen" auf, wodurch eine Faktorisierung der gesamten Feldabhängigkeit in zeit- und ortsabhängige Anteile nicht mehr möglich ist. Der zweite Unterschied zu nichtdestruktiv gepulsten Magneten ist die außerordentlich kurze Pulsdauer, die eine Anpassung der Pick-up-Spule an die Leitung bzw. impedanzrichtig abgeschlossene Leitungen unerläßlich macht sowie zu extrem hohen Feldänderungsgeschwindigkeiten dB/dt führt.

Da beide Randbedingungen die Herstellung sehr gut kompensierter *Pick-up*-Spulen mit hoher Spannungsfestigkeit erfordern, bevorzugen wir Kompensationsspulen des radialen Typs, deren Windungen alternierend gewickelt sind. Typische Kompensationsverhältnisse von 10^{-4} sowie eine völlige Fehlerfreiheit bestätigen dieses Konzept.

Vollkommen neuartig ist die Anwendung einer elektromagnetischen Abschirmung, die ein sogenanntes ,,Drahtmetall" verwendet. Dieses Konzept wurde neu ausgearbeitet und erfolgreich umgesetzt. Problematisch bei elektrischen Messungen mit Sonden in der Nähe oder innerhalb der *single-turn coil* sind die starken elektromagnetischen Störeinflüsse, die vom Feldgenerator ausgehen. Obwohl die daraus resultierenden Störungen oft als unvermeidbar angesehen werden, lassen sie sich durch eine geeignete Abschirmung vermeiden. Der Schirm, der teilweise aus einem ,,Drahtmetall" besteht, verhindert einerseits weitgehend die Einkopplung unerwünschter elektromagnetischer Störungen, reduziert jedoch die Amplitude des magnetischen Feldpulses nicht. Wie sich herausgestellt hat, ist diese Abschirmung einer der Schlüsselfaktoren für empfindliche Magnetisierungsmessungen.

Neben den Eigenschaften des Magnetometers können sich auch bestimmte inhärente Eigenschaften des Feldpulses auf die Qualität und Empfindlichkeit der Messungen auswirken. Unabhängig von der Ladespannung ergeben sich hochfrequente Einschaltschwingungen, deren Ursache die endliche Kollektorkapazität darstellt. Die Dämpfung dieser Schwingungen hängt implizit von der Ladespannung ab. Ein weiteres Phänomen, das bei den höchsten Ladespannungen am Ende des Feldpulses auftreten kann, sind starke Inhomogenitäten des Magnetfeldes. Sie resultieren wahrscheinlich aus Plasma- oder Bogenentladungen. Abgesehen von diesen beiden Effekten ist der Feldpuls jedoch eine relative glatte Funktion der Zeit. Einige dieser Charakteristiken wurden bereits vorausgesagt oder beobachtet — zweifelsfrei und detailliert werden sie erstmals in dieser Arbeit dargestellt.

Obwohl das gesamte Meßsystem wie beabsichtigt gut funktioniert, gibt es eine Einschränkung, die aus dem nicht kompensierten Untergrundsignal resultiert, das dem Probensignal überlagert ist. Da die Zeitabhängigkeit dieses Untergrundsignals deutlich vom idealen Verhalten – der Proportionalität zur zeitlichen Ableitung des Feldes – abweichen kann, ist eine zuverlässige Berücksichtigung dieses Anteils nicht möglich. Dies stellt ein nicht zu vernachlässigendes Problem dar und ist der entscheidende Grund dafür, daß absolute Werte der Magnetisierung in den höchsten Feldern nicht verläßlich bestimmt werden können. Glücklicherweise verringert sich die Auswirkung dieses Problems, je niedriger die Amplitude des Feldpulses ist. Das ist auch für die experimentelle Untersuchung der Selten-Erd-Zirkon-Verbindungen $PrVO_4$ und $TmPO_4$ von Nutzen, da nur relativ geringe Felder nötig sind.

Bei tiefen Temperaturen zeigen beide van Vleck-Paramagnete Anomalien in der differentiellen Suszeptibilität, die durch die Überkreuzung (*level crossing*) der beiden niedrigsten Energieniveaus verursacht werden. Die entsprechenden Magnetfelder betragen etwa 50 T in $PrVO_4$ und rund 30 T in $TmPO_4$. Diese Anomalien treten im Feld parallel zur tetragonalen Achse ($H \parallel [001]$) auf und wurden an Einkristallen beider Materialien für unterschiedliche Temperaturen und Feldänderungsgeschwindigkeiten untersucht. Während *level crossing*-Phänomene in anderen Selten-Erd-Zirkon-Verbindungen schon früher untersucht worden sind, fand die erste experimentelle Studie der *level crossing*-Phänomene an $PrVO_4$ und $TmPO_4$ erstmals in Rahmen dieser Arbeit statt.

Es wurde gezeigt, daß der magnetokalorische Effekt in (sehr kurzen) gepulsten Feldern eine wichtige Rolle spielt. Dies führt zu einer Abkühlung der Probe, wenn sich das Magnetfeld dem kritischen Wert der Überkreuzung nähert und einer anschließenden Erwärmung bei weiter ansteigendem Feld. Die Folge ist eine deutlichere Ausprägung des Peaks der differentiellen Suszeptibilität verglichen mit dem isothermen Fall. Der Charakter des magnetokalorischen Effekts hängt dabei von der Anfangstemperatur ab und kann in drei verschiedene Regime eingeteilt werden, was experimentell auch bestätigt wurde. Rechnungen zufolge kann bei einer Anfangstemperatur von 4.2 K eine minimale Temperatur von einigen Zehntel Kelvin für $PrVO_4$ und einigen mK für $TmPO_4$ erreicht werden. Daraus ergeben sich zwei wichtige Konsequenzen.

Die sehr tiefen erreichbaren Temperaturen können sich auf die Spin-Gitter-Relaxationszeiten auswirken; desweiteren spielt die Hyperfeinwechselwirkung, die in beiden Systemen verstärkt ist, eine wichtige Rolle in der unmittelbaren Umgebung des *level crossing.* Diese Tatsache ist dadurch begründet, daß die Kreuzung der Energieniveaus in beiden Systemen tatsächlich ohne Energielücke auftritt, wenn das Magnetfeld exakt parallel zur tetragonalen Achse ausgerichtet ist. Jede Abweichung davon führt dagegen zu einer Energielücke und bewirkt eine Deformation der Magnetisierungskurve. Damit verschmiert auch der Peak der Suszeptibilität. Während dieser Effekt in $PrVO_4$ nur unwesentlich ausgeprägt ist, ist er in $TmPO_4$ entscheidend.

In beiden Verbindungen wurden auch Hystereseeffekte des kritischen Feldes beobachtet. Der Peak der differentiellen Suszeptibilität tritt in steigenden bzw. fallenden Feldern bei größeren bzw. kleineren Feldern auf. Die genaue Ursache hierfür ist derzeit noch ungeklärt, aber eine vergrößerte Spin-Gitter-Relaxationszeit in der Umgebung des *level crossing* kann sowohl zu diesem Phänomen beitragen als auch zu einer Verbreiterung des Peaks der Suszeptibilität. Ohne zusätzliche, ergänzende Messungen kann diese Frage jedoch nicht geklärt werden.

Für $TmPO_4$ ist aber eine Reihe von interessanten Messungen möglich, da das *level crossing* sogar in DC-Feldern erreicht werden kann, in denen das Magnetfeld um das kritische Feld von 31 T genau abgestimmt oder moduliert werden kann. Ebenso nützlich sind isotherme Bedingungen über einen weiten Temperaturbereich. Vom Standpunkt der Theorie ist die korrekte Berücksichtigung der Hyperfeinwechselwirkung (sowie die Bestimmung der zugehörigen der Parameter) ein Problem, das noch zu lösen ist. Dies ist wichtig, da die Breite des Peaks der Suszeptibilität für $H \parallel [001]$ stark von diesem Beitrag abhängt.

Pulverproben der intermetallischen Verbindungen $R\mathrm{Mn_2Ge_2}$ (R = schweres Selten-Erd-Metall, Y) wurden bei tiefen Temperaturen in Feldern bis zu 150 T untersucht, wobei in allen Verbindungen feldinduzierte metamagnetische Phasenübergänge beobachtet wurden. Abhängig vom Selten-Erd-Ion und der Temperatur treten jeweils ein oder mehrere Phasenübergänge auf, wobei die meisten erstmals im Rahmen dieser Arbeit experimentell nachgewiesen wurden.

Die kritischen Felder jener Phasenübergange, die in den höchsten Feldern auftreten, reichen von 90 T in $ErMn_2Ge_2$ bis zu 118 T in $TbMn_2Ge_2$, wobei das Feld in YMn_2Ge_2 mit 55 T wesentlich geringer ist. Wie es für Phasenübergänge erster Ordnung typisch ist, sind die kritischen Felder unterschiedlich in steigendem bzw. fallendem Feld.

Die beobachteten Übergänge werden dabei auf eine Änderung der magnetischen Struktur des Mn-Teilsystems allein zurückgeführt. Bestätigt wird diese These durch die Tatsache, daß auch YMn_2Ge_2 solche feldinduzierten Phasenübergänge aufweist, wobei Y nichtmagnetisch ist und YMn_2Ge_2 somit einzig das antiferromagnetische Mn-Teilsystem enthält.

Einzelheiten der verschiedenen Selten-Erd-Verbindungen wurden innerhalb des Yafet-Kittel Modells und eines erweiterten Molekularfeld-Modells diskutiert. Die in dieser Arbeit beobachteten Phasenübergänge helfen dabei, die vielfältigen möglichen Konfigurationen innerhalb der H-T Phasendiagramme zu identifizieren, als auch Austauschparameter innerhalb der verwendeten Modelle zu bestimmen. Diese Ergebnisse beinhalten die kritischen Felder derjenigen Peaks der Suszeptibilität, die mit den Phasenübergängen in den höchsten Feldern und relativ großer Änderung in der Magnetisierung verbunden sind.

Dank der gesteigerten Empfindlichkeit des Meßsystems wurden später in einigen intermetallischen Verbindungen $R\mathrm{Mn}_2\mathrm{Ge}_2$ weitere Peaks in der Suszeptibilität gefunden, die mit einer wesentlich kleineren Änderung in der Magnetisierung verbunden sind. Die Natur dieser neuen Phasenübergänge konnte bis jetzt noch nicht aufgeklärt werden. Nachteilig in dieser Hinsicht ist auch, daß absolute Werte der Magnetisierung nicht bestimmt werden konnten.

Ein sehr interessantes Magnetisierungsverhalten weist $TbMn_2Ge_2$ auf. Mindestens drei Phasenübergänge erster Ordnung wurden bei tiefen Temperaturen beobachtet. Zusätzlich besitzt die M-H Kurve ein ausgeprägtes Hystereseverhalten.

Bis jetzt haben wir die feldinduzierten Phasenübergänge nur bei sehr tiefen Temperaturen untersucht. Zusätzliche Messungen bei höheren Temperaturen würden eine experimentelle Konstruktion des Phasendiagramms gestatten. Dies würde jedoch nicht die Unsicherheiten über die tatsächliche Konfiguration der entsprechenden Phasen beseitigen. Zu diesem Zweck sind absolute Werte der Magnetisierung notwendig, die mit dem gegenwärtigen System aber nur in sehr wenigen Fällen bestimmt werden können. Eine weitere Frage betrifft die Auswirkung des (freien bzw. losen) Pulvers auf die Meßergebnisse, das anstelle eines Einkristalls verwendet wird. Obwohl diese Frage in eine komplizierte, eigene Problematik mündet, könnten Zweifel bei der Interpretation bestimmter Peaks durch die Verwendung orientierter Pulverproben ausgeräumt werden. Solche Proben, bei denen die Pulverpartikel ausgerichtet und fixiert werden, können im Falle der $R\mathrm{Mn}_2\mathrm{Ge}_2$-Verbindungen relativ einfach angefertigt werden. Ursache hierfür ist die starke Anisotropie der magnetischen Suszeptibilität.

Ein Anliegen dieser Arbeit war es, die Möglichkeiten und die Grenzen von Magnetisierungsmessungen in ultrahohen Magnetfeldern im allgemeinen und in der *single-turn coil* im besonderen zu untersuchen. Wir glauben, daß es noch einigen Spielraum für Verbesserungen gibt, die solche Messungen genauer machen oder aber ihre Anwendungsmöglichkeiten weiter ausdehnen können. Bezüglich des letztgenannten Punktes haben wir bereits mit Experimenten begonnen, die die Spin-Dynamik kleinster molekularer Magnete untersuchen. Diese Experimente nutzen die sehr schnell veränderlichen Magnetfelder, wie sie von der *single-turn coil* erzeugt werden, benötigen aber nur Felder mit relativ geringer Amplitude.

Appendix A

A Reciprocity Theorem

One practical problem related to magnetism is to determine the signal of a detection coil caused by the magnetization change of a sample. More precise, one has to determine the magnetic flux Φ induced in the pick-up coil by a sample with (non-uniform) magnetization $\mathbf{M}(\mathbf{r}')$. The reciprocity theorem relates this flux to the field $\mathbf{h}(\mathbf{r}')$ produced in the sample volume by a unit current flowing in the pick-up coil when there is no magnetic sample [Lév00].

The magnetic scalar potential $\phi(\mathbf{r})$ produced by the sample with distribution $\mathbf{M}(\mathbf{r}')$ is given by

$$\phi(\mathbf{r}) = -\frac{1}{4\pi}\int_V d^3r' \, \frac{\operatorname{div}\mathbf{M}(\mathbf{r}')}{|\mathbf{r}-\mathbf{r}'|} = -\frac{1}{4\pi}\int_V d^3r' \, \mathbf{M}(\mathbf{r}')\boldsymbol{\nabla}_r \frac{1}{|\mathbf{r}-\mathbf{r}'|} = \frac{1}{4\pi}\int_V d^3r' \, \mathbf{M}(\mathbf{r}')\cdot\frac{\hat{\mathbf{R}}}{|\mathbf{R}|^2} \tag{A.1}$$

using $\mathbf{R} = \mathbf{r} - \mathbf{r}'$ and $\hat{\mathbf{R}} = \mathbf{R}/|\mathbf{R}|$. The magnetic field can be derived from that by

$$\mathbf{H}(\mathbf{r}) = -\boldsymbol{\nabla}\phi(\mathbf{r}) = \frac{1}{4\pi}\int_V d^3r' \, \frac{3(\mathbf{M}(\mathbf{r}')\cdot\hat{\mathbf{R}})\,\hat{\mathbf{R}} - \mathbf{M}(\mathbf{r}')}{|\mathbf{R}|^3}. \tag{A.2}$$

The magnetic flux through the pick-up coil is defined as integral of the field over its surface with a normal unit vector $\hat{\mathbf{n}}(\mathbf{r})$, see figure A.1(a),

$$\Phi = \int_S \mu_0 \mathbf{H}\cdot d\mathbf{s} = \mu_0 \int_S \mathbf{H}\cdot\hat{\mathbf{n}}(\mathbf{r})\, d^2r \tag{A.3}$$

and is therefore

$$\Phi = \frac{\mu_0}{4\pi}\int_S d^2r \int_V d^3r' \, \frac{3(\mathbf{M}(\mathbf{r}')\cdot\hat{\mathbf{R}})\,(\hat{\mathbf{R}}\cdot\hat{\mathbf{n}}(\mathbf{r})) - \mathbf{M}(\mathbf{r}')\cdot\hat{\mathbf{n}}(\mathbf{r})}{|\mathbf{R}|^3}. \tag{A.4}$$

On the other hand, when a current I is flowing through the pick-up coil and there is no magnetic sample, a field $\mathbf{h}(\mathbf{r}')$ will be produced in the sample volume V, see figure A.1(b). From Ampere's

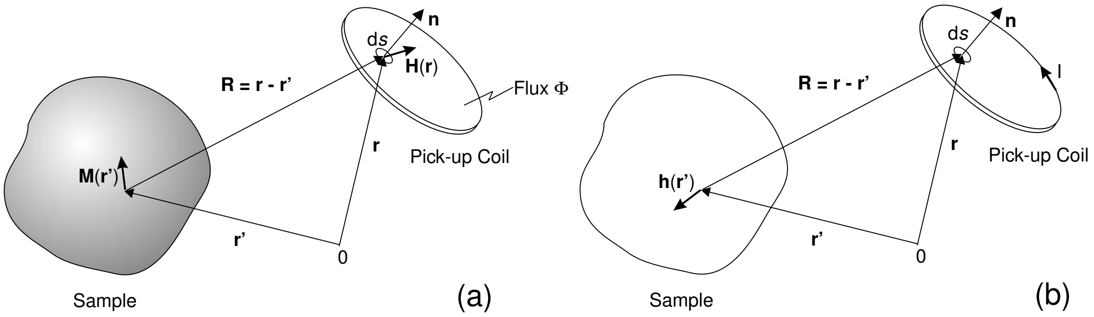

Figure A.1: (a) Sample of volume V and magnetization $\mathbf{M}(\mathbf{r}')$ inducing the flux Φ in the pick-up coil, (b) Magnetic field $\mathbf{h}(\mathbf{r}')$ produced by a current I in the pick-up coil when there is no magnetic sample.

theorem, we have

$$\mathbf{h}(\mathbf{r}') = -\frac{I}{4\pi}\oint_{c=\partial S} d\mathbf{r} \times \frac{\hat{\mathbf{R}}}{|\mathbf{R}|^2} \tag{A.5}$$

or multiplied with an arbitrary vector $\mathbf{v}(\mathbf{r}')$

$$\mathbf{v}(\mathbf{r}') \cdot \mathbf{h}(\mathbf{r}') = -\frac{I}{4\pi}\mathbf{v}(\mathbf{r}') \cdot \oint_{\partial S} d\mathbf{r} \times \frac{\hat{\mathbf{R}}}{|\mathbf{R}|^2} = -\frac{I}{4\pi}\oint_{\partial S} d\mathbf{r} \cdot \left(\frac{\hat{\mathbf{R}}}{|\mathbf{R}|^2} \times \mathbf{v}(\mathbf{r}') \right). \tag{A.6}$$

Transforming the line integral into a surface integral, we obtain

$$\mathbf{v}(\mathbf{r}') \cdot \mathbf{h}(\mathbf{r}') = -\frac{I}{4\pi}\int_S d^2r \, \hat{\mathbf{n}}(\mathbf{r}) \cdot \mathrm{rot} \left(\frac{\hat{\mathbf{R}}}{|\mathbf{R}|^2} \times \mathbf{v}(\mathbf{r}') \right). \tag{A.7}$$

After numerous transformations using various vector identities and setting $\mathbf{v}(\mathbf{r}') = \mathbf{M}(\mathbf{r}')$ we get finally

$$\mathbf{M}(\mathbf{r}') \cdot \mathbf{h}(\mathbf{r}') = \frac{I}{4\pi}\int_S d^2r \frac{3(\mathbf{M}(\mathbf{r}') \cdot \hat{\mathbf{R}})\,(\hat{\mathbf{R}} \cdot \hat{\mathbf{n}}(\mathbf{r})) - \mathbf{M}(\mathbf{r}') \cdot \hat{\mathbf{n}}(\mathbf{r})}{|\mathbf{R}|^3}. \tag{A.8}$$

Comparing this expression with equation (A.4), we can deduce the reciprocity theorem

$$\Phi = \frac{\mu_0}{I}\int_V d^3r' \, \mathbf{M}(\mathbf{r}') \cdot \mathbf{h}(\mathbf{r}'). \tag{A.9}$$

That means, knowing the magnetic field $\mathbf{h}(\mathbf{r}')$ produced by a (unit) current I in the pick-up coil inside the sample volume V (with no magnetic sample present), one can easily determine the flux Φ induced by any sample having the magnetization $\mathbf{M}(\mathbf{r}')$ without the need to solve the magnetostatic problem. This theorem turns out to be extremely useful in practice and simplifies detector optimization and calibration.

Appendix B

Frequency Response of the Probe System

The response of a common probe system described by the circuit of figure B.1 is analyzed in this section in both, frequency and time domain.

Frequency Domain

If we want to study the response of the circuit to a steady sinusoidal input signal $\widetilde{U}_{\mathrm{G}}(\omega) = U_0\,\mathrm{e}^{i\omega t}$ and look for solutions of the form $\widetilde{U}(\omega) = U\,\mathrm{e}^{i(\omega t+\varphi)}$ as function of the angular frequency ω, we have to examine the transfer function $\widetilde{A}(\omega)$, defined as quotient of the complex output and input voltages, respectively. It is given by

$$\widetilde{A}(\omega) = \frac{\widetilde{U}(\omega)}{\widetilde{U}_{\mathrm{G}}(\omega)} = \frac{Z_C||R}{Z_L + r + Z_C||R}. \tag{B.1}$$

For further calculations it is useful to introduce some dimensionless quantities, namely the DC-attenuation factor A_0,

$$A_0 = R/(R+r), \tag{B.2}$$

the damping constant k,

$$k = (1/2)\sqrt{A_0}\,[R_0/R + r/R_0] \quad , \quad R_0 = \sqrt{L/C} \tag{B.3}$$

and the normalized frequency Ω,

$$\Omega = \omega\sqrt{LCA_0}. \tag{B.4}$$

Evaluating (B.1) we can now write

$$\widetilde{A}(\Omega) = A_0\left[\left(1-\Omega^2\right) + i\,2\Omega k\right]^{-1}. \tag{B.5}$$

The attenuation or amplitude transfer function $A(\Omega)$ is thus

$$A(\Omega) = |\widetilde{A}(\Omega)| = A_0\left[\left(1-\Omega^2\right)^2 + 4\Omega^2k^2\right]^{-1/2}. \tag{B.6}$$

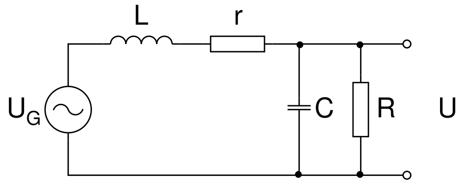

Figure B.1: Circuit of an inductive probe system with inductance L and lumped elements r, C and R.

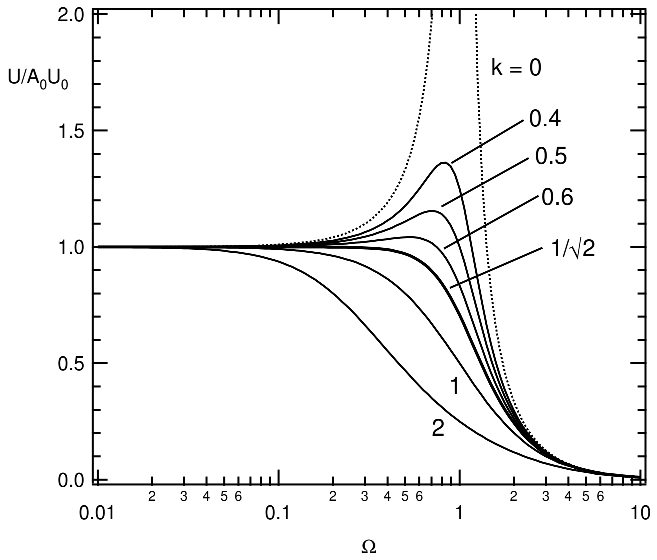

Figure B.2: Normalized amplitude transfer function $A(\Omega)/A_0 = U(\Omega)/A_0U_0$ for a steady sinusoidal input. The parameter k is the damping constant as defined in (B.3).

and depicted in figure B.2. From equation (B.6) it follows that the amplitude transfer function has a resonance at

$$\Omega = \Omega^* = \sqrt{1 - 2k^2} \tag{B.7}$$

provided that $k < 1/\sqrt{2}$ or $R > R_0(2 - r^2/R_0^2)^{-1/2}$. With R decreasing to the latter value or k increasing to $1/\sqrt{2}$, the resonance frequency approaches zero, the resonance step-up is damped out. The maximum resonance frequency is given by

$$\omega^*_{\mathrm{max}} = 1/\sqrt{LC} \tag{B.8}$$

and can be reached for $k \to 0$, i.e. for large R and small r.

According to (B.5) the phase shift φ is given by

$$\varphi = -\arctan\frac{2\Omega k}{1 - \Omega^2}. \tag{B.9}$$

It is impossible to have $\varphi \approx 0$ for $k > 0$, but for $k = 1/\sqrt{2}$ the ratio φ/ω is nearly constant for frequencies not higher than $1/\sqrt{LCA_0}$ as can be seen from figure B.3.

With respect to the amplitude the response of the circuit can be considered as satisfactory (for any k) for frequencies much smaller than the resonance frequency, i.e. $\Omega \ll \Omega^*$. However, the optimum damping constant is $k \approx 1/\sqrt{2}$ because the amplitude transfer function is the flattest for this value (figure B.2).

Time Domain

In order to discuss the response of the system in the time domain, we will analyze the corresponding differential equation, which is for our case a linear differential equation of the second order with constant coefficients for the output voltage $U(t)$

$$LC\,\ddot{U}(t) + \left(\frac{L}{R} + rC\right)\dot{U}(t) + \left(1 + \frac{r}{R}\right)U(t) = U_{\mathrm{G}}(t) \tag{B.10}$$

where $U_{\mathrm{G}}(t)$ represents again the induced input voltage in the coil.

Before evaluating this equation in detail, it is interesting to investigate the two possible extreme cases, if the capacitance can be neglected, i.e. $C = 0$. The two cases are:

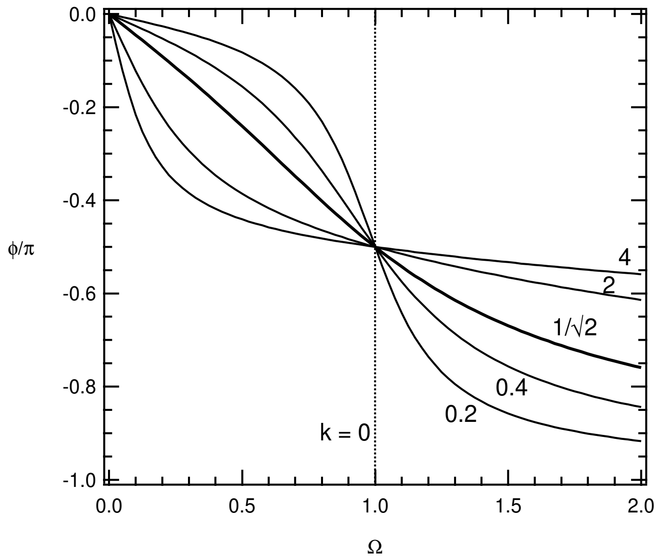

Figure B.3: Phase shift $\varphi(\Omega)$ for a steady sinusoidal input. The parameter k is the damping constant as defined in (B.3).

1. "Low frequencies" or $\omega L \ll R + r$ or $(L/R)\,\dot{U} \ll A_0 U$
   Here the solution is $U(t) \approx A_0 U_{\mathrm{G}}(t)$. Hence the output signal is proportional to the derivative of the flux enclosed in the coil. The above condition will break down if U crosses zero but $\dot{U}$ remains finite. However, errors are still negligible in most cases.

2. "High frequencies" or $\omega L \gg R + r$ or $(L/R)\,\dot{U} \gg A_0 U$
   Now we have $\dot{U}(t) \approx (R/L)\,U_{\mathrm{G}}(t)$. In this case the output signal is proportional to the flux enclosed in the coil. Another effect is that the coil behaves diamagnetically and may disturb the original field pattern.

Now let us introduce another dimensionless quantity, namely the normalized time τ,

$$\tau = t/\tau_{\mathrm{p}} \quad , \quad \tau_{\mathrm{p}} = 2\pi\sqrt{LCA_0}. \tag{B.11}$$

Rewriting (B.10), we obtain the new differential equation in $U(\tau)$

$$\ddot{U}(\tau) + 2(2\pi)k\,\dot{U}(\tau) + (2\pi)^2 U(\tau) = (2\pi)^2 A_0\, U_{\mathrm{G}}(\tau), \tag{B.12}$$

which shall be solved for a step-function $U_{\mathrm{G}}(\tau)$ as input:

$$U_{\mathrm{G}}(\tau) = \begin{cases} 0 & \text{for} \quad \tau \le 0 \\ U_0 & \text{for} \quad \tau > 0 \end{cases} \tag{B.13}$$

We can solve (B.12) by assuming a solution of the form $U(\tau) = U_0\, \mathrm{e}^{p\tau}$. The characteristic equation is then $p_{1/2}/(2\pi) = -k \pm \sqrt{k^2 - 1}$ from which the complete solution can be calculated. The behaviour of the solution depends on k and three cases may occur: $k < 1$ (underdamped, damped oscillatory circuit), $k = 1$ (critically damped) and $k > 1$ (overdamped, aperiodic). The result is

$$U(\tau) = \begin{cases} A_0 U_0 \left[1 - \omega_0 \omega^{-1} \mathrm{e}^{-\delta\tau} \sin(\omega\tau + \arctan(\omega/\delta))\right] & \text{for} \quad k < 1 \quad \text{(underdamped)} \\ A_0 U_0 \left[1 - (1 + \omega_0 \tau) \mathrm{e}^{-\omega_0 \tau}\right] & \text{for} \quad k = 1 \quad \text{(critically damped)} \\ A_0 U_0 \left[1 - \omega_0 \omega^{-1} \mathrm{e}^{-\delta\tau} \sinh(\omega\tau + \tanh^{-1}(\omega/\delta))\right] & \text{for} \quad k > 1 \quad \text{(overdamped)} \end{cases} \tag{B.14}$$

where $\omega_0 = 2\pi$, $\delta = 2\pi k$ and $\omega = \sqrt{|\delta^2 - \omega_0^2|}$ and is shown in figure B.4.

A rise time t_{r} can be defined as the time interval in which the output rises from 0.1 to 0.9 of the final value. For the critically damped case we get from (B.12) $t_{\mathrm{r}} = 0.53\tau_{\mathrm{p}} = 3.35\sqrt{LCA_0}$.

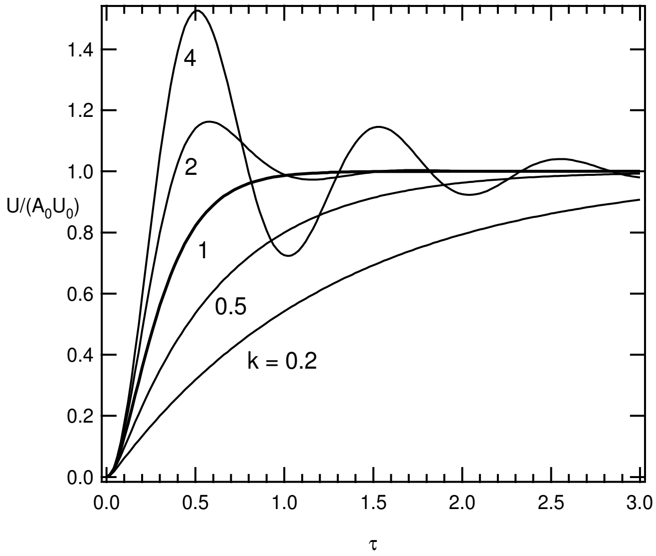

Figure B.4: Response $U(\tau)$ of the probe circuit of figure 1.9 to a step input of amplitude U_0. The parameter k is the damping constant as defined in (B.3).

Thus we can conclude that a reasonable response (both with respect to the reduction of the amplitude and the deformation of the pulse shape) can be expected only for $k \approx 1$ and only if τ_p is (much) smaller than the length of the input pulse.

The results of the previous subsections can be summarized as follows: The best response, with respect to frequency and time behaviour is obtained for a damping constant $k \approx (1/\sqrt{2} \ldots 1)$. This parameter can be tuned easily by variation of the resistances r or R.

Appendix C

Atomic Configurations and Related Properties

Table C.1: Electron configurations, atomic quantum numbers, ground terms, Landé g-values, effective moments (predicted free ion magnetic moments $g_J\sqrt{J(J+1)}\,\mu_B$ according to Hund's rules) and saturation moments $g_J J \mu_B$

Ion	Configuration	S	L	J	Russell-Saunders ground term	g_J	$g_J\sqrt{J(J+1)}$	$g_J J$
(a) Iron group, $3d$; doubly ionized								
Mn^{2+}	$3\mathrm{d}^5$	5/2	0	5/2	$^6\mathrm{S}_{5/2}$	2	5.92	5.0
Fe^{2+}	$3\mathrm{d}^6$	2	2	4	$^5\mathrm{D}_4$	3/2	6.71	6.0
Co^{2+}	$3\mathrm{d}^7$	3/2	3	9/2	$^4\mathrm{F}_{9/2}$	4/3	6.63	6.0
(b) Palladium group, $4d$; triply ionized								
Y^{3+}	–	0	0	0	$^1\mathrm{S}_0$	0	0	0
(c) Rare-earth series, $4f$; triply ionized								
La^{3+}	$5\mathrm{s}^2 5\mathrm{p}^6$	0	0	0	$^1\mathrm{S}_0$	0	0	0
Ce^{3+}	$4\mathrm{f}^1 5\mathrm{s}^2 5\mathrm{p}^6$	1/2	3	5/2	$^2\mathrm{F}_{5/2}$	6/7	2.54	2.14
Pr^{3+}	$4\mathrm{f}^2\ \ldots$	1	5	4	$^3\mathrm{H}_4$	4/5	3.58	3.2
Nd^{3+}	$4\mathrm{f}^3$	3/2	6	9/2	$^4\mathrm{I}_{9/2}$	8/11	3.62	3.27
Pm^{3+}	$4\mathrm{f}^4$	2	6	4	$^5\mathrm{I}_4$	3/5	2.68	2.4
Sm^{3+}	$4\mathrm{f}^5$	5/2	5	5/2	$^6\mathrm{H}_{5/2}$	2/7	0.85	0.71
Eu^{3+}	$4\mathrm{f}^6$	3	3	0	$^7\mathrm{F}_0$	0	0	0
Gd^{3+}	$4\mathrm{f}^7$	7/2	0	7/2	$^8\mathrm{S}_{7/2}$	2	7.94	7.0
Tb^{3+}	$4\mathrm{f}^8$	3	3	6	$^7\mathrm{F}_6$	3/2	9.72	9.0
Dy^{3+}	$4\mathrm{f}^9$	5/2	5	15/2	$^6\mathrm{H}_{15/2}$	4/3	10.65	10.0
Ho^{3+}	$4\mathrm{f}^{10}$	2	6	8	$^5\mathrm{I}_8$	5/4	10.60	10.0
Er^{3+}	$4\mathrm{f}^{11}$	3/2	6	15/2	$^4\mathrm{I}_{15/2}$	6/5	9.58	9.0
Tm^{3+}	$4\mathrm{f}^{12}$	1	5	6	$^3\mathrm{H}_6$	7/6	7.56	7.0
Yb^{3+}	$4\mathrm{f}^{13}$	1/2	3	7/2	$^2\mathrm{F}_{7/2}$	8/7	4.54	4.0
Lu^{3+}	$4\mathrm{f}^{14}$	0	0	0	$^1\mathrm{S}_0$	0	0	0

Bibliography

[AAB94] R.R. Andronenko, S.I. Andronenko, and A.N. Bazhan. Crystal field and magnetic properties of Pr^{3+} in $PrVO_4$. *Fiz. twerd. tela*, **36**:2396–2401 (in Russian), 1994.

[AK72] S.A. Al'tshuler and B.M. Kozyrev. *Electronii Paramagnitnii Rezonans Soyedinenii Elementov Promezhutochnikh Grupp.* Nauka, Moscow, 1972.

[Aku36] N. Akulov. *Z. Phys.*, **100**:197, 1936.

[Ama93] K. Amaya. In *Recent Advances in Magnetism of Transition Metal Compounds*, page 327. World Scientific, Singapore, 1993.

[AMT96] L.K. Aminov, B.Z. Malkin, and M.A. Teplov. In K.A. Gschneidner, Jr. and L. Eyring, editors, *Handbook of Physics and Chemistry of Rare Earths*, volume 22, pages 295–506. Elsevier Science Publishers B.V., 1996.

[ATN$^+$89] K. Amaya, S. Takeyama, T. Nakagawa, M. Ishizuka, K. Nakao, T. Sakakibara, T. Goto, N. Miura, Y. Ajiro, and H. Kikuchi. Magnetization measurements in very high pulsed fields produced by a single-turn coil system. *Physica B*, **155**:396–399, 1989.

[Bar99] M. Barczewski. *The Single-Turn Coil Technique: Installation and Application to IR Magnetospectroscopy on HgSe:Fe Layer Structures.* Dissertation, Humboldt-Universität zu Berlin, May 1999.

[BBB99] J.H.V.J. Brabers, K.H.J. Buschow, and F.R. de Boer. Field-induced first-order antiferromagnetic-ferromagnetic transitions in RMn_2Ge_2 compounds and their relation to the magnetostriction of the Mn sublattice. *Phys. Rev. B*, **59**(14):9314–9323, 1999.

[BBD$^+$] B.A. Boyko, A.I. Bykov, M.I. Dolotenko, N.P. Kolokol'chikov, I.M. Markevtsev, O.M. Tatsenko, and A.M. Shuvalov. Generation of magnetic fields above 2000 T with the cascade magnetocumulative generator MC-1. In H.-J. Schneider-Muntau, editor, *Proc. 8th Int. Conf. Megagauss Magnetic Field Generation and Related Topics*, pages 18–23, Tallahassee, FL, October 1998. World Scientific, Singapore.

[BBG64] G. Bardotti, B. Bertotti, and L. Gianolio. Magnetic Configuration of a Cylinder with Infinite Conductivity. *J. Math. Phys.*, **5**(10):1387–1390, 1964.

[BDK$^+$01] A.I. Bykov, M.I. Dolotenko, N.P. Kolokolchikov, V.D. Selemir, and O.M. Tatsenko. VNIIEF achievements on ultra-high magnetic fields generation. *Physica B*, **294–295**:574–578, 2001.

[BGH$^+$88] B. Bleaney, J.F. Gregg, C.H.A. Huan, M. Lazzouni, M.J.M. Leask, I.D. Morris, and M.R. Wells. *Proc. Roy. Soc. London*, **63**:416, 1988.

[BGV88] B. Barbara, D. Gignoux, and C. Vettier. *Lectures on Modern Magnetism.* Springer-Verlag, Berlin Heidelberg New York, 1988.

[BHR+78] B. Bleaney, R.T. Harley, J.F. Ryan, M.R. Wells, and M.C.K. Wiltshire. Energy levels in $PrVO_4$. *J. Phys. C: Sol. St. Phys.*, **11**:3059–3069, 1978.

[Ble88] B. Bleaney. Magnetic resonance spectroscopy and hyperfine interactions. In K.A. Gschneidner, Jr. and L. Eyring, editors, *Handbook of Physics and Chemistry of Rare Earths*, volume 11, chapter 2, pages 323–407. Elsevier Science Publishers B.V., 1988.

[BPKK91] H. Bischoff, B. Pilawa, A. Kasten, and H.G. Kahle. Crystal-field spectra of trivalent holmium in $HoVO_4$, $HoAsO_4$, $HoPO_4$ and $Y(OH)_3$ in the infrared region. *J. Phys.: Condens. Matter*, **3**:10057–10064, 1991.

[BPW83] B. Bleaney, J.H.T. Pasman, and M.R. Wells. Nuclear magnetic resonance of ^{169}Tm (enhanced) and ^{31}P in $TmPO_4$. *Proc. Roy. Soc. London*, **A 387**:75–90, 1983.

[Bra34] W. Braunbek. Die Erzeugung weitgehend homogener Magnetfelder durch Kreisströme. *Zeitschr. f. Phys.*, **88**:399–402, 1934.

[BS65] Z. Ban and M. Sikirica. The crystal structure of ternary silicides ThM_2Ge_2 (M = Cr, Mn, Fe, Co, Ni and Cu). *Acta Cryst.*, **18**:594–599, 1965.

[Bus88] K.H.J. Buschow. In E.P. Wohlfarth and K.H.J. Buschow, editors, *Ferromagnetic Materials*, volume 4, chapter 1. North Holland, Amsterdam, 1988.

[Cam72] I.A. Campbell. Indirect exchange for rare earths in metals. *J. Phys. F: Met. Phys.*, **2**:L47–L50, 1972.

[CC66] H.B. Callen and E. Callen. The present status of the temperature dependence of magnetocrystalline anisotropy, and the $l(l+1)/2$ power law. *J. Phys. Chem. Solids*, **27**:1271–1285, 1966.

[DAE+02] E. Duman, M. Acet, Y. Elerman, A. Elmali, and E.F. Wassermann. Magnetic interactions in $Pr_{1-x}Tb_xMn_2Ge_2$. *J. Magn. Magn. Mater.*, **238**:11–21, 2002.

[Ede72] F.X. Eder. *Moderne Messmethoden der Physik*, volume 3. VEB Deutscher Verlag der Wissenschaften, Berlin, 1972.

[EGD+01] D. Eckert, R. Grössinger, M. Doerr, F. Fischer, A. Handstein, D. Hinz, H. Siegel, P. Verges, and K.-H. Müller. High precision pick-up coils for pulsed field magnetization measurements. *Physica B*, **294–295**:705–708, 2001.

[FF01] T. Fujiwara and H. Fujii. Unconventional magnetic and transport properties in $Gd_{1-x}La_xMn_2Ge_2$ with two-dimensional arrangement of Mn atoms. *Physica B*, **300**:198–214, 2001.

[FIO+86] H. Fujii, M. Isoda, T. Okamoto, T. Shigeoka, and N. Iwata. Antiferromagnetic to ferromagnetic transition in $Y_{1-x}La_xMn_2Ge_2$. *J. Magn. Magn. Mater.*, **54-57**:1345–1346, 1986.

[FM67] D.W. Forster and C.J. Martin. 2.5 Megagauss from a Capacitor Discharge. In R. Pauthenet, editor, *Proc. Int. Conf. Les Champs Magnétiques Intenses, leur Production et leurs Applications, Grenoble, France, September 1966*, pages 361–370, 1967.

[FZ69] L.A. Ferrari and M.S. Zucker. Transient Response of Magnetic Probes. *Rev. Sci. Instrum.*, **40**(7):925–926, 1969.

[GAC87] M.-D. Guo, A.T. Aldred, and S.-K. Chan. Magnetic susceptibility and crystal field effects of rare-earth orthovanadate compounds. *J. Phys. Chem. Solids*, **48**(3):229–235, 1987.

[GCFT68] W.B. Garn, R.S. Caird, C.M. Fowler, and D.B. Thomson. Measurement of Faraday Rotation in Megagauss Fields over the Continuous Visible Spectrum. *Rev. Sci. Instrum.*, **39**:1313–1317, 1968.

[GEK+01] G. Guanghua, M.V. Eremin, A. Kirste, N.P. Kolmakova, A.S. Lagutin, R.Z. Levitin, M. von Ortenberg, and A.A. Sidorenko. Magnetic phase transitions and phase diagrams of $DyMn_2Ge_2$. *J. Exp. Theor. Phys.*, **93**(4):796–804, 2001.

[GEK+02] G. Guanghua, M.V. Eremin, N.P. Kolmakova, A.S. Lagutin, and R.Z. Levitin. Magnetic properties of the $HoMn_2Ge_2$ intermetallic compound. *Phys. Solid State*, **44**(11):2091–2094, 2002.

[GES+95] R. Grössinger, D. Eckert, E.H.C.P. Sinnecker, M. Taraba, and G.W. Jewell. An accurate pulsed field hystersograph. *Physica B*, **211**:348–350, 1995.

[GG75] G.A. Gehring and K.A. Gehring. Co-operative Jahn-Teller effects. *Rep. Prog. Phys.*, **38**:1–89, 1975.

[GLS+00a] G. Guanghua, R.Z. Levitin, V.V. Snegirev, D.A. Filipov, and A.Y. Sokolov. Magnetic Phase Diagram of the Intermetallic Compounds $Gd_{1-x}La_xMn_2Ge_2$ and the Effect of a Field on Transitions of the Mn Subsystem from the Antiferromagnetic into the Ferromagnetic State. *J. Exp. Theor. Phys.*, **90**(6):979–986, 2000.

[GLS+00b] G. Guanghua, R.Z. Levitin, A.Y. Sokolov, V.V. Snegirev, and D.A. Filipov. Study of ferrimagnets with negative interaction within one of the sublattices: magnetic phase diagram of the $Gd_{1-x}La_xMn_2Ge_2$ intermetallic compounds. *J. Magn. Magn. Mater.*, **214**:301–308, 2000.

[Gro98] C.H. de Groot. *Rare-Earth Intermetallics, from magnetic interactions to permanent magnets.* Dissertation, University of Amsterdam, June 1998.

[Gua99] G. Guanghua. *Investigation of spontaneous and induced domains of magnetic phase transitions in the intermetallic compounds RMn_2Ge_2 (in Russian).* Dissertation, Moscow State University, Russia, 1999.

[Her98] F. Herlach. Magnets for the 21st century. *Physica B*, **246–247**:152–157, 1998.

[Her99] F. Herlach. Pulsed Magnets. *Rep. Prog. Phys.*, **62**:859–920, 1999.

[Her01] F. Herlach. Innovations and trends in magnet laboratories and techniques. *Physica B*, **294–295**:500–504, 2001.

[Hut64] M.T. Hutchings. Point-charge calculations of energy levels of magnetic ions in crystalline electric fields. *Solid State Phys.*, **16**:227–273, 1964.

[IHS86] N. Iwata, K. Hattori, and T. Shigeoka. Exchange interaction and magnetocrystalline anisotropy in $GdMn_2Ge_2$. *J. Magn. Magn. Mater.*, **53**:318–322, 1986.

[JFO+04] Harry Jones, Paul H. Frings, Michael von Ortenberg, Alex Lagutin, Luc Van Bockstal, Oliver Portugall, and Fritz Herlach. First experiments in fields above 75 T in the European coilin-coilex magnet. *Physica B*, **346–347**:553–560, 2004.

[JM91] J. Jensen and A.R. Mackintosh. *Rare Earth Magnetism.* Clarendon Press, Oxford, 1991.

[Kap31] P. Kapitza. *Proc. Roy. Soc. London*, **A131**:224–321, 1931.

[Kaz01] Z.A. Kazei. Private communications, 2001. Moscow State University, Moscow, Russia.

[Kin01] K. Kindo. 100 T magnet developed in Osaka. *Physica B*, **294–295**:585–590, 2001.

[Kir01] A. Kirste. Magnetization of magnetic materials in pulsed fields with different techniques. Report on exchange programme, Second annual meeting of the High Field Infrastructure Cooperative Network, Sept. 2001, Nijmegen, The Netherlands, 2001.

[KKH$^+$04] A. Kirste, N.P. Kolmakova, S. Hansel, H.-U. Mueller, and M. von Ortenberg. Rare-earth zircons and intermetallic compounds in megagauss-fields: investigation of new magnetic phenomena. *Physica B*, **346–347**:191–195, 2004.

[KKK$^+$01] Z.A. Kazei, A. Kirste, N.P. Kolmakova, M. von Ortenberg, V.V. Platonov, N. Puhlmann, A.A. Sidorenko, I. Stolpe, and O.M. Tatsenko. Peculiarities of energy level crossing effects in a singlet paramagnet $PrVO_4$. *J. Magn. Magn. Mater.*, **224**:76–84, 2001.

[KKKSS87] A. Kasten, H.G. Kahle, P. Klöfer, and D. Schäfer-Siebert. Specific heat experiments at the cooperative Jahn-Teller transition in the mixed crystal systems $(Tb_xTm_{1-x})AsO_4$ and $(Tb_xTm_{1-x})VO_4$. *Phys. Stat. Sol. B*, **144**:423–436, 1987.

[KKP$^+$97] Z.A. Kazei, N.P. Kolmakova, V.V. Platonov, O.A. Shishkina, and O.M. Tatsenko. In *Abstracts of Third Int. Conf. on f-Elements, Paris, France, September 1997*, page 396, 1997.

[KKP$^+$00] Z.A. Kazei, N.P. Kolmakova, V.V. Platonov, A.A. Sidorenko, and O.M. Tatsenko. Cooling in rare-earth paramagnets at ultrahigh pulsed magnetic fields due to energy level crossing. *Physica B*, **284–288**:1483–1484, 2000.

[KKS98] Z.A. Kazei, N.P. Kolmakova, and O.A. Shishkina. Magnetoelastic contribution to thermal expansion of rare-earth zircons. *Physica B*, **245**:164–172, 1998.

[KLO$^+$01] A. Kirste, R.Z. Levitin, M. von Ortenberg, V.V. Platonov, N. Puhlmann, V.V. Snegirev, D.A. Filippov, and O.M. Tatsenko. Induced magnetic phase transitions in rare-earth intermetallic compounds RMn_2Ge_2 in ultrastrong magnetic fields. *Phys. Solid State*, **43**(9):1731–1734, 2001.

[KMAW01] T. Kiyoshi, S. Matsumoto, T. Asano, and H. Wada. Recent advances in high-field magnets at TML. *Physica B*, **294–295**:535–540, 2001.

[Kno70] H. Knoepfel. *Pulsed High Magnetic Fields.* North-Holland Publishing Company, Amsterdam, London, 1970.

[Kno00] H. Knoepfel. *Magnetic Fields: A Comprehensive Theoretical Treatise for Practical Use.* John Wiley & Sons, Inc., New York, 2000.

[KOD$^+$03] A. Kirste, M. von Ortenberg, A.A. Demidov, Z.A. Kazei, N.P. Kolmakova, V.V. Platonov, A.A. Sidorenko, and O.M. Tatsenko. Crossover in the van vleck paramagnet $TmPO_4$. *Physica B*, **336**:335–343, 2003.

[KOO$^+$95] H. Kobayashi, M. Ohashi, H. Onodera, T. Ono, and Y. Yamaguchi. Magnetic phase transitions in $GdMn_2Ge_2$ studied by neutron diffraction. *J. Magn. Magn. Mater.*, **140-144**:905–906, 1995.

[KOY89] H. Kobayashi, H. Onodera, and H. Yamamoto. Magnetic properties of single crystal $GdMn_2Ge_2$ in high magnetic field. *J. Magn. Magn. Mater.*, **79**:76–80, 1989.

[KOYY91] H. Kobayashi, H. Onodera, Y. Yamaguchi, and H. Yamamoto. Magnetization and neutron-diffraction studies of single-crystal $DyMn_2Ge_2$. *Phys. Rev. B*, **43**(1):728–734, 1991.

[KP94] Z.A. Kazei and Y.F. Popov. *Fiz. tverd. tela (in Russian)*, **36**:2099, 1994.

[LD75] P.A. Lindgård and O. Danielsen. Theory of magnetic properties of heavy rare-earth metals: Temperature dependence of magnetization, anisotropy, and resonance energy. *Phys. Rev. B*, **11**:351–362, 1975.

[Lév00] L.-P. Lévy. *Magnetism and Superconductivity.* Springer, 2000.

[LLVB02] A.S. Lagutin, R.Z. Levitin, J. Vanacken, and Y. Bruynseraede. Field-induced transitions of the intermetallic compound $DyMn_2Ge_2$. *J. Magn. Magn. Mater.*, **241**:190–195, 2002.

[LSA+93] C.-K. Loong, L. Soderholm, M.M. Abraham, L.A. Boatner, and N.M. Edelstein. Crystal-field excitations and magnetic properties of $TmPO_4$. *J. Chem. Phys.*, **98**:4214–4222, 1993.

[LSBS90] J. Leciewicz, A. Szytuła, W. Baźela, and S. Siek. Neutron-diffraction investigation of long range magnetic order in $CeMn_2Ge_2$, $HoMn_2Si_2$ and $HoMn_2Ge_2$. *J. Magn. Magn. Mater.*, **98**:29–32, 1990.

[LSK+97] R.Z. Levitin, V.V. Snegirev, A.V. Kopylov, A.S. Lagutin, and A. Gerber. Magnetic method of magnetocaloric effect determination in high pulsed magnetic fields. *J. Magn. Magn. Mater.*, **170**:223–227, 1997.

[LVHH95] A.S. Lagutin, J. Vanacken, N. Harrison, and F. Herlach. A probe for magnetization measurements of thin superconducting films in pulsed high magnetic fields. *Rev. Sci. Instr.*, **66**(8):4267–4270, 1995.

[Max] Maxwell Laboratories, Inc., San Diego, California, USA. *Series C High Energy Capacitor Application Guide.*

[Max86] Maxwell Laboratories, Inc., San Diego, California, USA. *Instructions for Using the Model 40151-B 100 kV Multiple Trigger Generator*, March 1986.

[Max89] Maxwell Laboratories, Inc., San Diego, California, USA. *Instructions for Using the Model 40200 Rail-Gap Switch*, June 1989.

[MH85] N. Miura and F. Herlach. Pulsed and ultrastrong magnetic fields. In F. Herlach, editor, *Strong and Ultrastrong Magnetic Fields and Their Applications*, volume 57 of *Topics in Applied Physics*, pages 247–359. Springer-Verlag, Berlin, Heidelberg, 1985.

[MK97] P. Morin and Z. Kazei. Stimulated cooperative Jahn-Teller effect in $TmPO_4$. *Phys. Rev. B*, **55**:8887–8893, 1997.

[MMD80] H. Mollymoto, M. Motokawa, and M. Date. High Field Transverse Magnetization of Ising Antiferromagnet $CoCl_2{\cdot}H_2O$. *J. Phys. Soc. Japan*, **49**(1):108–114, 1980.

[MMU+01] N. Miura, Y.H. Matsuda, K. Uchida, S. Todo, T. Goto, H. Mitamura, T. Osada, and E. Ohmichi. New Megagauss Laboratory of ISSP at Kashiwa. *Physica B*, **294–295**:562–567, 2001.

[MPP+98] A.A. Mukhin, V. Platonov, V.I. Plis, A.I. Popov, O.M. Tatsenko, and A.K. Zvezdin. Spin-flip transition and Faraday effect in antiferromagnet $KMnF_3$ in megagauss magnetic field. *Physica B*, **246–247**:195–199, 1998.

[MRK95] P. Morin, J. Rouchy, and Z. Kazei. Magnetoelastic properties and level crossing in $HoVO_4$. *Phys. Rev. B*, **51**(21):15103–15112, 1995.

[MRK96] P. Morin, J. Rouchy, and Z. Kazei. Magnetic and magnetoelastic properties of $TmPO_4$. *J. Phys.: Condens. Matter*, **8**:7967–7980, 1996.

[MRS85] M. Motokawa, L.W. Roeland, and C.J. Schinkel. High-field magnetism. In F. Herlach, editor, *Strong and Ultrastrong Magnetic Fields and Their Applications*, volume 57 of *Topics in Applied Physics*, pages 113–142. Springer-Verlag, Berlin, Heidelberg, 1985.

[MSP+98] H.-U. Müller, H. Scholz, N. Puhlmann, O. Portugall, M. Barczewski, I. Stolpe, and M. von Ortenberg. High sensitivity data acqusition during strong transient electromagnetic fields. *Physica B*, **246–247**:356–359, 1998.

[Mül02] H.-U. Müller. Private communications, 2002. Institut für Physik, Humboldt-Universität zu Berlin.

[NHG+85] K. Nakao, F. Herlach, T. Goto, S. Takeyama, T. Sakakibara, and N. Miura. A laboratory instrument for generating magnetic fields over 200 T with single turn coils. *J. Phys. E: Sci. Instrum.*, **18**:1018–1026, 1985.

[Noj03] H. Nojiri. Private communications, 2003. Department of Physics, Okayama University, Okayama, Japan.

[NRBW75] K.S.V.L. Narasimhan, V.U.S. Rao, R.L. Bergner, and W.E. Wallace. Magnetic properties of $R\text{Mn}_2\text{Ge}_2$ compounds (R = La, Ce, Pr, Nd, Cd, Tb, Dy, Ho, Er, and Th). *J. Appl. Phys.*, **46**(11):4957–4960, 1975.

[OPS+01] M. von Ortenberg, N. Puhlmann, I. Stolpe, H.-U. Mueller, A. Kirste, and O. Portugall. The Humboldt high magnetic field center at Berlin. *Physica B*, **294–295**:568–573, 2001.

[PPM+98] O. Portugall, N. Puhlmann, H.-U. Müller, M. Barczewski, I. Stolpe, and M. von Ortenberg. The generation and application of megagauss fields at the Humboldt High Magnetic Field Center. *Physica B*, **246–247**:54–60, 1998.

[PPM+99] O. Portugall, N. Puhlmann, H.-U. Müller, M. Barczewski, I. Stolpe, and M. von Ortenberg. Megagauss magnetic field generation in single-turn coils: new frontiers for scientific experiments. *J. Phys. D: Appl. Phys.*, **32**:2354–2366, 1999.

[SA60] S.E. Segre and J.E. Allen. Magnetic probes of high frequency response. *J. Sci. Instrum.*, **37**:369–371, 1960.

[Sch91] A.J. Schwab. *Elektromagnetische Verträglichkeit.* Springer, Berlin Heidelberg New York, 1991.

[SFF+83] T. Shigeoka, H. Fujii, H. Fujiwara, K. Yagasaki, and T. Okamoto. Magnetic properties of RMn_2Ge_2 single crystal compounds (R = heavy rare earth). *J. Magn. Magn. Mater.*, **31–34**:209–210, 1983.

[SGG+99] A.Y. Sokolov, G. Guanghua, S.A. Granovskii, R.Z. Levitin, H. Wada, M. Shiga, and T. Goto. Spontaneous and field-induced magnetic phase transitions in the intermetallic compounds $(\text{Gd}_{1-x}\text{Y}_x)\text{Mn}_2\text{Ge}_2$. *J. Exp. Theor. Phys.*, **89**(4):723–733, 1999.

[Shi84] T. Shigeoka. *J. Sci. Hiroshima Univ. A*, **48**(2):103, 1984.

[SHO80] H. Suzuki, Y. Higashino, and T. Ohtsuka. *J. Low Temp. Physics*, **41**:449, 1980.

[Sid02] A.A. Sidorenko. Private communications, 2002. Bryansk State Technical University, Bryansk, Russia.

[SIO81] H. Suzuki, T. Inoue, and T. Ohtsuka. Enhanced nuclear cooling and spin-lattice relaxation time in TmVO_4 and TmPO_4. *Physica B*, **107**:563–564, 1981.

[SL89] A. Szytuła and J. Leciewicz. Magnetic properties of ternary intermetallic compounds of the RT_2X_2 type. In K.A. Gschneidner, Jr. and L. Eyring, editors, *Handbook on the Physics and Chemistry of Rare Earths*, volume 12, pages 133–211. Elsevier Science Publishers, 1989.

[Smy50] W.R. Smythe. *Static and Dynamic Electricity.* McGraw-Hill, New York, 1950.

[SS82] A. Szytuła and S. Siek. Magnetic properties of the $Ce_{1-x}La_xMn_2Si_2$ system. *J. Magn. Magn. Mater.*, **27**(1):49–54, 1982.

[Ste52] K.W.H. Stevens. Matrix elements and operator equivalents connected with the magnetic properties of rare earth ions. *Proc. Phys. Soc.*, **165**:209–215, 1952.

[Sto00] I. Stolpe. *IR-Spektroskopie in extrem hohen Magnetfeldern bis 700 T.* Dissertation, Humboldt-Universität zu Berlin, 2000.

[SWSG98] A. Sokolow, H. Wada, M. Shiga, and T. Goto. Multiple magnetic phase transitions of $Gd_{1-x}La_xMn_2Ge_2$. *Solid State Comm.*, **105**(5):289–292, 1998.

[Szy92] A. Szytuła. Magnetic phase transition in tetragonal rare earth intermetallics. *J. Alloys Compounds*, **178**:1–13, 1992.

[TAN+88] S. Takeyama, K. Amaya, T. Nakagawa, M. Ishizuka, K. Nakao, T. Sakakibara, T. Goto, N. Miura, Y. Ajiro, and H. Kikuchi. Magnetisation measurements in ultrahigh magnetic fields produced by a single-turn coil system. *J. Phys. E: Sci. Instrum.*, **21**:1025–1028, 1988.

[VMR96a] G. Venturini, B. Malaman, and E. Ressouche. Magnetic ordering in ternary $R\mathrm{Mn_2Ge_2}$ compounds (R = Tb, Ho, Er, Tm, Lu) from neutron diffraction study. *J. Alloys Comp.*, **240**:139–150, 1996.

[VMR96b] G. Venturini, B. Malaman, and E. Ressouche. The $x - T$ magnetic phase diagram of the $La_{1-x}Y_xMn_2Ge_2$ system by neutron diffraction study. *J. Alloys Comp.*, **241**:135–147, 1996.

[VMT+92] G. Venturini, B. Malaman, K. Tomala, A. Szytuła, and J.P. Sanchez. Magnetic properties of $DyMn_2Ge_2$ from Mössbauer and neutron diffraction studies. *Phys. Rev. B*, **46**(1):207–216, 1992.

[VRF90] R. Verhoef, R.J. Radwański, and J.J.M. Franse. Strength of the rare-earth–transition-metal exchange coupling in hard magnetic materials, an experimental approach based on high-field magnetisation measurements: application to $Er_2Fe_{14}B$. *J. Magn. Magn. Mater.*, **89**:176–184, 1990.

[VWRM94] G. Venturini, R. Welter, E. Ressouche, and B. Malaman. Neutron diffraction studies of $LaMn_2Ge_2Si_2$ and $LaMn_2Si_2$ compounds: evidence of dominant antiferromagnetic components within the Mn planes. *J. Alloys Comp.*, **210**:213–220, 1994.

[VWRM95a] G. Venturini, R. Welter, E. Ressouche, and B. Malaman. Neutron diffraction study of $Nd_{0.35}La_{0.65}Mn_2Si_2$: A $SmMn_2Ge_2$-like magnetic behaviour compound. *J. Magn. Magn. Mater.*, **150**:197–212, 1995.

[VWRM95b] G. Venturini, R. Welter, E. Ressouche, and B. Malaman. Neutron diffraction study of the ferromagnetic to antiferromagnetic transition in $La_{0.3}Y_{0.7}Mn_2Ge_2$: phenomenological description of the magnetic behaviour of Mn in $ThCr_2Si_2$ silicides and germanides. *J. Alloys Comp.*, **223**:101–110, 1995.

[WTHS00] H. Wada, Y. Tanabe, K. Hagiwara, and M. Shiga. Magnetic phase transition and magnetocaloric effect of $DyMn_2Ge_2$. *J. Magn. Magn. Mater.*, **218**:203–210, 2000.

[Wyc65] R.W.G Wyckoff. *Crystal Structures*, volume 3. Interscience, New York, 1965.

[WYS96] H. Wada, H. Yamaguchi, and M. Shiga. Calorimetric study of RMn_2Ge_2 compounds ($R = La$, Gd, Tb and Dy). *J. Magn. Magn. Mater.*, **152**:165–173, 1996.

[YK52] Y. Yafet and C. Kittel. Antiferromagnetic Arrangements in Ferrites. *Phys. Rev.*, **87**:290–294, 1952.

[ZCBB93] Z.G. Zhao, P.F. de Chátel, F.R. de Boer, and K.H.J. Buschow. The free-powder magnetization of ferrimagnetic rare-earth transition-metal compounds. *J. Appl. Phys.*, **73**(10):6522–6524, 1993.

[ZLB$^+$93] Z.G. Zhao, X. Li, J.H.V.J. Brabers, P.F. de Chátel, F.R. de Boer, and K.H.J. Buschow. The free-powder magnetization of ferrimagnetic rare-earth–transition-metal compounds. *J. Magn. Magn. Mater.*, **123**:74–86, 1993.

[ZZCB97] Z. Zhang, T. Zhao, P.F. de Chátel, and F.R. de Boer. Spin configurations and magnetization processes in a free-sample two-sublattice system. *J. Magn. Magn. Mater.*, **174**:269–277, 1997.

[ZZXC92] Z. Zhang, T. Zhao, X.K.Sun, and Y.C. Chuang. Analysis of a magnetization processes based on a two-sublattice model. *J. Appl. Phys.*, **71**(7):3434–3438, 1992.

Acknowledgements

First of all, I would like to thank Prof. Dr. M. von Ortenberg, my research supervisor, for his exceptional personal engagement and permanent interest in the progress of this work, his patience and his profound physical insight. Furthermore I would like to thank all members of the ”Magnetotransport” group. In particular I am grateful to Dr. H.-U. Müller for help and fruitful discussions concerning problems in electronics and Dr. O. Portugall, Dr. N. Puhlmann and Dr. I. Stolpe for introducing me to the single-turn coil system.

I owe much thanks to our Russian colleagues: Dr. Z.A. Kazei, who provided most of the samples and theoretical advice; Prof. Dr. N.P. Kolmakova and Dr. A.A. Sidorenko, who helped me in many theoretical questions; Prof. Dr. O.M. Tatsenko and Dr. V. Platonov, who fostered and maintained this cooperation.

I am indebted to Dr. M. Goiran, Dr. H. Rakoto and Prof. Dr. J.M. Broto of the LNCMP Toulouse for their assistance and efforts in the course of all experiments performed together. During my stay at their laboratory I appreciated very much their hospitality.

I should also say a word of thanks to Prof. Dr. H. Nojiri and Prof. Dr. M. Motokawa for helpful discussions.

I am grateful to Dr. U. Preppernau and Mr. V. Misch for the reliable and uncomplicated supply of LHe as well as to Mr. J. Sölle for the preparation of the tiny samples. Finally I would like to thank all technicians who contributed to this work in various aspects. In particular I would like to mention Mr. T. Rausche, who is managing the mechanical workshop and Mrs. D. Fahnauer, who manufactured many of the ”small parts” necessary.

Publications

Stopping of slow ions in the electron selvedge of a metal surface,
H. Winter, C. Auth, A. Mertens, A. Kirste, M.J. Steiner,
Europhysics Letters **41** (1998) 437–442.

Magneto condensation and probing of nanostructures by high magnetic fields,
M. von Ortenberg, H. Wissmann, A. Kirste, O. Portugall, L. Parthier, K. Uchida, N. Miura, F. Heinrichsdorff, D. Bimberg,
Proc. of the 24th Int. Conf. on The Physics of Semiconductors 1998, Ed. D. Gershoni (World Scientific, Singapore, 1999) p. 83.

Self organized MBE growth of HgSe:Fe quantum wires on patterned GaSb substrates,
H. Wißmann, T. Tran-Anh, A. Kirste, O. Portugall, S. Rogaschewski, M. von Ortenberg,
Proc. of the 24th Int. Conf. on The Physics of Semiconductors 1998, Ed. D. Gershoni (World Scientific, Singapore, 1999) p. 7.

Self-organized MBE growth and characterization of conductive HgSe:Fe quantum wires,
H. Wißmann, T. Tran-Anh, S. Rogaschewski, A. Kirste, L. Parthier, P. Schäfer, M. von Ortenberg,
Narrow Gap Semiconductors, Proc. of the 9th Int. Conf., September 1999, Berlin Germany, Eds. N. Puhlmann, H.U. Müller M. von Ortenberg (Magnetotransport - Humboldt University at Berlin, 2000) p. 199.

Cyclotron Resonance at the L-point in GaAs in extreme magnetic fields,
N. Puhlmann, A. Kirste, I. Stolpe, M. von Ortenberg, O. Tatsenko, A. Bykov, V.D. Selemir, I.M. Markevtsev, V.V. Platonov,
Proc. of the 10th Int. Conf. on Narrow Gap Semiconductors and Related Small Energy Phenomena, Physics and Applications, May 2001, Ishikawa, Japan (IPAP Conf. Series 2, 2001, Tokyo) p.102.

Magnetic phase transitions and phase diagrams of $\mathbf{DyMn_2Ge_2}$,
G. Guanghua, M.V. Eremin, A. Kirste, N.P. Kolmakova, A.S. Lagutin, R.Z. Levitin, M. von Ortenberg, A.A. Sidorenko,
J. Exp. Theor. Phys. **93** (2001) 796–804.

Peculiarities of energy level crossing effects in a singlet paramagnet $\mathbf{PrVO_4}$,
Z.A. Kazei, A. Kirste, N.P. Kolmakova, M. von Ortenberg, V.V. Platonov, N. Puhlmann, A.A. Sidorenko, I. Stolpe, O.M. Tatsenko,
J. Magn. Magn. Mater. **224** (2001) 76–84.

Induced magnetic phase transitions in rare-earth intermetallic compounds $\mathbf{RMn_2Ge_2}$ in ultrastrong magnetic fields,
A. Kirste, R.Z. Levitin, M. von Ortenberg, V.V. Platonov, N. Puhlmann, V.V. Snegirev, D.A. Filippov, O.M. Tatsenko,
Phys. Solid State **43** (2001) 1731–1734.

The Humboldt high magnetic field center at Berlin,
M. von Ortenberg, N. Puhlmann, I. Stolpe, H.-U. Mueller, A. Kirste, O. Portugall,
Physica B **294–295** (2001) 568–573.

Energy level crossing effects in the rare-earth zircons $TmPO_4$ and $PrVO_4$,
A. Kirste, N. Puhlmann, I. Stolpe, H.U. Mueller, M. von Ortenberg, O.M. Tatsenko, V. Platonov, Z.A. Kazei, N.P. Kolmakova, A.A. Sidorenko,
Physica B **294–295** (2001) 132–135.

Spin dynamics in megagauss fields,
I. Stolpe, O. Portugall, N. Puhlmann, A. Kirste, H.U. Mueller, M. von Ortenberg, M. von Truchsess, A. Pfeuffer-Jeschke, C.R. Becker, G. Landwehr,
Physica B **298** (2001) 462–466.

Infrared magneto-spectroscopy at the L-point of GaAs,
M. von Ortenberg, A. Kirste, I. Stolpe, N. Puhlmann, O.M. Tatsenko, V.V. Platonov, N.A. Moisenko, I.M. Markevtsev,
Infrared and Millimeter Waves, Proc. of the 26th Int. Conf., September 2001, Toulouse, France, Eds. O. Portugall, J. Leotin, p. 4-39.

Megagauss-magneto-spectroscopy on II-VI compounds,
S. Hansel, I. Stolpe, A. Kirste, H.U. Mueller, M. von Ortenberg,
Infrared and Millimeter Waves, Proc. of the 26th Int. Conf., September 2001, Toulouse, France, Eds. O. Portugall, J. Leotin, p. 4-74.

Magnetic properties of quaternary $Zn_{1-x-y}Be_yMn_xSe$ system: The role of berylium,
P. Dziawa, F. Firszt, S. Legowski, A. Marasek, M. Meczynska, M. Arciszewska, W. Dobrowolski, E. Dynowska, W. Paszkowicz, J.M. Broto, O. Portugall, H. Rakoto, H. Raquet, A. Kirste, M. von Ortenberg,
Proc. of the XXXI Int. School on the Physics of Semiconducting Compounds, Jaszowiec, Poland, June 2002.

HgSe:Fe Quantum Dots in Megagauss Magnetic Fields,
T. Tran-Anh, S. Hansel, A. Kirste, H.U. Mueller, M. von Ortenberg, I.Barner, I.P. Rabe,
Megagauss-9, Proc. of the 9th Int. Conf. on Megagauss Magnetic Field Generation and Related Topics, Moscow - St. Petersburg, Russian Federation, July 2002, Eds. V.D. Selemir, L.N. Plyashkevich (VNIIEF, Sarov, 2004) p. 463.

High-Sensitivity Magnetization Measurements in Megagauss Fields,
A. Kirste, H.-U. Mueller, S. Hansel, M. von Ortenberg,
Megagauss-9, Proc. of the 9th Int. Conf. on Megagauss Magnetic Field Generation and Related Topics, Moscow - St. Petersburg, Russian Federation, July 2002, Eds. V.D. Selemir, L.N. Plyashkevich (VNIIEF, Sarov, 2004) p. 475.

High magnetic field study of charge-melting in $Bi_{1/2}(Sr,Ca)_{1/2}MnO_3$ perovskites: unconventional behaviour of Bi-Sr,
A. Kirste, M. Goiran, J. Vanacken, J.M. Broto, H. Rakoto, M. Respaud, M. von Ortenberg, C. Frontera, J.L. Garcia-Muñoz,
Megagauss-9, Proc. of the 9th Int. Conf. on Megagauss Magnetic Field Generation and Related Topics, Moscow - St. Petersburg, Russian Federation, July 2002, Eds. V.D. Selemir, L.N. Plyashkevich (VNIIEF, Sarov, 2004) p. 469.

Frontiers in Physics: Infrared Magnetospectroscopy on GaAs in Magnetic Fields up to 1000 Tesla,
M. von Ortenberg, N. Puhlmann, I. Stolpe, A. Kirste, H.-U. Mueller, S. Hansel, O.M. Tatsenko, I.M. Markevtsev, N.A. Moiseenko, V.V. Platonov, A.I. Bykov, V.D. Selemir,
Megagauss-9, Proc. of the 9th Int. Conf. on Megagauss Magnetic Field Generation and Related Topics, Moscow - St. Petersburg, Russian Federation, July 2002, Eds. V.D. Selemir, L.N. Plyashkevich (VNIIEF, Sarov, 2004) p. 454.

Infrared magnetospectroscopy at the L-Point in GaAs in Magnetic Fields up to 1000 T,
M. von Ortenberg, N. Puhlmann, I. Stolpe, A. Kirste, H.-U. Mueller, S. Hansel, O.M. Tatsenko, I.M. Markevtsev, N.A. Moisenko, V.V. Platonov, A.I. Bykov, V.D. Selemir
Physics of Semiconductors 2002, Proc. of the 26th Int. Conf. on the Physics of Semiconductors, July 2002, Edinburgh, United Kingdom, Eds. A.R. Long, J.H. Davies (IOP, Bristol, 2002) p. F1.2.

Growth and Characterization of HgSe:Fe Quantum Dots,
T. Tran-Anh, S. Hansel, A. Kirste, H.U. Mueller, M. von Ortenberg, T. Spangenberg, H. Niehus,
Physics of Semiconductors 2002, Proc. of the 26th Int. Conf. on the Physics of Semiconductors, July 2002, Edinburgh, United Kingdom, Eds. A.R. Long, J.H. Davies (IOP, Bristol, 2002), p. D161.

The influence of berylium on the magnetic properties of $\mathbf{Zn}_{1-x-y}\mathbf{Be}_y\mathbf{Mn}_x\mathbf{Se}$,
J.M. Broto, H. Rakoto, H. Raquet, O. Portugall, P. Dziawa, F. Firszt, S. Legowski, A. Marasek, M. Meczynska, M. Arciszewska, W. Dobrowolski, K. Racka, E. Dynowska, J. Kachniarz, W. Paszkowicz, A. Kirste, M. von Ortenberg,
Physics of Semiconductors 2002, Proc. of the 15th Int. Conf. on High Magnetic Fields in Semiconductor Physics, Oxford, United Kingdom, August 2002, Eds. A.R. Long, J.H. Davies (IOP, Bristol, 2002) p. C50.

The Effect of Quantum Dots on the Infrared Cyclotron Resonance in HgSe:Fe,
T. Tran-Anh, S. Hansel, A. Kirste, H.-U. Mueller, M. von Ortenberg,
27th Int. Conf. on Infrared and Millimetre Waves, September 2002, San Diego, CA, USA, Ed. R. Temkin (IEEE, 2002) p. 317.

Infrared Detection of Carrier Dynamics in Indiumantimonide in Megagauss Fields,
S. Hansel, A. Kirste, H.-U. Mueller, M. von Ortenberg,
27th Int. Conf. on Infrared and Millimetre Waves, September 2002, San Diego, CA, USA, Ed. R. Temkin (IEEE, 2002) p. 171.

Observation of infrared absorption in HgSe and HgTe in transient megagauss fields,
A. Kirste, S. Hansel, I. Stolpe, H.U. Müller, M. von Ortenberg,
Proc. of Solid Solutions of the II-VI Compounds – Growth, Characterization and Applications, Int. Symposium G, Zakopane, Poland, October 2002,
J. Alloys. Comp. **371** (2004) 133–137.

Growth and Characterization of HgSe:Fe Quantum Dots,
T. Tran-Anh, S. Hansel, A. Kirste, H.U. Mueller, M. von Ortenberg, J. Barner, J.P. Rabe,
Proc. of Solid Solutions of the II-VI Compounds – Growth, Characterization and Applications, Int. Symposium G, Zakopane, Poland, October 2002,
J. Alloys. Comp. **371** (2004) 198–201.

High magnetic field study of charge melting in $\mathbf{Bi}_{1/2}\mathbf{(Sr,Ca)}_{1/2}\mathbf{MnO}_3$ perovskites: Unconventional behavior of bismuth charge ordered compounds,
A. Kirste, M. Goiran, M. Respaud, J. Vanaken, J. M. Broto, H. Rakoto, M. von Ortenberg, C. Frontera, J. L. Garcia-Muñoz,
Phys. Rev. B **67** (2003) 134413.

Crossover in the Van Vleck paramagnet $\mathbf{TmPO_4}$,
A. Kirste, M. von Ortenberg, A.A. Demidov, Z.A. Kazei, N.P. Kolmakova, V.V. Platonov, A.A. Sidorenko, O.M. Tatsenko,
Physica B **336** (2003) 335–343.

HgSe:Fe quantum dots: growth and characterization,
Tuan Tran-Anh, Stefan Hansel, Alexander Kirste, Hans-Ulrich Mueller, Michael von Ortenberg
Proc. of the 11th Int. Conf. on Narrow Gap Semiconductors, Buffalo, New York, USA, June 2003,
Physica E **20** (2004) 444–448.

Rare-earth zircons and intermetallic compounds in megagauss-fields: investigation of new magnetic phenomena,
A. Kirste, N.P. Kolmakova, S. Hansel, H.-U. Mueller, M. von Ortenberg
Proc. of the 7th Int. Symposium on Research in High Magnetic Fields, Toulouse, France, July 2003,
Physica B **346–347** (2004) 191–195.

Are the crossover effects observable in $\mathbf{ErBa_2Cu_3O_{7-\delta}}$ and $\mathbf{ErVO_4}$ in pulsed magnetic fields,
Z.A. Kazei, A. Kirste, M. von Ortenberg, V.V. Platonov, O.M. Tatsenko, V.V. Snegirev
Proc. of the 7th Int. Symposium on Research in High Magnetic Fields, Toulouse, France, July 2003,
Physica B **346–347** (2004) 241–245.

High magnetic field study of charge/polaron ordering in $\mathbf{Bi_{1-x}Sr_xMnO_3}$ ($x \leq 0.50$) perovskites,
M. Respaud, A. Kirste, M. Goiran, J. Vanacken, J.M. Broto, H. Rakoto, A.E. Carillo, M. von Ortenberg, M. Hervieu, C. Frontera, J.L. Garcia-Muñoz,
Proc. of the 7th Int. Symposium on Research in High Magnetic Fields, Toulouse, France, July 2003,
Physica B **346–347** (2004) 70–73.

The Humboldt High Magnetic Field Center,
S. Hansel, A. Kirste, C. Puhle, M. Bayir, H.-U. Müller, M. von Ortenberg
Proc. of the 7th Int. Symposium on Research in High Magnetic Fields, Toulouse, France, July 2003,
Physica B **346–347** (2004) 623–626.

Investigation of magnetic properties in strong and ultrastrong magnetic fields using the single-turn coil technique: new phenomena in intermetallic compounds and rare-earth zircons,
A. Kirste, Z.A. Kazei, N.P. Kolmakova, S. Hansel, H.-U. Mueller, M. von Ortenberg
Proc. of the Int. Conf. on Magnetism, Rome, Italy, July 2003,
J. Magn. Magn. Mater. **272–276** (2004) e1677–e1678.

Infrared Spectroscopy in Transient Magnetic Fields,
S. Hansel, C. Puhle, A. Kirste, H.-U. Mueller, M. von Ortenberg, E. Hueynov
The 28th Int. Conf. on Infrared and Millimetre Waves, September 2003, Otsu, Shiga, Japan, Ed. N. Hiromoto (JSAP, 2003) p. 109.

Erklärung

Ich erläre hiermit, die Dissertation selbständig und nur unter Verwendung der angegebenen Hilfsmittel erarbeitet und verfaßt zu haben.

Ich habe mich weder anderwärts um einen Doktorgrad beworben noch besitze ich einen entsprechenden Doktorgrad.

Ich erkläre die Kenntnisnahme der dem Verfahren zugrundeliegenden Promotionsordnung der Mathematisch-Naturwissenschaftlichen Fakultät I der Humboldt-Universität zu Berlin.

Berlin, den 25. September 2003

(Alexander Kirste)